Characterisation of the intestinal epithelium and adult stem cell dynamics in the naked mole rats

Shamir Montazid

Balliol College

University of Oxford

Thesis submitted for the degree of

Doctor of Philosophy

Trinity Term 2023

Declaration

The research works described in this thesis have been carried out by myself in Irshad Lab, University of Oxford between October 2018 and June 2023. The data presented here were obtained by myself and contributions from collab§orators have been mentioned in relevant sections. No part of this thesis has been submitted for any degree in any university before.

Abstract

Naked mole rats (*Heterocephalus glaber*) are the longest-living rodents on earth that exhibit a low incidence of ageing-associated complexities (e.g. cancer, osteoarthritis, neurodegenerative diseases etc.). These subterranean eusocial mammals live in an arid, hypoxic environment with high oxidative stress. Evolution in such a damage-prone environment has made NMR an ideal model to study the adaptations of adult stem cells for long-term healthy tissue maintenance. In this study, we have characterised the intestinal epithelia, including the *Lgr5*$^{+}$ stem cells, in NMRs in a cross-species histological comparison with mice and humans. NMR intestines possess higher numbers of differentiated cells (enterocytes, goblet cells, and enteroendocrine cells) than mice, facilitating efficient nutrient absorption and protection against damage. Using *in vivo* cumulative DNA labelling, we show that intestinal *Lgr5*$^{+}$ cells in NMRs cycle slower than mice. However, these cells in the NMR colon have a similar cycling rate to humans. Additionally, we demonstrate that NMR intestines are more resistant to epithelial damage induced by Dextran Sodium Sulphate (DSS) than mice. However, despite not succumbing to any DSS-mediated tissue damage, *Lgr5*$^{+}$ cells in NMR intestines are hypersensitive to this colitogen and undergo apoptosis. In summary, the expanded pool of stem and differentiated cells in NMR intestines, along with the slow turnover rate of *Lgr5*$^{+}$ cells and their hypersensitivity to damage are a few adaptations we report here in this thesis that may allow these animals to maintain a healthy intestinal tissue for longer.

Acknowledgement

First, I would like to thank my primary supervisor, Dr. Shazia Irshad, for teaching me how to formulate a scientific hypothesis, design and conduct experiments in the lab, and interpret data to reach conclusions. During my DPhil, Dr. Irshad's close supervision has guided me to complete this thesis for which I am immensely grateful. I would also like to thank my secondary supervisors, Prof. Colin Goding and Prof. David Kerr, for supporting me whenever needed.

This thesis embodies a series of scientific experiments which have been possible due to the contributions of many researchers. I have conducted all the *in vivo* experiments on naked mole rats described in this thesis in the laboratory of Prof. Nigel C. Bennett (University of Pretoria). I would like to thank Dr. Daniel W. Hart (University of Pretoria) for hosting me during the field trips, organising the logistics, and supporting me to perform experiments in Pretoria during a strict lockdown due to the pandemic. Besides, I am thankful to Dr. Nan Gao and Dr. Sheila Bandyopadhyay (Rutgers University, Newark) for providing us with the intestinal tissues from mice administered with BrdU and Dextran Sodium Sulphate. My special thanks to Prof. Dustin J. Penn and Ms. Bettina Wernisch (Konrad Lorenz Institute of Ethology, Vienna) for sharing their colony of wild-caught mice from which tissues were collected by Dr. Shazia Irshad (University of Oxford) and Ms. Annamaria Tessitore (Novo Nordisk Research Centre, Oxford). I would also like to express my gratitude to Prof. James E. East (University of Oxford), Sri G. Thrumurthy, and Bu'Hussain Hayee (King's College Hospital) for providing the human colonoscopy samples used in this thesis. Besides, I am thankful to Dr.

Mukesh Bansal (Bristol Myers Squibb), Dr. Fabian Rost (Technische Universitat Dresden), Dr. Philipp Altrock (Max Planck Institute of Evolutionary Biology), and Mr. Brian Johnson (University of California San Diego) for their consultations regarding statistical analysis.

Many people from the Radcliffe Department of Medicine (Oxford) have assisted me during my degree. I want to thank Dr. Esther Bridges for facilitating my mouse experiments under her project license. I am also thankful to Dr. Jana Koth (Wolfson Imaging Facility) for her regular advice and support to use the confocal microscope. My heartiest gratitude to Dr. Helena Meyer-Berg, Dr. Aline Azabdaftari, and Ms. Gulnar Abdullayeva for sharing their technical expertise from time to time. My long hours of experiments in the lab were enriched by the presence of Gemma Owens, Aik Seng Ng, Dharamveer Tatwavedi, Vickram Tittrea, and Juseong Lee.

The first four years of my DPhil study in Oxford were sponsored by Bangabandhu Science and Technology Fellowship, Bangladesh. I am also thankful to the Nuffield Department of Clinical Laboratory Sciences and Balliol College, Oxford for providing additional financial support during the final year of study.

Finally, I would like to acknowledge all the departmental admin staffs, research nurses, and the graduate studies team for facilitating my study in Oxford.

Contents

List of figures

List of tables

Abbreviations

5-FU	5-Fluorouracil
ABC	Avidin-Biotin Complex
ADAM	A Disintegrin And Metalloprotease
aDMP	ageing-associated Differentially Methylated Positions
AP	Alkaline Phosphatase
APC	Adenomatous Polyposis Coli
ASC	Adult Stem Cell
BER	Base Excision Repair
BMP	Bone Morphogenetic Protein
BrdU	5-bromo-2'-deoxyuridine
BSA	Bovine Serum Albumin
CBC	Crypt Base Columnar
CDK	Cyclin Dependent Kinase
ChrA	Chromogranin A
CK1	Casein Kinase 1
DAB	Diaminobenzidine
DAPI	4',6-Diamidino-2-Phenylindole Dihydrochloride
dCol	distal Colon
ddH_2O	double distilled water
dH_2O	distilled water
DLL1	Delta-like 1
DMEM	Dulbecco's Modified Eagle Medium
DSS	Dextran Sodium Sulphate

DTR	Diphtheria Toxin Receptor
ECI	Early Contact Inhibition
EdU	5-ethynyl-2-deoxyuridine
EGFP	Enhanced Green Fluorescent Protein
ENS	Enteric Nervous System
EpCAM	Epithelial Cell Adhesion Molecule
FBS	Fetal Bovine Serum
FFPE	Formalin-Fixed Paraffin-Embedded
FZ	Frizzled
GI	Gastrointestinal
GS	γ-Secretase
GSK-3	Glycogen Synthase Kinase 3
H and E	Haematoxylin and Eosin
HMM-HA	High Molecular Mass Hyaluronic Acid
HRP	Horseradish Peroxidase
HSP	Heat Shock Protein
HSPC	Haematopoietic Stem and Progenitor Cell
IACUC	Institutional Animal Care and Use Committee
IF	Immunofluorescence
IL	Interleukin
iPSC	induced Pluripotent Stem Cell
IR	Ionising Radiation
ISC	Intestinal stem cell
ISH	in situ Hybridisation
Lgr5	Leucine-rich repeat-containing G-protein coupled receptor 5

***Lgr5*$^{+CBC}$**	*Lgr5*$^{+}$ cell residing at the crypt base
LI	Labelling Index
LINE1	Long Interspersed Nuclear Element 1
LRC	Label Retaining Cell
mRNA	messenger RNA
NBF	Neutral Buffered Formalin
NER	Nucleotide Excision Repair
NICD	Notch IntraCellular Domain
NMR	Naked Mole Rat
NSPC	Neural Stem and Progenitor Cells
PARP	Poly (ADP-Ribose) Polymerase
PBS	Phosphate buffered Saline
pCol	proximal Colon
PFA	Paraformaldehyde
PHH3-S28	Phospho Histone H3 (Serine 28)
PI	Proliferation Index
QF	Quiescent Fraction
RCI	Regular Contact Inhibition
RFRP-3	RFamide-related peptide 3
rRNA	ribosomal RNA
SB1	Duodenum
SB2	Jejunum
SB3	Ileum
TA	Transit-amplifying
TBS	Tris-Buffered Saline

TER	Telomerase RNA
TERT	Telomere Reverse Transcriptase
T_{G0}	Duration of G0
T_{G1}	Duration of G1-phase
T_{G1+G2}	The combined duration of G1 and G2 phases
T_{G2}	Duration of G2-phase
T_{M}	Duration of M-phase
TNBS	Tri-Nitro Benzene Sulfonic-acid
T_{S}	Duration of S-phase
TUNEL	Terminal-deoxynucleotidyl-transferase dUTP Nick End Labelling
Uea-I	Ulex europaeus agglutinin-I

Chapter 1: Introduction

1.1 Unique biology of naked mole rats

In this chapter, I will first describe (section 1.1.1 to 1.1.4) several important characteristics of naked mole rats (NMRs) such as their evolutionary relatedness to other mammalian species (mice and humans), unique social structure, and lifecycle to provide an overview of their biology. Next, I will discuss (section 1.1.5 and 1.1.6) previously reported anti-ageing mechanisms in NMRs to highlight their importance in longevity research. In section 1.1.7, I will review the literature available on NMR intestinal tract, the organ I will be focusing on in this thesis, to identify gaps in the knowledgebase. Then, in section 1.2, I will summarise the tissue-structure, cell composition, and stem cell biology of the intestinal tract based on previous reports in mice and humans. Finally, in section 1.3, I will outline the major aims of this thesis to characterise the epithelial cell composition, stem cell kinetics, and damage response in naked mole rat intestines in a cross-species comparison with mice and humans.

1.1.1 Taxonomy of naked mole rats

The naked mole rats (Figure 1.1) are small rodents that weigh about 35 gm[1] and live in the arid-subterranean environment of Africa (Somalia, Ethiopia, Kenya, and Djibouti)[2]. They exhibit unique cranial (smaller jugal supported anteriorly by the zygomatic maxillary) and postcranial features (lack of papillae in the colon, uncoiled caecum etc.), dental pattern (fewer molar teeth), and social characteristics (facultative inbreeding, frequent reproduction etc.) compared to other African mole rat species[3]. Therefore, NMRs are categorized as the only member of the Heterocephalidae family, separate from other African mole rats who belong to the Bathyergidae family[3]. Their genus name *Heterocephalus* also refers to the unique

anatomical features of the skull (mentioned above) while the species adjective *glaber* (bald) denotes the apparent hairlessness of their skin, giving them the name-*naked* mole rat[4]. Despite being called *naked*, NMRs have about 100 sensory hairs that help them perceive their environment[5].

Kingdom: Animalia

Phylum: Chordata

Class: Mammalia

Order: Rodentia

Family: Heterocephalidae

Genus: *Heterocephalus*

Species: *Heterocephalus glaber*

Figure 1. 1: Digital photograph of an adult naked mole rat (4 inches in length).
The image was reproduced from the Flickr stream of the Smithsonian's National Zoo[6] under the creative commons license (CC BY-NC-ND 2.0). An adult naked mole rat weighs about 35 gm and is roughly 4-inch-long (head to body)[1].

1.1.2 Phylogeny of naked mole rats

Phylogenetic analysis is a useful tool to comprehend the evolutionary kinship between different species. The whole genome sequencing of NMR has revealed 93% synteny (co-localisation of genes on the same chromosome) of its genome to mouse and human[5]. This suggests a low rate of rearrangement in NMR genomes after they had separated from a common ancestor with mouse and human[5], highlighting their evolutionary closeness. A phylogenetic tree constructed by comparing the sequence similarity between single-copy orthologous genes has shown that the NMR genome is evolutionarily related to other mammals (mouse, rat, rabbit, human, monkey, and dog) (Figure 1.2)[5]. NMRs diverged from their common ancestors with mice and humans 73 and 93 million years ago respectively, showing a similar evolutionary kinship between these species (Figure 1.2)[5].

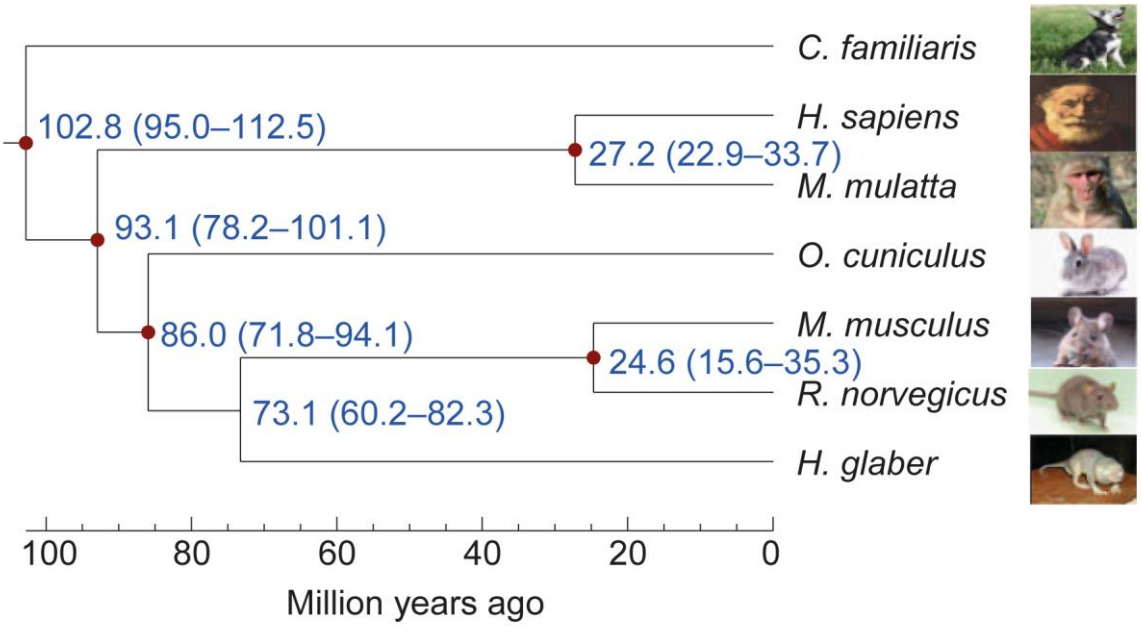

Figure 1. 2: Phylogenetic relationship of naked mole rats to other mammals.
Based on the sequence similarity between single-copy orthologous genes, the times (error range in brackets) when naked mole rats diverged from six other mammalian species have been shown in a phylogenetic tree. Distances of divergence are shown in million years. The figure was reproduced from Kim *et al.*[5] under the creative commons licence (CC BY-NC-SA 3.0).

Van Dijk *et al.* performed another phylogenetic analysis based on the distribution of principal hippocampal cell number in 20 mammalian species and reported that NMRs are more closely related to other African mole rats, mice, humans, rats, and monkeys than dogs and pigs[7]. These studies have highlighted the evolutionary kinship of NMRs with other mammalian species indicating that NMR-specific molecular mechanisms might be transferrable to mice and humans.

1.1.3 Social structure of naked mole rats

Despite the high genomic similarity to other mammalian species, NMRs lead a unique social life. They are one of the two mammalian species (the second one is the Damaraland Mole Rat) known to exhibit a eusocial colony structure[8]. NMR colonies have a dominance hierarchy based on body size[9] and generally consist of 60-90 individuals[10]. The workload of the colony is divided between two roles: breeders, which include the queen and 1-3 large male members that perform all the reproductive activities inside a colony and non-breeders/subordinates which are smaller in size and carry out multiple activities like digging underground tunnels, foraging for food, caring for the pups, and protection from predators[8,11]. Due to the consanguineous nature of mating, NMR has the highest inbreeding coefficient (probability of having same number of repeats at minisatellite loci) among wild animals[12]. However, sometimes physiologically and morphologically distinct subordinates called *dispersers* can outbreed with non-colony members[13]. Additionally, isolated non-breeders paired with a member of the opposite sex can mature sexually, indicating that abstinence by subordinate NMRs is socially stimulated by the queen[14].

Communication between the colony members is maintained by a distinct soft chirp which is unique to each NMR colony[15]. After gestation, the queen releases estradiol in the faeces which stimulates the subordinates, following coprophagy, to respond to the pup's vocalization and provide alloparental care[16]. The queen can also pressurize lazy subordinates to work by an aggressive behaviour called shoving[17]. Each colony also has a distinct scent that helps members identify each other and exclude intruders (xenophobia)[18].

1.1.4 Lifecycle of naked mole rats

A queen NMR breeds throughout the year[19,20]. During an oestrous period of 2-24 hours, the queen copulates with the oldest, largest, and most distantly related male member(s) of the colony[21]. A typical gestation period in NMR lasts 70 days on average, resulting in 11-13 small pups (body mass 1-2 gm) per litter[20]. A single litter can contain offspring from up to 3 sires. After the birth of a litter, the queen becomes ready to reproduce again within 7-11 days[22].

The newborn NMRs are cared for by the queen and non-breeders from the same colony[8]. Juveniles are weaned at 36 days and become active workers of the colony[22]. Female NMRs can reach puberty within 7-8 months of birth while male NMRs take up to a year[22]. However, the sexual maturation process in NMRs remains socially suppressed by the aggressive behaviour of the queen[14] that results in the production of RFamide-related peptide 3 (RFRP-3), a negative regulator of gonadotropin-releasing hormone, responsible for delaying puberty[23].

Once a queen dies, larger female members of the colony compete and reach sexual maturation to gain the new queen status[11]. After becoming reproductively mature, a queen will produce, on average, 5 litters per year[20]. She will continue to reproduce at the same efficiency until the end of her lifespan (25 years)[24]. Major causes of death in NMRs are fighting between colony members, scarcity of food, infection by parasites and pathogens, and predation by snakes, owls and raptors[10].

1.1.5 Naked mole rat as a model of healthy ageing

Lopez-Otin *et al.* have summarised the biological hallmarks of ageing across different organisms in their seminal review article[25]. With increasing age, there is an accumulation of DNA damage, shortening of telomeres, alteration of DNA methylation, histone modification and chromatin remodelling, disruption of proteostasis, impairment of nutrient sensing and uptake, mitochondrial malfunction, elevated level of cellular senescence, exhaustion of the regenerative capacity of stem cells, and disrupted intracellular communication[25]. All these abrasions lead to a higher incidence of chronic diseases like cancers, loss of reproductive ability, and wound-healing capacity in older individuals of a species. However, numerous studies have reported that the naked mole rat is an exception to this.

Up to 80% of NMRs live up to 25 years in captivity[26] while the oldest reported NMR survived 37 years, making them the longest-living rodents[2]. The maximum lifespan of NMR is five times longer than its expected longevity of 6 years based on body weight (35 gm)[24]. During this remarkably long life, minimal cancers (one case each of hepatocellular carcinoma, nephroblastoma, lymphosarcoma, and esophageal adenocarcinoma) have been recorded after analysing more than 800

individuals[24,27]. Breeding NMRs maintain an undiminished fertility beyond 30 years[24]. Primordial Germ Cells (PGCs) in female NMRs continues proliferation at least until 90 days after birth resulting in a large ovarian reserve which is thought to support their lifelong fecundity[28]. Additionally, there is no age-associated decline in cardiac function of NMRs assessed up to 24 years of age[29]. Over a similar period, researchers have also reported no change in the basal metabolic rate, body composition (body mass, proportion of body fat, and bone mineral density), and intestinal glucose transport in NMRs with age[30]. These studies highlight the unique anti-ageing features of NMRs.

1.1.6 Anti-ageing mechanisms in naked mole rats

1.1.6.1 Maintenance of genome integrity by naked mole rats

Longer living species are thought to have evolved a better genome maintenance system[31]. Sequencing of colon crypts in 16 mammalian species has shown that longer-living animals have a slower mutation accumulation rate compared to short-lived mammals[26]. Similarly, somatic mutation frequency in lung fibroblasts from mice, guinea pigs, humans, blind and naked mole rats following bleomycin treatment exhibits an inverse correlation with lifespan[32]. These observations suggest the presence of unique mechanisms in long-lived species like NMR to reduce mutation accumulation during homeostasis and under stress.

Publication of the whole genome assembly of NMRs revealed several molecular basis about how they maintain genomic integrity[5]. Despite having a similar genome size (around 3 Gb), NMR genomes contain a lower percentage (approximately 25%) of transposon-derived repeat sequences compared to humans, mice, and rats (35-

40%)[5]. Long Interspersed Nuclear Element 1 (LINE1), a retrotransposon element that can act as an endogenous mutagen by jumping between genomic regions and initiating sequence deletion and/or genomic instability via homologous recombination, represents a 24% lower proportion of the genome and 90% less transposition activity in NMR skin fibroblasts when compared to mice and humans[33].

Few additional mechanisms have been reported to contribute to genomic integrity in NMRs. Alternate splicing of tumour suppressor genes *Cdkn2a–Cdkn2b* in NMR results in a fusion between $p15^{INK4B}$ (exon 1) and $p16^{INK4A}$ (exon 1 and 3) to produce an additional Cyclin Dependent Kinase (CDK) inhibitor, pALT, which can arrest proliferation signals during homeostasis[34]. Under stressful conditions (UV/gamma radiation and oncogenic transformation), pALT exhibits higher efficiency in arresting cell cycle progression by Early Contact Inhibition (ECI) compared to $p15^{INK4B}$ and $p16^{INK4A}$. Thus, pALT-mediated cell cycle suppression results in better maintenance of the genome during mutagenic insults in NMRs.

In contrast to mice and humans where regular contact inhibition (RCI) is usually mediated by $p27^{Kip1}$, NMR fibroblasts induce ECI via $p16^{INK4A}$. However, upon downregulation of $p16^{INK4A}$, NMRs can still activate the canonical $p27^{Kip1}$-mediated pathway to induce RCI[35]. Therefore, cancerous growth in NMRs would require the dual inactivation of the genes encoding $p16^{INK4A}$ and $p27^{Kip1}$. Additionally, skin fibroblasts in NMR also secrete a High Molecular Mass Hyaluronic Acid (HMM-HA) that can activate the tumour suppressor *Cdkn2a–Cdkn2b* locus by interacting with the CD44 receptor resulting in an ECI[36]. In summary, while human and mouse fibroblasts perform RCI via the $p27^{Kip1}$ pathway, NMR fibroblasts manifest ECI via

p16^{INK4A} and/or pALT. This ECI is further assisted by a unique glycosaminoglycan, HMM-HA.

p53 and Rb1 are tumour suppressor proteins that halt cell cycle progression and activate senescence/apoptosis following DNA damage[37]. While mutations in either *Tp53* or *Rb1* genes result in rapid proliferation in human and mouse cells[38], NMR skin fibroblasts undergo rapid apoptosis following a loss of function of these two key tumour suppressors[35]. Additionally, the p53 protein in NMR embryonic fibroblasts has a ten times longer half-life than in same cells in mice and humans[39]. Even before DNA damage, the stable p53 is constitutionally localized in the nucleus[39].

DNA repair pathways significantly contribute to the genome maintenance of a species. NMR genome contains three copies of the *CEBPG* (CCAAT/Enhancer Binding Protein-Gamma) gene, a positive regulator of the DNA repair pathway, while other mammalian genomes have a single copy[40]. NMR skin fibroblasts demonstrate a 2-times more efficient Base Excision Repair (BER) and Nucleotide Excision Repair (NER) system than mice following UV irradiation[41]. Quantification of the activity of poly (ADP-ribose) polymerase (PARP), a protein involved in the BER pathway, has shown a strong positive correlation with lifespan in 13 mammalian species[42]. In agreement with this, a study has reported NMR fibroblasts to have a higher level of PAR synthesis (i.e., PARP activity) compared to mice[43]. In brief, NMRs have evolved molecular mechanisms to induce early contact inhibition, apoptosis, and optimised repair mechanisms following DNA damage which most likely contribute to maintain genomic integrity during their long lifespan (Figure 1.3).

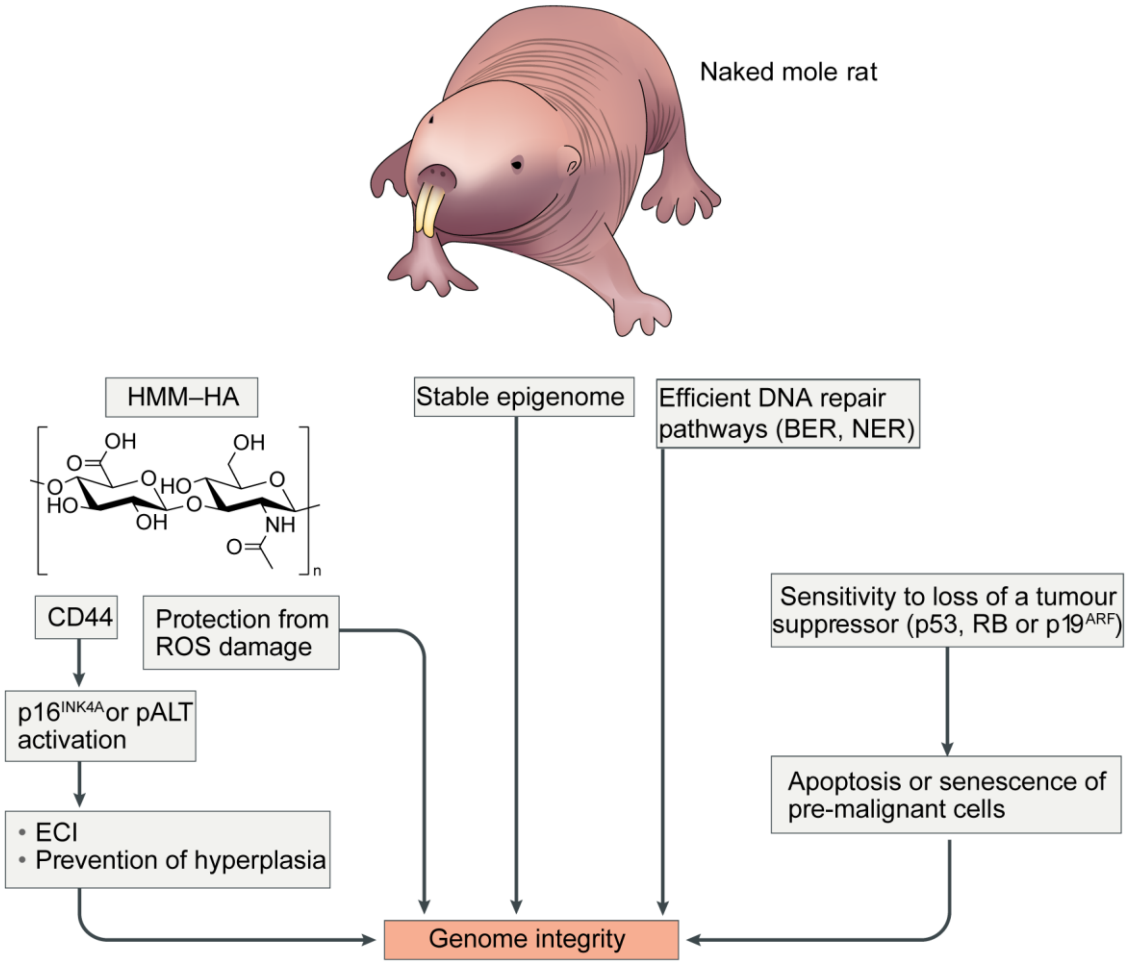

Figure 1. 3: Mechanisms of maintaining genome integrity in naked mole rats.
Multiple pathways in naked mole rats that aid in preserving genome integrity have been presented in this figure. Here, HMM-HA: High Molecular Mass Hyaluronic Acid, ROS: Reactive Oxygen Species, ECI: Early Contact Inhibition, BER: Base excision repair, NER: Nucleotide excision repair. The figure was reproduced from Suleanov *et al.*[31] with permission from Springer Nature (license no 5521880025528).

Despite these protective mechanisms, Hadi *et al.* have demonstrated anchorage independent growth of NMR fibroblasts (from intestine, pancreas, lung, skin, and kidney) in soft agar by simultaneous transduction with two oncogenic viruses (*SV40LT* and *HRAS*^{G12V}) where transduction with *SV40LT* alone does not result in cancerous growth in culture[44]. Therefore, NMR fibroblasts are not resistant to *SV40LT* and *HRAS*^{G12V}-mediated oncogenic transformation which suggests the

possibility of non-cell autonomous mechanisms (microenvironment/immune system) of tumour suppression in NMRs that are yet to be discovered.

1.1.6.2 Telomere retention in naked mole rats

Telomeres act as protective caps for chromosomes and guard against replicative senescence. The length of telomere is species-specific and determines the so-called “Hayflick limit” of cellular replication[45]. NMRs have roughly 50% shorter telomere length than mice and rats in blood, but exhibit no reduction in telomere length with age[46]. While mice and humans exhibit continuous telomere attrition during ageing[46,47], telomere retention in NMRs probably acts as an anti-ageing mechanism by delaying replicative senescence (that can result in ageing-associated diseases[48]) in this species.

Telomere are repaired by a telomerase complex that contains two major components: the Telomere Reverse Transcriptase (TERT) enzyme that performs the telomere repair and the Telomerase RNA subunit (TER) that carries a non-coding RNA serving as a template for telomere synthesis[49]. There is another protein complex called Shelterin (includes TRF1, TRF2, TINF2, RAP1, TPP1, and POT1) that binds to the telomere and protects it from being repaired by the DNA repair pathways leading to chromosome fusion[49].

Various adaptations have been reported in the telomerase complex of NMRs in previous studies. A stable expression of TERT has been reported across ages in NMRs, consistent with the unchanged telomere length during ageing in this species[50]. The *TER* sequence contains two polymorphisms in NMRs that might

result in higher telomerase activity[51]. Additionally, the *TER* promoter sequence contains an additional enhancer binding site for Sox17 transcription factor in NMRs that may contribute to superior telomerase function[51]. In the Shelterin complex, the NMR genome contains two copies of the *TINF2* gene while other mammalian species have a single copy[40]. The *TRF1* sequence in NMRs also contains two polymorphisms that result in tighter binding of telomere by TRF1/TINF2 under hypoxic conditions[52]. All these features of the telomerase complex in NMRs to maintain telomere length have been speculated as anti-ageing strategies to protect from diseases associated with cellular senescence.

1.1.6.3 Epigenetic stability in naked mole rats

Epigenetic modification of the genome involves changes in the methylation pattern of DNA, post-translational modification of histones, and remodelling of chromatin structures resulting in altered expression of genes. Using Assay for Transposase-Accessible Chromatin (ATAC)-sequencing, NMR skin fibroblasts were shown to contain a 10% lower number of open chromatin peaks in the coding region of the genome than mice[53]. This is thought to make the NMR epigenome stable (Figure 1.3) and show higher resistant to iPSC (induced Pluripotent Stem Cell) reprogramming using OSKM (Oct4, Sox9, Klf4, Myc) factors than mice[53]. Analysis of CpG islands in NMR blood, skin, and liver has found a 5-times increase in methylation status in ageing-associated Differentially Methylated Positions (aDMPs) with age (0 to 19 years), a sign of epigenetic ageing in NMRs[54,55]. However, consistent with previous predictions for long-lived species[56], NMRs exhibit a relatively slower rate of methylation in aDMPs when compared to mice and humans[54]. Interestingly, despite epigenetic clock being ticked (accumulation of CpG

methylation with age) in all NMRs, non-breeders have been shown to age faster than the queen[57]. Further studies on chromatin remodelling and members of the Sirtuin protein family (protein deacetylases and ADP ribosyltransferases) are yet to be conducted in NMRs which might provide additional explanations for their remarkable longevity.

1.1.6.4 Protein homeostasis in naked mole rats

Protein homeostasis (proteostasis) is maintained in a cell via efficient translation by ribosomes, chaperon-mediated post-translational folding of proteins, degradation by proteasome complexes, and autophagy. The expression levels of proteins involved in the proteasomal activity and autophagy in the livers and muscles of eight rodent species have been shown to be proportional to the lifespan of a species[58]. Another cross-species study involving skin fibroblasts from 12 mammalian species (from mouse to bow-head whale) has identified an inverse correlation between the rate of protein degradation and lifespan[59]. Additionally, the speed of RNA polymerase II increases with age across different phyla of the animal kingdom (fly, nematode, rodent, and mammal) and reduction of its speed (due to genetic variation or by overexpressing histone proteins) has been shown to extend longevity in fruit flies and roundworms[60]. These studies indicate that cellular machineries involved in maintaining proteostasis contribute to longevity.

A study on skin fibroblasts has reported that 28S ribosomal RNA (rRNA) in NMRs is divided into two fragments which might be linked to more efficient protein translation[61]. Further comparative analysis with mice demonstrated that translation fidelity in NMRs is 4 times higher, indicating better proteostasis in this species[61].

Additionally, NMR skin fibroblasts also have enhanced macro-autophagy, an elevated response by Heat Shock Proteins (HSP), and higher 20S proteasome activity than mice[62]. With age, NMRs also maintain an undiminished level of autophagy[63] and 20S proteasome activity[64], and resist oxidation of thiol groups in proteins[64] indicating better proteostasis than short-lived mice. Under stress conditions leading to protein misfolding (i.e., exposure to Urea[64] and L-AZC[59]), NMR proteins can prevent alteration of their structures to a greater extent than mice[59,64]. All these studies collectively indicate that NMRs have evolved improved cellular mechanisms that maintain protein homeostasis both under physiological and stress conditions. These mechanisms also remain unchanged during ageing and may contribute to their remarkable lifespan.

1.1.6.5 Preservation of stem cell function in naked mole rats

Studies of stem cells in naked mole rats have unveiled several interesting differences to mice. With age, NMRs exhibit no sign of immuno-senescence[65] while mice show alterations in blood cell lineages[66]. Haematopoietic Stem and Progenitor Cells (HSPC) in NMRs are marked by CD34 and THY1 expression which is similar to other primates but different from mice[65]. HSPC population in NMRs has a 4-times lower metabolic rate, 2-times lower proportion of cells in S-phase, and 20% higher proportion of the cells in G1-phase than mice, indicating an evolutionary adaptation to prevent stem cell exhaustion in NMRs by slowing down cell division rate[65]. Moreover, HSPCs in NMRs are more sensitive to genotoxic insults (5-fluorouracil) and exhibit 100% loss of cells within 15 days of treatment while almost no cell loss is observed in mice[65], highlighting another strategy to avoid damage accumulation in NMRs over time.

In the NMR brain, neural stem and progenitor cells (expressing Sox2, Nes, Msi1) also exhibit a 50% longer doubling time in culture than mice by having 10% higher fraction of the population in G0 and/or G1 phase[67]. These cells can also initiate a more efficient response to radiation-induced DNA damage by expressing p53-Binding Protein 1 (53BP1) foci in 2-times higher percentage of cells (10 min after radiation) and phosphorylated Ataxia-Telangiectasia Mutated (pATM) foci in 3-times higher proportion of cell (1 hour after radiation) than mice which can guard against mutation accumulation in NMR neural stem cells[67]. In the skin, NMRs maintain a similar number of stem cells and undiminished wound-healing potential over time[68]. Unlike humans and mice, skin stem cells in NMRs express a higher level of *Igfbp3* in older animals[68]. *Igfbp3* can activate PI3K/Akt/mTOR signalling pathway and downregulates autophagy during ageing[69]. So far, these studies on Adult Stem Cells (ASCs) in blood, brain, and skin have revealed evidence of slower cell cycle rate in NMRs compared to mice which can contribute to healthy tissue maintenance during ageing. While all three studies established relatively slower kinetics of ASCs in NMRs than mice, none has determined the *in vivo* total cell division time of ASCs including the duration of each cell cycle phases (G0, G1, S, G2, M) in NMRs. Besides, studies on ASCs of other tissues (e.g., intestine, lung, liver, prostate, and kidney) in NMRs are yet to be reported. Hence, this thesis would focus on determining the *in vivo* ASC division time in NMR small intestine and colon in comparison with mice while delineating the durations spent by ASCs in each cell cycle phase.

1.1.6.6 Efficient nutrient sensing in naked mole rats

Downregulation of mTOR1, a key signalling molecule promoting anabolism, extends lifespan in yeast, worms, and flies[70]. Additionally, dietary restriction and downregulation of glucose uptake by insulin and Igf1 signalling result in increased longevity in worms, flies, mice, and primates[71]. Therefore, a link between low nutrient uptake and healthy ageing seems evident as lower metabolism results in the production of fewer reactive oxygen species. In NMRs, exposure to hypoxia decreases *Igf1r* expression in the liver[72], indicating an adaptive mechanism to slow down metabolism. Overall, there is a downregulation of ribosomal protein biosynthesis in NMR muscle, lung, and brain in NMRs under a hypoxic environment[72]. Another study reported that *Igf1* remains downregulated during ageing in NMRs[73]. Though study targeting nutrient sensing mechanism in NMRs is scarce, the existing literature suggests longevity in NMR may be linked to reduced nutrient uptake and slowing down of metabolism.

1.1.7 The Intestinal biology of naked mole rats

The intestine performs the crucial function of digestion and absorption of food that supplies metabolic energy for the entire body. NMRs have the most distinct anatomical features within the intestine, that includes the lack of coiling in the caecum and ascending colon, among six African mole rat species[74]. NMRs also have the shortest intestinal length among African mole rats[74]. Among all mammals, NMR is the only species known to have a caecum with a lower temperature than other body parts, creating an internal heat sink to dissipate metabolic energy[75]. With ageing, Sodium/glucose co-transporter-1 (Sglt1) receptor activity for glucose absorption is reduced up to 60% in mice while a modest 30% decrease is observed

in NMRs[30], indicating less susceptibility to age-induced disruption of nutrient uptake in this species.

Characterisation of the gut microbiome in NMRs has also shown distinct features linked to longevity. NMR microbiota can alter significantly based on environment and diet[76,77]. Their gut microbiota shows a high propensity for oxidative metabolism, enhanced capacity to produce short-chain fatty acids, and mono and disaccharides[78]. Interestingly, the NMR gut also exhibits microbiome features similar to human centenarians and Hadza hunter-gatherers (high proportions and diversity of *Spirochetaceae* and *Mogibacteriaceae*), a sign of longevity adaptation[78]. However, there is no report on the intestinal microstructures, epithelial cell distribution, and intestinal stem cell properties that can provide further insights into their gut function. Therefore, this thesis will aim to characterise the cellular composition of the intestinal epithelia, including the stem cells, in NMRs in a cross-species comparison with mice and humans to identify any difference that might shed light into their healthy tissue maintenance.

1.2 Structure of the mammalian intestine

The gastrointestinal (GI) tract performs the digestion and absorption of nutrients from the food that fuels metabolic activities in a mammalian body. It spans from mouth to anus and is composed of the oral cavity, oesophagus, stomach, small and large intestines, and rectum. The intestine, located inside the abdominal cavity, is the largest part of the GI tract spanning from the beginning of the duodenum (proximal third of the small intestine) to the end of the colon. A large part of digestion and almost the entire process of absorption of food takes place within this organ. Besides, in conjunction with the enteric nervous system, the intestine performs a rhythmic movement (peristalsis) that propels the passage of food and the excretion of stool[79]. To perform these coordinated and complicated functions, the mammalian intestines have evolved a hierarchical structure to divide their workload among different compartments and specialized cells[80,81]. This section describes the architecture of the intestinal tissue, as well as its microstructure and various types of cells that perform specific functions.

1.2.1 The tissue layers of the intestinal tract

The intestinal tract is composed of four adjacent layers of tissue that surround the gut lumen (Figure 1.4)[82]. The innermost layer in direct contact with the lumen is called mucosa. It is divided into three major components- the intestinal epithelium, lamina propria, and muscularis mucosa[82]. The intestinal epithelium is composed of a single layer of columnar epithelial cells that serve as a barrier between the lumen and the intestinal tissue. The digestion and absorption of nutrients in the intestine are performed by several differentiated cell types in this layer[80]. Intestinal stem cells (ISC) are also located in the epithelium and drive the self-renewal of the tissue[83].

Underneath the epithelia, a network of loose connective tissue amalgamated with mesenchymal cells (fibroblast and myofibroblast) forms the lamina propria that provides the key niche signalling for the maintenance and differentiation of stem cells[84,85]. The muscularis mucosa, consisting of several thin layers of fibrous smooth muscle, is located beneath the lamina propria[82]. It segregates the mucosa from the submucosa region and agitates the intestinal epithelium to release mucus and other secretory components[79].

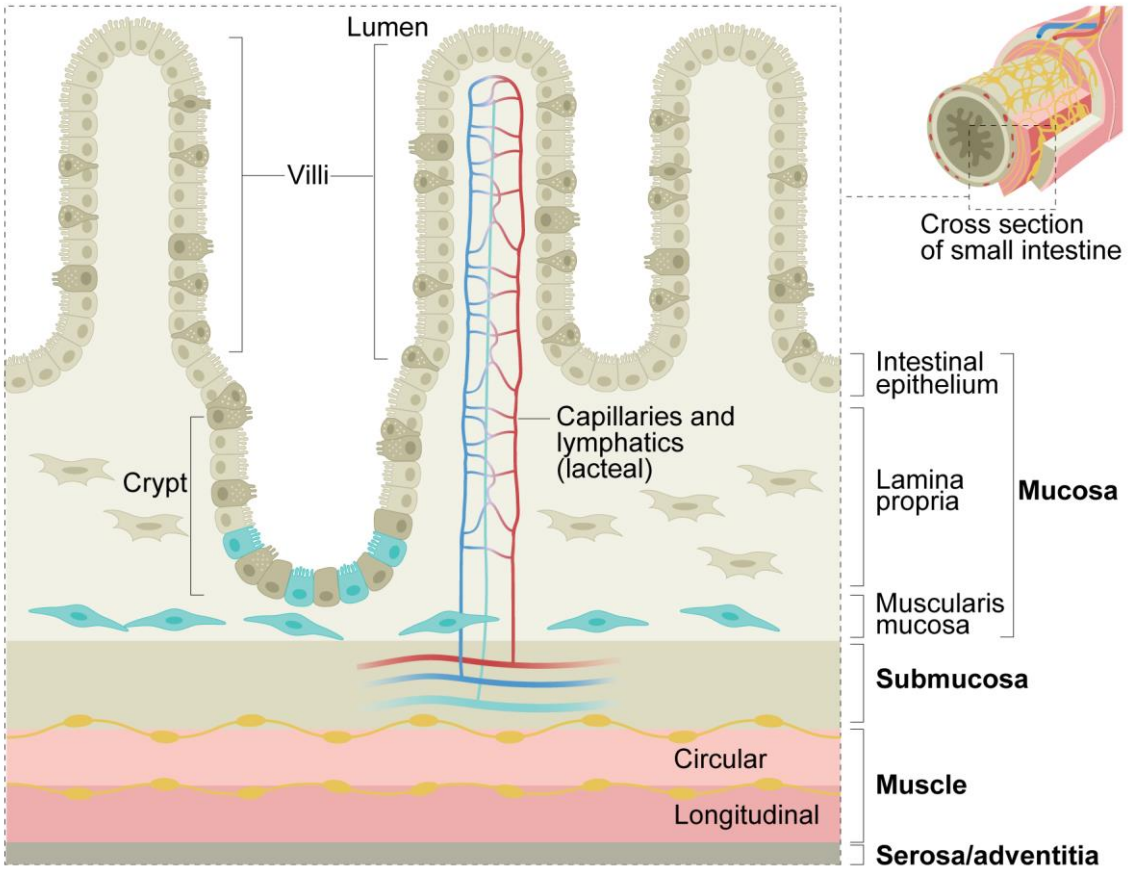

Figure 1. 4: Tissue architecture of the intestinal tract.
Schematic representation of the cross section of four layers of tissues in the intestine: Mucosa surrounds the lumen and comes in direct contact with food. Submucosa wraps around the mucosa and consists of blood vessels and elastic fibres. A muscle layer consisting of circular and longitudinal smooth muscles and nerve cells creates peristaltic movement. The outermost serosa/adventitia is composed of connective tissue coated in mucin that prevents damage from mechanical friction with other tissues. The figure was reproduced from Tullie *et al.*[82] with permission from Springer Nature (license no 5521860943770).

The submucosa is a layer of connective tissue that provides elasticity to the intestine while maintaining its structure[82]. It contains blood vessels and lymphatics that penetrate the mucosal structures as capillaries and lacteals, respectively[86]. Together with the lymphovascular system, the submucosa layer performs a key role in maintaining fluid homeostasis, transport of dietary fat and other nutrients, and screening by the immune system for detecting pathogen invasion[82].

The muscle layer is the third tissue from the lumen, and it consists of two sheets of circular (inner) and longitudinal (outer) smooth muscles. Between these two muscles, there are ganglionated submucosal and myenteric plexuses that form the Enteric Nervous System (ENS), often termed the *second brain* due to the presence of a large number of neurons in the gut[87]. Under the regulation of the ENS, the muscle layer generates peristalsis, a rhythmic movement of the intestine that assists the passage of food through the gut lumen[88]. In the small intestine, the circular muscle layer creates a second type of involuntary movement called segmentation that helps the excretion of gastric fluids from the epithelia by agitation and improves the contact of the epithelia with food[79]. The mucosa, submucosa, and the muscle layer of the gut wall work together by providing feedback regulation for epithelial growth, hormone secretion, and interaction with luminal microbes[87].

The outermost layer in the intestinal wall is composed of loose connective tissue coated with mucus to prevent mechanical damage to the intestine by its friction with other organs. This layer is termed serosa for the region of the intestine located in the body cavity (peritoneal: stomach and small intestine) and adventitia for the retroperitoneal sections (oesophagus, colon, and rectum)[89]. In summary, the four

tissue layers in the intestinal wall are made of various epithelial, mesenchymal, muscular, endothelial, and nerve cells that support the structural integrity of the organ, assist in digestion, absorption, bowel movement, and maintain vascular connections with other organs of the body.

1.2.2 Intestinal crypts and villi

The intestinal epithelium performs the crucial task of digestion and absorption of nutrients while enduring sheer mechanical stress, extreme pH of stomach acid, and microbial invasions[80,82]. All these pressures have forced the intestinal epithelium to evolve specialised structures to compartmentalise its functions. In the small intestine, the epithelial layer protrudes into the lumen creating finger-like structures called *villi* (Figure 1.4). The villi consist of differentiated cells having large surface area and secretory abilities that help the digestion and absorption of food[80]. The mesenchymal region inside the villi is riddled with blood and lymph capillaries that ensure efficient delivery of absorbed nutrients to the liver (Figure 1.4)[82]. However, as villi are continuously exposed to the harsh environment of the lumen, the cells in murine villi have a rapid turnover of 2-7 days[90]. Thus, having villi-like structures has enabled the intestine to increase the surface area for luminal contact while avoiding the accumulation of damage with a rapid cellular turnover as differentiated cells exposed to the harsh environment of the lumen will regularly undergo apoptosis at the tip of the villus[80]. But such structures are not suitable for harbouring the sensitive Intestinal Stem Cell (ISC) population.

At the bottom of the villi, the intestinal epithelium invaginates into the lamina propria region and creates a U-shaped structure called a *crypt* (Figure 1.4)[91]. The intestinal

stem cells (ISC) reside at the base of the crypt[83], away from the damage-prone environment of the lumen. The ISCs continuously receive key signalling molecules from the mesenchymal cells to maintain their proliferation and differentiation into either absorptive or secretory cell populations[84,85]. From a cellular signalling point of view, the crypt can be divided into three regions- stem cell zone, transit amplifying zone, and differentiated zone (Figure 1.5)[80]. The cell at the crypt apex is labelled as position 0 and differentiated/transit amplifying cells on the either side of the crypt are numbered as +1, +2, +3, and so on. ISCs reside in the stem cell zone at the base of a crypt (positions 0 to +3 in mouse small intestine) where niche signalling to maintain stemness is at its highest level[92]. These cells are numbered as position 0, 1', and 2' (Figure 1.5)[83]. As ISCs divide and push themselves upwards, they become progenitor cells in the transit amplifying zone by committing to one of the two cell lineages (secretory or absorptive)[80]. Progenitors are a rapidly cycling crypt cell population that multiply faster than the ISCs[93,94]. Further cell divisions push the progenitor cells into the differentiated zone (crypt neck to the villous tip) where they mature to perform specialised functions. Mesenchymal cells in the lamina propria create an intricate balance of morphogen gradients by secreting Wnt, Grem1, Sox9, EphB2, and Bone Morphogenetic Protein (BMP) that maintain the three regions of the crypt[84,85].

In summary, the cellular hierarchy in the intestine can be described as a *conveyer belt* of cells moving from the base of the crypt to the tip of the villi where they undergo apoptosis and shed into the lumen[95]. The rapid turnover of tissue is propelled by the division of stem cells located at the crypt base. These cell divisions are tightly regulated by mesenchymal cells' signalling. The progenitor cells,

produced by the ISCs, commit to the differentiation lineages in the transit-amplifying zone and undergo changes to perform secretory or absorptive functions in the differentiated zone (crypt-villous junction and villi). When differentiated cells reach the tip of the villi, they initiate programmed cell death to protect the tissue from accumulating damage[80].

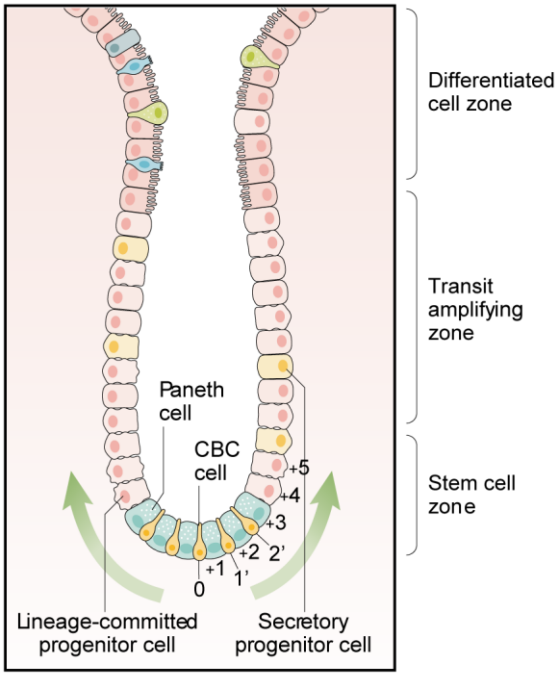

Figure 1. 5: Organisation of cellular hierarchy in the intestinal crypt.
A schema showing the hierarchical positions of stem, transit amplifying, and differentiated cells in the small intestinal crypt of mice. The figure was reproduced from Gehart *et al.*[80] with permission from Springer Nature (license no 5521860408012).

In contrast, the colon does not perform any digestive function and only absorbs the remaining water in the diet, lacking the requirement of metabolically expensive villi[96]. Generally, colonic crypts are longer than intestinal ones[97], with a broader differentiated zone containing mucus-secreting goblet cells and absorptive colonocytes.

1.2.3 Differentiated cell populations in the intestine

There are six major differentiated cell populations in the intestinal epithelia that can be divided into two major types: absorptive and secretory cells[80]. When the ISCs reach the transit amplifying zone, they commit to one of the lineages based on the state of Delta-Notch signalling (Figure 1.6)[98]. Notch-activated progenitor cells commit to the absorptive lineage to become enterocytes and microfold (M) cells[80]. On the other hand, progenitor cells with inactive Notch signalling commit to the secretory lineage and express Delta-like 1 (DLL1)[80]. Some $DLL1^+$ cells from the transit amplifying zone migrate to the crypt base and become mature Paneth cells[98]. However, the majority of $DLL1^+$ cells migrate upwards to differentiate into goblet, enteroendocrine and tuft cells[98].

The majority of the differentiated cells in the intestine are enterocytes that perform the crucial function of terminal digestion of peptides and polysaccharides using enzymes present on their surface and absorption of the final products (Figure 1.7A)[99,100]. They are characterised by the presence of microvilli on the apical side (facing the lumen) that increase the surface area for absorption (Figure 1.7B)[101]. This long stretch of microvilli creates the *brush border* around villi marked by their expression of Villin[102], Aldolase B[103], and Alkaline Phosphatase (AP)[104,105]. Different types of transporter proteins present on enterocyte cell membranes uptake key nutrients: glucose by Sodium/glucose cotransporter, type 1 (Sglt1), fructose by Fructose transporter, type 5 (Glut5), and peptides by Peptide transporter, type 1 (Pept1)[106]. Lipid molecules are uptaken as chylomicrons (small vesicles) via simple diffusion through the enterocyte membrane[107]. All these absorbed nutrients are

passed onto the blood and lymphatic systems present under the basolateral membrane of the enterocytes (Figure 1.4)[82].

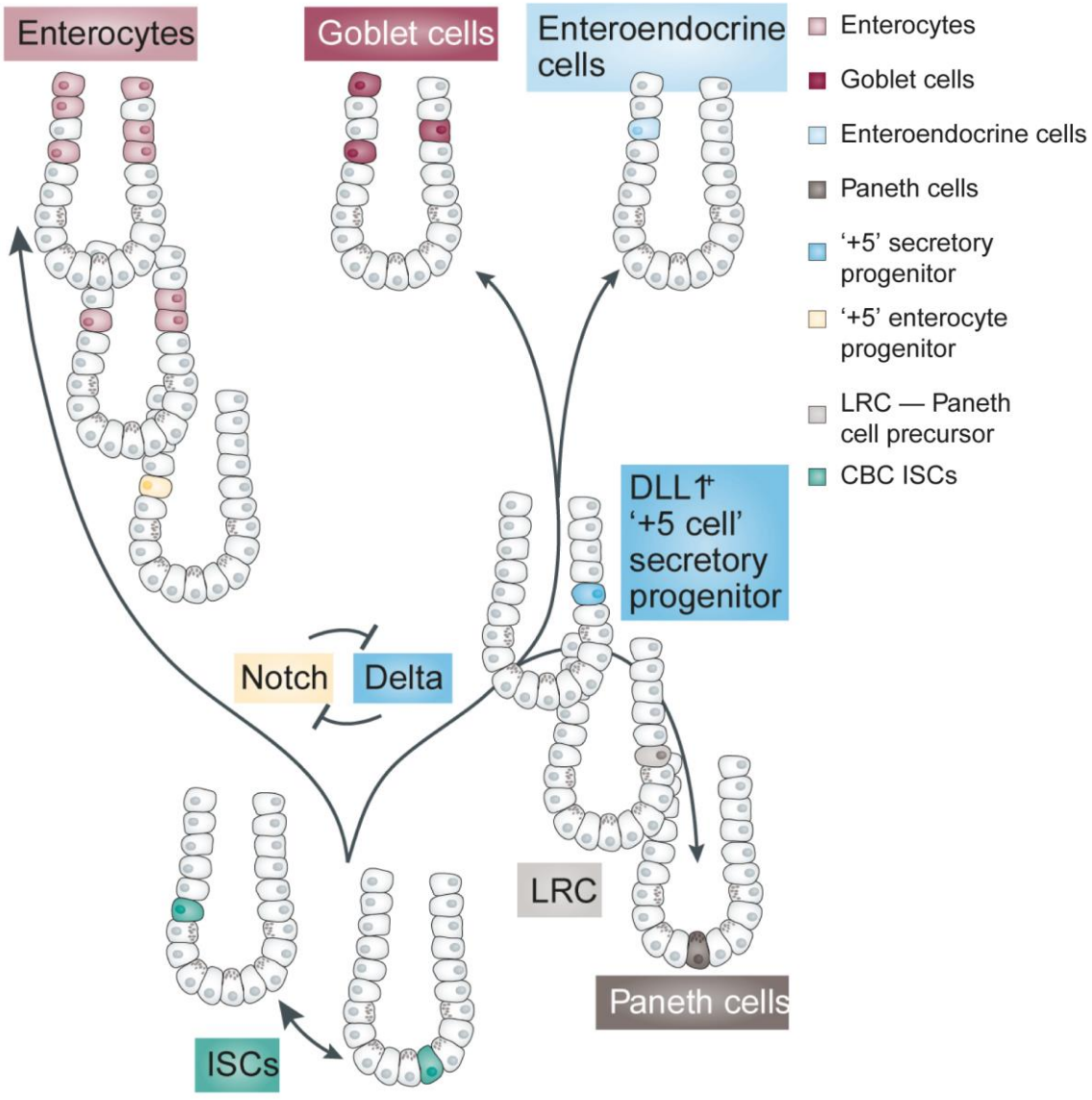

Figure 1. 6: Differentiation pathways of intestinal stem cells.
Upon leaving the crypt base (+5 position), the intestinal stem cells commit to either one of the two differentiation pathways: active Notch signalling (left) leads cells to become absorptive enterocytes while triggering of Delta pathway (right) stimulates the cells towards secretory lineages (Paneth, goblet and enteroendocrine cells). Here, ISC: Intestinal Stem Cell, DLL1: Delta-like1, LRC: Label Retaining Cell. The figure was reproduced from Vermeulen *et al.*[98] with permission from Springer Nature (license no 5521861389530).

Microfold (M) cells are the second absorptive cell population present in villi located above Payer's patches, lymphoid follicles present in the intestine containing B-cells

and T-cells. M-cells perform immune surveillance in the lumen and present antigens to the adaptive immune cells beneath them[108]. Expression of *Ulex europaeus* agglutinin-I (Uea-I) lectin specific for recognizing α(1,2)-fucose is used to identify M-cells in immunological assays[109].

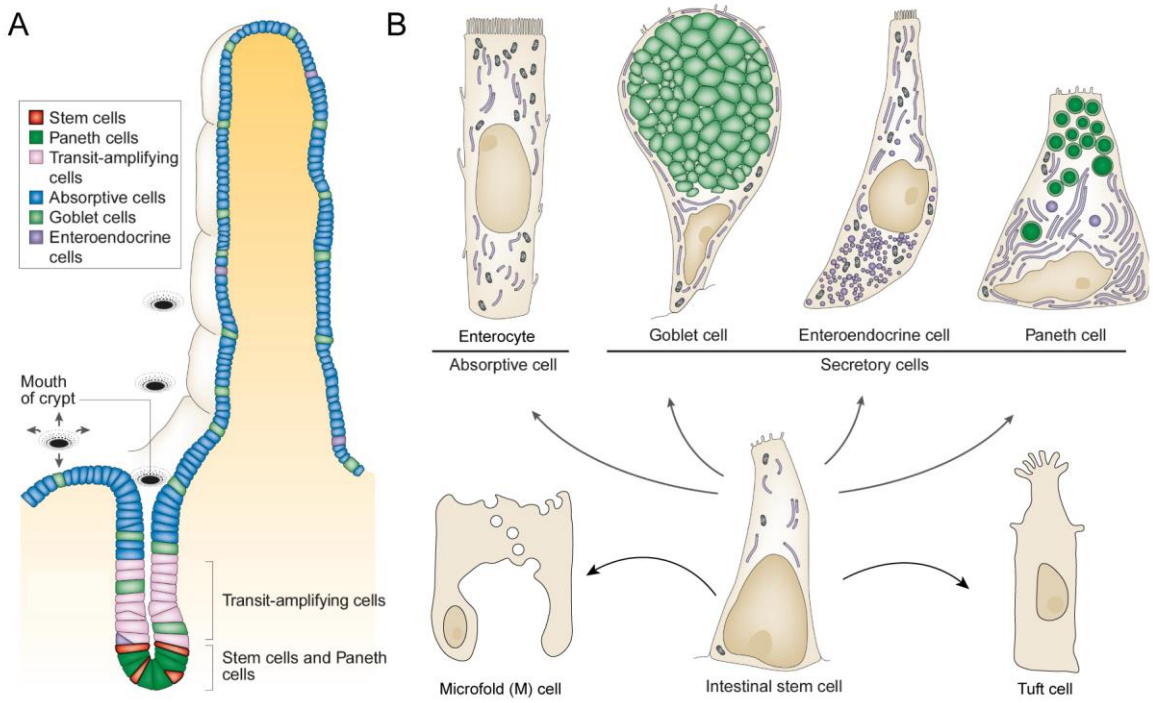

Figure 1. 7: Structure and localisation of differentiated cells in the intestine.
(A) A single crypt-villous structure showing relative positions of various cell types of the small intestine. Stem cells (red) reside at the crypt base intercalated with fully differentiated Paneth cells (dark green). Transit-amplifying cells (pink) that have committed to one of the two differentiation pathways are positioned just above the base. From the neck of the crypt to the tip of the villi mark the fully differentiated cell region that consists of enterocytes (blue), enteroendocrine (violet), and goblet cells (light green). (B) The cellular structures of six differentiated cell populations. The absorptive enterocytes are characterised by the apical brush border that increases the surface area of absorption. M-cells have vesicles containing antigens from the lumen to be presented to immune system. The secretory cells are identified by the presence of cytoplasmic secretory vacuoles containing mucus (goblet cell), peptides and catecholamines (enteroendocrine cells), and lysozyme and defensins (Paneth cells). Tuft cells have villi like structures on the apical surface. The nucleus-to-cytoplasm ratio is lower in the differentiated cells compared to the stem cells. The figure was reproduced from Crosnier *et al.*[110] with permission from Springer Nature (license no 5521870316399).

Goblet cells represent the highest proportion of secretory cells in the intestine. These cells have a distinct structure resembling a *goblet* (wine glass) where the

enlarged apical region is filled with secretory vesicles containing mucin[111]. The narrow basal region of a goblet cell contains the nucleus (Figure 1.7B). The mucins secreted by goblet cells lubricate the passage of food and forms a glycoprotein layer above the intestinal epithelia to protect it from microbial and chemical damage[112,113].

Paneth cells are located at the crypt base intercalated with the stem cells and exhibit several unique features. They are the only differentiated cell population located in the stem cell zone (crypt base)[80]. Paneth cells are found in the small intestine, but not in the colon[83]. While most of the differentiated cells are replaced every 2-7 days[90], Paneth cells survive up to 2 months[114,115]. Unlike other differentiated cells, Paneth cells have a narrower apical region compared to the basal part that harbours the nucleus (Figure 1.7B). The apical region contains secretory vesicles filled with lysozyme and defensins, antimicrobial molecules that protect the stem cells[116]. Paneth cells also provide WNT signalling stimulus to maintain the stemness of the ISCs[117].

Enteroendocrine cells comprise only a small (1%) fraction of intestinal epithelial cells[118]. They are filled with dense-core cytoplasmic vesicles containing several key hormones- synaptophysin, chromogranin A, cholecystokinin, somatostatin, serotonin etc[119-122]. These hormones play crucial roles to sense the presence of food in the lumen and trigger ENS to cause segmentation and peristalsis movement[123]. Based on the secreted hormones, enteroendocrine cells can be classed into several subtypes. However, the specific pathways for the differentiation of each subtype of enteroendocrine cells remain largely unknown[80].

Tuft cells are the least abundant secretory cells in the intestine[124]. They can provide protection against parasites (Helminths) by mounting a type 2 cell-mediated immune response orchestrated by IL-4, IL-13, and IL-25[125,126]. Despite their origin from DLL1$^+$ cells, debate exists regarding the classification of tuft cells as secretory cells[80].

1.2.4 Intestinal stem cells (ISC)

1.2.4.1 Identification and localisation of ISCs

In 1974, Cheng and Loblond used radiolabeled-Thymidine injection to demonstrate that all intestinal differentiated cell lineages are produced by slender columnar cells residing at the base of the crypt of Lieberkuhn in mice[127]. Later, microarray analysis of Wnt-target genes in human colon cancer cells and normal crypts identified *Lgr5*[128]*,* a gene that encodes a serpentine receptor for Wnt-agonists (Rspondins)[129], and it is expressed in crypts but not in villi[83]. In 2007, a lineage tracing experiment demonstrated that intestinal Lgr5$^+$ cells can generate all other differentiated cell lineages[83]. In this paper, Barker *et al.* created a conditional knock in mouse model by inserting an *EGFP-IRES-creERT2* sequence at the first ATG codon of *Lgr5* gene and then crossing it with *Rosa26-LacZ* reporter mice. Tamoxifen injection in these mice activated the creERT2 fusion enzyme in Lgr5$^+$ cells. The activated Cre then deleted the roadblock sequence in *Rosa26-LacZ* reporter allele by homologous recombination. Thus, Lgr5$^+$ cells in the knock in mouse model exclusively expressed functional LacZ enzyme and were detected by beta-galactosidase staining in tissue sections (Figure 1.8). 1 day after tamoxifen treatment, only crypt base Lgr5$^+$ cells were positive for LacZ-expression in small intestine and colon (Figure 1.8, left). However, as Lgr5$^+$ cells moved upwards with time because of cell division at the

crypt base, LacZ expression was detected in villi (small intestine) and upper region of crypt (colon) on 5th day after tamoxifen injection (Figure 1.8, middle). Within 60 days after tamoxifen injection, the entire crypt-villous structure became positive for LacZ expression, indicating that Lgr5^{+} cells at the crypt base generated all the other cells present in the crypt-villous structure (Figure 1.8, right). Similarly, by performing lineage tracing using an orthotopic xenotransplantation model that transplanted human colon organoids into mouse colon resulting in the formation of human colonic crypts inside mice, it was also shown that LGR5 expression marks stem cells in the human colon[94].

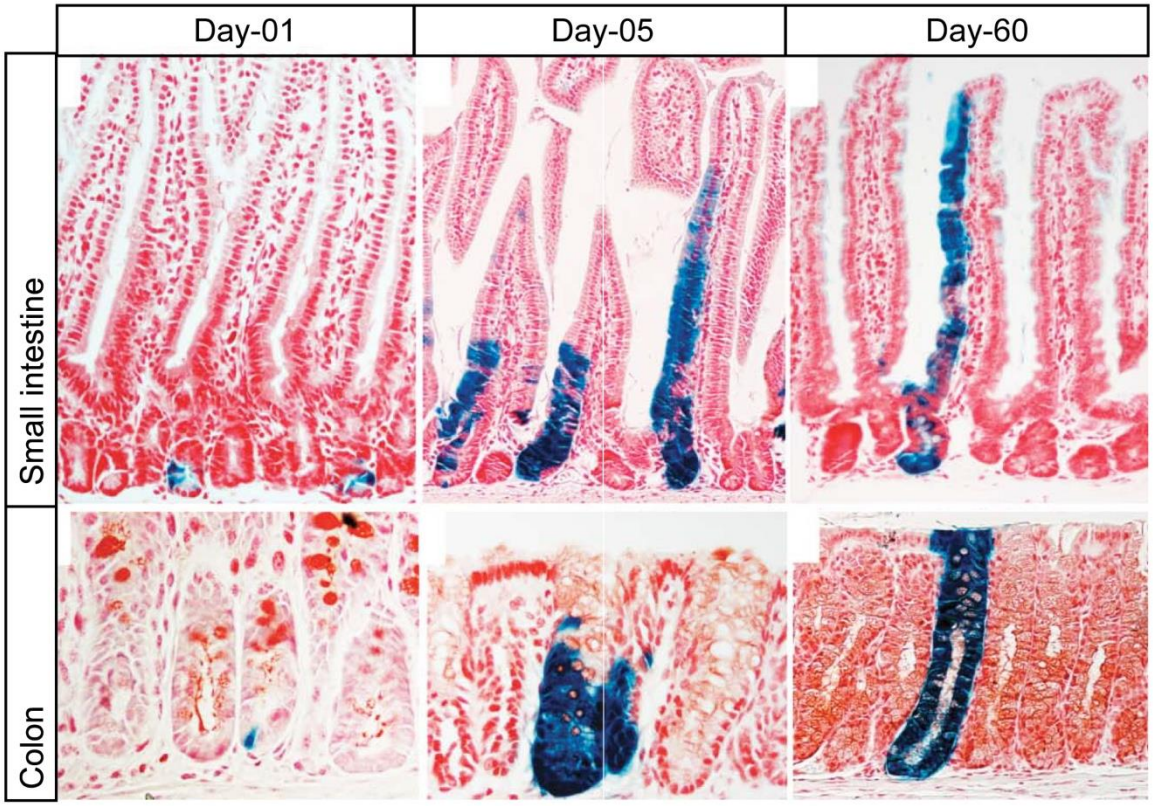

Figure 1. 8: Lineage tracing of Lgr5^{+} cells in the small intestine and colon of mice.
Beta-galactosidase staining in the small intestine (top) and colon (bottom) of *Lgr5-EGFP-IRES-creERT2* knock-in mice crossed with *Rosa26-LacZ* reporter mice after 01, 05, and 60 day(s) of tamoxifen injection. The figure was reproduced from Barker *et al.*[83] with permission from Springer Nature (license no 5521870642844).

The identity of the *de facto* intestinal stem cells is not only determined by Lgr5 expression but also by their position along the crypt-villus axis. In addition to Crypt Base Columnar (CBC) cells, Lgr5 is also expressed by stromal cells near the villous tip (telocytes)[130] and progenitor cells in the transit-amplifying zone[94,131]. Even within the crypt base of the mouse small intestine, cells located in the more basal positions (0 to +2) have a higher survival advantage and outcompete the border cells (+3 and +4)[132]. These basal cells also express higher levels of Lgr5 ($Lgr5^{high}$)[131] and give rise to monoclonal crypts in 1-6 months in the mouse small intestine[133].

The heterogeneity among CBCs is attributed to the very short range of Wnt-gradient (secreted by Paneth cells, Figure 1.9) that maintains stemness only at the crypt apex[134]. Additionally, in the mouse small intestine, the border cells perform a Wnt-dependent retrograde movement to achieve the central positions (0 to +2) and thus increase the number of effective stem cells that can produce monoclonal crypts[135]. However, due to the absence of Wnt-secreting Paneth cells, such movement is nearly absent in the colon. Therefore, the mouse colon is not capable of expanding the number of effective stem cells that can produce monoclonal crypts, unlike the small intestine[135]. The stemness of Lgr5-expressing cells at the small intestinal crypt base ($Lgr5^{+CBC}$) is thus maintained by niche signalling from Paneth cells. $Lgr5^{+CBC}$ cells are intercalated by Paneth cells in a fashion where they would share a border with at least one Paneth cell[117]. In addition to the secretion of antibacterial agents (lysozyme and defensins) that protects the stem cells[136], Paneth cells express EGF, TGF-alpha, Wnt3, and Notch-ligand Dll4[117]. All these molecules are essential signals to maintain the ISCs. From the base to the top of the crypt, there are decreasing gradients of Wnt and Notch signalling and increasing gradients of BMP

and Hedgehog signalling that determine the stem, transit amplifying and differentiated zones of the crypt[137]. These four key signalling transduction pathways have been summarized in Figure 1.9.

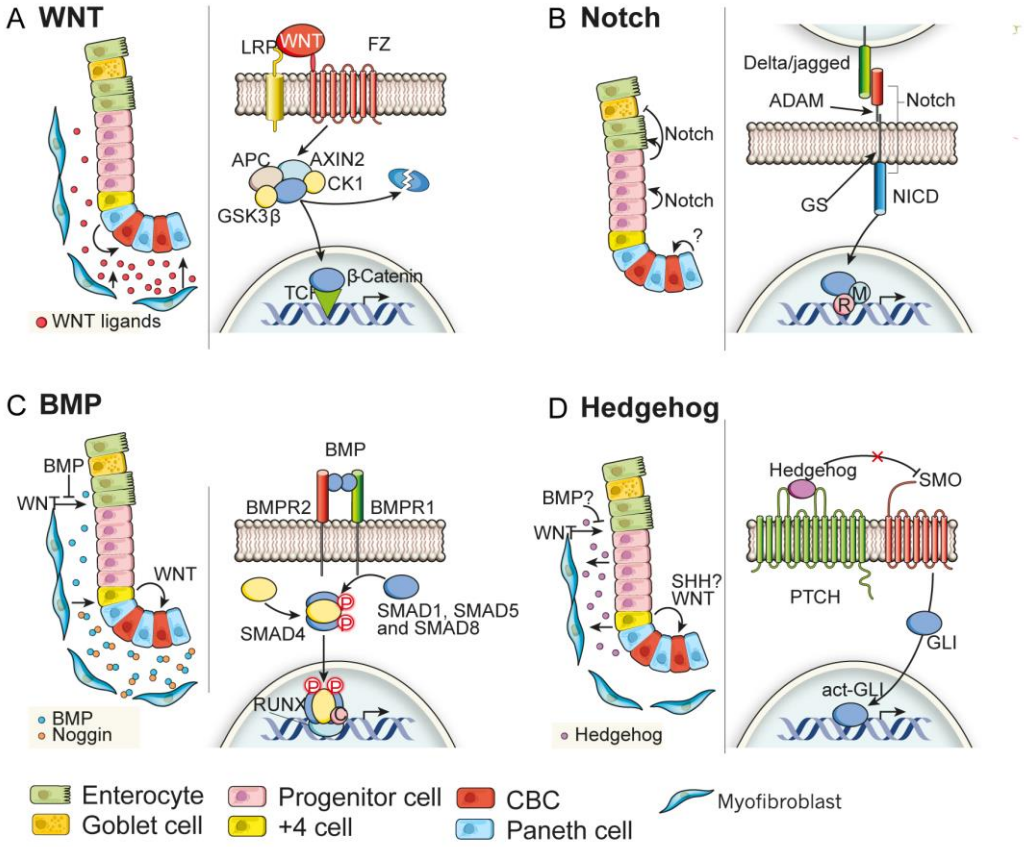

Figure 1. 9: Signalling pathways at the stem cell niche under homeostasis in mice.
(A) Canonical WNT signalling pathway: Paneth cells at the crypt base secrete Wnt ligands (red dots) which bind to the frizzled (FZ) and low-density lipoprotein receptor-related protein (LRP) complex and inhibit the beta-Catenin destruction complex consisting of adenomatous polyposis coli (APC), AXIN2, glycogen synthase kinase 3-beta (GSK-3beta) and casein kinase (CK1). In the presence of WNT ligands, beta-catenin accumulates inside the cell and translocates to the nucleus to activate WNT target genes with the help of transcription factors (TCF and lymphocyte enhancer factor-1). **(B) Notch signalling pathway:** Notch can further enhance the proliferation stimuli created by the WNT pathway and aid in the determination of cell fate. The Delta and jagged ligands on the surface of progenitor cells can activate the Notch receptor on the neighbouring cell surface. Two proteolytic cleavages are then catalysed by a disintegrin and metalloprotease (ADAM) and γ-secretase (GS) resulting in the release of Notch Intracellular Domain (NICD). After being transported to the nucleus, NICD activates Notch gene targets with the help of recombining binding protein suppressor of hairless (R) and mastermind-like protein 1 (M). **(C) BMP signalling pathway:** Bone Morphogenetic Protein (BMP), secreted by the stromal cells, reduces proliferation, and drives differentiation. At the crypt base, Noggin (pink) specifically binds BMP (blue) and inactivates it. In the upper region of the crypt, BMP binds on the cell surface receptors BMPR1 and BMPR2 to form a heterodimer that leads to the phosphorylation of SMAD1, SMAD5 and SMAD8. The phosphorylated SMAD complex then translocates to the nucleus to activate the BMP target genes aided by RUNX2 and a cofactor (C). **(D) Hedgehog signalling pathway:** Hedgehog, secreted by the crypt epithelial cells, stops WNT-activation by the mesenchymal cells probably via the BMP

pathway. Hedgehog binds to the patched (PTCH) receptor on the cell surface which results in the termination of inactivation of smoothened (SMO). De-inactivated SMO activates GLI transcription factors (act-GLI) that move to the nucleus and activates the Hedgehog target genes. The figure was reproduced from Medema *et al.*[137] with permission from Springer Nature (license no 5521871340769).

Several other markers (e.g., Ascl2, Olfm4, Musashi1, Prominin1/CD133) are also co-expressed with Lgr5 in the CBCs[81]. However, their expression is not strictly restricted to the stem cells and often extends to the progenitor compartment[138-140]. Therefore, these molecules mark both stem and progenitor cells in intestinal crypts and should not be used as an exclusive marker for ISCs.

Single Lgr5^{+} cells isolated by flow cytometry can create mini crypt-villi structures *in vitro* known as organoids[131]. The culture conditions of organoids mimic the respective niche signalling molecules and vary from small intestine to colon, healthy tissue to cancer, and mouse to human[141]. Organoids are often used as a model to test the regenerative capacity of stem cells by quantifying their colony-forming efficiency (percentage of plated cells that form an organoid) and budding efficiency (average number of buds created by each organoid)[142,143]. This *in vitro* stem cell culture recapitulates the self-renewal and multipotency of *in vivo* stem cells, making them a very suitable model to study ISCs[131].

1.2.4.2 Cellular kinetics of ISCs

Most stem cells in hair follicles and bone marrow reside in a quiescent state (G0) to protect themselves from DNA replication errors[144]. On the contrary, stem cells (Lgr5^{+CBC}) in the mouse intestine are actively proliferating and double their population every 24 hours[145,146], making them the fastest-cycling adult stem cells in mice. During homeostasis, the majority of Lgr5^{+CBC} cells stay in an unlicensed G1 phase which gives them a long duration to make proliferation decisions before DNA

replication in S-phase[147]. However, APC mutant mice undergo rapid licensing upon entering G1-phase resulting in uncontrolled cell division and cancer[147]. Stress on crypts using ionizing radiation also activates ISCs to complete G1-phase and commit to the active cell cycle by transitioning the G1/S-check point. Following ablation of $Lgr5^{+}$ cells in the mouse colon using Dextran Sodium Sulphate (DSS), ISCs divide at a quicker rate than under homeostasis[148]. $Lgr5^{+}$ cells also cycle faster (every 15 hours) during the developmental stage of 6-day-old mice, than in adult mice (every 24 hours)[93]. Therefore, ISCs in mice represent an actively cycling stem cell population that can modulate its division rate upon oncogenic transformation, ionising radiation, colitogenic damage, and during the developmental stage of newborns.

ISC kinetics also varies between species as human colonic stem cells ($LGR5^{+CBC}$) have been shown to exhibit different kinetics than mice. The majority of ISCs in the human colon are in a quiescent (G0) state and divide every 7 days which was determined by an orthotopic xenotransplantation model using human colon organoids[94].

1.2.4.3 Reserve stem cell population in the intestine

$Lgr5^{+CBC}$ cells serve as *bona fide* stem cells in the mouse intestine contributing to the homeostatic maintenance of this rapidly dividing tissue. However, these cells are sensitive to stressful conditions such as radiation[83] and colitogenic damage[148]. When $Lgr5^{+CBC}$ cells are destroyed during injury, slow-cycling, radio-resistant reserve populations of stem cells replenish the lost $Lgr5^{+CBC}$ cells to restore homeostasis[81]. The lineage-tracing strategy has enabled researchers to assess the

molecular identity of these reserve stem cells. In mice, Bmi1 expression marks one of the reserve stem cell populations, mostly residing above the crypt base near the +4 cell positions, majority of which are negative for Lgr5-expression[149]. After ablation of $Lgr5^+$ cells by inducing Diphtheria Toxin Receptor (*DTR*) knocked into the *Lgr5* gene or irradiation, homeostasis was restored by $Bmi1^+$ cells indicating $Lgr5^+$ cells are dispensable in the mouse intestine[150,151]. Further experimentation with Hopx[152], Lgri1[153], and Smoc2[139]-expressing cells also yielded similar results, indicating the existence of multiple reserve stem cell populations in the small intestine of mice. Finally, lineage tracing of $Lgr5^-Krt19^+$ cells following irradiation of $Lgr5^+$ cells revealed the only reported reserve stem cell population ($Krt19^+$) in the mouse colon[154].

Reserve-like ISCs exist even within the $Lgr5^+$ cell population. $Lgr5^+$ cells at +3 positions expressing higher levels of Mex3a are more resistant to irradiation and cycle slower than $Lgr5^+Mex3a^{low}$ cells[155]. In short, slow cycling, stress-tolerant cells residing above the basal positions of the crypt act as reserve stem cell populations upon injury. When $Lgr5^+$ ISCs are lost, these quiescent reserve stem cells enter the cell cycle to replenish $Lgr5^+$ cells and restore homeostasis.

Using orthotopic xenotransplantation of human colon organoids into mice that resulted in the formation of human colonic crypts inside a mouse model, it was shown that $LGR5^+$ cells at the crypt base are slower cycling (every 7 days) than $LGR5^+$ cells residing above the crypt base (every 1.5 days) in human colonic crypts[94]. Administration of 5-fluorouracil results in a complete ablation of the $LGR5^+$ cells residing above the crypt base leaving the crypt base cells intact. Surviving

LGR5^{+CBC} cells undergo proliferation to replenish the lost cell population above the crypt base and restore homeostasis[94]. Thus, the positions of the dispensable and reserve stem cell population in human colonic crypts are found in different positions than the mouse crypts. Additional reserve stem cell populations expressing other markers in the human colon are yet to be reported.

1.3 Aims

Previous studies conducted on naked mole rats have elucidated mechanisms for the preservation of genomic integrity (by HMM-HA[36] and pALT[34] mediated early contact inhibition, more efficient DNA repair pathways[40,41,43], stable epigenome[54,55], and maintenance of telomere length[40,50-52]), proteostasis[61-64], nutrient sensing[72,73], and stem cell function both in homeostasis and injury[65,67,68] that likely contribute to long-term tissue maintenance in this long-lived species. Studies of the intestine in long-lived species (humans) have reported slower cell kinetics of ASCs than short-lived mice[94]. Haematopoietic stem and progenitor cells in NMRs also exhibit slower cellular dynamics and hypersensitivity to genotoxic agents than mice. The aim of this study was to identify distinct features of intestinal stem and differentiated cells in naked mole rats, in a cross-species comparison with mice and humans, that may provide further clues to their disease-free long life. The specific aims of this thesis were:

1. To quantify the proportions of stem and various differentiated cells in the NMR intestines in a cross-species comparison with mice and humans. (Chapter 3)

2. To determine the ASC division rates in NMR intestines *in vivo* including the durations of the different cell cycle phases and contrast the differences with the kinetics of mouse and human ISCs. (Chapter 4)
3. To assess the response of NMR intestinal epithelia to damage inducing agent (Dextran Sodium Sulphate) and compare with mice. (Chapter 5)

The overall aim of this thesis was to characterise the composition, kinetics, and injury-response of intestinal stem cells in NMRs that may shed light into their healthy tissue maintenance. As short-lived mice exhibit a different ISC kinetics to long-lived humans, it may be challenging to translate a therapeutic strategy identified by studying murine stem cells to humans. Therefore, long-lived animal models such as naked mole rats may provide a more comparable stem cell compartment to human and thus assist the discovery of translational drugs that can enable long-term healthy tissue maintenance in humans.

Chapter 2: Materials and Methods

2.1 Materials

2.1.1 Buffer solutions

1X Phosphate buffered Saline (PBS), pH 7.4

140 mM Sodium Chloride

3 mM Potassium Chloride

10 mM Phosphate buffer

1X PBSTX, pH 7.4

1X PBS

0.1% Titron-X100 (Merck, X100)

1X PBST, pH 7.4

1X PBS

0.1% Tween-20 (Merck, P9416)

1X Tris-buffered Saline (TBS), pH 7.4

50 mM Tris-Cl, pH 7.4

150 mM Sodium Chloride

1X TBST, pH 7.4

1X TBS

0.1% Tween-20 (Merck, P9416)

10 mM Sodium Citrate Buffer, pH 6.0

8.25 mM Sodium Citrate Dihydrate

1.75 mM Citric acid

0.1 M Borate Buffer, pH 6.0

0.1 M Boric acid

0.1 M Sodium Tetrahydroborate

2.1.2 Antibodies

Table 2. 1: Antibodies used for immuno-histochemical staining in this study.

Antibody	**Source**	**Catalogue**	**Dilution**
Primary antibodies			
Rabbit polyclonal anti-Chromogranin A	AbCam	ab15160	1:2000
Rat monoclonal anti-BrdU	AbCam	ab6326	1:500 (for IHC/IF) 1:2000 (for ICC)
Rabbit monoclonal anti-Ki67	Cell Signaling Tech.	12202	1:500
Rabbit monoclonal anti-p27	Cell Signaling Tech.	3686	1:200

Antibody	**Source**	**Catalogue**	**Dilution**
Rabbit polyclonal anti-EpCAM	AbCam	ab71916	1:500
Rabbit monoclonal anti-Histone H3 (phospho S28) PHH3-S28	AbCam	ab32388	1:2000
Secondary antibodies			
Goat anti-Rabbit IgG (H+L) secondary antibody, Biotinylated	Vectorlabs	BA-1000	1:300
Goat anti-Rat IgG (H+L) secondary antibody, Biotinylated	AbCam	ab207997	1:300
Goat anti-rabbit IgG (H+L) secondary antibody, Alexa 488 conjugated	Invitrogen	A11008	1:500
Goat anti-rat IgG (H+L) secondary antibody, Alexa 488 conjugated	Invitrogen	A11006	1:500
Goat anti-rabbit IgG (H+L) secondary antibody, Alexa 633 conjugated	Invitrogen	A21070	1:500

2.1.3 Chemicals

Table 2. 2: Chemical reagents used in this study.

Reagent	Source	Catalogue
Harris Haematoxylin	Merck	HHS32
Gill's No 3 Haematoxylin	Merck	GHS316-500ML
Eosin	Merck	117081
DPX mounting medium	Merck	06522
Aquatex mounting media	Merck	108562
Alcian blue 8GX	Merck	A5268
Nuclear Fast Red	Merck	N3220
Diaminobenzidine (DAB)	R&D Systems	4800-30-07
DAPI (4',6-Diamidino-2-Phenylindole, Dihydrochloride)	Invitrogen	D1306
Diamond antifade mounting media	Invitrogen	P36961
BrdU (5-bromo-2'-deoxyuridine)	Abcam	ab142567
EdU (5-ethynyl-2-deoxyuridine)	Merck	900584
High-glucose DMEM	Merck	D6546
Fetal Bovine Serum	Gibco	10270

Reagent	Source	Catalogue
Penicillin-Streptomycin	Merck	P4333-100ML
L-glutamine	Gibco	25030-024
Dextran sulfate sodium salt	Merck	42867
Goat serum	Merck	G9023-10ML

2.1.4 Commercial assays

Table 2. 3: Commercially available kits used in this study.

Assay name	Source	Catalogue
Alkaline phosphatase (AP) Staining kit	SystemBio.	AP100B-1
VECTASTAIN® Elite® ABC-HRP Kit, Peroxidase (Rabbit IgG)	Vector Laboratories	PK-6101
RNAScope Multiplex Fluorescent Detection Kit v2	ACD bio.	323110
EdU-Click 488 kit	Base Click	BCK-EdU488-1
Click-iT™ Plus TUNEL Assay Kits	Invitrogen	C10617

2.1.5 Commercial cell line

Name: HEK293T

Supplier: ATCC (USA)

Catalogue: CRL-3216

Organism: *Homo sapiens* (human)

Morphology: Epithelial

Tissue: Embryonic Kidney

Growth Properties: Adherent

2.1.6 Oligonucleotides

Table 2. 4: Oligonucleotide probes used for mRNA ISH in this study.

Oligonucleotide*	**Source**	**Catalogue**
Mouse *Lgr5*-C1 probe	ACD bio.	312171
Naked mole rat *Lgr5*-C1 probe	ACD bio.	584631
Human *LGR5*-C3 probe	ACD bio.	311021
Human *PPIB-C1* probe (positive control)	ACD bio.	313901

*All probes were suitable for the manual staining protocol using RNAScope Multiplex Fluorescent Detection Kit v2 (ACD, 323110)

2.2 Animal procedures

2.2.1 Ethics

Tissues from C57BL/6J mice were harvested following schedule-1 methods performed under the Animals (Scientific Procedures) Act, 1986, UK bearing the

personal license no PIL-I4EA8A0B0. Wild-caught mouse tissues used in this study were gifted by Prof. Dustin J. Penn, University of Veterinary Medicine, Vienna, Austria (license no: GZ BMWF-68.205/0135-WF/V/3b/2014 and GZ BMWFW-68.205/0141-WF/V/3b/2017). Tissues from DSS-administered C57BL/6J mice were gifted by Dr. Nan Gao, Rutgers University Newark collected under the regulation of the Institutional Animal Care and Use Committee (IACUC) of the USA.

All naked mole rat tissues, collected under ethics approval (NAS046-19 and NAS289-2020) by the Animal Ethics Committee, were gifted by Prof. Nigel C. Bennette, University of Pretoria, South Africa. These tissues were collected during two sample collection trips to the University of Pretoria, South Africa (July-August 2019 and July-August 2021).

Normal human colonoscopy samples were collected following written informed consents and requested under the research tissue bank ethics approval (16/YH/0247 by Dr. Shazia Irshad, University of Oxford) supported by NIHR Biomedical Research Centre, Oxford, U.K. and under the London Dulwich Research Ethics Committee (reference number 15/LO/1998).

2.2.2 Animal housing

2.2.2.1 Housing conditions of mice

All C57BL/6J mice used in this study were purchased from Charles River (Kent, UK) and housed at Biomedical Services Unit in John Radcliffe Hospital, Oxford, UK. Mice were housed in individually ventilated cages under specific pathogen-free

conditions, maintained in alternating 12-hour light/12-hour dark cycles and fed with food and water *ad libitum*.

2.2.2.2 Housing conditions of naked mole rats

Naked mole rats were housed at the animal facility of the Department of Zoology and Entomology, University of Pretoria, South Africa under the conditions described previously[15]. In brief, the NMRs were kept in tunnel systems consisting of several Perspex chambers containing wood shavings as nestling material. The NMR room was maintained at temperatures ranging between 29–32°C, alternating 12-hour light/12-hour dark cycles with relative humidity around 40-60%. NMRs were fed chopped fresh fruits and vegetables (apple, sweet potato, cucumber, and capsicum) daily *ad libitum* along with weekly supplement of ProNutro (Bokomo). Since NMRs obtain all their necessary water from food sources, no additional drinking water was provided to the animals. All naked mole rats used in this study are non-breeders belonging to two colonies established by founder breeders (mixed-parentage) captured in Mtito Andei and Lerata, Kenya by Prof. Jennifer Jarvis[11].

For all analyses, both male and female animals/individuals were included in the study.

2.2.3 *In vivo* experiments

2.2.3.1 *In vivo* administration of nucleoside analogues

15 mg/mL solution of BrdU (5-bromo-2'-deoxyuridine, Abcam, ab142567) and 12.3 mg/mL solution of EdU (5-ethynyl-2-deoxyuridine, Merck, 900584) were prepared in sterile 1X PBS (Gibco, 10010023) and filtered through a 0.2 µm strainer. Using a

27-gauge needle and 1 mL syringe, 100 mg per kg bodyweight BrdU and 82.14 mg per kg bodyweight EdU were administered intraperitoneally. Animals were checked regularly for signs of discomfort (hunched back, shivering, low mobility etc.) after the injection.

2.2.3.2 *In vivo* administration of Dextran Sodium Sulphate

Dextran sulphate sodium (DSS, 40 kDa) salt (Merck, 42867) was dissolved in sterile ddH_2O to prepare 0-8.75% (w/v) solutions. Animals were separated from their colony and acclimatized to their new cage 7 days prior to the onset of treatment. Using a 2 mL syringe fitted with a plastic feeding tube (FTP-20-38), 12 mL per kg bodyweight (for mice) or 50 mL per kg bodyweight (for NMRs) DSS solution was administered orally every 4 hours during the light period (0700, 1100, 1500, 1900 hour) for 3 days. For each animal, body-mass was measured, and stool samples were collected daily at 0700 hour. To collect stool samples, a single animal was placed in an empty cage without bedding materials for 10-15 minutes or until fecal pellet was excreted by the animal. During the course of treatment, animals were also checked for signs of discomfort (e.g. hunched back, shivering, low mobility) every 4 hours.

2.2.4 *In vitro* experiments

2.2.4.1 Measuring plasma BrdU concentration in naked mole rats

Plasma BrdU concentration was determined following the protocol described by Barker *et al*[156]. In brief, 100 µL naked mole rat blood was collected by tail vein puncture after 8 hours and 16 hours of a single BrdU injection. The blood was mixed with 3 USP heparin inside a 1.5 mL tube to stop clotting and centrifuged at 13,000

g for 15 minutes at room temperature to separate all blood cells. Plasma was collected from the top layer and stored at -80°C.

HEK293T cells (ATCC, CRL-3216) were cultured in high-glucose DMEM (Merck, D6546) containing 10% Fetal Bovine Serum (FBS, Gibco, 10270), 1X Penicillin-Streptomycin (Merck, P4333-100ML), and 2 mM L-glutamine (Gibco, 25030-024) at 37°C incubator with 5% CO_2. 50,000 cells were plated on a 13 mm sterile glass coverslip in 24-well plates that were pre-coated with 300 µL of 50 µg/ml poly L-lysine and cultured overnight. The media was replaced with fresh culture media containing 10 µL plasma or standard (0 to 50 µg/mL) BrdU solution and incubated at 37°C for 4 hours. Cells were then washed with 1X PBS and fixed in 4% paraformaldehyde for 20 minutes at room temperature. Fixed cells were kept in 1X PBS at 4°C before performing immunocytochemistry (section 2.3.2.5).

2.2.4.2 Expansion of organoids from mouse intestinal crypts

Intestinal crypts were isolated from C57BL/6J mice (2 to 4-month old) as described by Sato *et al*[141]. In brief, intestinal tissues were harvested from the abdominal cavity of mice following cervical dislocation. The intestines were cleaned with 1X PBS and sliced into 1-2 mm pieces using a scalpel. The tissue pieces were washed 3 times (5 minutes each, room temperature) with ice-cold chelation solution (containing 5.6 mM Na_2HPO_4, 8 mM KH_2PO_4, 96 mM NaCl, 1.6 mM KCl, 44 mM Sucrose, 55 mM D-Sorbitol, and 0.5 mM DL-dithiothreitol in sterile ddH_2O, all reagents from Sigma) to remove the floating fragments. The cleaned tissue pieces were incubated in 20 mL of 5 mM EDTA (Corning, 46-034-Cl) dissolved in chelation solution for 1 hour at 4°C on a rotating wheel. At the end of the incubation, crypts were isolated from the

mesenchyme by pipetting the tissue pieces at high speed for 1-2 minutes using a 10 mL serological pipette (precoated with 5% FBS). From this point, all tips, pipettes and tubes were pre-coated with 5% FBS. The isolated floating crypts were collected into a new pre-coated 15 mL tube and washed three times with 5 mL Advanced DMEM/F-12 medium (ADF, Gibco, 12634) followed by centrifugation (150 g for 5 minutes at 4°C, braking speed 3).

200 to 300 isolated small intestinal crypts were seeded into 50 µL Matrigel (R&D systems, 3533-005-02) and cultured in a 24-well plate containing 500 µL of ENR media [50 ng/mL EGF (Sigma, E9644), 100 ng/mL Noggin (Peprotech, 12010C), 1 µg/mL RSpondin1 (R&D systems, 4645-RS-100/CF), 1X N2 (Gibco, 17502048), 1X B27 (Gibco, 17504044), 1.25 mM N-acetly-L-cysteine (Sigma, A9165), 100 µg/mL Primocin (InvivoGen, ant-pm-1), 10 mM HEPES (Gibco, 15630080), and 2 mM Glutamax (Gibco, 35050061), and 1X Penicillin-Streptomycin (Sigma, P4333-100ML) in Advanced DMEM/F-12 medium (Gibco, 12634)] at 37°C incubator containing 5% CO_2. For colon organoids, the growth media was supplemented with 100 ng/mL Wnt-3a (5036-WN-010, R&D systems). The culture media was replaced every 2-3 days. For the first 2 days of culture, organoid media was supplemented with 10 µM Rho-kinase inhibitor, Y-27632 (Y0503, Merck), to avoid anoikis.

Organoids were passaged (1:4) using TrypLE (12604013, Gibco) digestion every 7 days. Mature organoids (containing dead cells in the lumen) were released from the matrigel by pipetting into ice-cold ADF medium using a pre-coated P1000 tip. The organoids were then incubated in 10 mL cold ADF medium for 5 minutes on ice to dissolve the Matrigel, followed by centrifugation (150 g for 5 minutes at 4°C). After

removing the supernatant, the organoids were broken into smaller fragments (containing 10-20 cells) by incubating in 5 mL TrypLE for 5-10 minutes at 37°C and vortexing for 5-10 sec. TrypLE activity was inhibited by adding 1 mL FBS and organoid fragments were centrifuged (500 g for 5 minutes at 4°C) before plating in Matrigel using the same growth medium described above.

2.2.4.3 Cumulative BrdU labelling in mouse organoids

To determine the duration of S-phase in murine intestinal *Lgr5*$^{+}$ cells in culture, organoids were expanded from intestinal crypts and passaged 5 times every 7 days (when dead cells start to accumulate inside the lumen) following the protocol described in section 2.2.4.2. On day 4 after the 5th passage, the growth media was supplemented with 10 µM BrdU (ab142567, Abcam) dissolved in 1X PBS and organoids were harvested at specific time points. All tips, pipettes, and tubes were coated with 5% FBS at every step of the protocol. To collect organoids for histological staining, organoid culture media was replaced with 1 mL ice-cold Advanced DMEM/F-12 medium (Gibco, 12634) and the Matrigel was dissolved by repeated gentle pipetting with pre-coated P1000 tips. The isolated organoids were then transferred to a pre-coated 15 mL tube, mixed with an additional 9 mL ice-cold ADF, and incubated on ice (5 minutes) before centrifugation at 150 g (5 minutes at 4°C). After removing the supernatant, the organoid pellet was dissolved in 500 µL 4% paraformaldehyde (PFA) solution and incubated overnight at 4°C on a rotating wheel. The next day, the PFA solution was removed after centrifugation (500 g, 5 minutes at room temperature) and organoids were washed in 1X PBS, followed by centrifugation at 500 g for 5 minutes at room temperature. Finally, fixed organoid

pellets were dissolved in 70% ethanol and stored at 4°C before processing them for histology following the steps described in section 2.3.1.3.

2.3 Histological techniques

2.3.1 Collection, fixation, and processing of intestinal tissues

2.3.1.1 Processing of intestinal tissue of mice and naked mole rats

After sacrificing the animals by cervical dislocation, the intestine was immediately isolated from the abdominal cavity and fatty tissues were removed. The small intestine was then divided into three equal sections—SB1 (duodenum), SB2 (jejunum), and SB3 (ileum). All three parts of the small intestine and colon were then flushed with 1X PBS solution ten times using a P1000 pipette to remove faecal material. A metal rod was passed through the lumen and positioned on a 3 mm filter paper (Thermo Fischer, 84784) in a gut-cutting device[157]. The intestine was cut open longitudinally with a blade and placed on the filter paper with the luminal side up. The tissues were then fixed in 10% neutral buffered formalin (NBF) overnight at room temperature. The following day, fixed intestinal tissues were rolled using the Swiss-rolling technique[158], and stored in 70% ethanol at 4°C. Next, formalin-fixed intestinal gut rolls were dehydrated through increasing concentrations of ethanol (70% ethanol for 1 hour, 90% ethanol for 1 hour, and three rounds of 100% ethanol for 1 hour each), cleared through xylene (three times, 1 hour each), and embedded in paraffin blocks.

2.3.1.2 Mucus layer fixation in mouse and naked mole rat colon

To preserve the mucus layer lining the colonic epithelium, any contact with an aqueous solution was avoided after the dissection of the intestinal tissue. Several segments of the colon containing faecal matter were separated using a scalpel and fixed in methacran solution (60% methanol, 30% chloroform, and 10% glacial acetic acid) overnight at room temperature. The next day, fixed tissues were processed through 100% methanol (2 times, 30 minutes each) and 100% ethanol (3 times, 60 minutes each), cleared through xylene (3 times, 60 minutes each), and embedded in paraffin blocks.

2.3.1.2 Processing of human colon biopsies

2 mm punch biopsies were collected from the sigmoid colon of healthy participants (undergoing routine screening for cancer and inflammatory bowel disease but did not exhibit any sign of inflammation and polyps confirmed by colonoscopy) and immediately stored in 1X PBS on ice. The biopsies were transferred to 10% Neutral Buffered Formalin (NBF) on the same day of collection and fixed overnight at room temperature. The next day, NBF was replaced with 70% ethanol and the samples were stored at 4°C until tissue processing. Fixed samples were positioned in 3% low-melting-point agarose (Merck, A4018; prepared in ddH_2O) with the luminal sides of all the biopsies facing up. The agarose-embedded biopsies were processed through ethanol (70% ethanol for 1 hour, 90% ethanol for 1 hour, and three rounds of 100% ethanol for 1 hour each) and xylene (three times, 1 hour each) before embedding in paraffin blocks.

2.3.1.3 Processing of organoids for histological analysis

Formalin-fixed organoids were prepared from 3D culture following the steps described in section 2.2.4.3 and stored in 70% ethanol at 4°C until processing. On the day of processing, organoids were pelleted by centrifugation at 500 g for 5 minutes at 37°C. After discarding the ethanol solution, pellets of fixed organoids were gently resuspended in 50 µL of 3% low-melting-point agarose (Merck, A4018; prepared in ddH_2O) and allowed to gel for 30 minutes at room temperature. The organoid gel block was released from the 200 µL PCR tube by cutting the base with a scalpel. The gel block was then manually processed through ascending concentrations of ethanol (70% ethanol for 30 min, 85% ethanol for 30 min, 90% ethanol for 30 min, two rounds of 100% ethanol for 30 minutes each), xylene (two rounds, 30 minutes each), and embedded in paraffin (Formalin Fixed Paraffin Embedded, FFPE) blocks.

2.3.2 Histological staining

2.3.2.1 Haematoxylin and Eosin staining

Tissues were cut on a microtome (Anglia Biosciences) at 4 µm thickness and dried overnight at room temeperature. On the day of staining, sections were baked at 60°C for 1 hour and deparaffinised by submerging in xylene (2 times, 10 minutes each) and rehydrated in 100% ethanol (2 times, 5 minutes each), 95% ethanol (2 minutes), 70% ethanol (2 minutes), 50% ethanol (2 minutes), and distilled water (5 minutes). Slides were then stained with Harris Haematoxylin (Merck, HHS32) for 2 minutes 45 seconds, followed by washing in running tap water for 5 minutes. Next, sections were dipped in 95% ethanol ten times before counterstaining with Eosin solution (Merck, 117081) for 3 minutes. Finally, slides were dehydrated in 95%

ethanol (15 seconds) and 100% ethanol (2 times, 15 seconds each), dipped in xylene (2 times, 5 minutes each), and mounted with coverslips using DPX mounting medium (Merck, 06522).

2.3.2.2 Alcian blue staining

4 µm thin intestinal tissues were deparaffinised and hydrated as described in section 2.3.2.1. Slides were then submerged in 3% acetic acid solution (3 minutes) before staining with Alcian blue solution (1% Alcian Blue 8GX (Merck, A5268) in 3% aqueous acetic acid, adjusted to pH 2.5) for 30 minutes at room temperature. Then slides were washed (5 minutes) in running tap water followed by counter-staining (5 minutes) with undiluted Nuclear Fast Red (Merck, N3220). After 1 minute wash in running tap water again, slides were dehydrated with ethanol (70%, 90% and 100%, 2 minutes each), washed in xylene (2 times, 5 minutes each), and mounted with coverslips using DPX (Merck, 06522).

2.3.2.3 Alkaline phosphatase staining

Tissue sections from FFPE blocks (4 µm thin) were deparaffinised and hydrated as described in section 2.3.2.1. A hydrophobic barrier was drawn around the tissue sections by a PAP pen (Vector Lab, H-4000) before applying AB solution (AP Staining kit, SystemBio, AP100B-1) for 20 minutes at room temperature in the dark. All slides were then washed with 1X PBS (5 minutes, on a shaker), counterstained with undiluted Nuclear Fast Red (Merck, N3220) (5 minutes), washed in running tap water (1 minute), dehydrated through ascending ethanol concentrations (70%, 90% and 100%, 2 minutes each), washed in xylene (2 times, 5 minutes each), and finally cover-slipped with DPX medium (Merck, 06522).

2.3.2.4 Immunohistochemical staining with anti-BrdU and anti-Chromagranin A antibodies

4 µm thin formalin-fixed paraffin-embedded (FFPE) sections were cut using a microtome and dried overnight on extra-adhesive Superfrost glass slides (VWR, 631-0108). Sections were then deparaffinised and hydrated following the steps described in section 2.3.2.1. Endogenous peroxidase activity was quenched by a 20-minute incubation in 3% H_2O_2 (Merck) at room temperature. A heat-mediated antigen retrieval was performed by boiling slides in 10 mM sodium citrate buffer (pH 6.0) for 10 minutes at 98-100°C. The slides were then cooled down to room temperature in the same solution for 20 minutes. This was followed by the permeabilization of the cell and nuclear membrane by incubating the tissue sections in 1X PBSTX for 10 minutes. All sections were then blocked with 5% serum (from the species in which the secondary antibody has been raised) for 1 hour at room temperature. Next, primary antibodies diluted in 1% Bovine Serum Albumin (BSA) dissolved in 1X PBS were applied to the tissue sections which were then incubated overnight at 4°C. The catalogue numbers and concentrations used for different primary antibodies in this study are enlisted in Table 2.1. For BrdU detection, no HCl-mediated DNA denaturation was performed as heat-mediated antigen retrieval (98-100°C) has been shown to produce brighter detection of BrdU than acid hydrolysis[159].

Next day, after 3 rounds of washes (5 minutes each) with 1X PBST (0.1% Tween20 in 1X PBS), sections were incubated with biotinylated secondary antibodies (Vector Laboratories, BA-1000 and AbCam, ab207997; diluted at 1:300 ratio in 1% BSA

dissolved in 1X PBS) for 1 hour at room temperature. The signal was amplified by incubating in ABC solution (Vector Laboratories, PK-6101) for 30 minutes at room temperature, followed by 3 rounds of washing in 1X PBST (5 minutes each). The chromogenic signal was developed by incubating the sections in Diaminobenzidine (DAB) solution (R&D systems, 4800-30-07) for 2 minutes at room temperature. Finally, the sections were counterstained (5 seconds) with Harris Haematoxylin (Merck), washed in running tap water (5 minutes), dehydrated in 70%, 90% and 100% ethanol for 15 seconds each, bathed twice in xylene (5 minutes each), and mounted with a glass coverslip using DPX (Merck, 06522).

2.3.2.5 Immunocytochemistry with anti-BrdU antibody

HEK293T cells cultured in media supplemented with standard BrdU solution or NMR plasma and fixed on coverslips in a 24-well plate (section 2.2.4.1) were incubated with 3% H_2O_2 for 10 minutes at room temperature. After washing with 1X PBS, cells were incubated in 2 N HCl for 1 hour at room temperature to denature DNA strands. Incubation for 30 minutes in 0.1 M Borate buffer (pH 8.5) (Merck, B0394) was performed at room temperature to restore the pH balance of the cells. Cells were then incubated in 1X PBSTX for 10 minutes at room temperature to permeabilise the cell and nuclear membranes. Cells were blocked with 5% goat serum (Sigma, G9023-10ML) for 1 hour at room temperature and incubated overnight at 4°C with rat anti-BrdU primary antibody (Abcam, ab6326, 1:2000). The next day, sections were washed three times (5 minutes each) in 1X PBST and incubated with goat anti-rat biotin-linked secondary antibody (Abcam ab207997, diluted in 1% BSA dissolved in 1X PBS at 1:300 ratio) for 1 hour at room temperature. After washing 3 times with 1X PBST (5 minutes each, room

temperature), the signal was amplified using ABC Kit (Vectastain, PK-6101) for 30 minutes at room temperature. The slides were washed 3 times (5 minutes each) in 1X PBST and the signal was developed with DAB (R&D systems, 4800-30-07) solution for 16 minutes at room temperature. After counterstaining with Gill's No 3 Haematoxylin (Merck, GHS316-500ML) for 1 minute 15 seconds, cells were washed 2 times in 1X PBS for 5 minutes each and the coverslips were mounted on glass slides using aquatex mounting media (Merck, 108562). Slides were dried overnight before imaging and stored indefinitely at room temperature.

2.3.2.6 mRNA *in situ* hybridisation (ISH) with *Lgr5* probes

4 µm thick FFPE tissue sections were cut on a microtome (Anglia Bioscience) and dried overnight at room temperature. The next day, slides were baked at 60°C for 1 hour to improve attachment. Sections were deparrafinised using Xylene (2 times, 5 minutes each) and 100% ethanol (2 times, 2 minutes each) at room temperature. After air drying the slides, sections were incubated with RNAScope Hydrogen Peroxide solution (ACD, 322330) for 10 minutes at room temperature to quench endogenous peroxidase activity. After washing the slides (2 rounds, 3-5 dips) in ddH_2O, formalin-fixed RNAs were exposed by boiling the sections in RNAScope Target Retrieval Reagent (ACD, 322000) for 15 minutes at 98-100°C. Immediately after target retrieval, slides were washed twice (3-5 dips each) in ddH_2O and once (3-5 dips) in 100% ethanol. After air drying the slides, sections were incubated in RNAScope Protease Plus solution (ACD, 322330) for 30 minutes at 40°C inside a HybEZ II oven (ACD). Slides were then washed twice in ddH2O (two rounds, 3-5 dips each) and incubated with RNAScope probes for 2 hours at 40°C.

A list of species-specific RNAscope probes used in this study has been presented in Table 2.4. The probe diluent (ACD, 300041) was used as a negative control for the assay.

After probe hybridisation, tissue sections were washed twice (2 minutes each) in RNAScope Wash Buffer (ACD, 320058). The signal was then amplified by incubating the slides in AMP1 (30 minutes), AMP2 (30 minutes) and AMP3 (15 minutes) solutions from Multiplex Fluorescent Detection Kit v2 (ACD, 323110) at 40°C. Each incubation was followed by two rounds (2 minutes each) of washing in 1X RNAScope Wash Buffer. Next, tissue sections were incubated with HRP-C1 (mouse and NMR) or HRP-C3 (human) solutions (ACD, 323110) for 15 minutes at 40°C followed by washing (2 rounds, 2 minutes each) in 1X RNAScope wash buffer. Signals were developed by incubating the slides in Opal 570 dye (diluted in RNAScope Multiplex TSA Buffer (ACD, 322810) at 1:1500) for 30 minutes at 40°C. After two rounds of washing (2 minutes each) in 1X RNAScope wash buffer, any remaining HRP activity was quenched by incubating the sections in HRP-blocker (ACD, 323110) for 15 minutes at 40°C. Finally, sections were counterstained with 300 nM DAPI (Invitrogen, D1306) diluted in 1X TBS for 15 minutes at room temperature. After washing the sections in 1X TBS twice (5 minutes each), slides were mounted with coverslips (VWR 631-0138) using Diamond antifade mounting media (Invitrogen P36961).

2.3.2.7 Multiplex mRNA ISH with immunofluorescence (ISH-IF)

After developing the signal for the *Lgr5* mRNA probe as described above (section 2.3.2.6) without any protease treatment, tissue sections were washed twice (2

minutes each) in 1X TBST and blocked with 10% serum for 1 hour at room temperature. Sections were then incubated with primary antibodies (diluted in 1% BSA dissolved in TBS) overnight at 4°C. The concentrations used for various primary antibodies have been summarised in Table 2.1. Antibodies were diluted in 1% BSA dissolved in 1X TBS solution. For BrdU detection, no additional acid hydrolysis step was performed as a previous report has demonstrated that heat-mediated antigen retrieval produces brighter labelling of BrdU than HCl treatment[159] which enables co-labelling with ISH probes and other antibodies. The next day, slides were washed three times in 1X TBST (5 minutes each) before incubating with Fluorophore-linked secondary antibodies diluted at 1:500 in 1% BSA dissolved in 1X TBS for 1 hour at room temperature (Goat anti-rabbit Alexa 488, Invitrogen, A11008; Goat anti-rat Alexa 488, Invitrogen, A11006, and Goat anti-rabbit Alexa 633, Invitrogen, A21070). After three rounds of wash in 1X TBST (5 minutes each), tissue sections were counterstained with 300 nM DAPI (Invitrogen, D1306) diluted in 1X TBS for 15 minutes at room temperature before a coverslip (VWR 631-0138) was mounted using 25 µL Diamond antifade mounting media (Invitrogen, P36961).

2.3.2.8 TUNEL assay

Apoptotic cells were detected in FFPE tissue sections using Click-iT™ Plus TUNEL Assay Kits (Invitrogen, C10617). 4 µm thick tissue sections were deparaffinized by incubating the slides at room temperature in the following solutions: 100% xylene (twice, 5 minutes each), 50% xylene and 50% ethanol mixture (3 minutes), 100% ethanol (twice, 5 minutes each), 95% ethanol (3 minutes), 85% ethanol (3 minutes), 75% ethanol (3 minutes), 50% ethanol (3 minutes), 0.85% NaCl (5 minutes), and

1X PBS (5 minutes). Slides were then fixed in 4% PFA (Sigma) for 15 minutes at 37°C followed by washing in 1X PBS (5 minutes).

Tissue sections were permeabilized by an incubation in Proteinase K solution (Component H) for 15 minutes at room temperature. After washing the slides in 1X PBS (5 minutes), sections were re-fixed in 4% PFA for 5 minutes at 37°C. Following washes in 1X PBS (5 minutes) and ddH_2O (5 minutes), tissue sections were incubated in TdT reaction buffer (Component A) for 10 minutes at 37°C. At the end of the incubation, the reaction buffer was replaced with a TdT reaction mixture (containing EdUTP and TdT enzyme) and sections were incubated for 1 hour at 37°C for the incorporation of EdUTP into double-stranded DNA breaks by terminal deoxynucleotidyl transferase. Slides were then washed with ddH2O (5 minutes), 1X PBS containing 3% BSA and 0.1% Triton X-100 (5 minutes), and 1X PBS (5 minutes). TUNEL signal was developed by incubating the slides in the TUNEL reaction cocktail (containing Alexa Fluor™ picolyl azide and reaction buffers) for 30 minutes at 37°C in the dark. After rinsing the slides in 1X PBS, tissue sections were counterstained with 300 nM DAPI (Invitrogen, D1306) diluted in 1X PBS. Upon washing the slides twice in 1X PBS (5 minutes each), sections were mounted on coverslips (VWR 631-0138) using Prolong Diamond anti-fade mounting media (Invitrogen, P36961).

2.3.2.9 Detection of EdU by Click-chemistry

EdU was detected in FFPE tissue sections using the EdU-Click 488 kit (Base Click, BCK-EdU488-1). Tissue sections were cut at 4 µm thickness on a microtome (Anglia Bioscience) and dried overnight at room temperature. On the day of staining,

slides were deparaffinised and hydrated according to the steps described in section 2.3.2.1. DNA denaturation (for BrdU detection) was performed by boiling the slides in 10 mM sodium citrate buffer (pH 6.0) for 10 minutes at 98-100°C, followed by cooling them down in the same solution for 20 min. After washing the slides in 1X PBS (5 minutes) and 3% BSA dissolved in 1X PBS (5 minutes), sections were incubated in the reaction cocktail (containing 6-FAM-Azide, catalysts and buffer additives) for 30 minutes at room temperature in the dark to develop EdU signal by Click chemistry. Slides were then washed in 3% BSA dissolved in 1X PBS (5 minutes) and 1X PBS (5 minutes).

To co-detect BrdU with EdU, sections were blocked with 5% goat serum for 1 hour at room temperature followed by overnight incubation at 4°C with rat anti-BrdU antibody (Abcam, ab6326, 1:500) diluted in 1% BSA dissolved in 1X PBS solution. Next day, after three rounds of washing in 1X PBST solution (5 minutes each), BrdU signals were developed by incubating with goat anti-rat Alexa 555 (Invitrogen, A21434) secondary antibody (diluted 1:500 in 1% BSA dissolved in 1X PBS solution) for 1 hour at room temperature. Sections were then washed thrice with 1X PBST (5 minutes each) before counterstaining with 300 nM DAPI (Invitrogen, D1306) diluted in 1X PBS for 15 minutes at room temperature. After washing in 1X PBS twice (5 minutes each), sections were mounted on coverslips (VWR 631-0138) using 25 µL Diamond antifade mounting media (Invitrogen, P36961).

2.4 Image acquisition and analysis

2.4.1 Microscopy

2.4.1.1 Brightfield microscopy

Brightfield images of tissue sections were captured using an Olympus BX51 microscope coupled with an Olympus DP70 camera system using DP controller software. The objective lenses used for imaging were 10X for small intestinal villi, 20X for colonic crypts, and 60X for small intestinal crypts. For measuring mucus layer thickness, a 60X objective lens was used.

2.4.1.2 Fluorescent microscopy

Fluorescent images of intestinal crypts were acquired with a Plan Apochromat 63X or 100X oil objective (numeric aperture 1.4) on a Zeiss LSM 780 upright or inverted confocal microscope with Zen SP7 FP3 (black) software. Z-stacking was used to capture 6-12 optical sections with 50% overlap between subsequent planes within the span of a single cell at 0.3-0.4 µm z-distance, 0.09 µm pixel dimension, and 12-bit depth[138].

2.4.2 Post-processing of confocal images

Z-stack images were processed in batch mode of Fiji package[160]. First, a maximum intensity projection was created to generate a 2D image from the stacks. Next, each channel of the image was separated in Fiji software, and maximum and minimum displayed pixel values were adjusted (minimum: 150-250, maximum: 1500 to 2500) across the entire image set including negative controls. Finally, a pseudo-colour

was assigned to each channel and composite RGB images were exported in TIFF format for quantification described in the following section (2.4.3.2).

2.4.3 Image quantification

2.4.3.1 Quantification of brightfield images

To quantify cell numbers in crypt-villous structures from brightfield images, the *cell counter* plugin of Fiji software was used. The dimensions of crypt-villous structures and the thickness of the mucus layer were calculated using the *measure* tool in Fiji[160].

2.4.3.2 Quantification of fluorescent images

To quantify the number of *Lgr5/LGR5* mRNA expressed in a single cell, all the ISH dots were manually counted within the cell periphery marked by EpCAM staining. However, the existence of overlapping mRNA dots can result in an underestimation of the quantification from a 2D image. In a previous study, only 5-15 *Lgr5* mRNA dots were detected in each cell of intestinal crypts[139], indicating a low concentration of *Lgr5* mRNA in crypt base cells. Therefore, overlapping/merged *Lgr5* mRNA signal dots were rarely observed in this study as the *Lgr5/LGR5* probes were imaged using a confocal microscope at a high resolution (237 nm) capable of resolving sparse mRNA dots in a cell. To calculate the distribution of *Lgr5/LGR5*$^+$ cells in crypts, the cell at the crypt bottom was manually assigned position 0 and cells on either side were counted for each crypt. Any cell containing more than three *Lgr5/LGR5* mRNA was considered as a *Lgr5/LGR5*$^+$ cell[161].

2.5 Measuring cell cycle duration using BrdU incorporation

2.5.1 Estimating the length of S-phase by cumulative BrdU labelling

The length of S-phase (T_S) was determined in the crypt-based columnar (CBC) cells (*Lgr5*$^{+CBC}$) of naked mole rats by counting the number of *Lgr5*$^{+CBC}$BrdU^{+} cells on days 0.33, 0.67, 1, 2, 3, 4, and 5 after 15 successive BrdU pulsing (every 0.33 day). As the crypt-based columnar cells (*Lgr5*$^{+CBC}$) are on average asynchronously and asymmetrically dividing[93,162], the labelling index (LI) which provides the ratio of labelled cells to the total population (LI = *Lgr5*$^{+CBC}$BrdU^{+}/*Lgr5*$^{+CBC}$) at any given time (t) can be modelled by equation 1 where T_T is the total cell division time.

$$LI = (1/T_T) \times t + (T_S/T_T), \quad \text{for } t \leq T_T - T_S \qquad (1)[163]$$

$$LI = 1 \text{ for } t > T_T - T_S$$

Equation 1 assumes that there are no or only very few stem cells that remain quiescent (based on p27 negativity) for the duration of the BrdU experiment. The *lfit* tool in STATA was used to calculate the least square fit of the data by only considering the time points before LI reached saturation. When t = 0, $LI_0 = T_S/T_T$ which is the y-intercept of the graph. Thus, the duration of the S-phase (T_S) was estimated from the y-intercept of the regression line. The T_S for *Lgr5*$^{+}$ cells in mouse small intestine and colon were determined using the same method in organoids (section 2.2.4.3).

2.5.2 Quantification of total cell division time from single time point analysis of BrdU labelling

Having estimated the length of T_S from cumulative BrdU labelling, the total cell division time (T_T) of *Lgr5*$^{+CBC}$ cells was estimated using equation 1 by measuring the labelling index (LI) at a single time point (t) after pulsing animals with BrdU *in vivo*. More specifically, in C57BL/6J mice (n=3, 4-month-old), BrdU was administered once and intestinal tissues were analysed at t = 0.5 hour. In NMRs (n=3, 6-24-month-old), the animals were pulsed with BrdU every 8 hours and intestines were analysed after t = 1 day. To determine the T_T of *Lgr5*$^{+outside\ crypt\ base}$ cells using equation 1, the T_S determined for *Lgr5*$^{+CBC}$ cells in NMRs (section 2.5.1) was used under the assumption that S-phase duration among *Lgr5*$^{+}$ cells does not vary based on their positions in the crypt. A similar assumption has been made previously to determine the T_T of *LGR5*$^{+outside\ crypt\ base}$ cells in human colonic crypts[94].

2.5.3 Estimating the duration of specific cell cycle phases

The T_T value for human colonic *LGR5*$^{+CBC}$ cells (7.3 days) was taken from Ishikawa *et al.*[94] As these cells are reported to be quiescent[94], it was assumed that KI67 is undetectable at G1/S transition and detected in the later phases of the cell cycle (S to M)[164]. The fraction of *LGR5*$^{+CBC}$ cells that are KI67 positive was determined in age-matched colon biopsies (65 to 70-year old, n=5) and the duration *LGR5*$^{+CBC}$ cells spend in S, G2 and M-phase ($T_{(S,\ G2,\ M)}$) was calculated using equation 2:

$$T_{(S,\ G2,\ M)}^{KI67+} = T_T^{(Ref94)} \times LGR5^{+CBC}KI67^{+}/LGR5^{+CBC} \qquad (2)$$

The time in mitosis (T_M) was calculated after quantifying the fraction of *Lgr5*$^{+CBC}$ cells positive for phospho-histone H3 (Ser28) using equation 3.

$$T_M^{KI67+} = T_T^{(Ref94)} \times Lgr5^{+CBC}PHH3^{+}(Ser28)/Lgr5^{+CBC} \quad (3)$$

Using prior experimental values of the duration of S-phase in human LGR5^{+} cells determined using organoids (T_S = 0.25 day)[94], the duration of G2-phase (T_{G2}) was estimated by using equation 4.

$$T_{G2}^{KI67+} = T_{(S, G2, M)}KI67^{+} - (T_S^{KI67+} + T_M^{KI67+}) \quad (4)$$

Next, using the previously reported estimate of T_T[94] in equation 5, the combined time spent in G0 and G1 ($T_{(G1, G0)}^{P27+}$) phases was calculated.

$$T_{(G1, G0)}^{P27+} = T_T^{(Ref94)} \times LGR5^{+CBC}P27^{+}/ LGR5^{+CBC} \quad (5)$$

The fraction of LGR5^{+}P27^{+} cells in G0 (83%), determined by quantifying relative DNA-RNA content in flow cytometry, was taken from Ishikawa *et al.*[94] (Quiescent fraction, QF = number of LGR5^{+}P27^{+} cells in G0 phase/total number of LGR5^{+}P27^{+} cells). Using equation 6, the T_{G0} for human colonic *LGR5*$^{+CBC}$ cells was calculated.

$$T_{G0}^{P27+} = QF^{(Ref94)} \times T_{(G1, G0)}^{P27+} \quad (6)$$

Finally, using equation 7, the time human colonic *LGR5*$^{+CBC}$ cells spend in G1 (T_{G1}) when it is positive for P27-expression (T_{G1}^{P27+}) was calculated.

$$T_T = T_{G0}^{P27+} + T_{G1}^{P27+} + T_S^{KI67+} + T_{G2}^{KI67+} + T_M^{KI67+} \quad (7)$$

In NMR and mouse, *Lgr5*$^{+CBC}$ cells are negative for p27 such that $T_{G0}^{P27+} = 0$. For these species, the combined duration spent in G1 and G2 ($T_{G1+}T_{G2}$) was derived from equation 7 using the values of T_S^{KI67+} (section 5.2.1), T_T (section 5.2.2), and T_M^{KI67+} (section 5.2.3, equation 3).

2.6 Statistical analysis

All statistical tests and graphs displayed in this thesis were generated using StataMP (StataCorp. 2015. Stata Statistical Software: Release 14. College Station, TX: StataCorp LP.). Details of each statistical test performed are described in the figure legends. *P*-values were generated by conducting two-tailed t-tests, F-tests, and Wilcoxon rank-sum tests. No blinding and randomization were performed during the analysis.

For the comparison of means between two cohorts, at least 30 observations were acquired for each group to satisfy the normality assumption for conducting a t-test under the central limit theorem[165]. Before conducting a t-test with less than 30 observations, first a Shapiro-wilk test was performed to ensure the assumption of normal distribution of the data. Finally, the *ttest* function in STATA was used at a 95% confidence level to conduct a two-tailed unpaired t-test with unequal variances (Welch) under the null hypothesis assuming the means of the two cohorts are equal. A *P*-value < 0.05 was considered significant to reject the null hypothesis.

To compare the distributions of two groups having a smaller sample size ($n < 30$) and non-normal distributions, a non-parametric Wilcoxon rank-sum test was deployed using the *ranksum* function in STATA. The two-tailed, unpaired test was conducted under the null hypothesis that the independent samples are from populations with the same distribution. Fischer's exact *P*-value was calculated for the rank-sum test. Any *P*-value < 0.05 was deemed significant to reject the null hypothesis.

To assess any existing linear relationship between an independent and a dependent variable, an ordinary least-squares regression was performed in STATA using the *regress* function at a 95% confidence level under the assumption that each coefficient of the linear regression is zero. A robust standard error was calculated to account for the presence of any variance in the residual component of regression line (i.e., heteroskedasticity). Finally, a *P*-value (calculated by conducting a two-tailed F-test) less than 0.05 was considered significant to reject the null hypothesis.

To describe the magnitude of difference in various parameters between mice and NMRs, the fold change was calculated using the formula: Fold change = (NMR-Mouse)/Mouse. If the fold change is between 0 and 1 (e.g., 0.57), it was expressed as percentage (e.g., 57% higher in NMRs compared to mice). However, for fold change greater than 1 (e.g., 2.1), the magnitude of difference was described as (2.1) times higher in NMRs than mice. Any negative fold change was interpreted as lower value in NMRs compared to mice.

Chapter 3: Cross-species comparison of intestinal tissues

3.1 Introduction

Researchers have long studied the adaptation of animal intestines to their environment, lifestyle, and food habits. Buret *et al.* have reported that desert-dwellers like gerbils and sand rats have a significantly larger intestinal microvillous surface area (normalised to per μm^2 of cell surface) and an improved electrolyte absorption ability to ensure a higher nutrient uptake than household rabbits and rats[166]. Convergently, to reduce body mass, birds have shorter intestines but longer villi, increasing their intestinal surface area compared to non-flying mammals[167]. Additionally, birds exhibit an enhanced paracellular pathway to ensure efficient absorption of glucose and amino acids within their short gut[167]. On the contrary, herbivorous animals have larger intestines, compared to carnivores, with specialised compartments for the fermentation of difficult-to-digest cellulose in leaves[168]. This evidence suggests that intestinal tracts of various species adapt to the environment by altering the total surface area and devising an enhanced digestion and absorption mechanism.

The adaptation of the intestine to food and environment also extends to alterations in the stem cell compartment. Yilmaz *et al.* have demonstrated that caloric restriction in mice results in an increase in the number of small intestinal stem cells per crypt and their regenerative potency by modulating the niche signals[169]. Surgical resection of the murine small intestine also results in an expansion of the stem cell population[170]. Additionally, Muenchau *et al.* have reported that human intestinal epithelial cells improve their barrier function by regulating tight-junction proteins in hypoxic environments[171]. Therefore, it is reasonable to assume that intestinal

structures and epithelial cell populations, including stem cells, respond to environmental cues.

Naked mole rats (NMRs) inhabit subterranean burrows of arid African deserts, with very low oxygen levels[11]. These animals have an extremely long and disease-free lifespan[24]. Despite decades of research into NMR biology, not much is known about their intestines. In this chapter, I will describe the structural features and cellular composition of naked mole rat intestines and compare these data with mouse and human intestines. First, I will determine the suitable ages for optimal comparisons between mouse and NMR intestines. Next, I will compare the percentages of various differentiated cell populations in mouse and NMR intestines. Finally, I will compare the difference in the proportion and localisation of intestinal *Lgr5/LGR5*$^{+}$ stem cells between mice, humans and NMRs.

3.2 Results

3.2.1 Age selection of different species in our study

While 80% of mice live for 3.7 years (45 months) in captivity, a similar fraction of NMRs survive up to 25 years (300 months)[26]. Both mice and NMRs undergo sexual maturation within 4% of their observed lifespan (Figure 3.1A), at 1 year of age in NMRs and 0.125 year (6.5 weeks) in mice. However, the rates at which animals attain a proportion of their adult body-mass (i.e., maturation rate) in different species at various fractions of their lifespan do not exhibit a linear relationship. Mice mature 150 times faster than humans during the first month of life but only 45 times quicker in the next five months[172]. Hence, comparing different species at similar percentages of their total lifespan might not provide the ideal conditions for a fair cross-species comparison. In our study, we reasoned that the age at which maximum growth of intestinal villi had been achieved would be used to compare mice and NMRs.

Small intestinal villi are finger-like structures protruding inside the lumen consisting of a single layer of epithelial cells serving the crucial job of nutrient absorption[96]. The majority of epithelial cells of the small intestine are found in these villi[173]. Reicher *et al.* have reported that intestinal villi grow larger from the juvenile stage to adulthood in mice[174]. However, in older mice, these structures shrink in size as a sign of ageing in their gut[175]. Hence, the number of cells per villi can be considered an adequate parameter to compare between different age groups in each species to determine the age when maximum intestinal growth has been achieved. In this section, the small intestinal (SB1) villi of 2, 12, and 18-month-old mice (Figure 3.1A, top) were compared which span from the early adulthood (sexual maturation 1.5

months) to late-middle age of this species[172]. For NMRs, SB1 villi from 6, 12, and 36-month-old animals were analysed, covering a period from their juvenile stage to early adulthood (Figure 1A, bottom).

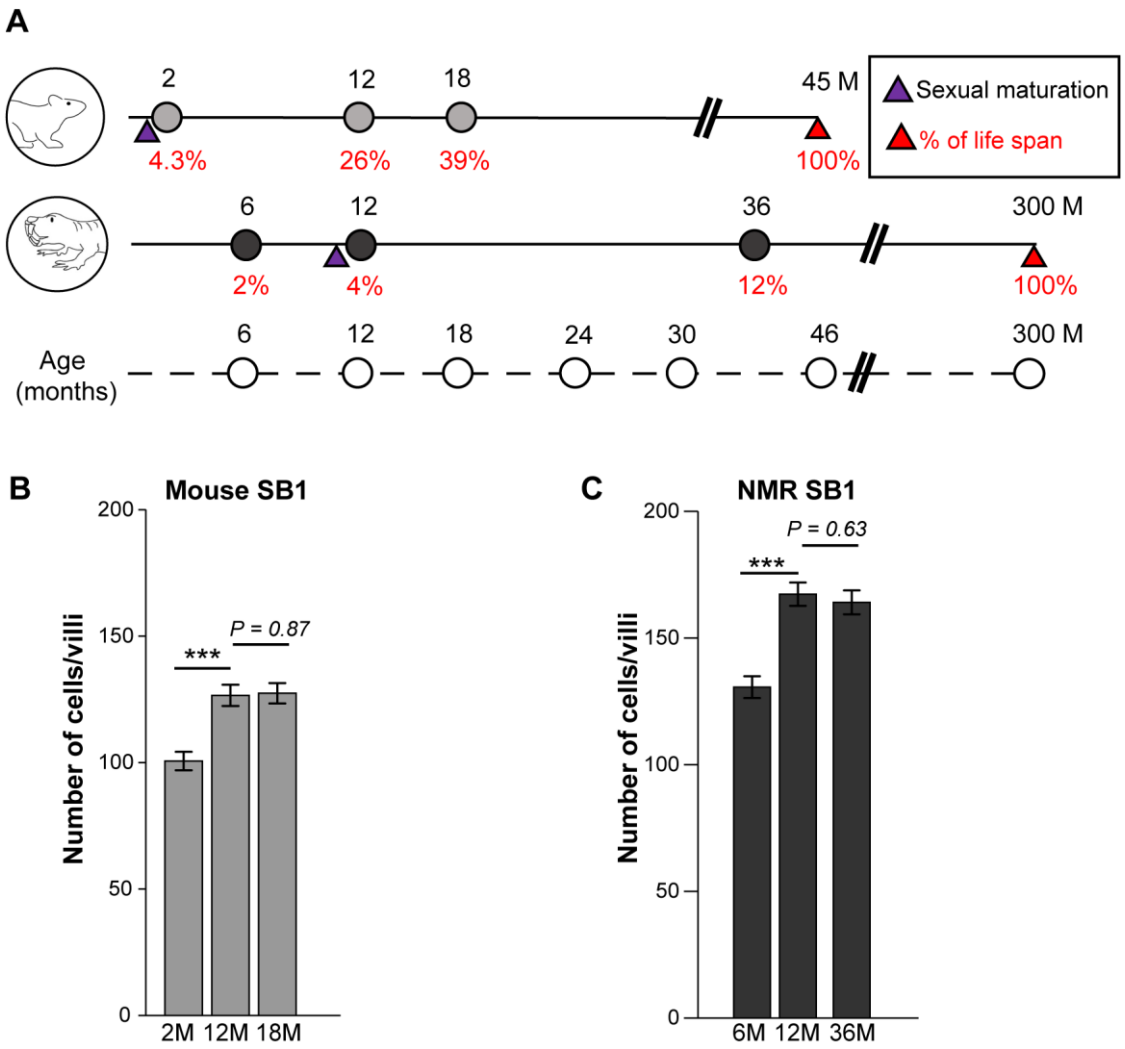

Figure 3. 1: Comparison of villus cell count in small intestine (SB1) between different age cohorts of wild-caught mice and naked mole rats (NMRs).
(A) Timelines showing the relative positions (circles) of selected age cohorts of mice (top) and NMRs (bottom) as percentages of total life span. Purple triangles indicate the age of sexual maturation. Red triangles denote the lifespan of the species as reported by Cagan *et al*[26]. Bar graphs showing the number of cells per villi in small intestine (SB1) across different age groups of **(B)** wild-caught mouse and **(C)** wild-caught NMR (n=30 villi from 3 animals were counted per group). In all cases, statistical significances were determined by performing a two-tailed unpaired Student's *t*-tests using an unequal variance. Significant *P*-values are denoted as such: ***<0.001. Each bar represents the mean ± standard error of the mean.

Quantification of cell numbers from the brightfield images of villi stained with Haematoxylin and Eosin showed that cell count per villi increased by 25% from 2-

month-old (101 ± 4 cells) to 12-month-old mice (127 ± 4 cells) (Figure 3.1B). But no difference in villus cell count was observed between 12- and 18-month-old mice (Figure 3.1B). It was concluded that mice reach their maximum level of growth in the intestinal villi before 12 months of age.

A similar analysis in NMRs revealed an identical pattern where villus cell count increased by 28% from 6-month-old (131 ± 4 cells) to 12-month-old (167 ± 5 cells) animals and then no change was observed at 36 months of age (Figure 3.1C). In summary, 12-month-old mice and NMRs were selected for cross-species comparison as their intestines have reached a growth saturation within the villi.

3.2.2 Epithelial cell populations in naked mole rat and mouse intestines

In this section, the macro and microscopic features of the NMR small intestine and colon were analysed and compared with mice. It was observed that NMRs have 55% shorter small bowels and 31% shorter colons compared to mice (Figure 3.2A-B and Table 3.1). Normalising the absolute intestinal length to body mass showed that the NMR intestine was still significantly shorter than in mice (Figure 3.2C and Table 3.1). Next, by staining longitudinal sections of formalin-fixed paraffin-embedded intestinal tissues with Haematoxylin and Eosin solution, I found that small intestinal villi (average from SB1, SB2, and SB3) in NMRs were 79% longer than mice (Figure 3.2D-E and Table 3.1). NMR villi cell count was also observed to be 40% higher than that in mice (Figure 3.2F and Table 3.1). In both species, villi in the ileum (SB3) were shorter than in the duodenum (SB1) or jejunum (SB2) (Figure 3.2E-F and Table 3.1).

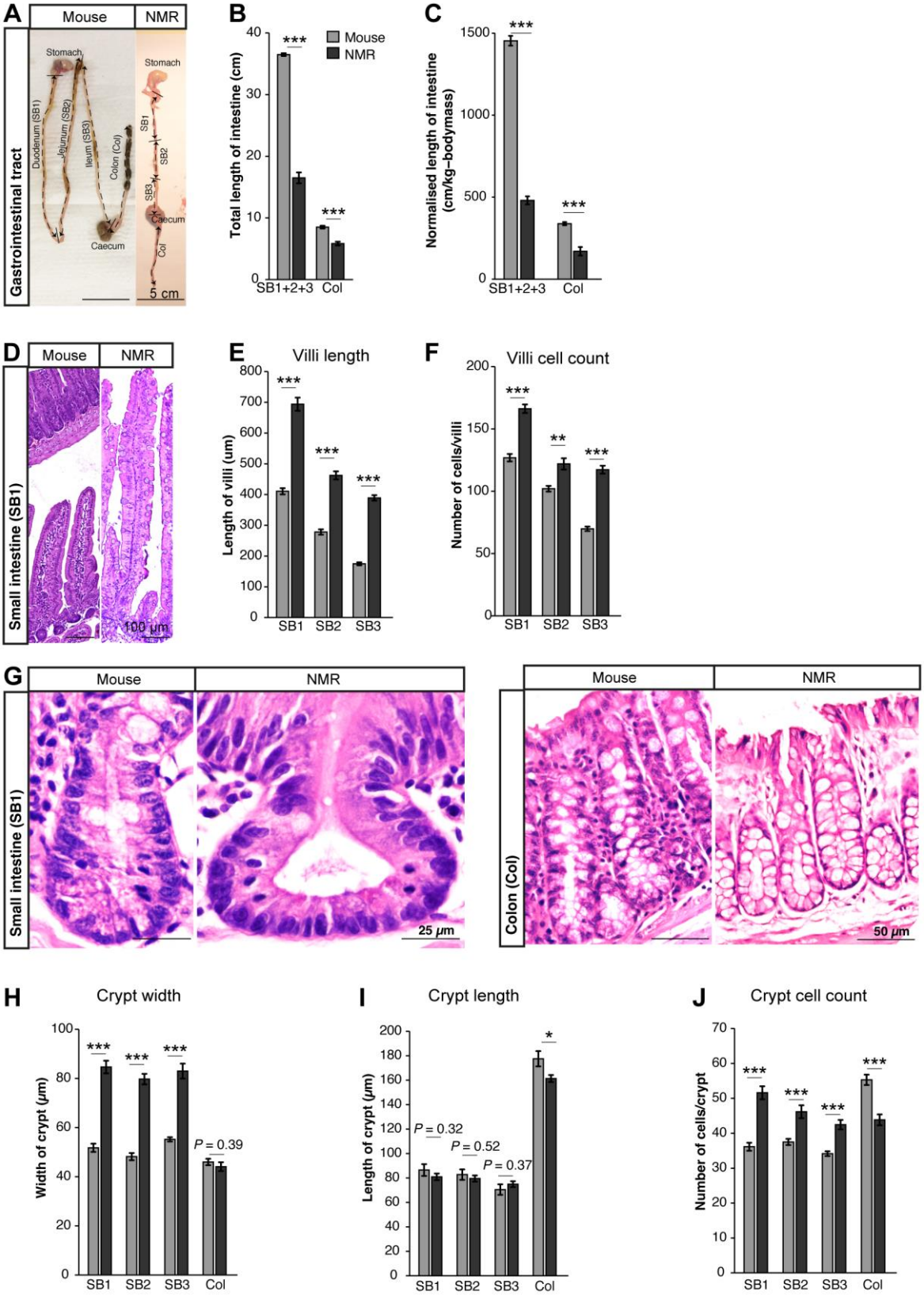

Figure 3. 2: Macroscopic and microscopic analysis of wild-caught naked mole rat (NMR) versus wild-caught mouse intestines (12-month-old).
(A) Photomicrographs of the intestinal tracts of mouse and NMR fully stretched on a paper towel. Different segments of the intestine have been marked on the images (SB1 = duodenum, SB2 = jejunum, SB3 = ileum, and Col = colon). Bar graphs showing significant differences between NMR

and mouse in (**B**) absolute intestinal length and **(C)** normalised intestinal length (12-month-old, n=6 animals per group; *P*<0.001). **(D)** Photomicrographs of NMR and mouse SB1 villi stained with haematoxylin and eosin. Significant differences were observed in **(E)** villus length (n=60 villi from 6 animals per group, *P*<0.001) and **(F)** villus cell counts (n=60 villi from 6 animals per group, *P*<0.001) between NMRs and mice. **(G)** Brightfield images of NMR and mouse SB1 (left) and colonic (right) crypts stained with haematoxylin and eosin. **(H)** Bar graphs showing significant differences in the width of small intestinal crypts (n=30 crypts from 3 animals per group, *P*<0.001) but no difference in the colon (n=30 crypts from 3 animals per group, *P*=0.39). **(I)** No difference was observed in the length of small intestinal crypts (n=30 crypts per group, *P*>0.05) but a slight decrease in the colon in NMRs compared to mice (n=30 crypts from 3 animals per group, *P*<0.05). **(J)** Significant differences were observed in the number of cells in NMR crypts compared to mice in the small intestine and colon (n=30 crypts from 3 animals per group, *P*<0.001). In all cases, statistical significances were determined by performing a two-tailed unpaired Student's *t*-tests using an unequal variance. Significant *P*-values are denoted as such: *<0.05, **≤0.01, ***<0.001. Each bar represents the mean ± standard error of the mean. Scale bars are indicated on the images (25 µm, 50 µm, 100 µm and 5 cm).

By measuring the crypt dimensions in the brightfield images of H and E stained intestinal tissues, it was observed that NMR crypts were 59% wider in the small intestine (Figure 3H and Table 3.1), containing a 30% higher number of cells (Figure 3J and Table 3.1), while exhibiting no difference in length compared to mice (Figure 3I and Table 3.1). Conversely, in the colon, NMR crypts were 10% shorter in length than mice (Figure 3I and Table 3.1), having a 20% lower number of cells (Figure 3J and Table 3.1), with no difference in width (Figure 3H and Table 3.1). In brief, NMRs have shorter intestines and larger crypt-villus structures in the small intestine, but smaller crypts in the colon when compared to mice. The absolute values of various parameters described in this section are presented in Table 3.1.

Table 3. 1: Summary of histological comparison between wild-caught NMR and wild-caught mouse intestines

Parameter	**Region of intestine**	**Mouse[1]**	**NMR[1]**	***P*-value[2]**
Length of GI track (cm)	SB1 + SB2 + SB3	36.5 ± 0.22	16.5 ± 0.88	<0.001
	Col	8.5 ± 0.22	5.83 ± 0.31	<0.001
Length of villi (µm)	SB1 + SB2 + SB3	288.01 ± 8.60	515.15 ± 13.13	<0.001
	SB1	410.76 ± 10.0	693.91 ± 21.38	<0.001

Parameter	**Region of intestine**	**Mouse[1]**	**NMR[1]**	***P*-value[2]**
	SB2	278.31 ± 8.67	462.29 ± 13.22	<0.001
	SB3	174.95 ± 4.89	389.25 ± 8.86	<0.001
Number of EPCAM+ cells/villi	SB1 + SB2 + SB3	100.23 ± 1.99	140.36 ± 2.72	<0.001
	SB1	126.88 ± 3.01	166.22 ± 3.43	<0.001
	SB2	102.05 ± 2.29	121.93 ± 4.53	<0.01
	SB3	69.85 ± 1.78	117.30 ± 3.19	<0.001
Crypt width (µm)	SB1 + SB2 + SB3	51.71 ± 0.84	82.45 ± 1.50	<0.001
	SB1	51.76 ± 1.67	84.65 ± 2.55	<0.001
	SB2	48.17 ± 1.48	79.73 ± 2.14	<0.001
	SB3	55.20 ± 0.86	82.97 ± 3.04	<0.001
	Col	45.99 ± 1.30	44.09 ± 1.80	0.39
Crypt length (µm)	SB1 + SB2 + SB3	80.13 ± 2.64	78.54 ± 1.48	0.60
	SB1	86.48 ± 4.81	80.96 ± 2.71	0.32
	SB2	82.74 ± 4.29	79.54 ± 2.51	0.52
	SB3	70.50 ± 4.31	74.93 ± 2.41	0.37
	Col	177.56 ± 6.26	161.40 ± 2.84	<0.05
Crypt cell count (µm)	SB1 + SB2 + SB3	35.93 ± 0.55	46.74 ± 1.05	<0.001
	SB1	36.14 ± 1.15	46.17 ± 1.84	<0.001
	SB2	37.50 ± 0.89	42.47 ± 1.36	<0.001
	SB3	34.17 ± 0.69	43.83 ± 1.57	<0.001
	Col	55.29 ± 1.48	43.83 ± 1.57	<0.001
Alcian+ cell/villi (%)	SB1 + SB2 + SB3	12.11 ± 0.26	20.23 ± 0.46	<0.001
	SB1	11.41 ± 0.33	18.68 ± 0.82	<0.001
	SB2	11.62 ± 0.35	22.11 ± 0.66	<0.001
	SB3	13.43 ± 0.62	20.74 ± 0.66	<0.001
Alcian+ cell/crypt (%)	SB1 + SB2 + SB3	19.79 ± 0.88	29.27 ± 1.03	<0.001
	SB1	16.88 ± 1.11	25.77 ± 1.78	<0.001
	SB2	16.29 ± 1.05	26.48 ± 1.54	<0.001
	SB3	26.20 ± 1.62	35.58 ± 1.47	<0.001
Thickness of mucus layer (µm)	Col	9.19 ± 0.48	24.37 ± 3.46	<0.001
	SB1 + SB2 + SB3	0.38 ± 0.04	1.57 ± 0.08	<0.001

Parameter	Region of intestine	Mouse[1]	NMR[1]	*P*-value[2]
ChrA+ cell/villi (%)	SB1	0.44 ± 0.07	1.93 ± 0.11	<0.001
	SB2	0.50 ± 0.06	1.56 ± 0.14	<0.001
	SB3	0.19 ± 0.06	1.01 ± 0.13	<0.001
ChrA+ cell/crypt (%)	SB1 + SB2 + SB3	1.00 ± 0.18	3.59 ± 0.38	<0.001
	SB1	1.11 ± 0.38	4.80 ± 0.85	<0.001
	SB2	1.33 ± 0.29	3.78 ± 0.59	<0.001
	SB3	0.56 ± 0.21	2.37 ± 0.44	<0.001
	Col	0.05 ± 0.05	2.38 ± 0.48	<0.001

[1]mean ± standard error of mean
[2]p-value for two-tailed, unpaired Student's t-test using unequal variance

3.2.2.1 Intestinal goblet cells in mice and naked mole rats

Goblet cells are highly polarized exocrine cells of the intestine that secrete mucins, creating a physical barrier against microbial and chemical contents (digestive enzymes and acids, and food-associated toxins), located between the lumen and the epithelial layer[113]. Alcian blue (pH 2.5) can stain all acid-mucins in the secretory cells of the intestine[176,177]. Staining with Alcian blue in the small intestine revealed 67% higher percentage of goblet cells in NMR villi (20.23% ± 0.46%) compared to mice (12.11% ± 0.26%), and 48% higher proportion of goblet (Alcian^{+}) cells in NMR crypts (29.27% ± 1.03%) than in that of mice (19.79% ± 0.88%) (Figure 3.3A and Table 3.1).

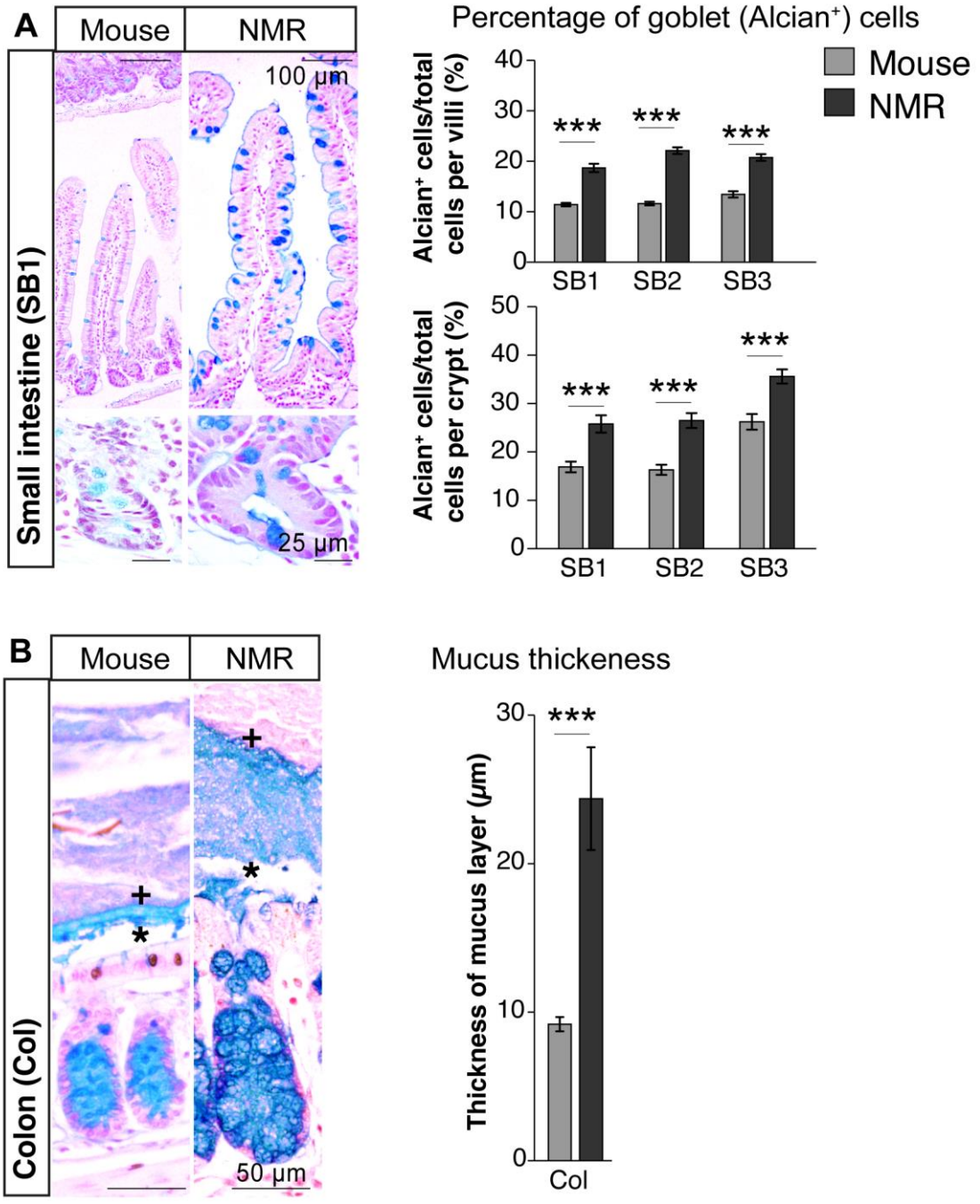

Figure 3. 3: Comparison of the percentage of goblet cells between wild-caught mouse and NMR intestines.

(A) Photomicrographs (left) showing SB1 villi and crypts stained with Alcian blue. Bar graphs (right) showing significant differences in the proportion of goblet cells (Alcian blue$^+$) in the villi (top) and the crypts (bottom) of the duodenum (SB1), jejunum (SB2) and ileum (SB3) (n=60 crypts/villi from 6 animals per group, P<0.001). (**B**) Photomicrographs (left) showing mucus layer in the colon preserved by Carnoy fixation. Measurement of the secreted mucin from the inner (denoted by *) to the outer (+) layer revealed a significantly thicker layer in the NMR colon (n=30 measurements from 3 animals per group, P<0.001). In all cases, statistical significances were determined by performing a two-tailed unpaired Student's t-tests using an unequal variance. Significant P-values are denoted as such: ***<0.001. Each bar represents the mean ± standard error of the mean. Scale bars are indicated on the images (25 µm and 50 µm).

In the colon crypts, it was not possible to quantify the goblet cells using Alcian blue due to the difficulty of identifying stained vacuoles in a particular cell (Figure 3.3B, left). To indirectly measure the relative abundance of goblet cells in the colon, tissues were fixed in Carnoy's solution that preserved the mucus layer between the faecal matter and the surface epithelia. After staining with Alcian blue, a continuous layer of mucin gel above the epithelial cells in the colon was observed (Figure 3.3B, left). Measuring the distance from the inner to the outermost layer of the mucus (Figure 3.3B, left), NMRs were observed to have a 1.65-times thicker mucus layer in the colon (24.37 µm ± 3.46) than mice (9.19 µm ± 0.48) (Figure 3.3B, right and Table 3.1). Together these results indicate that the NMR intestine has a higher proportion of mucus-secreting goblet cells than mice.

3.2.2.2 Intestinal enteroendocrine cells in mice and naked mole rats

Chromogranin A (ChrA), an acidic glycoprotein found in secretory vesicles containing large and dense cores, marks the hormone-secreting enteroendocrine cells in the intestine[120]. Performing immunohistochemistry using an antibody specific for ChrA protein (Figure 3.4A), 3.1-times higher proportion of $ChrA^+$ enteroendocrine cells in the villi (1.57% ± 0.08 in NMRs and 0.38% ± 0.04 in mice) and a 2.6-times higher percentage in the crypts (3.59% ± 0.38 in NMR and 1.00% ± 0.18 in mice) were detected in NMR small intestine compared to mouse (Figure 3.4B and Table 3.1). Similarly, colonic crypts in NMR (2.38% ± 0.48) contained a higher proportion of $ChrA^+$ cells than mice (0.05% ± 0.05) (Figure 3.4B, bottom and Table 3.1). A gradual decrease in the percentages of $ChrA^+$ cells was observed from the proximal to the distal end of the small intestine in both species (Figure 3.4B

and Table 3.1). In brief, NMRs have a higher percentage of enteroendocrine cells than mice throughout the intestinal tract.

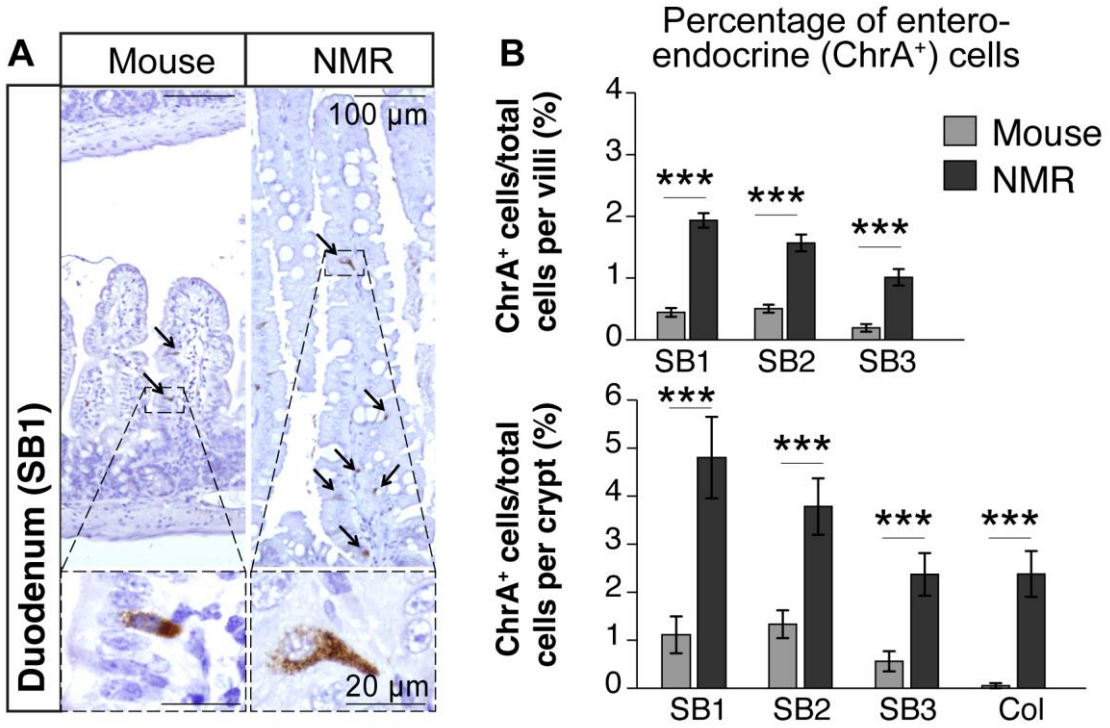

Figure 3. 4: Comparison of the percentage of enteroendocrine cells between wild-caught mouse and NMR intestines.
(**A**) Immunohistochemical staining (left) of mouse and NMR SB1 villi showing enteroendocrine cells detected using an anti-ChrA antibody. **(B)** Proportions of ChrA$^+$ cells were higher in both the NMR villi (top panel) as well as crypts (bottom panel) compared to mice (n=60 crypts/villi from 6 animals per group, P<0.01). In all cases, statistical significances were determined by performing a two-tailed unpaired Student's t-tests using an unequal variance. Significant P-values are denoted as such: ***<0.001. Each bar represents the mean ± standard error of the mean. Scale bars are indicated on the images (20 µm and 100 µm).

3.2.2.3 Intestinal enterocytes in mice and naked mole rats

In the intestine, enterocytes play an essential role in the absorption of nutrients[99]. These cells are characterised by the expression of alkaline phosphatase (AP), an enzyme that hydrolyses dietary phospholipids[178]. Previously, enterocytes in tissue sections have been detected in mice, rats, and primates using AP staining[105,178-180]. Using a commercially available kit, the intestinal tissues were stained for AP and a gradual decrease in the expression was observed from the proximal (SB1) to the

distal end (SB3) of the small intestine in mice (Figure 3.5, left panel). In contrast, NMR small intestine (SB1, SB2, and SB3) showed a constant level of AP expression throughout the small intestine, including the ileal (SB3) villi (Figure 3.5, right panel). It was, however, difficult to accurately quantify the number of AP^+ cells based on histology, since AP is only expressed along the brush borders.

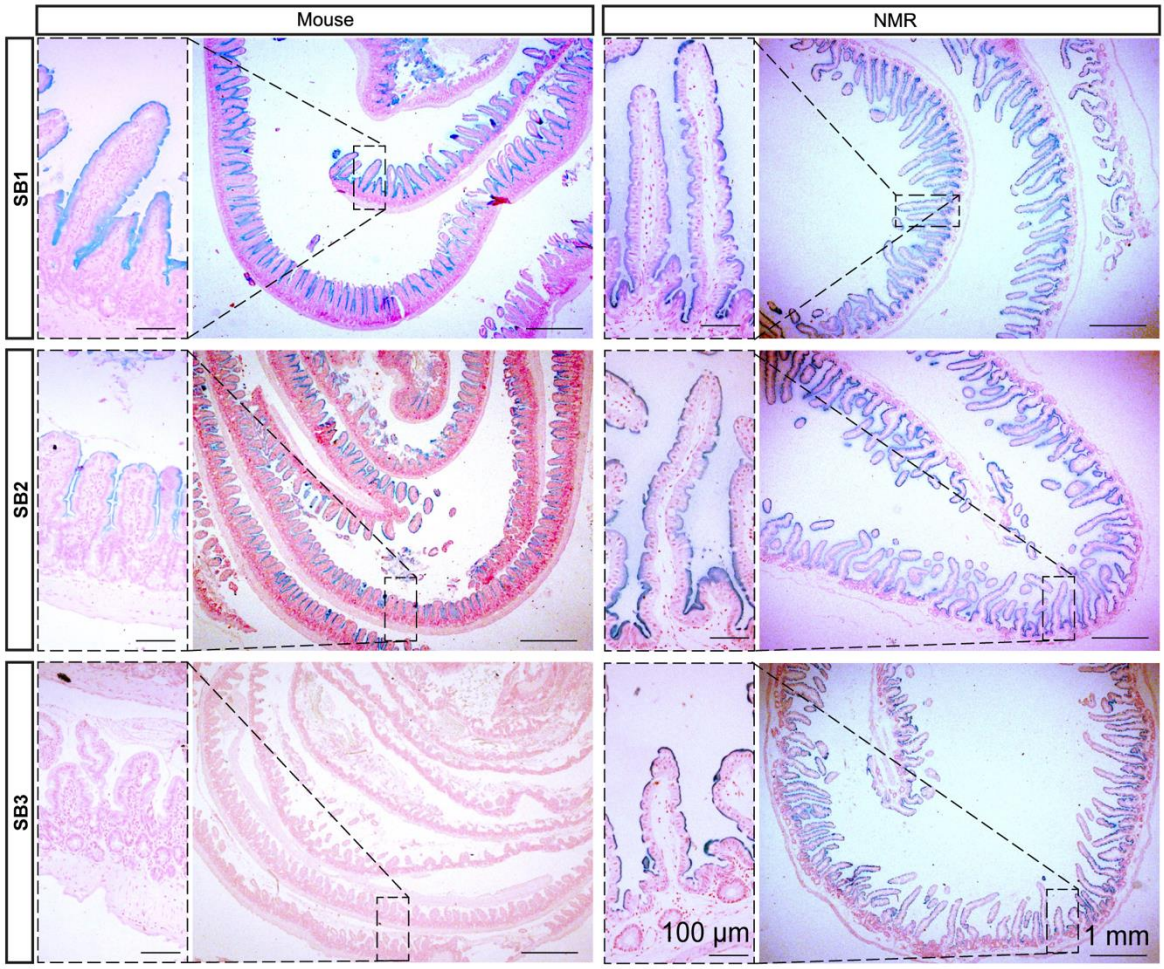

Figure 3. 5: Comparison of enterocyte expression in wild-caught mouse and NMR small intestines.
Photomicrographs of alkaline phosphatase staining (blue) in the small intestine (SB1, SB2, and SB3) showing a gradual decline of enterocyte expression in mice (left panel, from top to bottom) whereas sustained expression was observed throughout the small intestine in NMRs (right panel). Nucleus was counterstained with Nuclear Fast Red dye. Scale bars are indicated on the images (100 µm and 1 mm).

The cross-species histological analysis was not extended to Paneth, Tuft, and M-cells due to the scarcity of commercially available antibodies that would cross-react with NMR epitopes. Overall, based on the histological quantification performed in section 3.2.2, naked mole rats have a shorter intestine containing a higher proportion of every differentiated cell population evaluated in this study compared to mice.

3.2.3 Cross-species comparison of intestinal *Lgr5(LGR5)*$^{+}$ cells

Leucine-rich repeat-containing G-protein coupled receptor 5 (Lgr5) mark a population of adult stem cell (ASC) in the intestines of mouse[83] and human[181]. Lgr5 is also expressed by stem cells in different organs such as stomach[182], liver[183], hair follicle[184], and kidney[185]. Given the evidence supporting the role of Lgr5 as a stem cell marker across a variety of organs and species, this section will explore if this gene is expressed in the intestinal cells of NMRs. *In Situ* Hybridisation (ISH) was performed in formalin-fixed paraffin-embedded tissue sections using RNAScope probes to detect *Lgr5* mRNA in the epithelial cells of the intestine. The following sections of this chapter will describe the optimisation steps to detect *Lgr5*$^{+}$ cells in intestinal tissues, and the proportion and localisation of *Lgr5*$^{+}$ cells in NMR intestines in comparison with mice and humans.

3.2.3.1 Optimising *Lgr5* mRNA detection in individual intestinal cells

In order to detect *Lgr5* mRNA in a particular cell within the intestinal tissue, a combination of ISH using an *Lgr5* probe and immunofluorescence (IF) using an anti-Epithelial Cell Adhesion Molecule (EpCAM) antibody was used. EpCAM

demarcates the outer periphery of all epithelial cells and, therefore, can be useful to locate *Lgr5* mRNA signals in a single cell. However, the ISH protocol involves a protease treatment that can cause degradation of the protein epitopes detected by the IF antibody. To determine whether ISH for *Lgr5* mRNA can be performed by omitting the protease treatment, NMR duodenal tissues were stained using the RNAScope *Lgr5* probe with and without protease incubation. Confocal imaging of crypts detected mRNA signal dots in both sets of tissue sections (Figure 3.6A). Quantification of the number of *Lgr5* mRNA captured within the periphery of each crypt showed no differences between sections developed with and without protease treatment (Figure 3.6B). Therefore, it appears that the removal of protease treatment to preserve protein epitopes during the development of ISH did not result in any variation in the detection of *Lgr5* mRNA in NMR intestinal tissue.

After the successful development of the *Lgr5* mRNA signal without protease treatment, the same tissue sections were stained for EpCAM using an antibody following a standard immunofluorescence protocol (details in section 2.3.2.7). Imaging with a high numerical aperture lens (NA=1.4) in a confocal microscope (Zeiss 780 LSM), fluorescent signals were detectable for *Lgr5* mRNA within the cell periphery marked by EpCAM staining in the intestinal crypts of NMR (Figure 3.6C). Thus, the ISH-IF protocol resolved the issue of accurately counting mRNA signals present in each cell of the tissue sections.

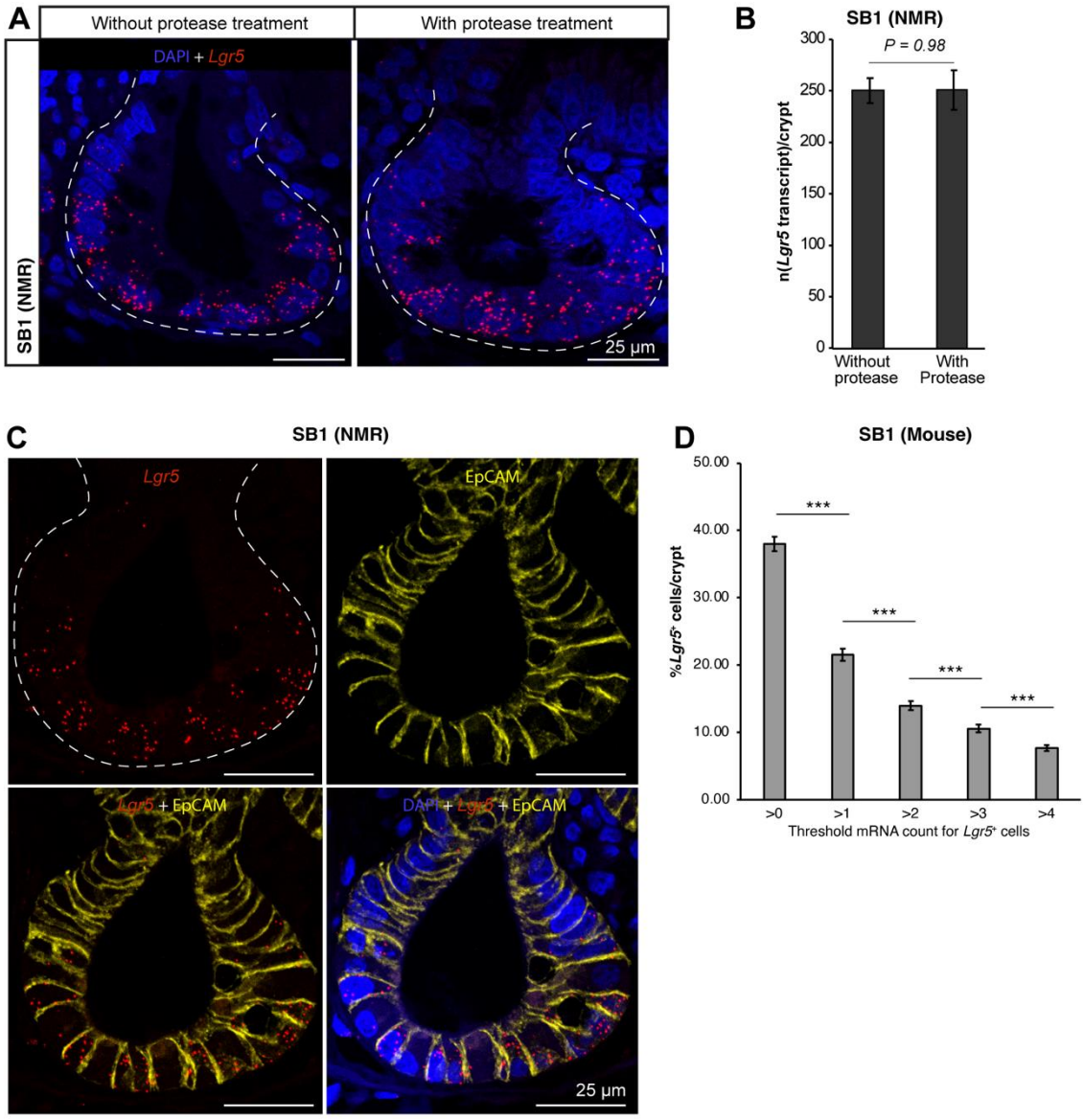

Figure 3. 6: Optimisation of the parameters for the detection of *Lgr5*⁺ cells using *in situ* hybridisation.
(A) Confocal images depicting *Lgr5* mRNA (red) in NMR SB1 crypt sections developed without (left) and with (right) protease treatment using RNAScope probes. Dashed lines indicate the outer periphery of the crypt. **(B)** Bar graphs showing no difference between the number of *Lgr5* mRNA dots detected between SB1 crypt sections stained without and with protease solution. Dots were counted within the demarked periphery of n=30 crypts per group using the *particle analyzer* function of the Fiji package[160]. **(C)** Single channels from a confocal image of NMR SB1 crypt displaying specific staining for DAPI (blue), *Lgr5* (red dot, ISH), and EpCAM (yellow, IF). The dashed line indicates the outer periphery of the crypt. **(D)** Bar graphs showing decreasing percentages of *Lgr5*⁺ cells detected by ISH in mouse SB1 crypts with increasing thresholds (n=100 crypts from 6 animals counted for each threshold). In all cases, statistical significances were determined by performing a two-tailed unpaired Student's t-tests using an unequal variance. Significant *P*-values are denoted as such: ***<0.001. Each bar represents the mean ± standard error of the mean. Scale bars are indicated on the images (25 µm).

Using an Lgr5-EGFP knock-in mouse model, Dehmer *et al.* have reported the presence of 10% Lgr5$^+$ cells in the murine small intestinal crypts[186]. Using this information, the threshold number of *Lgr5* mRNA puncta that would allow the detection of a similar proportion of cells positive for *Lgr5* expression (*Lgr5*$^+$) in our *in situ* hybridisation assay was attempted to calibrate. After quantifying percentages of *Lgr5*$^+$ cells considering various increasing thresholds (>0, >1, >2, >3, and >4 mRNA puncta), a significantly lower proportion of *Lgr5*$^+$ cells was detected in murine crypts for each increment, as expected (Figure 3.6D). For a threshold of >3 mRNA, around 10% of cells per crypt in the murine duodenum were *Lgr5*$^+$ (Figure 3.6D), similar to the previously reported value using the knock-in model[186]. Therefore, according to our calibration, a cell was considered *Lgr5*$^+$ in this study if it contained >3 *Lgr5* mRNA puncta.

3.2.3.2 Quantification of *Lgr5(LGR5)*$^+$ cells across species

Previous studies have reported the presence of *Lgr5*$^+$ cells at the base of intestinal crypts in mice[83] and humans[181]. Staining with *Lgr5* mRNA ISH probe and anti-EpCAM antibody identified *Lgr5*$^+$ cells at the base of small intestinal and colonic crypts in NMR (Figure 3.7A-B, left). Similar to the previous report in mice[83], *Lgr5*$^+$ cells in the NMR intestine exhibited the slender morphology of Crypt Base Columnar (CBC) cells (Figure 3.7A, left). Quantification of cells containing >3 *Lgr5* mRNA within the periphery outlined by EpCAM staining showed NMR SB1 crypts contained 1.5-times higher proportion of *Lgr5*$^+$ cells (26.62% ± 0.70) than in mice (10.58% ± 0.55) (Figure 3.7A, right). Like mice, *Lgr5*$^+$ cells in NMR small intestinal crypts were interspersed with large, post-mitotic (Ki67$^-$, data not shown) cells (Figure 3.7 A, left). Considering the localisation pattern and the low nucleus-to-cytoplasm ratio of these

cells, they were speculated to be intestinal Paneth cells, a differentiated cell population located at the crypt base that secretes Wnt signalling molecules to neighbouring *Lgr5*$^{+}$ cells and protects them by excreting anti-microbial substances[117].

In the distal colon, NMR crypts contained 56% and 50% higher proportion of *Lgr5*$^{+}$ cells (6.64% ± 0.38) than mice (4.25% ± 0.37) and humans (4.42% ± 0.34), respectively (Figure 3.7 B). Percentages of *Lgr5*$^{+}$ cells in the colonic crypts were lower than small intestinal ones in both mice and NMRs. In summary, NMR intestinal crypts exhibit a higher percentage of *Lgr5*$^{+}$ cells than mice and humans.

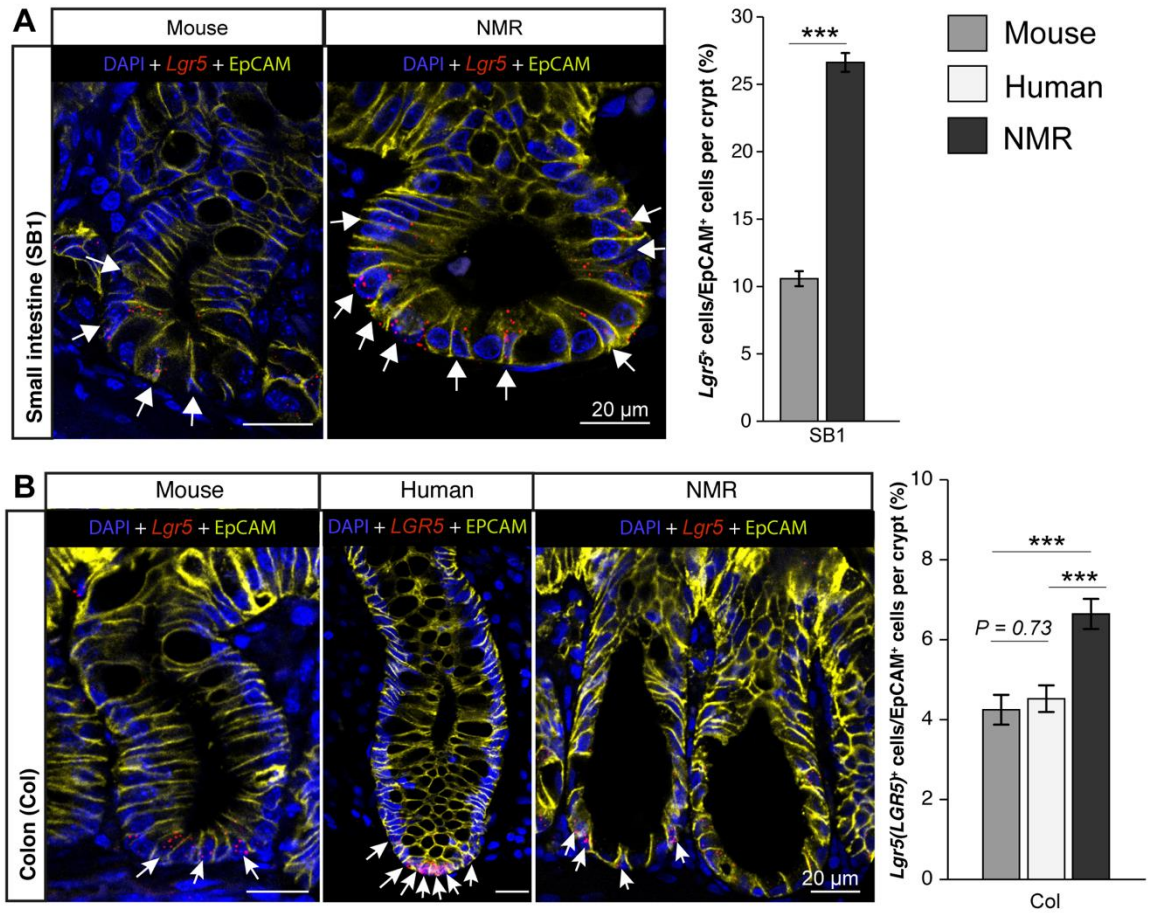

Figure 3. 7: Comparison of the percentage of intestinal *Lgr5(LGR5)*$^{+}$ cells per crypt in wild-caught mice, humans, and wild-caught NMRs.
(A) Confocal images (left) showing NMR and mouse small intestinal (SB1) crypts co-stained with RNAScope probe for *Lgr5* mRNA (red), anti-EpCAM antibody (yellow), and DAPI (blue). White

arrows indicate *Lgr5*$^{+}$ cells. Bar graphs (right) showing NMRs (12-month-old) having a higher percentage of *Lgr5*-expressing (*Lgr5*$^{+}$) cells in the small intestinal crypts compared to 12-month-old mice (n=138 crypts from 3 animals per group, *P*<0.001). **(B)** Multicolour images (left) of mouse, human, and NMR distal colonic crypts co-stained for *Lgr5(LGR5)*-mRNA (red), EpCAM (yellow) and DAPI (blue). White arrows indicate *Lgr5(LGR5)*$^{+}$ cells. Bar graphs (right) showing differences in the percentages of *Lgr5(LGR5)*$^{+}$ cells in the colonic crypts of mice, humans, and NMRs (n=129 crypts from 3 animals for mice and NMRs, and 65 crypts from 4 healthy humans (28 to 33-year-old), *P*-values are indicated on the graph). In all cases, statistical significances were determined by performing a two-tailed unpaired Student's t-tests using an unequal variance. Significant *P*-values are denoted as such: ***<0.001. Each bar represents the mean ± standard error of the mean. Scale bars are indicated on the images (20 µm).

3.2.3.3 Localisation of intestinal *Lgr5(LGR5)*$^{+}$ cells across species

After comparing the proportion of *Lgr5*$^{+}$ cells between mice and NMR, any difference in their localisation within crypts at a single-cell resolution was assessed. Counting percentages of *Lgr5*$^{+}$ cells at each cell position showed a gradual decrease of *Lgr5* expression from the base (position 0) to the top of intestinal crypts of mice, humans, and NMRs (Figure 3.8). For murine duodenal crypts, the same numbering strategy used by Barker *et al.* that accommodates five pairs of CBC-Paneth cells at the crypt base was followed[83] (Figure 3.8A, left). As NMR small intestinal crypts are wider than in mice (section 3.2.2), a higher number of CBC-Paneth pairs can be accommodated at the crypt base in this species. Therefore, after determining the number of cells exhibiting the alternate morphology of CBC-Paneth pairs (data not shown), the numbering schema was modified for the NMR small intestine to include seven such pairs at the crypt base (Figure 3.8A, right). In short, cell positions 0 to 3 on either side of the crypt in the murine small intestine harbour CBCs. In NMR duodenum, CBCs reside at positions 0 to 4. Quantification of the area under the curve at these positions revealed that 87% of *Lgr5*$^{+}$ cells were residing at the crypt base (i.e. *Lgr5*$^{+CBC}$) in mice (Figure 3.8A, left) while 76% of *Lgr5*$^{+}$ cells were at the crypt base of NMR small intestine (Figure 3.8A, right). *Lgr5*$^{+}$ cells above the crypt base are found at higher cell positions in NMR (up to position 9) than in murine (up to position 5) intestinal crypts.

As there are no Paneth cells in the colon, a simple numbering pattern was followed for all three species (Figure 3.8B). Analysis of the distribution graph showed, among all *Lgr5/LGR5*$^{+}$ cells in the colonic crypts, 62% in mice, 68% in humans, and 80% in NMRs are located in cell positions 0 to 4 (Figure 3.8B). No difference was observed in the distribution of “above +4” cells in the colonic crypt among the three species.

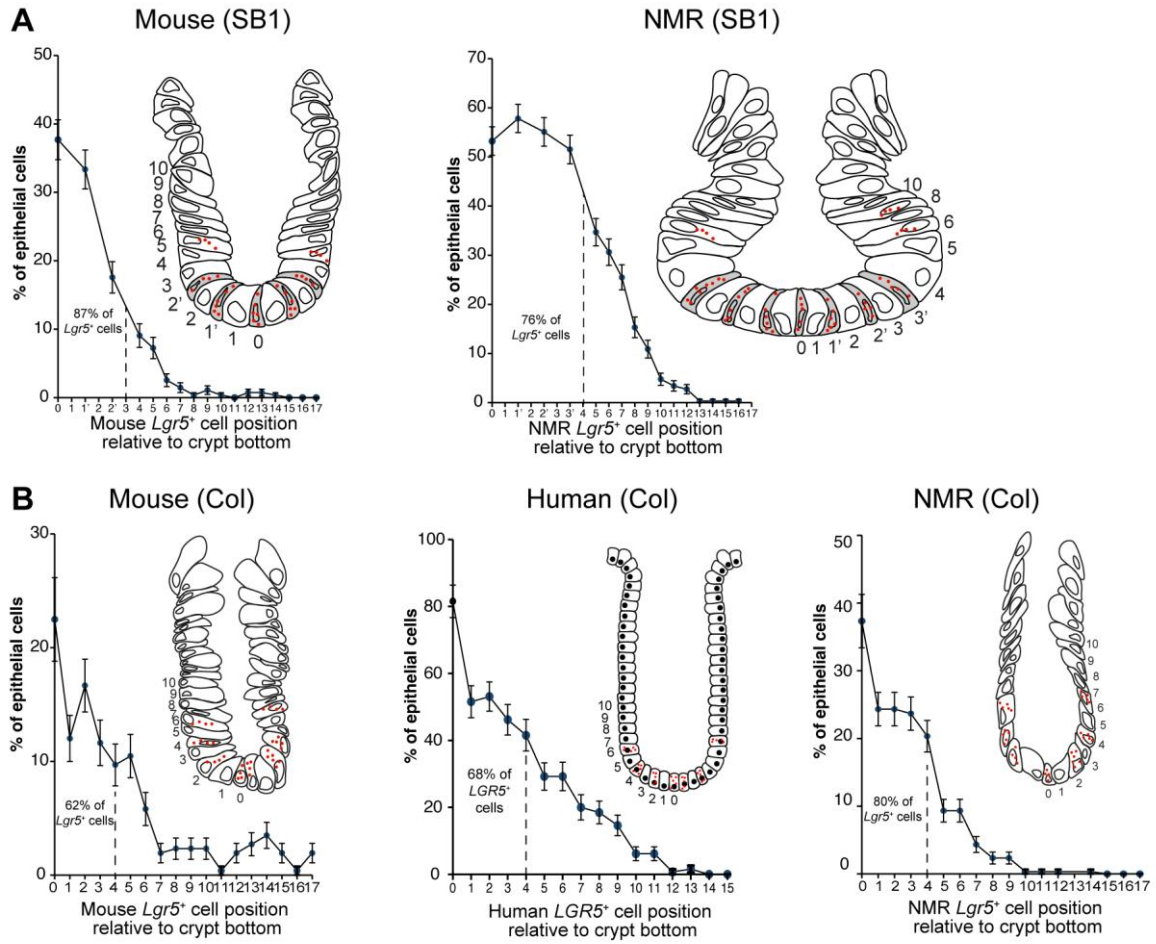

Figure 3. 8: Comparison of the location of *Lgr5*$^{+}$ cells between wild-caught mouse, human, and wild-caught NMR intestinal crypts.
Frequencies at which the *Lgr5(LGR5)*$^{+}$ cells appeared at specific positions relative to the crypt bottom in **(A)** mouse (left) and NMR (right) small intestine (SB1), and **(B)** mouse (left), human (middle), and NMR (right) colon (n=258 cells per position counted from 129 crypts from 3 animals for rodents and 130 cells per positions counted from 65 crypts from 4 individuals for human). Each scatter dot represents the mean ± standard error of the mean. The schema in the inset of each graph

summarises the numbering configuration used for counting cell positions. Red dots indicate *Lgr5(LGR5)*-mRNAs.

In brief, proportions of *Lgr5*$^{+}$ cells are higher in NMR intestinal crypts than in mice and humans. In all three species, the majority of *Lgr5(LGR5)*$^{+}$ cells are located at the crypt base.

3.3 Discussion

The NMRs live underground in the hot and arid environment of Africa, amid a scarcity of food and water[11]. Their diet, like that of African mole rats, mostly consists of geophytes (e.g. sweet potato, gemsbok cucumber, wild onion bulbs etc. enriched in starch) which is the sole source of hydration for these animals[187]. As a result of adaptation to such an extreme environment and specific diet, the epithelial cell population in their intestine has evolved strategies to efficiently absorb nutrients and water from their limited food resources.

The data in this chapter have shown that NMRs have 55% shorter small intestines than mice which is compensated by an increased efficiency in absorption mechanisms within this short length. The intestine is one of the largest organs in an animal's body, making it metabolically expensive to maintain[188]. Most herbivores have longer intestines due to the microbial fermentation required for cellulose digestion and absorption[189]. Despite being herbivores, the naked mole rats strictly consume starch-enriched tubers and bulbs that are easier to metabolise than cellulose. These food habits may help the NMRs digest their food within a shorter intestine, making it more energy efficient for these xerocoles.

We also observed 79% longer intestinal villi in NMRs than in mice. Having longer villi increases the surface area for nutrient absorption within the short length of the gut. Also, these animals have absorptive enterocytes even in the distal portion of the intestine, which can enhance food absorption in a short intestinal tract[178]. In section 3.2.2.2, I have reported roughly a 3-times higher percentage of enteroendocrine cells in NMR intestines compared to mice. These cells are involved

in the sensing and absorption of nutrients[123]. Hence, having an increased proportion of enteroendocrine cells can further contribute to the effective uptake of food and water in the NMR gut. To summarise, an energy-efficient shorter intestine in the naked mole rat may have arisen in response to its adaptation to a starch-enriched diet found in the arid environment. These includes longer intestinal villi, and higher percentages of enterocytes and enteroendocrine cells that may ensure adequate nutrient absorption within the shorter length of the intestine.

In section 3.2.2.1, I reported that NMRs exhibit a higher proportion of goblet cells secreting a thicker layer of mucus in their intestine compared to mice. The intestinal mucus layer protects epithelial cells from microbial and chemical insults[190]. Therefore, NMR intestines might be more resistant to epithelial damage than mice. Additionally, as NMRs do not drink water, this extra mucus can facilitate the lubrication and passage of food during bowel movements. Along with protection from a thicker mucus layer, ChrA$^+$ enteroendocrine cells can produce catestatin upon cleavage, exerting anti-inflammatory effects on macrophages and monocytes[121]. In summary, the results in section 3.2.2 indicate that naked mole rats have a specialised intestine with higher proportions of differentiated cell populations that enable efficient nutrient absorption as well as provide protection against damage in the intestine.

As the NMR intestine is composed of a large proportion of differentiated cells, it requires a pool of stem and progenitor cells to maintain the tissue. In the intestine, *Lgr5*$^+$ stem cells drive the renewal of tissue following two lineage-commitment and differentiation pathways (for secretory and absorptive cells) controlled by

morphogen gradients (Wnt, BMP, Grem1, Sox9, EphB2) surrounding the crypt[97,137,191]. The number of stem cells in the intestine is, therefore, a key determinant of its long-term maintenance.

In section 3.2.3, NMR intestinal crypts were reported to have a higher proportion of *Lgr5*$^{+}$ cells than mice, residing mostly at the base of the crypt. This is in agreement with the result in section 3.2.2 showing small intestinal crypts in NMRs are wider than murine ones. Wider crypts can accommodate more cells at the crypt base where niche signalling operates strongly. As *Lgr5*$^{+}$ cells in the duodenum always reside intermingled with Paneth cells[117], it is probable that the proportion of Paneth cells in NMRs should also be greater than in mice. This could be confirmed in future studies by staining small intestinal crypts from mice and NMRs with species-specific *Defa1* mRNA ISH probes.

Ritsma *et al.* have reported a dynamic heterogeneity in the survival advantage of *Lgr5*$^{+}$ cells in the mouse duodenum. The more central (position 0 to +2) cells have a higher clonal expansion (fold increase in clone size) and can outcompete the border cells (position +3 to +4) in mouse[132]. Due to the wider, flat base of duodenal crypts, an expanded number of cell positions can be expected in NMRs to demonstrate such enhanced survival advantage. This will make a mutation in *Lgr5*$^{+}$ cells in NMR less likely to become dominant (resulting in a monoclonality) in the crypt as there will be a higher number of central *Lgr5*$^{+}$ cells to compete with. Future studies can test this hypothesis by administering genotoxic agent (5-FU) to NMRs (to induce mutation at crypt base) and compare the somatic mutation burden in their crypts with control animals after 1-6 months (when monoclonality is established) of

the treatment. In summary, because of a unique crypt architecture containing more stem cells, NMRs are better suited for mutation-free long-term intestinal function than mice.

The major limitation of this chapter is the lack of a lineage tracing experiment to demonstrate the stemness of *Lgr5*$^{+}$ cells in NMR intestines. *Lgr5*$^{+}$ cells have been considered as the putative stem cells of the NMR intestine in this study. However, due to the lack of a knock-in model, it was not possible to demonstrate the true "stemness" of this cell population in the NMR intestine using lineage tracing. Next, the proportion of stem cells was quantified by detecting *Lgr5* mRNA in tissue sections after staining with an *Lgr5* mRNA probe (ISH) and an anti-EpCAM antibody (IF). However, the detection of *Lgr5* mRNA does not guarantee that all *Lgr5*$^{+}$ cells will also express Lgr5 protein. There can be a small pool of *Lgr5*$^{+}$ cells containing a low level of mRNA that does not get translated to protein, resulting in an overestimation of the number of stem cells detected by ISH-IF. In histological comparison, goblet cells were detected using Alcian blue 2.5 which can stain all acid mucins. However, a small population of cells in the intestine can exclusively secrete neutral mucins which will not be detected with Alcian blue. This can result in an underestimation of the goblet cell population in our quantification. Finally, all naked mole rats used for histological quantification in this chapter are non-breeders (subordinates) belonging to two colonies established by founder breeders (mixed-parentage) captured in Mtito Andei and Lerata, Kenya by Prof. Jennifer Jarvis[11]. The conclusions drawn in this chapter might not be the same for NMRs involved in active reproduction (i.e. breeders) as queen NMRs have been reported to exhibit a slower rate of cytosine methylation during ageing than subordinates[57].

3.3.1 Conclusion

In this chapter, I have reported that mouse and NMR intestines reach their highest villi growth before 12 months of age, the appropriate time to perform a cross-species comparison of intestinal tissue. NMRs have shorter intestines and larger crypt-villi structures containing higher proportions of enterocytes, goblet, and enteroendocrine cells compared to mice. NMR intestinal crypts harbour higher proportions of *Lgr5*$^{+}$ cells than mice and humans. The majority of these *Lgr5*$^{+}$ cells are located at the crypt base in all three species. In summary, I have characterised the naked mole rat intestine in a cross-species comparison with mice and humans to show they have more stem and differentiated cells. In the next chapter, I will compare the turnover rate of *Lgr5*$^{+}$ cells in NMR intestines to that of mice and humans.

Chapter 4: Cellular kinetics of intestinal stem cells across species

4.1 Introduction

The intestine has the highest cellular turnover rate of all mammalian tissues[192-194]. The ($Lgr5^+$) stem cells at the crypt base in the intestine drive a hierarchical architecture by controlled cell divisions that maintain their population at the crypt base and differentiate into specialized cells outside the crypt base[80]. The division rate of small intestinal stem cells (ISC) can change during the development of an embryo to an adult stage[93], upon intestinal damage[148] and between species[94,145]. Barker *et al.* reported that ISCs in the murine small intestine (SB1) divide roughly every 24 hours *in vivo*. Later, two other research groups also determined the *in vivo* ISC turnover time in the mouse small intestine (SB1) to be between 21 to 28 hours[145,146]. In 6-day-old mice, *Lgr5*$^+$ cells divide at a quicker rate (every 16 hours) in the small intestine (SB1)[93] than in adult mice (every 24 hours)[145,146]. In adult fruit flies (*Drosophila)*, stem cells in the posterior midgut also divide approximately every day *in vivo*[195]. In the descending colon of adult rats, the division time of crypt base cells *in vivo* is in the order of 2 days[196]. However, in humans, colonic ($LGR5^+$) stem cells cycle once every week which was determined using an orthotopic xenotransplantation model where human colon organoids were transplanted into a mouse colon[94]. Based on these previous reports, it appears that short-lived species may have faster cycling ISCs than long-lived ones. In this chapter, we analysed ISCs in long-lived naked mole rats' small intestine (SB1) and colon and found that NMR *Lgr5*$^+$ cells have a slower cycling rate than short-lived mice.

The most accurate strategy to determine the total division time of an asynchronous cell population is to measure the rate of cumulative accumulation of nucleoside analogues into their genome *in vivo*[163]. In this strategy, animals are injected with 5-

bromo-2'-deoxyuridine (BrdU) or other nucleoside analogues at regular time intervals for a duration long enough to ensure that no cycling cell can pass through S-phase without being exposed to the label[94,145,163]. Under the assumption that the cells are dividing asynchronously and asymmetrically, the proportion of BrdU-labelled cells increases linearly with time and the slope of this graph is used to derive the total division time of the cell population[163]. This strategy has been deployed to determine *in vivo* cell division time in blood[197], brain[163], and intestine[145] of mice. In this chapter, I will describe the optimisation steps for BrdU administration in NMRs and determine the total cell division time of their intestinal *Lgr5*$^{+}$ cells *in vivo*. I will also quantify the durations of different cell cycle phases of *Lgr5/LGR5*$^{+}$ ISCs in mice, humans, and NMRs and conduct a cross-species comparison of the cellular kinetics of ISCs.

4.2 Results

4.2.1 Proliferation status of *Lgr5*-expressing cells across species

Ki67 is a widely accepted marker of proliferating cells. It was previously reported to be expressed during all phases of the cell cycle and absent during quiescence[198]. However, it has been shown in a later study that Ki67 only accumulates from S to M-phases of the cell cycle[164]. The expression level of this protein can fluctuate during the G1-phase based on the duration a cell has spent in G0 and G1[164]. Ki67 is expressed within the nucleus upon activation of E2F[199] and inactivation of Rb[200]. It is concentrated in the nucleolus during the S and G2 phases of the cell cycle but expressed as discrete foci throughout the nucleoplasm during G1-phase[201]. This protein has been demonstrated to organise heterochromatin, separate mitotic chromosomes, and participate in ribosomal biogenesis[164].

Lgr5^{+} cells exhibit differences in proliferation status and stemness based on their positions in the crypt. A recent study has reported that *Lgr5*$^{+}$ cells at the crypt base (*Lgr5*$^{+CBC}$) and above the crypt base have different proliferation status in mouse and human colon[94]. Additionally, *Lgr5*$^{+CBC}$ cells have been shown to behave as ISCs[132] while *Lgr5*$^{+}$ cells above the crypt base have been reported as transit-amplifying cells[94]. Therefore, in this section, the cross-species comparison of stem cell kinetics will be focused on *Lgr5*$^{+CBC}$ cells. To assess the fraction of actively proliferating *Lgr5*$^{+CBC}$ cells, NMR, mouse, and human intestinal tissues were co-stained with species-specific *Lgr5*-mRNA probe and Ki67 antibody (Figure 4.1A, C). In the murine small intestine (SB1), 82.38% ± 2.47 of the *Lgr5*$^{+CBC}$ cells were detected to proliferate which is similar to the proliferation index (*Lgr5*$^{+CBC}$Ki67^{+}/*Lgr5*$^{+CBC}$)

reported by a previous study using a knock-in mouse model[202] (Figure 4.1B). On the other hand, a lower percentage (64.54% ± 1.92) of *Lgr5*$^{+CBC}$ cells in the NMR small intestine were found to be positive for Ki67-expression (Figure 4.1B).

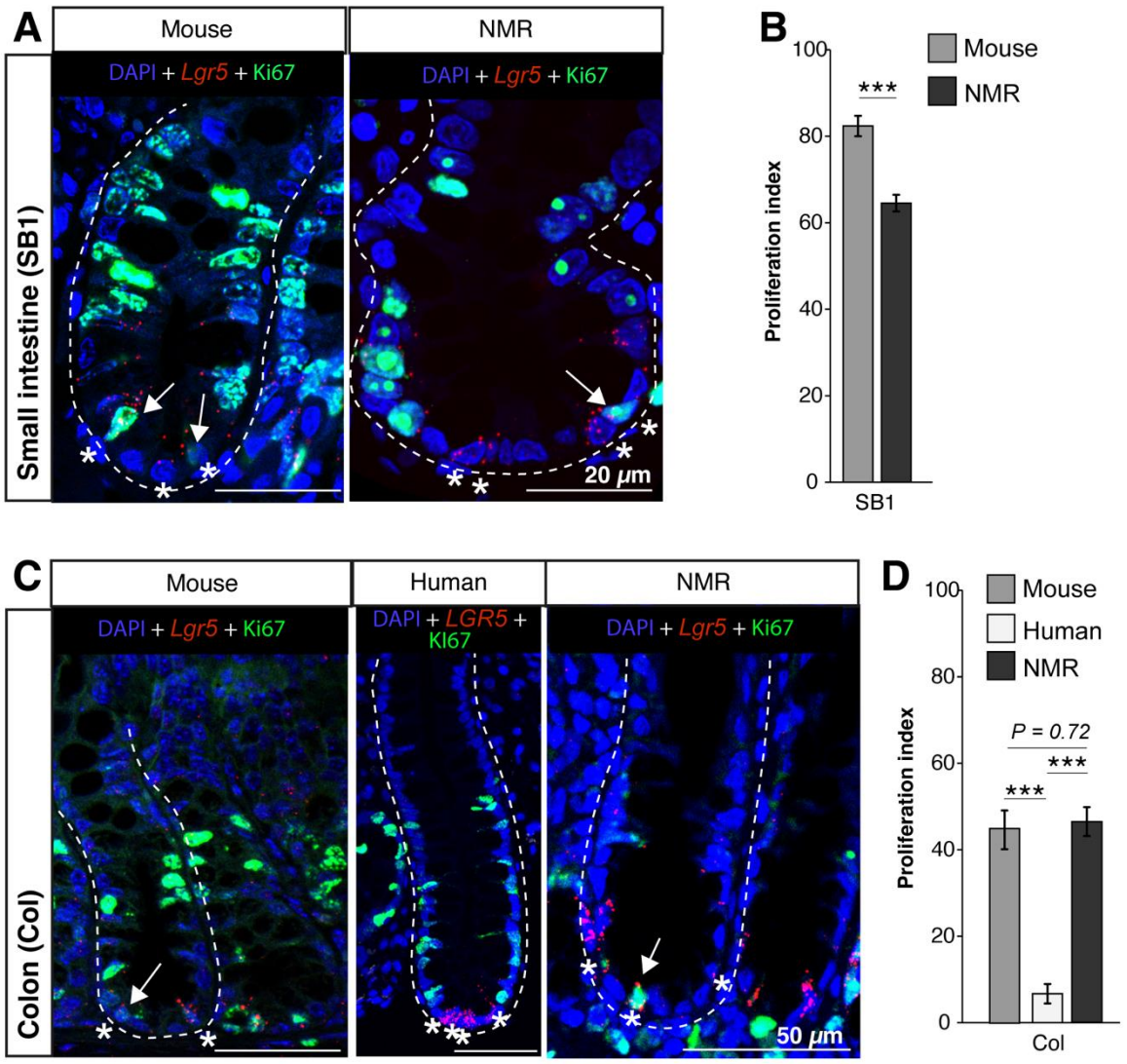

Figure 4. 1: Cycling status of intestinal *Lgr5(LGR5)*$^{+CBC}$ cells in mice, humans, and NMRs. **(A)** Representative confocal images of mouse and NMR small intestinal (duodenum) crypt that was co-stained with *Lgr5* RNAscope probe (red), Ki67 (green) antibody, and DAPI (blue). Asterisks (*) indicate crypt-based *Lgr5*-expressing cells (*Lgr5*$^{+CBC}$) and white arrows mark *Lgr5*$^{+CBC}$Ki67^{+} cells. **(B)** Bar graph showing the percentages of *Lgr5*$^{+CBC}$Ki67^{+} cells among all *Lgr5*$^{+CBC}$ cells per crypt (proliferation index) in wild-caught mouse (12-month-old) and wild-caught NMR (12-month-old) small intestine (n=128 crypts from 3 animals per group, $P<0.001$). **(C)** Confocal images of the mouse, human (28 to 33-year-old), and NMR distal colonic crypts that were co-stained with species-specific *Lgr5*/*LGR5* RNAscope probe (red), Ki67 antibody (green) and DAPI (blue). Asterisks (*) indicate crypt-based *Lgr5*-expressing cells (*Lgr5*$^{+CBC}$) cells and white arrows mark *Lgr5*$^{+CBC}$Ki67^{+} cells. **(D)** Bar graph showing the proliferation index of NMR and mouse colonic *Lgr5*$^{+CBC}$ cells (n=92 crypts from 3 animals per species), and human colonic *LGR5*$^{+CBC}$ cells (n=65 crypts from 4 normal human samples). *P*-values are indicated on the graph. In all cases, statistical significance was determined

by performing a two-tailed unpaired Student's t-test using an unequal variance. Significant *P*-values are denoted as ***<0.001. Each bar represents the mean ± standard error of the mean. Scale bars are indicated on the images (20 µm and 50 µm).

In the colon, similar proliferation indexes (45.50% ± 4.77 in mice and 47.58% ± 3.37 in NMRs) were detected for both NMR and mouse *Lgr5*$^{+CBC}$ cells (Figure 4.1D). However, in humans, only 6.75% ± 2.43 of *LGR5*$^{+CBC}$ cells were found to be in the cell cycle which is in agreement with their slower cell division time reported in a previous study using an orthotopic xenotransplantation model[94] (Figure 4.1D). In both rodent species, small intestinal *Lgr5*$^{+CBC}$ cells were more proliferative than colonic *Lgr5*$^{+CBC}$ cells (Figure 4.1B, D). Based on these data, it was concluded that small intestinal stem cells in mice are more proliferative than in NMRs. Murine colonic stem cells exhibit an equivalent proliferation index to NMRs while human colonic stem cells are the least proliferative among the three species.

4.2.2 Quiescence status of ISCs across species

Human colonic stem cells (LGR5^{+}) have been shown to enter quiescence (G0)[94]. More specifically, the LGR5^{+} cells found at the crypt base (LGR5^{+CBC}) have a higher proportion of their population expressing quiescence marker P27^{Kip1} and a lower proportion expressing proliferation marker KI67 compared to LGR5^{+} cells located above the crypt base in human colons[94]. To determine if NMR *Lgr5*$^{+}$ cells also entered quiescence, intestinal tissues were stained with *Lgr5*-probe and an antibody against p27, a Kinase inhibitor protein (Kip) that controls the entry and exit between the cell cycle and quiescence[203-205]. In the NMR small intestine, no expression of p27 was detected in any of the *Lgr5*$^{+CBC}$ cells analysed (Figure 4.2A). Similarly, in mouse small intestinal crypts, no *Lgr5*$^{+CBC}$ cell was found positive for p27-

expression (Figure 4.2A) which supports the absence of quiescent stem cells in murine intestinal stem cells in previous reports[94,145,146]. However, in both species, presence of $p27^+$ cells were seen in the upper region of the crypts (Figure 4.2D) where majority of the terminally differentiated cells are located.

In the colon, only 8.80% ± 1.76 of mouse *Lgr5*$^{+CBC}$ cells were found to be $p27^+$ which is in agreement with the data reported by Ishikawa *et al*[94] (Figure 4.2C). In NMR colon, similar to the small intestine, no $p27^+$*Lgr5*$^{+CBC}$ cell was detected in any of the 50 colonic crypts (from 3 animals) analysed. However, roughly 45-47% of *Lgr5*$^{+CBC}$ cells were found to proliferate in both mouse and NMR colons (Figure 4.1D). As Ki67 can remain undetectable due to its degradation in the G1 phase[164], the lack of Ki67-expression in mouse and NMR small intestine and colon most likely marks the cells arrested in G1, rather than in G0.

In contrast to the rodents species analysed, in the colonic crypts of humans aged 28 to 33-year-old, 86.01% ± 4.64 of *LGR5*$^{+CBC}$ cells were found positive for P27-expression (Figure 4.2C). This data supports the previous report of quiescence in human $LGR5^+$ cells (68-year-olds) where the majority (83%) of $P27^+LGR5^+$ cells were shown to be in the G0 phase (rather than in G1) based on their relative DNA/RNA content detected by flow cytometry[94].

In summary, Ki67 and p27 status of *Lgr5/LGR5*$^+$ cells revealed that only human colonic *LGR5*$^+$ at the crypt base exhibit quiescence (G0). In mice and NMRs, *Lgr5*$^+$ cells, both in the small intestine and colon, at the crypt base are actively proliferating and do not enter quiescence as indicated by their lack of p27-expression.

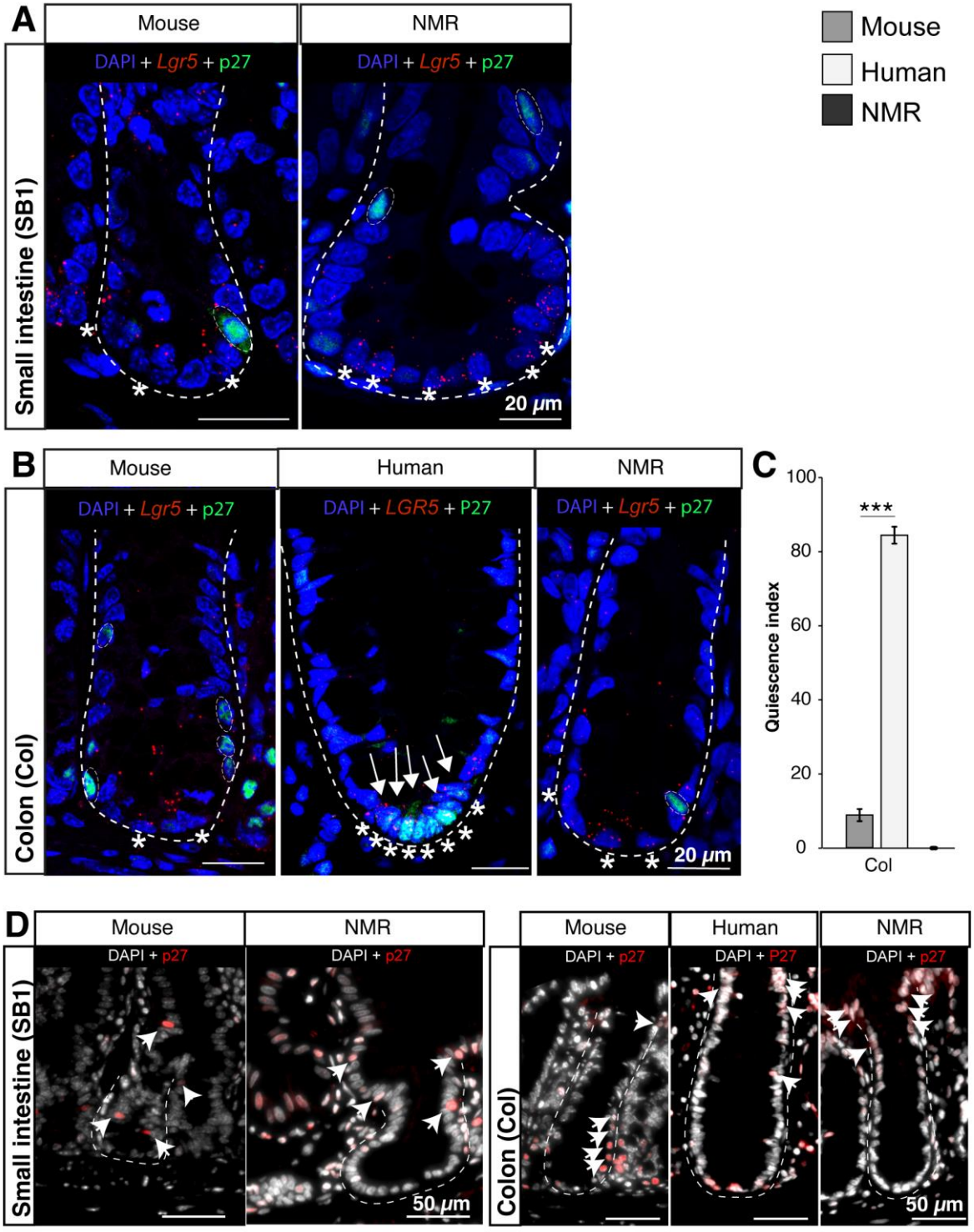

Figure 4. 2: Quiescence of intestinal *Lgr5(LGR5)*$^{+CBC}$ cells in mice, humans, and NMRs.
(A) Confocal images of mouse and NMR small intestinal crypts that were co-stained with species-specific *Lgr5* RNAscope probe (red), anti-p27 antibody (green) antibody and DAPI (blue). Asterisks (*) indicate *Lgr5*$^{+CBC}$ cells and white circles mark *Lgr5*$^{+CBC}$p27^{+} cells. All *Lgr5*$^{+CBC}$ cells in the mouse and NMR analysed (n=50 crypts from 3 animals per group) were negative for p27. **(B)** Confocal images of mouse, human, and NMR colonic crypts co-stained with species-specific *Lgr5(LGR5)* RNAscope probe (red), anti-p27 antibody (green) antibody, and DAPI (blue). Asterisks (*) indicate *Lgr5(LGR5)*$^{+CBC}$ cells and white circles and arrows mark p27(P27)$^{+}$ cells. **(C)** Bar graphs showing differences in the quiescence index, proportion of *Lgr5*(*LGR5)*$^{+CBC}$ cells that scored positive for p27(P27) (n=50 crypts from 3 animals per rodent group and n=30 crypts from 4 human samples,

P<0.001). **(D)** Photomicrographs showing intestinal crypts stained with anti-p27 antibody (red) and counterstained with DAPI (grey) in mouse and NMR small intestine (left) and mouse, human, and NMR colon (right). Dashed lines demarcate the outer periphery of crypt structures. White arrows indicate p27(P27)$^{+}$ cells outside the crypt base to the top of the crypts. In all cases, statistical significance was determined by performing a two-tailed unpaired Student's t-test on all the crypts counted per species using an unequal variance. Significant *P*-values are denoted as ***<0.001. Each bar represents the mean ± standard error of the mean. Scale bars are indicated on the images (20 µm and 50 µm).

4.2.3 *In vivo* administration of BrdU in naked mole rats

To directly measure the turnover rate of ISCs *in vivo*, one of the most accurate methods is administering a nucleoside analogue which will be incorporated into the DNA during replication in S-phase and then detected by immunohistochemical reaction[145,163]. A popular choice of such nucleoside analogue is BrdU which has been widely used to determine cell cycle duration in previous studies[163,197]. This experimental strategy involves administering BrdU into animals at regular time intervals and quantifying the rate of BrdU incorporation into the DNA. However, measuring BrdU uptake in proliferating cells *in vivo* first requires determining BrdU availability for incorporation in specific species as it has been shown to be cleared from the system at variable rates across different species[156]. For example, BrdU is cleared from the blood within 1 hour after intraperitoneal injection in C57BL/6J mice, 1 hour in canary birds and 2 hours in quails[156]. As NMR has a slower metabolic rate than mice[206,207], it was crucial to measure the BrdU clearance time in NMR plasma to establish an injection strategy that will allow the detection of all ISCs passing through the S-phase.

In 1989, Nowakowski *et al.* reported a BrdU administration regimen to determine total cell division time must fulfil two requirements[9]. First, the interval between two successive BrdU injections should be significantly shorter than the duration of the

S-phase to ensure no proliferating cell can pass through S-phase without getting labelled. Second, the total BrdU exposure time should be longer than the S-phase to allow all/most proliferating cells to acquire the label. As the duration of the S-phase in proliferating intestinal cells and plasma clearance time of BrdU in naked mole rats are not available in the literature, this section will focus on our strategy of optimising a few parameters to establish a BrdU injection paradigm that would ensure its bioavailability *in vivo* in NMR intestine for a duration long enough to allow all/majority of the proliferating cells to enter/pass through S-phase.

4.2.3.1 Optimum dose of BrdU in naked mole rats

The dose of intraperitoneal injection of BrdU can impact the number of labelled cells as reported in previous studies[208,209]. In the brain of C57BL/6J mice, a previous study has shown an increasing number of BrdU labelled cells were detected for doses ranging from 25 to 150 mg/kg bodyweight after which it saturated[208]. However, 20 – 100 mg/kg-bodyweight dose has been used to label proliferating cells in the murine intestine[142,210]. To establish the dose at which a labelling saturation is achieved in the NMR intestine, BrdU was injected intraperitoneally at two doses (100 and 200 mg/kg-bodyweight) every 8 hours and intestinal tissues were analysed 24 hours after the first injection (Figure 4.3A). Using an anti-BrdU antibody, BrdU-labelled cells were detected in NMR small intestinal crypts (Figure 4.3B) following a standard immunohistochemistry protocol (section 2.3.2.4). The percentage of $BrdU^+$ cells in intestinal crypts (labelling index) was similar in NMRs that had received two different doses of BrdU (32.56% ± 1.45 for 100mg/kg-bodywt and 33.72% ± 1.31 for 200 mg/kg-bodywt, Figure 4.3C). This suggests that the 100 mg/kg bodyweight dose had achieved a saturation of BrdU labelling in the NMR

intestine. However, the staining intensity of BrdU was stronger at a higher dose (Figure 4.3B). As BrdU solubility is 50 mM in an aqueous solution, it requires a larger volume (>300 µL) of injection in NMRs to administer a 200 mg/kg bodyweight dose which can cause stress in these animals. Therefore, 100 mg/kg-bodyweight concentration was selected as BrdU is detectable at this dose.

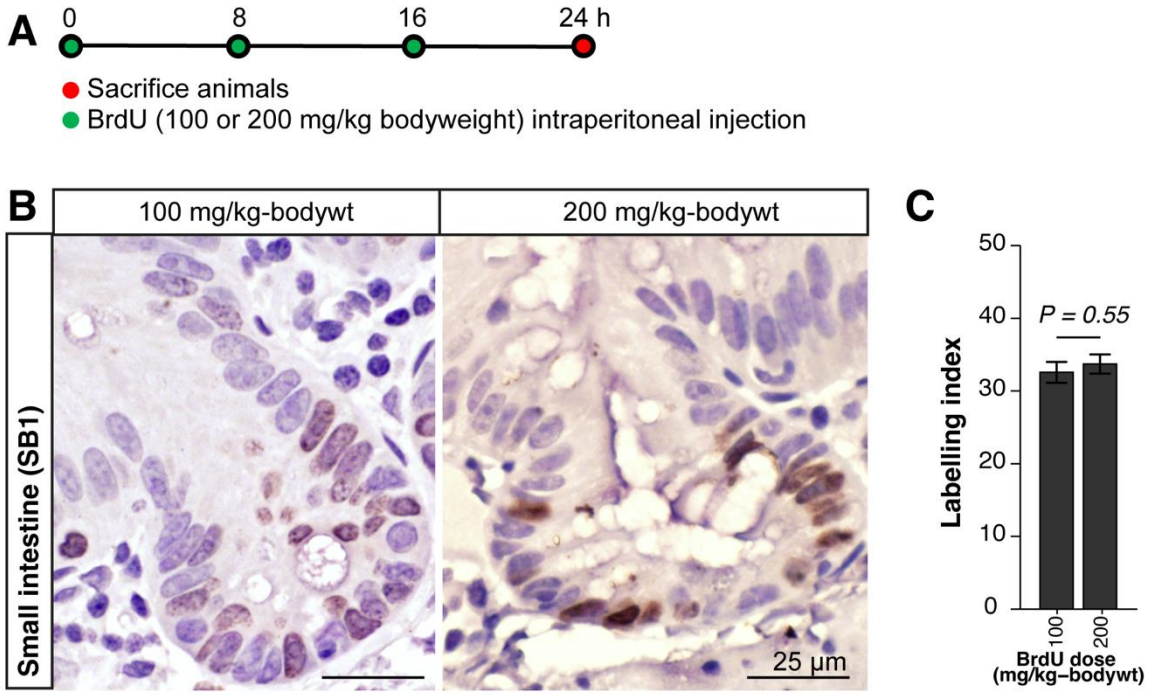

Figure 4. 3: Optimisation of BrdU dose to label proliferating intestinal cells in NMRs.
(A) Schema showing the timeline of 5-bromo-2'-deoxyuridine (BrdU) injections (green dots) into NMRs at two different doses (100 and 200 mg/kg bodyweight) and time of tissue harvest (red dot). **(B)** Photomicrographs showing small intestinal crypts from both cohorts stained with anti-BrdU antibody (brown) and counterstained with haematoxylin (blue). **(C)** Bar graphs showing no significant difference in the proportion of $BrdU^+$ cells in small intestinal crypts (labelling index) between the two doses of BrdU used (n=42 crypts from 2 animals per dose, *P*=0.55). Statistical significance was determined by performing a two-tailed unpaired Student's t-test on all the crypts counted per group using an unequal variance. Each bar represents the mean ± standard error of the mean. Scale bars are indicated on the images (25 µm).

4.2.3.2 Injection frequency of BrdU in naked mole rats

A key factor in estimating cell cycle duration using BrdU is determining its injection frequency[163]. An ideal experiment should ensure that no proliferating cell can pass through S-phase without being exposed to BrdU. If BrdU is administered at a

frequency longer than S-phase, some proliferating cells may complete DNA replication without acquiring the label resulting in an underestimation of the number of proliferating cells. To establish an optimum pulsing strategy in NMRs, BrdU was injected into these animals at two different frequencies (every 1 hour and every 8 hours) and tissues were harvested 8 hours after the first injection (Figure 4.4A). Staining and quantification of the small intestinal crypts revealed no significant difference in the percentage of $BrdU^+$ cells (labelling index) between animals receiving BrdU injections every hour (18.81% ± 0.77) and only one injection 8 hours before sacrificing the animals (19.18% ± 0.80, Figure 4.4B-C). This indicated that the duration of the S-phase in the proliferating cells of the NMR intestine is longer than 8 hours as more frequent injections (every hour) do not result in more labelled cells in the crypts. In brief, injecting BrdU in NMRs every 8 hours is sufficient to ensure the labelling of all proliferating cells passing through the S-phase.

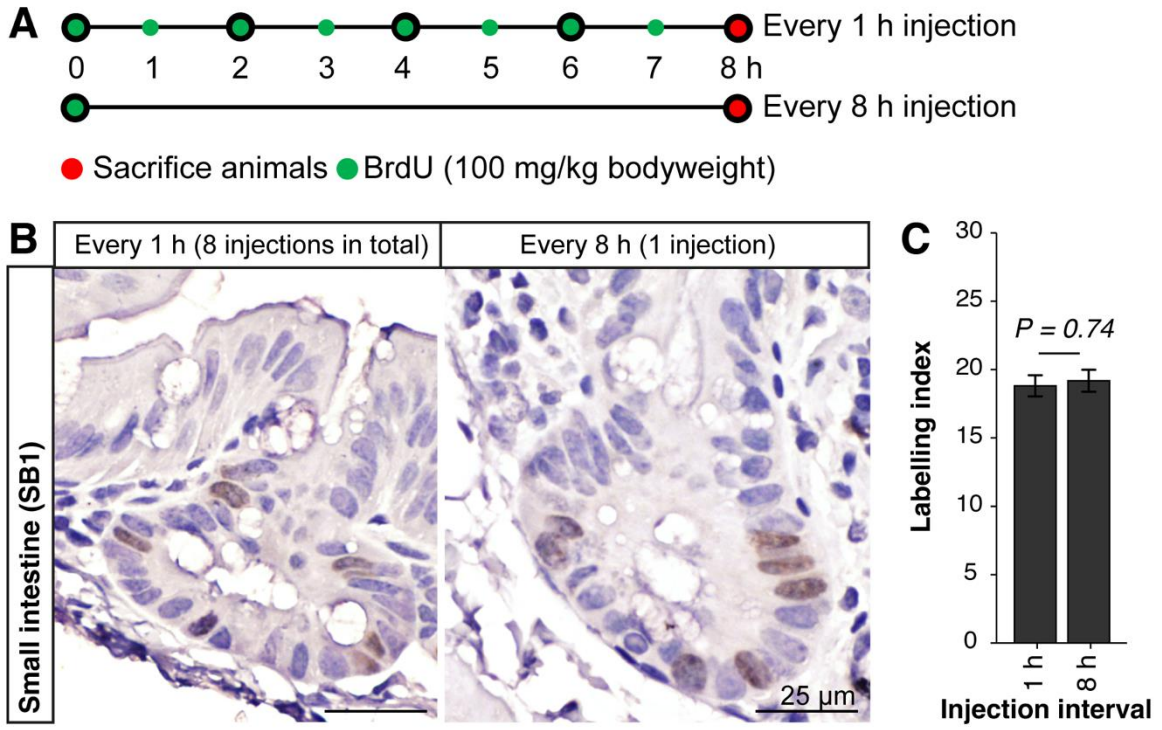

Figure 4. 4: Determination of BrdU injection frequency to label all proliferating intestinal cells in NMRs.

(A) Schema illustrating two different frequencies (once only and every 1 hour for 8 hours) of BrdU injections (green dots) and time of tissue collection (red dot). **(B)** Brightfield images showing small intestinal crypts from both cohorts stained with anti-BrdU antibody (brown) and counterstained with Haematoxylin (blue). Bar graphs showing no significant difference in the percentage of $BrdU^+$ cells in the small intestinal (SB1) crypt of NMRs (labelling index) injected at the two different frequencies (n=40 crypts from 2 animals per group, P=0.74). Statistical significance was determined by performing a two-tailed unpaired Student's t-test on all the crypts counted per group using an unequal variance. Each bar represents the mean ± standard error of the mean. Scale bars are indicated on the images (25 µm).

4.2.3.3 Plasma clearance time of BrdU in naked mole rats

BrdU has a faster clearance rate (1-2 h) in murine blood than in quails[156,209] and requires more frequent pulsing to ensure bioavailability in this species. However, NMR has a slower basal metabolic rate than mice[207] and, therefore, BrdU clearance time in these animals would need to be determined. To measure the plasma clearance time of BrdU in NMRs, blood was collected from the tail vein 8 hours and 16 hours after one BrdU injection (Figure 4.5A). Upon separating the blood cells by centrifugation, the isolated NMR plasma was added to a culture of HEK293T cells (details in section 2.2.4.1, Figure 4.5B). If BrdU was present in NMR blood at the time of collection, it would be available in the plasma-supplemented culture media of HEK293T cells to be incorporated into DNA during replication. Therefore, the fraction of $BrdU^+$ HEK293T cells (i.e., labelling index) was quantified after staining with anti-BrdU antibody (Figure 4.5C) following a standard immunocytochemistry protocol (section 2.3.2.5). In the wells treated with NMR plasma collected 8 hours after the BrdU injection, 18% ± 6% cells were detected as $BrdU^+$ (Figure 4.5C). This indicates the presence of BrdU in NMR blood even 8 hours after the injection which is longer than mouse[156,209]. However, no $BrdU^+$ HEK293T cell was detected in wells plated with NMR plasma collected 16 hours after BrdU administration (Figure 4.5C) demonstrating a plasma clearance time between 8 and 16 hours after one BrdU pulse in NMR.

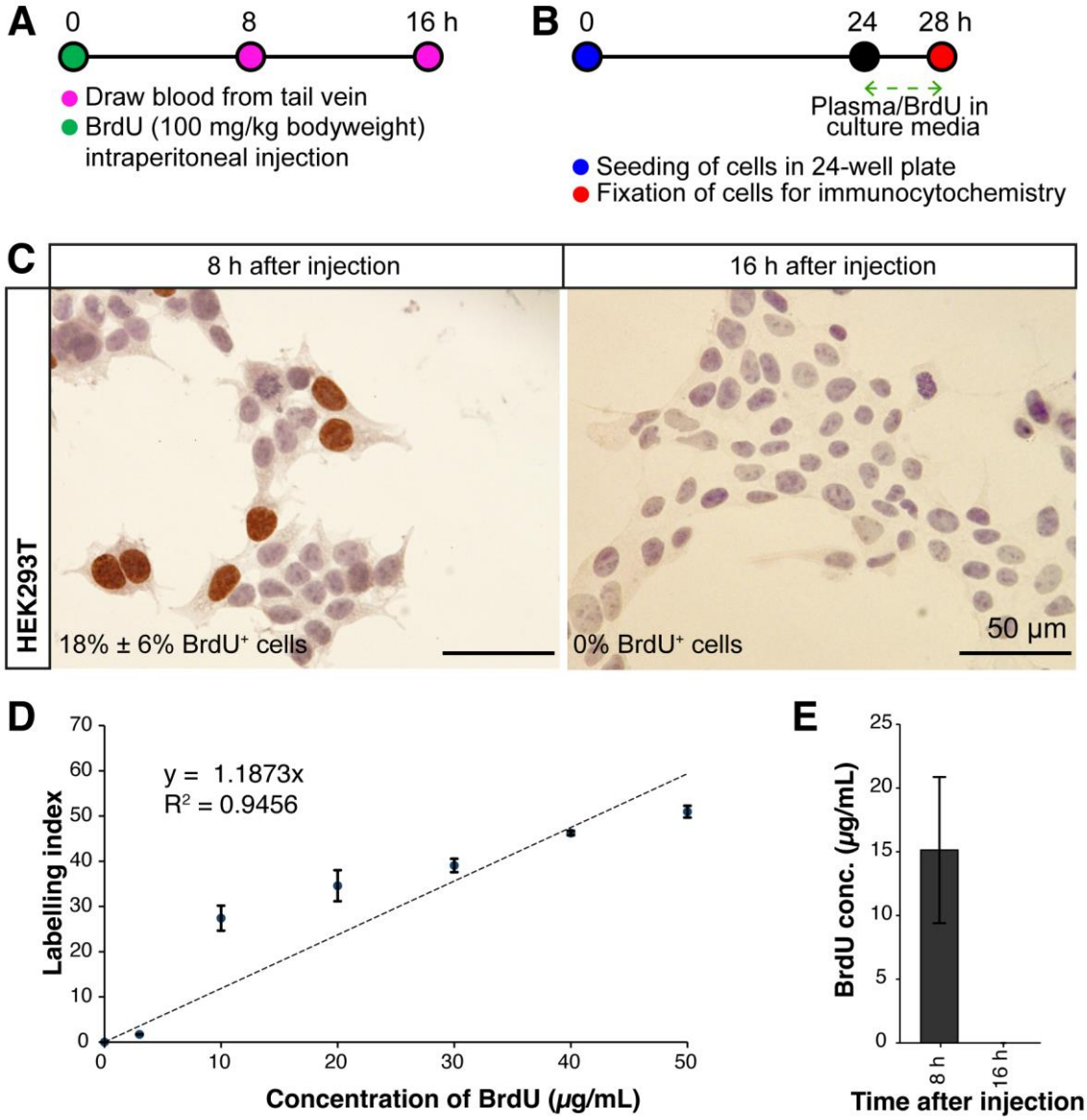

Figure 4. 5: Estimation of plasma clearance time of BrdU in NMRs.
(A) schema showing the time of blood collection (purple) from the tail veins of NMRs after one injection of BrdU (green). **(B)** An outline of experimental strategy showing the timeline when HEK293T cells were seeded in 24-well plates (blue dot), supplemented with NMR plasma/standard BrdU solution (dashed green line), and fixed for immunocytochemistry (red dot). **(C)** Photomicrographs of HEK293T cells supplemented with plasma collected from the NMRs at 8 hours and 16 hours after BrdU injection and stained with anti-BrdU antibody (brown). **(D)** Quantification of the percentage of $BrdU^+$ HEK293T cells (labelling index, counted from triplicate wells) exposed to known concentrations of BrdU was used to generate a standard titration curve which gave the plasma BrdU concentration of NMRs. **(E)** Bar graphs showing BrdU concentration detected in the plasma of NMRs at 8 and 16 hours after injection (n=2 animals at each time-point). Each bar represents the mean ± standard error of the mean. Scale bars are indicated on the images (25 µm).

For calculating the concentration of BrdU in NMR plasma from the fraction of labelled cells, HEK293T cells were plated with increasing concentrations of standard BrdU solution that resulted in a linear increase of the percentages of $BrdU^+$ cells (Figure 4.5D). By fitting a linear regression passing through the origin, the slope (1.1873) was calculated to determine the BrdU concentrations in NMR plasma (15 µg/mL BrdU 8 hours after injection) using the percentages of $BrdU^+$ HEK293T cells (Figure 4.5 C-E). In summary, BrdU clearance time in NMR blood is slower than in mice[156] and it declines to an undetectable level between 8 and 16 hours after the intraperitoneal injection.

4.2.3.4 Impact of repeated BrdU injections on the cellular kinetics of naked mole rat crypts

Upon determining the optimum dose, injection frequency, and plasma clearance time of BrdU in NMRs, these animals were injected every 8 hours for 5 days (15 injections in 120 hours) and tissues were harvested at regular intervals to detect cumulative labelling of BrdU in the proliferating cells of the intestine (Figure 4.6A). This ensured that the majority/all proliferating cells in NMR intestinal crypts would enter the S-phase and no cell will be allowed to complete DNA replication without being labelled. However, the repeated injections of BrdU itself may have impacted the kinetics of intestinal cells. To assess any influence on the cellular kinetics caused by the BrdU pulses, a second thymidine analogue, 2'-deoxy-5-ethynyluridine (EdU), was injected in NMRs that had received 15 BrdU injections and in untreated controls, and intestinal tissues were analysed 8 hours after the EdU pulse (Figure 4.6B). A similar fraction (14% ± 1%) of EdU^+ cells in NMR intestinal crypts (i.e., labelling index) were detected in both BrdU-treated cohort and

untreated controls (Figure 4.6C-D). Based on this data, it was concluded that the cellular kinetics of the NMR intestinal crypts was unaffected by the 15 BrdU injections administered to the animals every 8 hours.

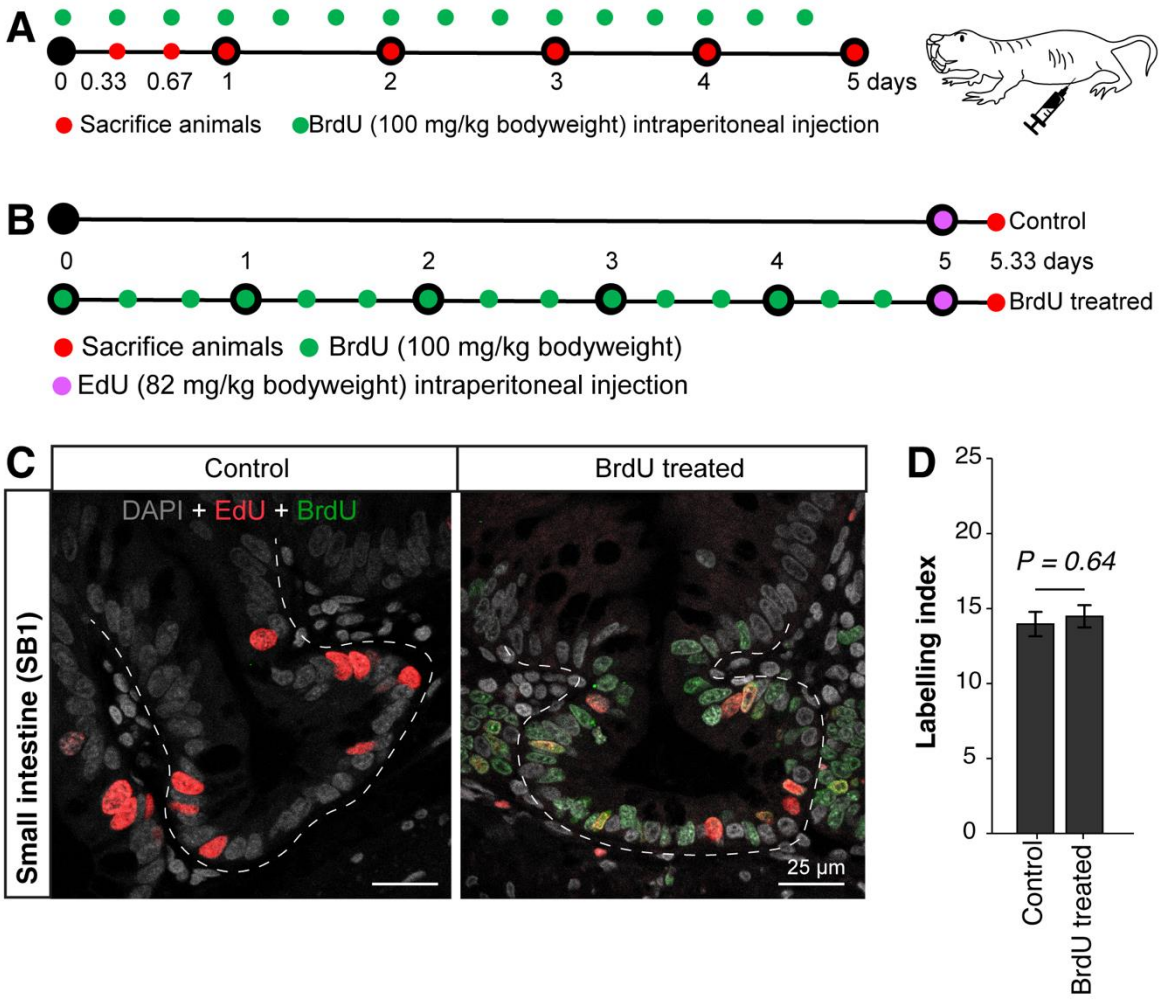

Figure 4. 6: Evaluation of cellular kinetics of NMR crypts after repeated BrdU injections. **(A)** A timeline showing an experimental strategy to label all proliferating cells in NMR crypts by injecting BrdU (green dots) and harvesting intestinal tissue (red dots) at specific times. **(B)** Schema showing injection of 2'-deoxy-5-ethynyluridine (EdU) (purple dots) in NMRs that had not received any BrdU injections (control) or at the end of 15 consecutive BrdU injections (green dots), and tissues analysed 8 hours later (red dots at 5.33 days). **(C)** Representative confocal images showing NMR small intestinal crypts stained with EdU-Alexa488 dye (red), anti-BrdU (green) antibody and DAPI (grey). **(D)** Bar graphs showing no significant difference in the percentage of EdU^+ cells in NMR small intestinal (SB1) crypts (labelling index) with no BrdU injections and after 15 successive BrdU injections (n=40 crypts from 2 animals per group, *P*=0.64). Statistical significance was determined by performing a two-tailed unpaired Student's t-test on all the crypts counted per group using an unequal variance. Each bar represents the mean ± standard error of the mean. Scale bars are indicated on the images (25 µm).

4.2.4 Cumulative BrdU labelling of crypt base cells in naked mole rats

Cumulative labelling of the crypt base columnar (CBC) cells in the murine small intestine has been reported in previous studies[83,145,146]. About one-third of the CBCs incorporate the nucleoside analogues (BrdU/CldU) within 4 hours of injection and all the CBC cells acquire the label within 24 hours, indicating the cycling time of mouse CBC cells is around one day[83,145]. However, upon performing BrdU injection in NMRs (Figure 4.7A), 27.66% ± 1.92 $BrdU^+$ CBCs in the small intestine and only 6.64% ± 0.92 $BrdU^+$ CBCs in the colon were detected after 8 hours of BrdU exposure (Figure 4.7B-C). After extending the analysis to later time points, 96.5% ± 1.5% BrdU labelling in the small intestinal CBC cells was observed within 4 days and 70.91% ± 3.02 BrdU labelling in the colonic CBC cells was measured after 5 days of repeated injections (Figure 4.7 B-C). Therefore, NMR small intestinal CBC cells showed a slower cycling rate than mice and colonic CBC cells are slower cycling than small intestinal CBC cells in NMRs. However, not all cells at the crypt base of mouse and NMR intestines are *Lgr5*$^+$ (Figure 3.8 A-B). Therefore, to estimate the division time of intestinal (*Lgr5*$^+$) stem cells, the analysis of cumulative BrdU labelling will focus exclusively on crypt base *Lgr5*$^{+CBC}$ cells in the next section.

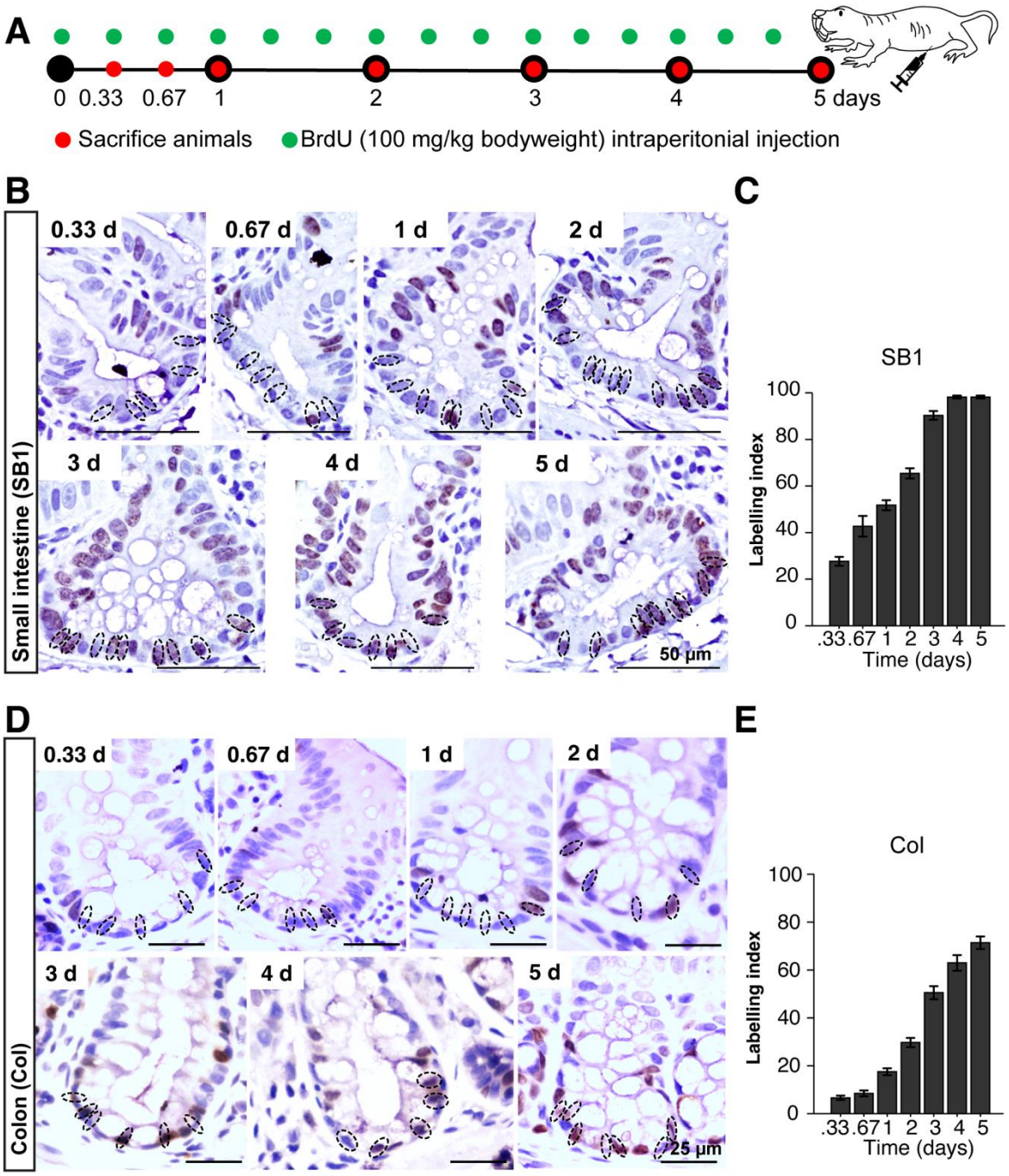

Figure 4. 7: Cumulative BrdU labelling in the crypt base columnar cells of NMR intestine. **(A)** Schema showing the timeline for injecting BrdU (green) intraperitoneally in NMRs and time points when intestinal tissues were collected (red). **(B, D)** Photomicrographs of NMR **(B)** small intestinal (SB1) and **(D)** colonic crypts from each time point stained with anti-BrdU antibody (brown) and counterstained with haematoxylin (blue). Dotted circles indicate crypt-base columnar (CBC) cells. **(C, E)** Bar graphs showing an increase in labelling index ($BrdU^+$CBCs/total CBCs) with time in the **(C)** small intestine (SB1) and **(E)** colon of NMRs (n=30 crypts from 2 to 3 animals per time-point). Each bar represents the mean ± standard error of the mean. Scale bars are indicated on the images (25 µm and 50 µm).

4.2.5 Estimating the S-phase duration of *Lgr5*$^{+CBC}$ cells in naked mole rats and mice

For estimating the duration of the DNA-synthesis phase (T_S) of *Lgr5*$^{+CBC}$ cells in the NMR intestine, tissue sections from NMRs injected with BrdU for 8 hours to 120 hours (Figure 4.8A) were stained with *Lgr5*-probe and anti-BrdU antibody and analysed under a confocal microscope (Figure 4.8 B, D). The labelling index, the fraction of *Lgr5*$^{+CBC}$ cells that have incorporated BrdU (*Lgr5*$^{+CBC}$BrdU^{+}/*Lgr5*$^{+CBC}$), was calculated in 100-150 crypts per time point. Under the assumption that *Lgr5*$^{+CBC}$ cells are cycling asynchronously and divide asymmetrically[163] with no time spent in quiescence (Figure 4.2A-C), the labelling index increased linearly with time and saturated (≈ 100% of cells) after 3 days in the *Lgr5*$^{+CBC}$ cells of the small intestine (Fig. 4.8C). For colonic *Lgr5*$^{+CBC}$ cells which cycle more slowly in NMRs than their small intestinal counterparts (Figure 4.7E), 69.51% ± 3.26 of *Lgr5*$^{+CBC}$ cells acquired BrdU within 5 days (Figure 4.8E). Based on the lack of p27-expression in the *Lgr5*$^{+CBC}$ cells of the NMR colon (i.e. no quiescent cells), it was assumed that if the BrdU pulsing was extended for a longer time (7-8 days), nearly 100% of colonic *Lgr5*$^{+CBC}$ cells would incorporate BrdU similarly to the small intestinal *Lgr5*$^{+CBC}$ cells in NMRs (Figure 4.8C).

Next, T_S was calculated from the slope and the y-intercept of the regression lines (T_S = y-intercept/slope) defined by the equation displayed on the graph (Figure 4.8 C, E). The duration of the S-phase was found to be 0.47 day ± 0.10 in the small intestinal *Lgr5*$^{+CBC}$ cells which is similar to the duration (0.42 day ± 0.08) spent by colonic *Lgr5*$^{+CBC}$ cells in NMRs. In summary, cumulative BrdU labelling of *Lgr5*$^{+CBC}$ cells revealed that NMR intestinal *Lgr5*$^{+CBC}$ cells spend around 10 hours in S-phase

which is very similar to the previously reported value for mouse small intestinal CBC cells[145].

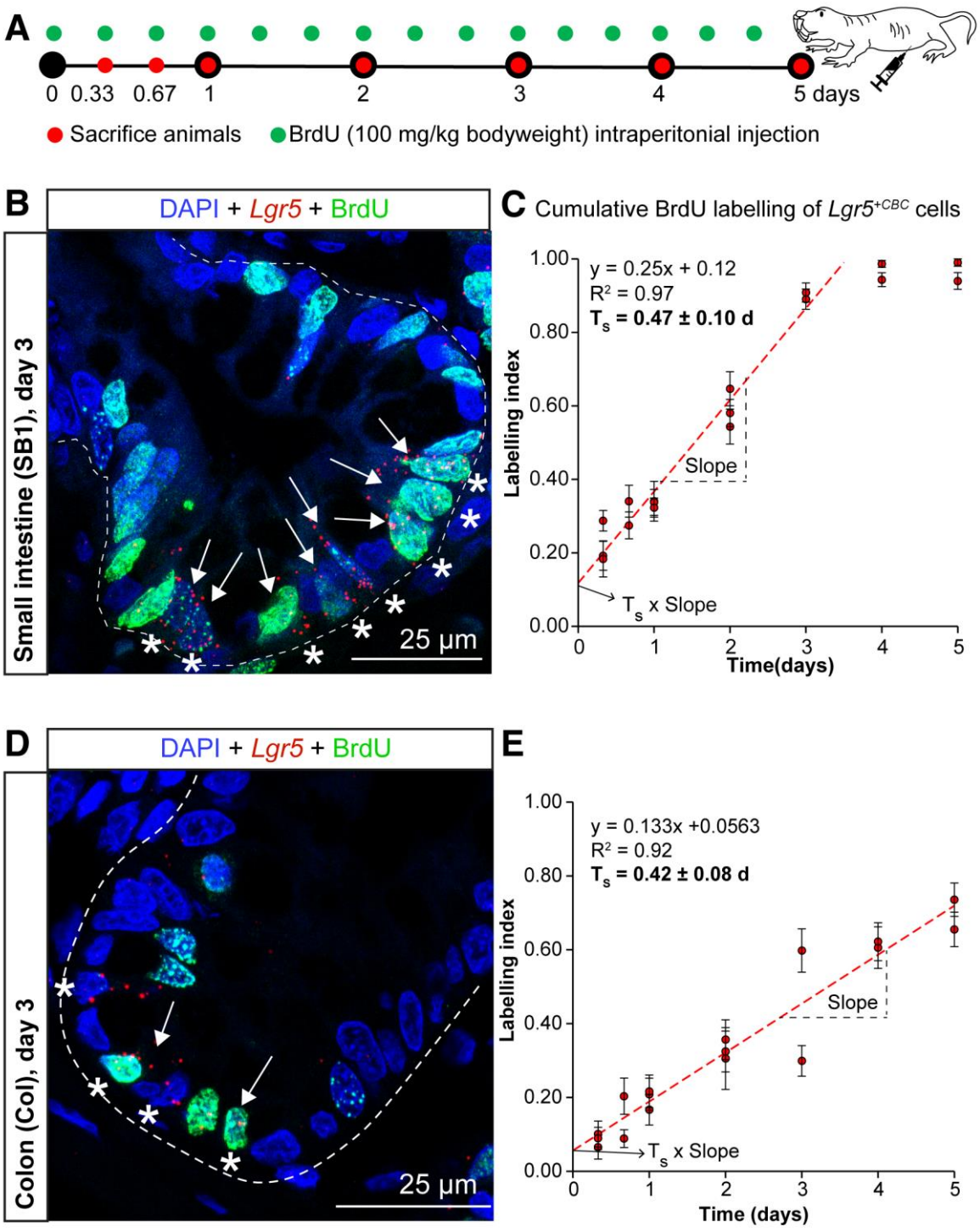

Figure 4. 8: Cumulative BrdU labelling of *Lgr5*$^{+CBC}$ cells in NMR intestine.
(A) Schematic representation of the timeline for injecting BrdU (green) intraperitoneally into NMRs and time points when colonic tissues were collected (red). **(B, D)** Representative confocal image showing staining with *Lgr5*-Cy3 *in-situ* hybridisation probe (red dots), anti-BrdU-Alexa 488 (green), and DAPI (blue) in the **(B)** small intestinal and **(D)** distal colonic crypts of NMR injected with BrdU for 3 days. Asterisks (*) mark *Lgr5*$^{+CBC}$ cells and white arrows indicate *Lgr5*$^{+CBC}$BrdU^{+} cells. **(C, E)**

Scatter plot (right) showing a linear increase in the labelling index (*Lgr5*$^{+CBC}$BrdU^{+}/*Lgr5*$^{+CBC}$) with time in the NMR **(C)** small intestine and **(E)** distal colon. Each data point (red dot) represents the mean ± standard error of the mean of 20 to 40 crypts counted from each animal and, at each time point, 2 to 3 animals were analysed. The dashed line (red) on the graph represents a linear projection defined by the equation displayed on the plot. Scale bars are indicated on the images (25 µm).

Escobar *et al.* have reported the *in vivo* kinetics of *Lgr5*$^{+CBC}$ cells in mouse small intestine (SB1) using cumulative BrdU labelling experiment[145]. However, such strategy involves sacrificing a large number of animals to establish a linear regression line of BrdU labelling index. We, therefore, aimed to assess whether mouse organoids can recapitulate the *in vivo* cellular kinetics of *Lgr5*$^{+}$ cells to reduce the number of mice used in our study. To determine the S-phase duration in mouse intestinal *Lgr5*$^{+}$ cells, organoids were expanded from crypts isolated from the small intestine (SB1) and colon of C57BL/6J mice (section 2.2.4.2) and cultured in media supplemented with BrdU before harvesting them at regular time intervals (section 2.2.4.3, Figure 4.9 A-B). After staining the organoids with murine *Lgr5*-probe and anti-BrdU-antibody, the fraction of BrdU-labelled *Lgr5*$^{+}$ cells (i.e. labelling index) was quantified which increased linearly with time (Figure 4.9 C-D). By fitting a regression line defined by the equation stated on the graph, the T_S (slope/y-intercept) for small intestinal *Lgr5*$^{+}$ cells was calculated to be 0.39 day ± 0.03 (Figure 4.9C) which is in agreement with the previously reported value (0.39 day) for mouse small intestinal CBCs quantified *in vivo*[145]. Therefore, we concluded that murine small intestinal (SB1) organoids recapitulate *in vivo* stem cell kinetics. Moreover, performing cumulative BrdU labelling in organoids does not require the extensive assessment of BrdU dose, injection frequency, and plasma clearance time *in vivo*. However, in novel species like NMRs where organoid culture protocol is yet to be established, *in vivo* cumulative BrdU labelling remains the preferrable choice to establish stem cell kinetics.

Cumulative BrdU labelling index analysis in the mouse colonic organoids revealed that the duration of the DNA synthesis phase of murine colonic *Lgr5*$^{+}$ cells was 0.396 day ± 0.17 (Figure 4.9D). In summary, the *in vitro* estimation of T_S of mouse small intestinal (SB1) *Lgr5*$^{+}$ cells was equivalent to the previously reported *in vivo* data[145]. The *in vitro* duration of the S-phase quantified from cumulative BrdU labelling was similar (nearly 9.5 hours) in both the small intestine (SB1) and colonic *Lgr5*$^{+}$ cells in mice.

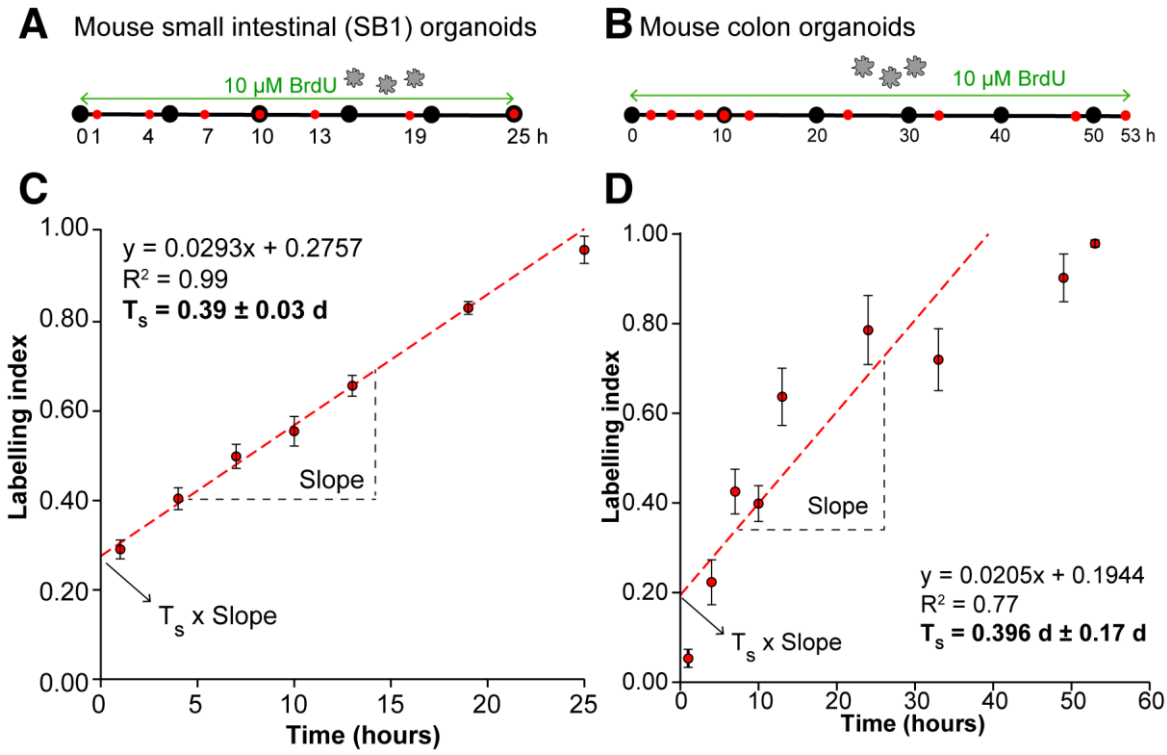

Figure 4. 9: Cumulative BrdU labelling of *Lgr5*$^{+}$ cells in mouse intestinal organoids.
(A-B) Schema showing the experimental timeline for culturing mouse **(A)** small intestinal and **(B)** colonic organoids in media supplemented with BrdU and time of harvest denoted in red. **(C-D)** Scatter plot showing a linear increase in the labelling index (*Lgr5*$^{+}$BrdU^{+}/*Lgr5*$^{+}$) of *Lgr5*$^{+}$ cells with time in organoids expanded from the crypts of the mouse **(C)** small intestine and **(D)** colon. Each data point represents the mean ± standard error of the mean of 20 to 30 organoids counted for each time point. The dotted line (red) on the graph represents a linear projection defined by the equation displayed on the plot. The duration of the S-phase (T_S) was derived from the y-intercept (T_S X slope).

4.2.6 Comparison of *Lgr5*$^{+}$ cell kinetics between naked mole rats and mice

After estimating the duration of S-phase (T_S) in the previous section, the total cell cycle duration (T_T) of the *Lgr5*$^{+}$ cell population *in vivo* can be determined by analysing BrdU labelling index at a single time point only. In this strategy, BrdU was injected in mice and NMRs, and tissues were analysed after t = 30 min and 1 day, respectively (Figure 4.10A). Next, the labelling index (LI) of *Lgr5*$^{+}$ cells residing at crypt base (0 to +4) and above crypt base (+5 to +10) were calculated in mouse and NMR small intestine (SB1) and colon. Using the prior value of T_S (from section 4.2.5), the *in vivo* total cell cycle duration (T_T) was determined using the equation: $T_T = (t+T_S)/LI$, for $t \leq T_T-T_S$[163] (section 2.5.2). A similar method has been used previously to determine cell cycle duration in mouse[93] and human[94] intestinal CBC cells. In the human colon, Ishikawa *et al.* have reported two distinct LGR5^{+} cell populations—at the crypt base and above the crypt base that cycle at different rates using a single time point analysis of their labelling index[94]. Therefore, this section will focus on measuring the total *in vivo* cell division time (T_T) in mouse and NMR *Lgr5*$^{+CBC}$ (0 to +4) and *Lgr5*$^{+outside\ crypt\ base}$ (+5 to +10) cell populations in both the small intestine (SB1) and colon using single time point analysis.

In the small intestine (SB1), single time point analysis revealed that mouse *Lgr5*$^{+CBC}$ cells were cycling every 1.56 days ± 0.10 while *Lgr5*$^{+CBC}$ cells in NMRs were cycling every 4.43 days ± 0.25 (Figure 4.10B, left). In the colon, the total division time of mouse *Lgr5*$^{+CBC}$ cells was also observed to be faster (2.21 days ± 0.18) than NMR (7.20 days ± 0.80) (Figure 4.10C, left). Based on these observations, it was concluded that *Lgr5*$^{+CBC}$ cells were cycling at roughly 2-times slower rate in NMRs

compared to mice. In both species, colonic *Lgr5*$^{+CBC}$ cells were slower cycling than their small intestinal counterparts.

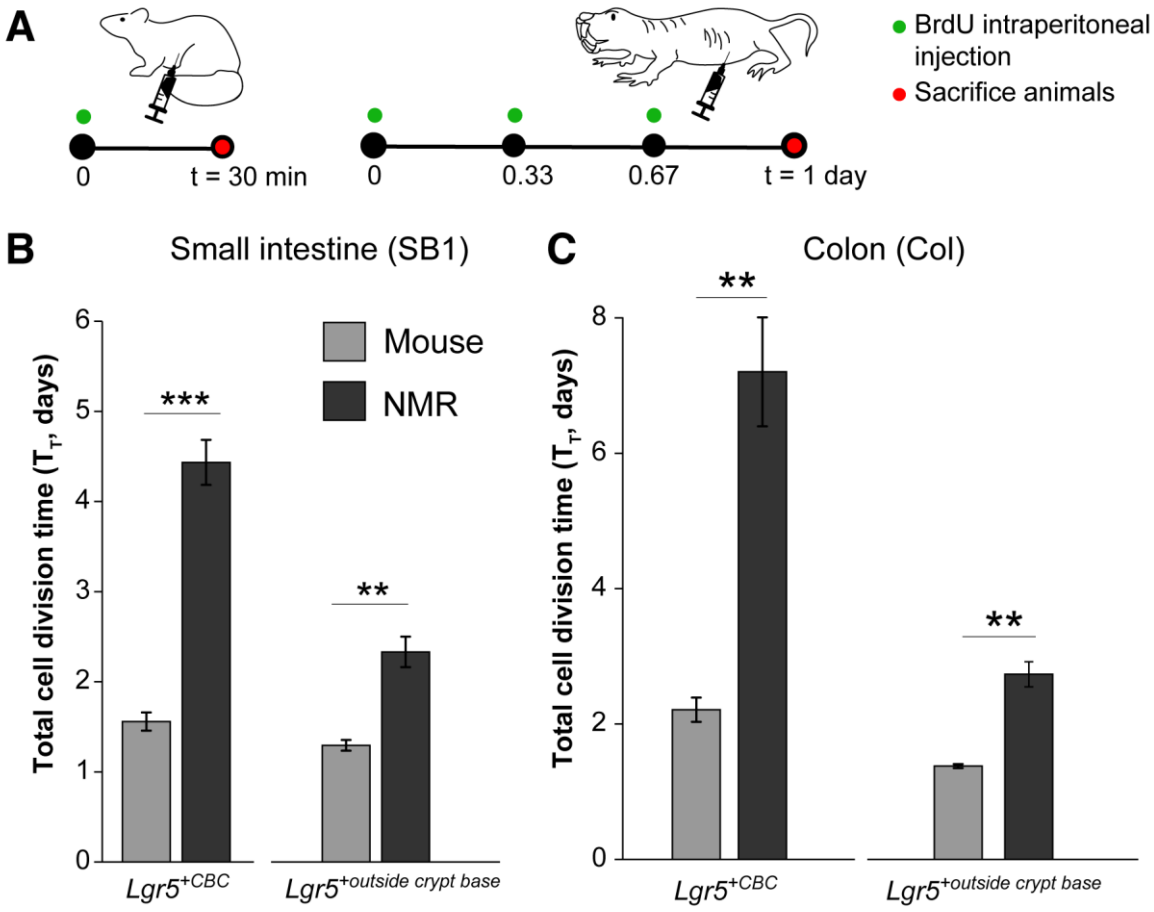

Figure 4. 10: Comparison of *Lgr5*$^{+}$ cell division time between mouse and NMR intestines. **(A)** Schema showing the experimental design for estimating total cell cycle (T_T) by injecting BrdU (green) intraperitoneally into mice and NMRs, and time points when tissues were collected (red). **(B-C)** Bar graphs showing the total division time (T_T) of the **(B)** small intestinal and **(C)** colonic *Lgr5*$^{+CBC}$ cells and *Lgr5*$^{+}$ cells outside the crypt base in mice and NMRs (n=3 animals per group). In all cases, statistical significance was determined by performing a two-tailed unpaired Student's t-test using an unequal variance. Significant *P*-values were denoted as **≤0.01, ***<0.001. Each bar represents the mean ± standard error of the mean.

The analysis was then extended to *Lgr5*$^{+}$ cells residing above the crypt base assuming the S-phase duration of *Lgr5*$^{+}$ cells remains unchanged in these two compartments. It was found that mouse small intestinal *Lgr5*$^{+outside\ crypt\ base}$ cells were cycling every 1.30 days ± 0.06 while *Lgr5*$^{+}$ cells above the crypt base in the NMR

small intestine took nearly double the time (2.34 days ± 0.17) (Figure 4.10B, right). Similarly, colonic *Lgr5*$^{+}$ cells above the crypt base in NMRs were also observed to take longer time (2.74 days ± 0.19) for completing one round of cell division than mice (1.38 days ± 0.03) (Figure 4.10C, right). In summary, *Lgr5*$^{+}$ cells outside the crypt base are cycling at 80-98% slower rate in the NMR intestine when compared to the mouse *Lgr5*$^{+CBC}$ cells. However, unlike the cells at the crypt base, *Lgr5*$^{+outside\ crypt\ base}$ cells are cycling at a similar rate in the small intestine and colon in both species.

Cells undergo phosphorylation at the Ser28 position of Histone H3 protein in the early stage (prophase) of mitosis and, therefore, phospho-Histone H3 (S28) has been described as a marker of M-phase in previous studies[211,212]. Using an antibody specific for pHH3(S28) and *Lgr5*-mRNA probe, intestinal tissues were stained to determine the mitotic index of adult stem cells (fraction of ASCs in mitosis: *Lgr5*$^{+CBC}$PHH3(S28)$^{+}$/*Lgr5*$^{+CBC}$*)* in mice, humans, and NMRs (Figure 4.11A). The duration of the M-phase (T_M) was then calculated using the equation[145]: $T_M = T_T$ X *Lgr5*$^{+CBC}$PHH3(S28)$^{+}$/*Lgr5*$^{+CBC}$. A similar duration of M-phase in *Lgr5*$^{+CBC}$ cells was observed in mouse and NMR small intestine (0.07 day ± 0.01 and 0.06 day ± 0.02 respectively) (Figure 4.11B, left). Similarly, T_M in colonic *Lgr5*$^{+CBC}$ cells was estimated to be 0.13 d ± 0.03 in NMRs and 0.08 d ± 0.02 in mice (Figure 4.11B, right). To sum up, M-phase durations in *Lgr5*$^{+CBC}$ cells were observed to be similar (2-3 hours) throughout the intestine between mice and NMRs.

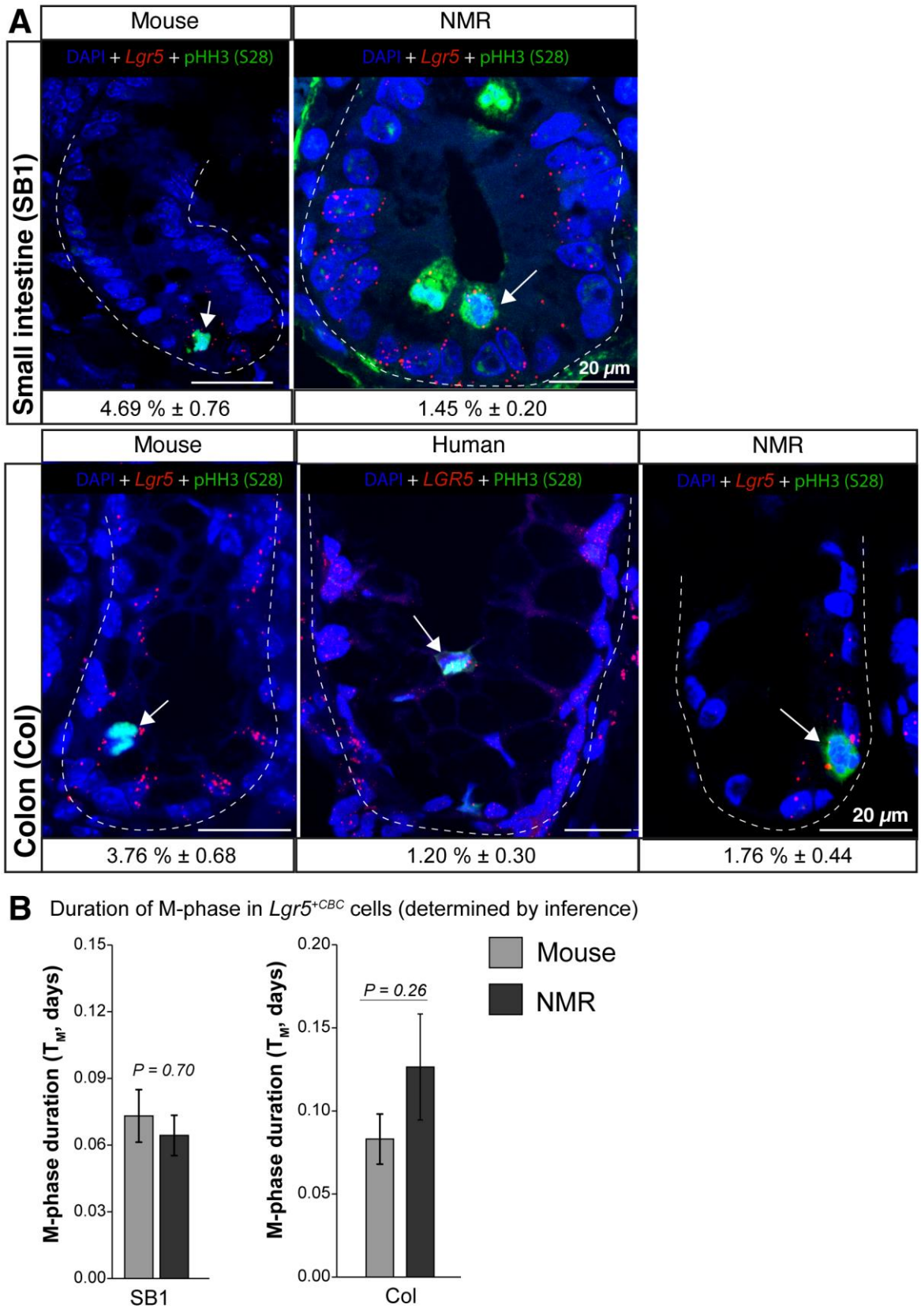

Figure 4. 11: Determination of M-phase duration in intestinal *Lgr5*$^{+CBC}$ cells.
(A) Confocal images showing intestinal crypts stained with *Lgr5/LGR5*-mRNA ISH probe (red), anti-phospho-histone-H3(S28) antibody (green), and counterstained with DAPI (blue) in wild-caught mouse (12-month-old) and wild-caught NMR (12-month-old) small intestines (top) and mouse,

human (65 to 70-year-old), and NMR colons (bottom). Percentages of *Lgr5/LGR5*$^{+CBC}$ cells positive for PHH3(S28)-expression have been shown under each image (mean ± SEM of n = 150 crypts counted from 3 individuals per species). Dashed lines demarcate the outer periphery of each crypt. White arrows indicate *Lgr5(LGR5)*$^{+CBC}$PHH3(S28)$^{+}$ cells. Scale bars are indicated on the images (20 µm). **(B)** Bar graphs showing the duration spent by *Lgr5*$^{+CBC}$ cells in the M phase in mouse and NMR small intestines (left) and colons (right) (n=3 animals per group, *P* values are indicated on the graphs). In all cases, statistical significance was determined by performing a two-tailed unpaired Student's t-test using an unequal variance. Each bar represents the mean ± standard error of the mean.

The gap phases (G1 and G2) of the cell cycle provide two key windows to make proliferation decisions (G1 to S) and amend any error after DNA replication[213]. The combined duration of the gap phases (T_{G1+G2}) was determined using the equation: $T_{G1+G2} = T_T – (T_S + T_M + T_{G0})$. As intestinal *Lgr5*$^{+CBC}$ cells in mice and NMRs did not enter quiescence ($T_{G0} = 0$, section 4.2.2), T_{G1+G2} was estimated by using the values of S, M-phase, and T_T calculated earlier in this chapter. The combined duration of the gap phases in mouse small intestinal *Lgr5*$^{+CBC}$ cells (1.09 days ± 0.10) was significantly shorter than NMR (3.9 days ± 0.27) (Figure 4.12, left). Similarly, in the colon, *Lgr5*$^{+CBC}$ cells in NMRs spend approximately 3-times longer duration (6.66 days ± 0.81) in G1 and/or G2 phases than in mice (1.74 days ± 0.18) (Figure 4.12, right). In conclusion, NMR intestinal *Lgr5*$^{+CBC}$ cells spend more time in the gap phases than mice.

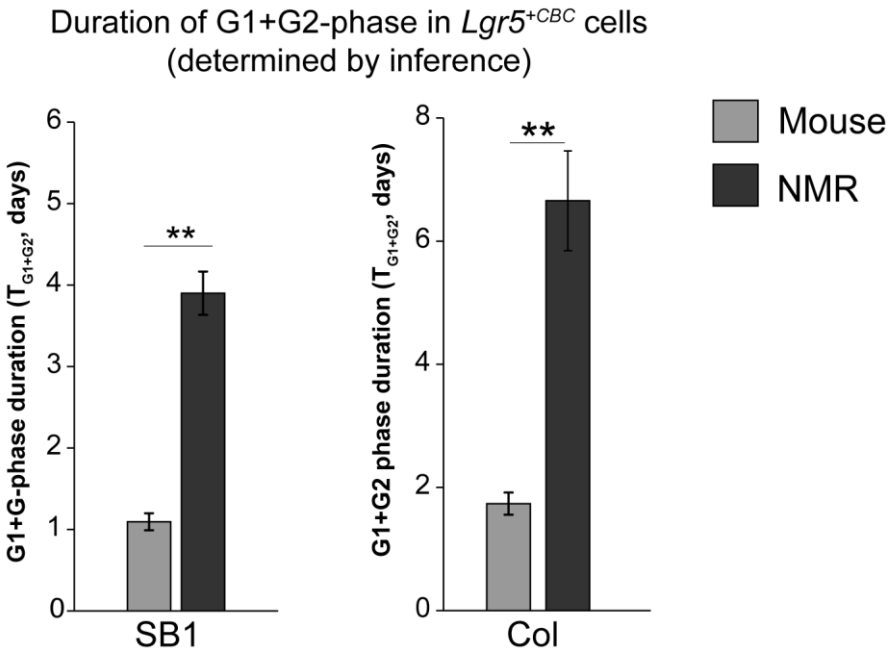

Figure 4. 12: Determination of G1+G2-phase duration in intestinal *Lgr5*$^{+CBC}$ cells.
Bar graphs showing the duration spent by *Lgr5*$^{+CBC}$ cells in G1 and G2 phases in mouse and NMR small intestines (left) and colons (right) (n=3 animals per group, significant *P*-values were denoted as **≤0.01.). In all cases, statistical significance was determined by performing a two-tailed unpaired Student's t-test using an unequal variance. Each bar represents the mean ± standard error of the mean.

Table 4.1 summarises the total cell division time (T_T) and the durations of each phase of the cell cycle presented in this chapter for *Lgr5*$^{+CBC}$ cells in mouse and NMR intestines. In brief, *Lgr5*$^{+CBC}$ cells in NMR intestines are approximately 2-times slower cycling than in mouse intestines. There is no difference between the exact durations *Lgr5*$^{+CBC}$ cells spend in S and M-phases between the two species. The difference in the *Lgr5*$^{+CBC}$ cell cycle duration between these two rodents is stemming from the 3-times longer G1 and/or G2 phases in NMRs compared to mice. So, intestinal *Lgr5*$^{+CBC}$ cells in naked mole rats are elongating their cell division time by spending a longer time in the gap phases than in mice.

Table 4. 1: Duration (days) of *Lgr5*$^{+CBC}$ cell cycle phases in mice, NMRs, and humans.

Region	Species	T_{Total}	T_{G1+G2}	T_S	T_M	T_{G0}
		Measured	**Inferred**	**Measured**	**Inferred**	**Inferred**
Small intestine (SB1)	Mouse	1.56 ± 0.10	1.09 ± 0.10	0.39 ± 0.03	0.07 ± 0.01	0
	NMR	4.43 ± 0.25	3.90 ± 0.27	0.47 ± 0.10	0.06 ± 0.02	0
Colon (Col)	Mouse	2.21 ± 0.18	1.74 ± 0.18	0.40 ± 0.17	0.08 ± 0.02	0
	NMR	7.20 ± 0.80	6.66 ± 0.81	0.42 ± 0.08	0.13 ± 0.03	0
	Human	7.3 (Ref[94])	1.83	0.25 (Ref[94])	0.09	5.13

4.2.7 Comparison of *Lgr5(LGR5)*$^{+CBC}$ cell kinetics between humans and naked mole rats

Using the single time point analysis of labelling index in NOD/Shi-scid mice (impaired B, T, and Natural Killer cell activity resulting in immunodeficiency) xenotransplanted with human colonic organoids, a recent study has reported that colonic LGR5$^+$ cells at the crypt base cycle every 7.3 days, while LGR5$^+$ cells above the base have a faster turnover of 1.5 days[94]. In section 4.2.6, a similar cell division time (7.2 days) was estimated for *Lgr5*$^{+CBC}$ cells in the NMR colon (Table 4.1). To conduct a side-by-side comparison of the kinetics of *Lgr5/LGR5*$^{+CBC}$ cells between humans and NMRs, expanding on the findings from Ishikawa *et al.*, we determined the time human colonic *LGR5*$^{+CBC}$ cells spend in each phase of the cell cycle (detailed methodology in section 2.5.3).

Co-stainings of *LGR5*-probe with KI67, P27, and phospho-Histone H3 (S28) antibodies in human colon biopsies were used to determine the proportion of the

total division time human colonic *LGR5*$^{+CBC}$ cells spend in each phase of the cell cycle (G1 to M) and quiescence (G0) (Figure 4.13A). In slower cycling cells, KI67 is detectable by immunohistochemical assays from the S to M phases of the cell cycle[164]. Therefore, for determining the fraction of human colonic stem cells in the cell cycle, the proportion of KI67^{+} cells was quantified among colonic *LGR5*$^{+CBC}$ cells (proliferation index = 11.23% ± 2.39) in an age-matched human cohort (65 to 70-year-old) (Figure 4.13B). Using this proliferation index and the total division time from previously reported data[94], it was estimated that human colonic *LGR5*$^{+CBC}$ cells spend 0.82 days in S, G2 and M-phases (Figure 4.13C). Using the fraction of colonic *LGR5*$^{+CBC}$ cells positive for PHH3(S28)-expression (1.20% in Figure 4.11A), it was quantified that these cells spend only 0.09 days in M-phase (Figure 4.13C), similar to the duration intestinal *Lgr5*$^{+CBC}$ cells spend in mouse and NMRs.

Using a Fucci-reporter organoid, Ishikawa *et al.* have reported the duration of S-phase in human LGR5^{+} cells to be 0.25 day[94]. Using our estimation of T_M, $T_{(S, G2, M)}$ and the previously reported value of T_S[94], the time human colonic *LGR5*$^{+CBC}$ cells spend in the G2 phase was inferred to be 0.48 days (Figure 4.13C).

For quantifying the duration human colonic *LGR5*$^{+CBC}$ cells spend in quiescence (G0), first the proportion of P27^{+} cells (84.82% ± 1.91) was determined in this population (Figure 4.13B) which represents cells residing either in G0 or G1 phase (Figure 4.13A). The proportion of LGR5^{+}P27^{+} cells in the G0 phase (Quiescent Fraction, QF=83%) reported in a previous study by analysing relative DNA/RNA content in FACS[94] was used to estimate the duration *LGR5*$^{+CBC}$ cells spend in quiescence (5.13 days) (Figure 4.13C). Finally, the duration of the G1 phase was

determined by subtracting the durations of S, G2, M and G0 from the total division time (T_T). It was quantified that human colonic *LGR5*$^{+CBC}$ cells spend around 1.35 days in G1 (Figure 4.13C). As the original study does not report the variance of their estimation of the total cell division time of human LGR5$^+$ cells[94], it was not possible to calculate any variance for the duration of these specific phases (Figure 4.13C).

As colonic stem cells (*Lgr5/LGR5*$^{+CBC}$) in both humans and NMRs take similar time (nearly 7 days on average) to complete one cell division, the percentages of this duration stem cells would spend in each of the phases for both the species were calculated to identify the key difference in their kinetics (Figure 4.13D). While human colonic *LGR5*$^{+CBC}$ cells spend 70% of their division time in G0, *Lgr5*$^{+CBC}$ cells in the NMR colon would spend 93% of their cell division time in G1 and/or G2 phases (Figure 4.13D). In short, despite having similar total cell division time, human colonic ASCs spend the majority of their time in quiescence (G0) while NMR colonic ASCs reside in the gap phases.

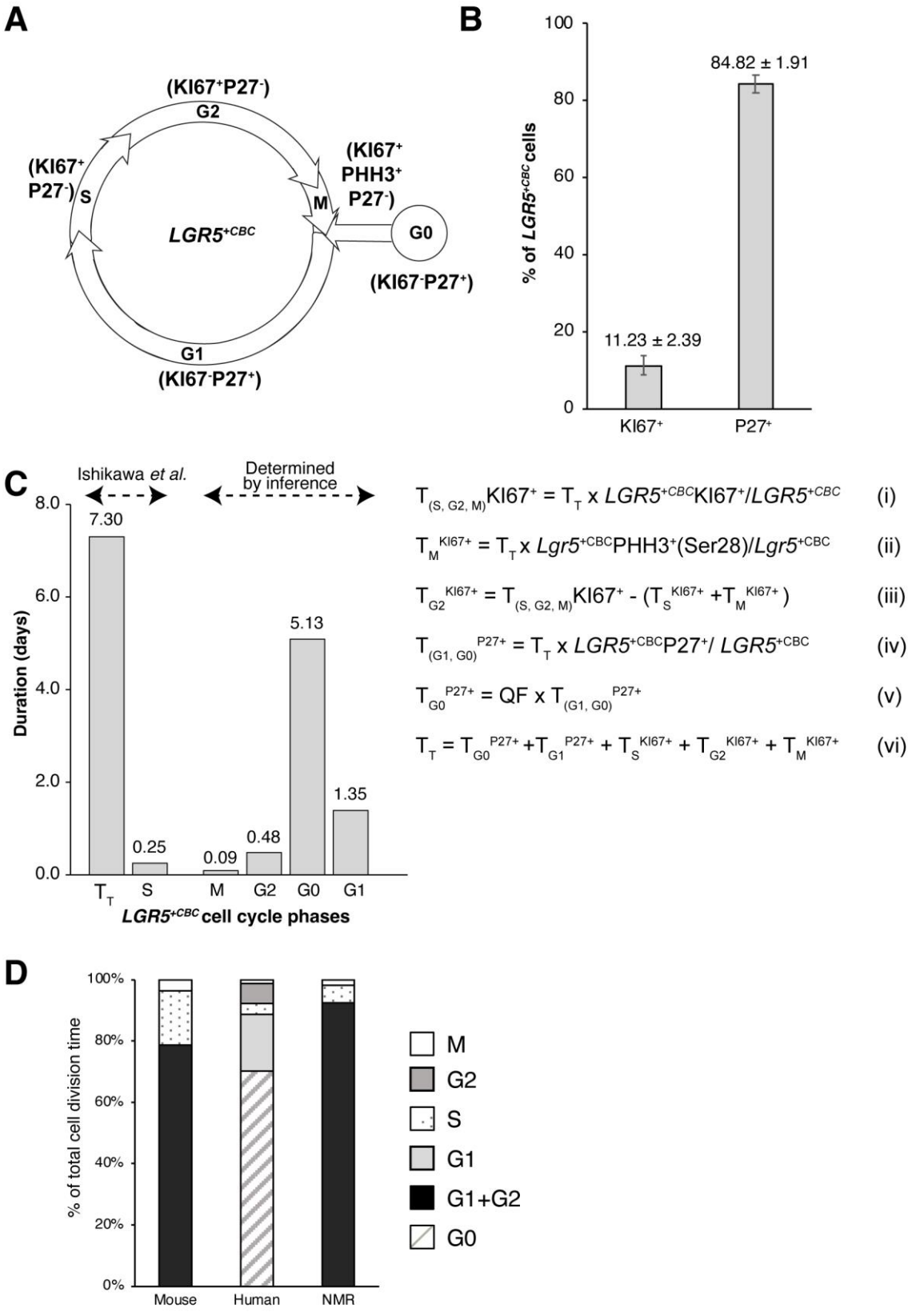

Figure 4. 13: Duration of specific cell cycle phases in human colonic *LGR5*$^{+CBC}$ cells.

(A) Schema showing the expression of KI67, P27 and phospho-H3 (S28) in relation to specific cell cycle phases of human colonic *LGR5*$^{+CBC}$ cells that were used to estimate the duration of each phase. **(B)** Bar graph showing percentages of *LGR5*$^{+CBC}$ cells positive for KI67 and P27 expression in the human colon. Each bar indicates the mean ± SEM of 50 crypts counted from 5 individuals (65-70 year-old). **(C)** Bar graph showing the duration of each phase of the cell cycle in human colonic *LGR5*$^{+CBC}$ cells which have been shown to cycle every 7.3 days (T_T), with an S phase duration of 0.25 days[94]. Using the fraction of *LGR5*$^{+CBC}$ cells positive for KI67, the cell cycle (S to M) duration was calculated using equation (i) shown alongside the graph. The fraction of *LGR5*$^{+CBC}$ cells that scored positive for PHH3(S28) (1.2% ± 0.30) was used to estimate the duration of M-phase (T_M) using equation (ii). The time spent in the G2 phase (T_{G2}) was calculated using equation (iii). The duration of G0 and G1 ($T_{G0,\ G1}$) in human colonic *LGR5*$^{+CBC}$ cells was estimated by using the proportion of *LGR5*$^{+CBC}$ P27^{+} and T_T in equation (iv). Then T_{G0} was estimated using the reported proportion of LGR5^{+}P27^{+} cells in G0 (Quiescence Fraction, QF= 83%)[94] in equation (v). T_{G1} was estimated using equation (vi). **(D)** Stacked bar graph showing the percentage of total cell division time spent in each cell cycle phase by mouse, human and NMR colonic *Lgr5*(*LGR5)*$^{+CBC}$ cells.

4.3 Discussion

In this chapter, the *in vivo* division rates of *Lgr5*$^{+CBC}$ cells in mouse and NMR intestines were determined. In section 4.2.6, I reported that adult stem cells (ASCs) in NMR small intestine (SB1) and colon are 2-times slower cycling than mice. Further analysis of the cell cycle revealed that NMR ASCs spend 3-times longer duration in G1 and/or G2 phases than mice. This data supports a recent study showing Hematopoietic Stem and Progenitor Cells (HSPC) in NMRs are slower cycling than mice and spend a prolonged duration in the G1-S checkpoint[65]. Moreover, Neural Stem and Progenitor Cells (NSPC) in NMRs also exhibit a slower proliferation rate than in mice, having a higher percentage of NSPCs in G0/G1 in NMRs[67]. Therefore, it appears that NMRs have slower cycling ASCs across different organs when compared to mice, where these cells spend an extended duration in the gap phases. Such long cycling duration can help NMRs to maintain genomic integrity during their long lifespan. The data presented in this chapter reports the *in vivo* duration of the total cell division time for the first time in NMR ASCs rather than inferring slower cell kinetics like a previous study where the labelling index of NMR HSPCs were compared with Murine HSPCs only after a dual-pulse[65].

As NMRs live underground in hypoxic conditions resulting in high oxidative stress[1], there is an evolutionary pressure to select for efficient genome surveillance machinery in this species. Recently it has been reported that NMR p53 has a higher half-life than mice and humans that maintains constitutive nuclear localisation even before genomic damage[39]. Additionally, upon DNA damage, NMRs express higher levels of genes involved in repair pathways (e.g., mismatch repair, non-homologous end joining, and base excision repair) than mice[214]. The findings in this chapter show prolonged G1 and/or G2 phases in NMR intestinal stem cells which may be an adaptation to allocate sufficient time for efficient genome repair in a damage-prone habitat.

A key finding in this chapter was that colonic stem cells in long-lived humans and NMRs have similar cell division rate which is significantly slower than in short-lived mice. While human ISCs in the colon remain quiescent for 70% of their life, NMR ISCs achieve an extended cycle duration by spending 93% of their life in the gap (G1/G2) phases. Therefore, ASCs in NMR colon appears to execute a different strategy than humans to slow down their cell division rates. While spending prolonged duration in G0 by human ASCs can help cells avoid accumulating DNA damage caused by cellular respiration[215-217], any mutation resulting in the cell cycle re-entry of these quiescent cells will most likely expose them to a high number of replication errors as they spend a short duration (1.83 days) in the gap phases (G1/G2). On the other hand, actively cycling NMR ASCs spend a longer duration (6.66 days ± 0.81) in gap phases (G1/S and G2/M checkpoints) probably to correct errors caused by DNA replication. In brief, the results presented in this chapter

provide an insight into how long-lived mammals (humans and NMRs) may avoid accumulating mutations in stem cells by slowing down their cycling rate for long-term tissue maintenance.

One of the major limitations of this chapter was using the S-phase duration of *Lgr5*$^{+CBC}$ cells from the cumulative BrdU labelling experiment to determine the total cell division time of *Lgr5*$^{+}$ cells residing outside the crypt base. It was assumed that T_S is similar in the two *Lgr5*$^{+}$ cell populations of the crypt, an assumption that has also been made in a previous study on the human colon[94]. Additionally, the division time of mouse colonic *Lgr5*$^{+}$ cells was determined *in vivo* using the S-phase duration from the *in vitro* BrdU labelling experiment under the assumption that *in vitro* and *in vivo* T_S is unchanged. Cameron *et al.* have reported that the duration of S-phase remains constant (around 7.5 hours) across different tissues in mice[218] and is close to the T_S determined for NMR and mouse colonic ASCs in this study (9-10 hours) and human colonic ASCs (6 hours, reported by Ishikawa *et al.* using organoids[94]). Therefore, it appears that the duration of DNA-synthesis phase is between 6 to 10 hours across different tissue types and species. For mouse small intestinal *Lgr5*$^{+}$ cells, it has been demonstrated earlier in this chapter (section 4.2.5) that the *in vitro* T_S (0.39 day ± 0.03) is similar to the previously reported *in vivo* value (0.39 day)[145]. Future studies can validate this further by determining the T_S in mouse colonic *Lgr5*$^{+CBC}$ cells *in vivo* from the cumulative labelling experiment. This would further establish that *in vitro* organoids can recapitulate the *in vivo* cellular kinetics of the intestinal *Lgr5*$^{+}$ cells.

4.3.1 Conclusion

In this chapter, I have shown that intestinal *Lgr5*$^{+CBC}$ cells in NMRs divide 2-times less frequently than mice due to spending longer time in the gap phases (G1/G2). These cells in mouse and NMR intestines do not enter quiescence (G0). Despite having a similar cell division time to NMRs, human colonic *LGR5*$^{+CBC}$ cells spend most of their life in quiescence while similar cells in NMRs spend a longer duration in G1 and/or G2 phases. In brief, NMR intestinal ASCs exhibit key differences in cell kinetics when compared to both humans and mice. In the next chapter, I will describe the response of the naked mole rat intestine, including the stem cells, to dextran sodium sulphate.

Chapter 5: Response of naked mole rat intestine to Dextran Sodium Sulphate

5.1 Introduction

In chapters 3 and 4, I have demonstrated how the intestinal tissue in long-lived naked mole rats (NMRs) is different to short-lived mice by having a higher proportion of (*Lgr5*$^{+}$) stem cells with slower division rate and increased proportions of differentiated cells (enterocytes, goblet, and enteroendocrine cells) per crypt. These features may explain how the NMR intestine is able to maintain homeostasis over a longer lifespan[219,220]. Moreover, longevity has also been linked to an organism's ability to respond to damage and stress[221,222]. For example, bats (lifespan 20 years) have an efficient ABC transporter protein ABCB1 that enhances the efflux of genotoxic compounds resulting in less DNA damage when exposed to doxorubicin[223]. Crocodile (lifespan 100 years) intestines have a unique microbiome with high immune surveillance and cell-autonomous defence mechanisms (e.g., antimicrobial components in serum) that protect against pathogens[224]. In the human (lifespan 83 years) colon, quiescent stem (LGR5^{+CBC}) cells survive exposure to 5-Fluoro Uracil (5-FU) and re-enter the cell cycle after removal of the genotoxic agent[94]. These studies indicate that longer-living species have evolved unique responses to stress.

Previous studies have described NMR as a unique model to study stress response. A wound-healing experiment in the skin of NMRs has found an undiminished regenerative capacity of their stem cells during ageing[68]. Single-cell transcriptomics analysis followed by exposure of NMRs to lipopolysaccharides has shown that these animals exhibit a more innate (myeloid) than adaptive (lymphoid) immune response to microbial challenges while an opposite reaction is observed in mice[225]. In the NMR brain, neural stem and progenitor cells can initiate a faster response to

DNA damage caused by gamma-irradiation than in mice[67]. All these reports suggest that naked mole rats have evolved unique mechanisms to endure damage-causing agents. Hence, in this chapter, I will investigate the response of intestinal epithelial cells to a colitogen (agent causing epithelial injury in the colon) in NMRs.

Most studies of damage response in the intestine have been conducted on various short-lived animal models (e.g. mice[83,226-228], rats[229,230], rabbits[231] and guinea pigs[232]). These studies involve three major strategies: administering chemical colitogens (Dextran Sodium Sulphate[226-228] and Tri-Nitro Benzene Sulfonic-acid[230]), exposure to ionising radiation[83], and ethanol enema[228]. To study the damage response of human colonic stem cells, Ishikawa *et al.* used an orthotopic xenotransplant model to demonstrate the presence of two spatially and kinetically distinct LGR5^{+} populations: one is sensitive (LGR5$^{+\text{ above crypt base}}$) and another one is resistance (LGR5^{+CBC}) to 5-FU induced damage[94]. While all these strategies are effective in inducing damage in animal models at varying degrees, Dextran Sodium Sulphate (DSS) has been the most popular choice due to its ease of administration and well-characterised, reproducible signs of epithelial injury in the murine colon[226-228]. Therefore, I selected DSS administration to assess epithelial injury in NMRs.

In this Chapter, I will first describe the response of NMR intestinal epithelial cells, including stem *(Lgr5^{+})* cells, to DSS exposure compared to mice. DSS causes mucosal damage by disrupting the epithelial monolayer of the colon, which has been shown to cause a pro-inflammatory response in mice[226,227], rats[229], rabbits[231] and guinea pigs[232]. Finally, I will also describe the recovery of NMR intestines upon DSS withdrawal.

5.2 Results

5.2.1 Dextran Sodium Sulphate (DSS) induced intestinal damage across species

In mice, the widely used method of DSS delivery is by adding this chemical to their drinking water and monitoring loss of body weight and development of bloody diarrhoea. Previous studies have shown that DSS administration via drinking water results in epithelial damage in the murine distal colon within 3-7 days of treatment[148,227]. However, administering DSS to the naked mole rats (NMRs) poses a challenge as these xerocoles do not drink water and get their hydration from their plant-based diet[233]. Therefore, oral gavaging was used to deliver DSS to NMRs. However, oral gavage can cause passive reflux in the stomach, pharyngeal and gastric irritation, and aspiration pneumonia in animals which can be very stressful[234]. So, we minimized the stress on NMRs by oral gavaging for three days only.

As oral gavaging of DSS in mice or any other animal has not been reported before, the next section will assess whether this delivery method induces similar damage to that of the drinking water method in mice. A further comparison of these methods will be made in the following section with intestinal tissues of C57BL/6J mice subjected to 2.5% DSS treatment in water for 7 days that were provided by Dr. Nan Gao's lab in Rutgers University, Newark, USA. In the final section, features of DSS-mediated responses in NMR intestines will be described.

5.2.1.1 DSS-induced epithelial damage (oral gavage) in mouse colon

After oral gavaging mice with 2.5% DSS every 4 hours during the day for three days (Figure 5.1A), the intestinal tissues were harvested, stained with H and E, and assessed for epithelial damage compared to control mice (gavaged with 0% DSS). Evaluation of H and E stained sections of the colonic tissues revealed mild epithelial injury in 30% of the distal colon of the DSS-treated mice (Figure 5.1B) while no damage was seen in the controls (Figure 5.1C). The affected regions of the distal colon in DSS-treated mice exhibited the beginning of erosion in the mucosal surface, expansion of crypt structures into muscularis externa, shortening of crypts, an increased presence of mononuclear inflammatory cells in lamina propria, irregular branching of crypts, and variation of crypt size. However, signs of severe epithelial damage (complete loss of crypts, ulceration, tissue granulation and neutrophil infiltration into bowel walls) in the colon described for 2.5% DSS administration in drinking water for 5 days[148,235] were not noticed in mice dosed with 2.5% DSS via oral gavage.

Histopathological evaluation by two independent pathologists (Dr. Patrycja Gazinska and Prof. Piotr Ziolkowski) based on tissue damage, immune infiltration, and involvement of the epithelial surface indicated significantly higher levels of damage in mice gavaged with 2.5% DSS compared to unsupplemented water (Figure 5.1D). Upon expanding the histopathological analysis based on a second scoring criterion focusing on architectural damage of crypt structures[235], mice treated with 2.5% DSS with oral gavage exhibited a significantly higher degree of

architectural damage than controls (Figure 5.1E). No change was observed between the degree of damage scored using the two scales (Figure 5.1D-E).

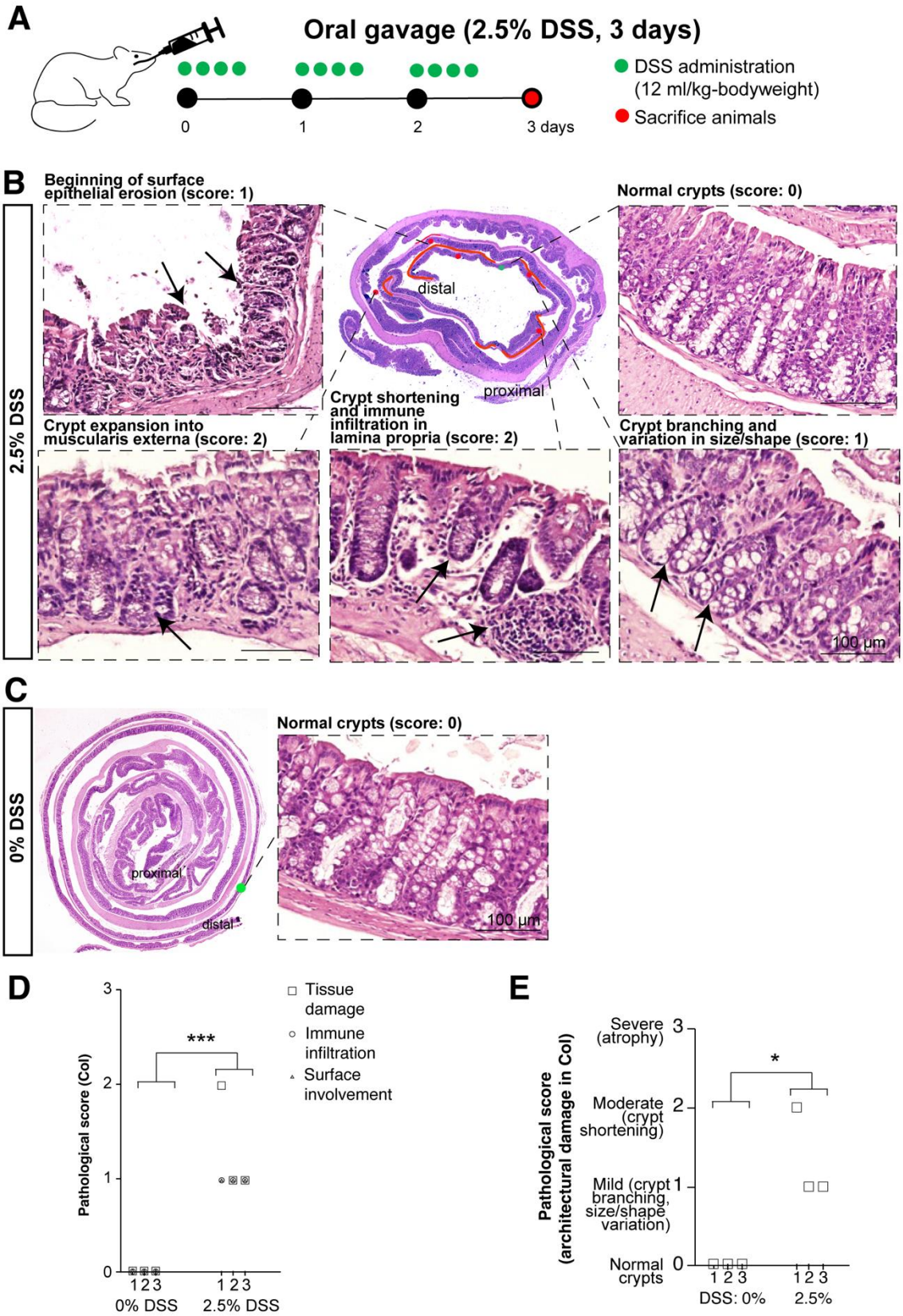

Figure 5. 1: Histological assessment of colonic damage after DSS administration via oral gavage in mice.
(A) Schema illustrating the experimental design for administering 2.5% DSS to C57BL/6J mice via oral gavage at specific time points (green dots) for 3 days and time of tissue harvest (red dot). **(B)** Haematoxylin and Eosin (H&E) staining of 2.5% DSS-treated mouse colon (oral gavage for 3 days) showing areas of tissue damage in the distal region highlighted in red. Magnified images showing crypt shortening, expansion and branching, and immune infiltration. Black arrows indicate damage. **(C)** H&E staining of the colon from a control mouse (0% DSS via oral gavage for 3 days) showing normal crypt structures in the distal colon. **(D)** Pathological scores showing significant differences in colonic tissue damage (square), neutrophil infiltration (circle) and percentage of the area involved in damage (triangle) between mice treated with 2.5% DSS via oral gavage (n=3) and unsupplemented water (n=3) ($p<0.05$, two-tailed Wilcoxon rank sum test). Numbers on the x-axis show numeric identifiers tagged to each animal. **(E)** Pathological scores of architectural damages (according to the scale described by Bonfiglio *et al.*[235]) showing only mild to moderate levels of damage in mice treated with 2.5% DSS compared to controls ($p<0.05$, two-tailed Wilcoxon rank sum test). Details of the scoring criteria have been summarised in the y-axis label. Significant *P*-values were denoted as *<0.05, ***<0.001.

In summary, 2.5% DSS administration via oral gavage for 3 days induced a mild degree of damage (score 1 to 2) in the distal region of the colon. This is similar to a previous report of a chronic colitis model where mice were administered 3 rounds of 1% DSS (1 week) followed by recovery (1 week) over 6 weeks resulting in a mild degree of dysplasia-like atypia[236].

5.2.1.2 DSS-induced epithelial damage (drinking water) in mouse colon

Colonic tissues of mice administered with 2.5% DSS for 7 days in drinking water (Figure 5.2A) and sacrificed on day 8 were obtained from Nan Gao's Laboratory at Rutgers' University, Newark, USA. Haematoxylin and Eosin staining of these tissues showed severe epithelial damage in 80% of the mid to distal colon (Figure 5.2B). Nearly 60% of these affected areas displayed total crypt atrophy characterized by complete loss of crypts, flattening of the colonic mucosa, ulceration, and tissue granulation (Figure 5.2C, top). Debris caused by fibrosis and

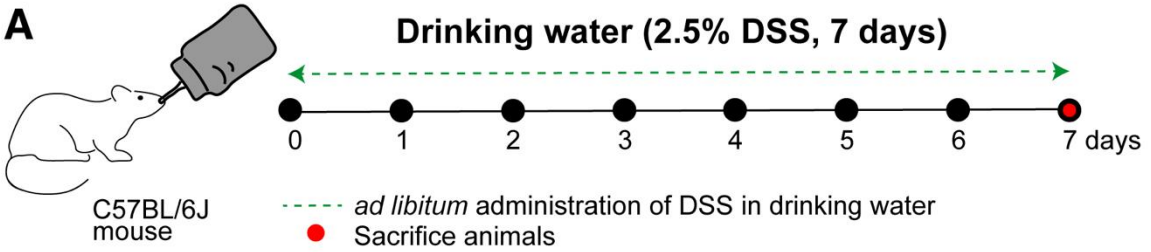

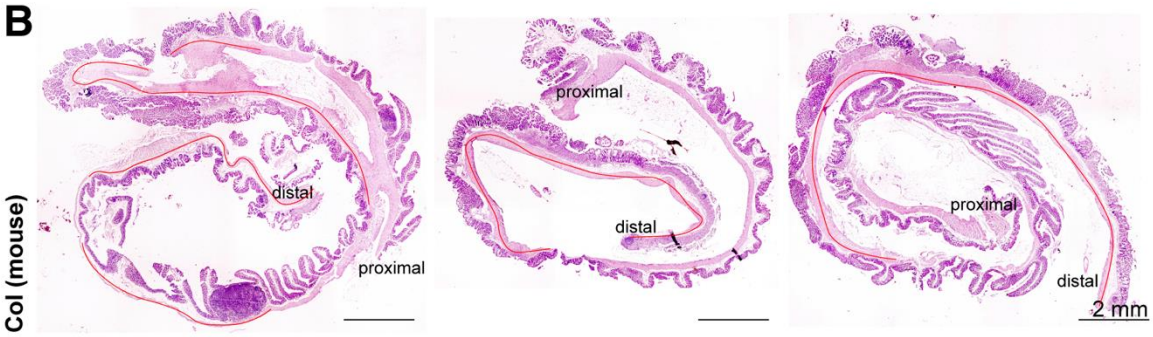

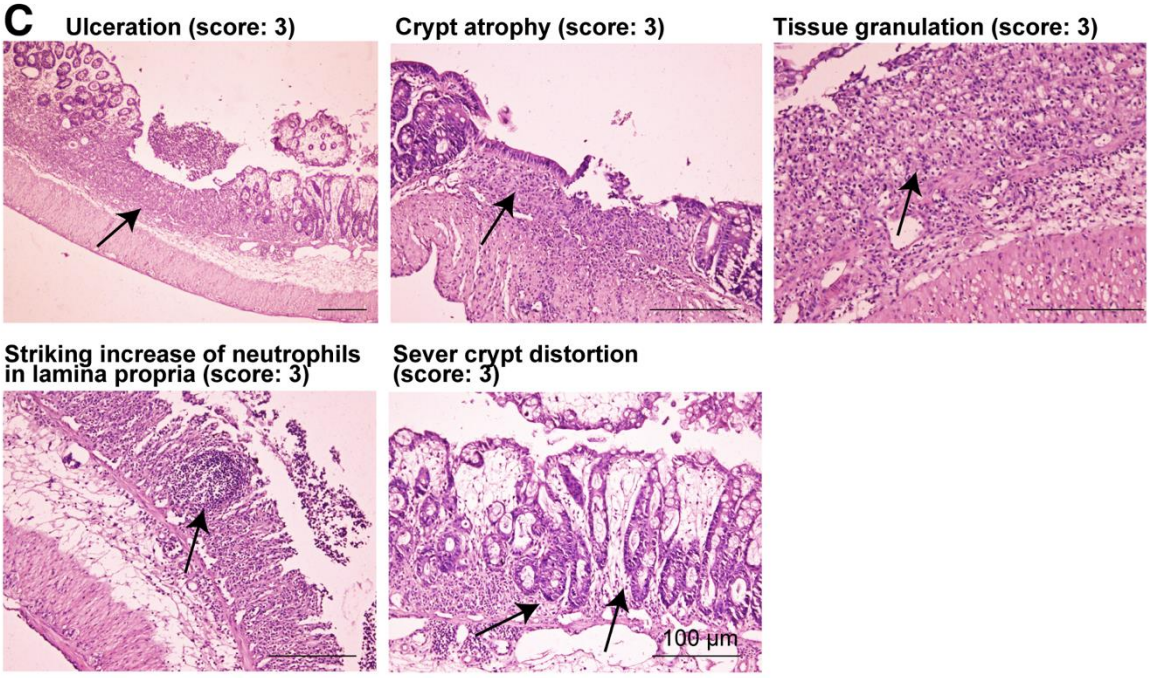

D

Scoring Matrix				
Level	**Score**	**Tissue Damage**	**Infiltration**	**Surface Involvement**
None	0	None	Infrequent	None
Mild	1	Isolated focal epithelial damage	Increased, some neutrophils	1-25%
Moderate	2	Mucosal erosions and ulceration	Submucosal present of inflammatory cell clusters	26-50%
Severe	3	Extensive damage deep into bowel wall	Transmural Cell Infiltration	51-75%
Extreme	4	--	--	76-100%

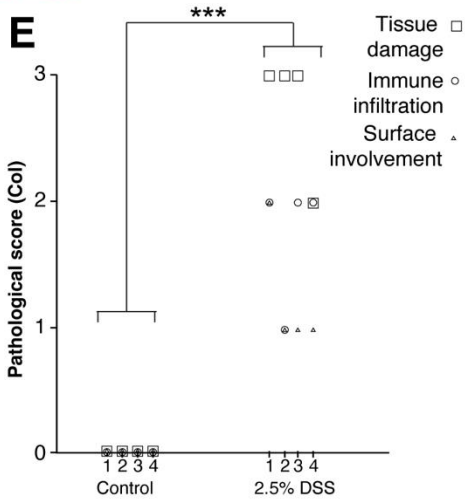

Figure 5. 2: Histopathological evaluation of murine colon following DSS administration in drinking water.
(A) Schematic representation of the experimental strategy for administering 2.5% DSS in drinking water (green dashed line) for 7 days in C57BL/6J mice and day of tissue harvest (red dot). **(B)** Haematoxylin and Eosin (H&E) staining of colon gut-rolls from mice treated with 2.5% DSS in drinking water for 7 days showing areas of severe tissue damage in the mid to distal colon highlighted in red. **(C)** Magnified H&E images show ulceration, crypt atrophy, tissue granulation, a striking increase of neutrophil infiltration, and severe crypt distortion in the colon of mice treated with DSS. Black arrows indicate damage. **(D)** A table showing the criteria used by the pathologists (Dr. Patrycja Gazinska and Prof. Piotr Ziolkowski) to score tissue damage in the colon. **(E)** Pathological scores showing significant differences in colonic tissue damage (square), neutrophil infiltration (circle) and percentage of the area involved in damage (triangle) between mice treated with 2.5% DSS in drinking water (n=4) and untreated controls (n=4) ($p<0.05$, two-tailed Wilcoxon rank sum test). Numbers on the x-axis show numeric identifiers tagged to each animal. Significant *P*-value was denoted as ***<0.001.

---

necrosis of epithelial cells infiltrated with neutrophils were also noticed above the mucosal region impacted by ulceration (Figure 5.2C, top-left) which has been described as a signature of severe epithelial abnormality in a previous report[235]. The remaining 40% areas displayed signs of severe architectural distortions such as glandular rarefaction (reduction in crypt density), loss of >50% of crypt length, branching of crypts, and depletion/loss of the mucin layer (Figure 5.2C, bottom-right). A striking increase of neutrophils was also observed in the mucosa and submucosa of the affected regions in the colon (Figure 5.2C, bottom-left).

The semi-quantitative analysis of epithelial damage by two independent pathologists scored the colonic tissues focusing on the extent of architectural damage, level of infiltration by immune cells and the fraction of the colon exhibiting signs of damage (Figure 5.1D). While the untreated control mice showed no signs of epithelial injury, all the mice receiving 2.5% DSS in drinking water for 7 days displayed a moderate degree of immune infiltration and a severe degree of tissue damage affecting up to 50% of the entire colon length (Figure 5.1E). This damage was more prominent in the distal colon (50% length of colon from rectal end) than in the proximal colon (50% length of colon from caecal end) (Figure 5.1B).

Therefore, 2.5% DSS administration in mice via oral gavage was effective to cause epithelial injury in mice, similar to previous reports[9-11].

5.2.1.3 Histopathology of DSS-treated (oral gavage) naked mole rat colon

Upon demonstrating the mild but consistence effect of oral gavage to induce DSS-mediated colonic injury in mice, naked mole rats were dosed with 2.5% DSS for 3 days following a similar strategy (Figure 5.3A). After staining the colonic tissue with H and E, no signs of epithelial damage were found in NMRs orally gavaged with 2.5% DSS (Figure 5.3B). The DSS concentration was then increased to 5.0% and 8.75% and administered to NMRs via oral gavage for 3 days. Compared to lower concentrations (0-2.5%), DSS administration at higher concentrations resulted in a change in stool consistency from normal (hard, black) to soft (5% DSS) and very soft (8.75% DSS) within 1 day of treatment (Figure 5.3C). However, histological evaluation of the colonic tissue did not reveal any signs of epithelial injury in 5% and 8.75% DSS-treated NMRs (Figure 5.3B). Finally, scoring by independent pathologists confirmed that NMRs administered with 2.5% to 8.75% DSS for 3 days via oral gavage did not show any noticeable colonic damage when compared to the control animals (Figure 5.3D). However, the possibility of colonic damage occurring in NMRs, if the experiment is extended for a longer duration (e.g. 7 days), cannot be excluded. Nevertheless, in a side-by-side comparison of 2.5% DSS administration via oral gavage for 3 days, NMRs were found to be more resistant to colitogenic damage than mice.

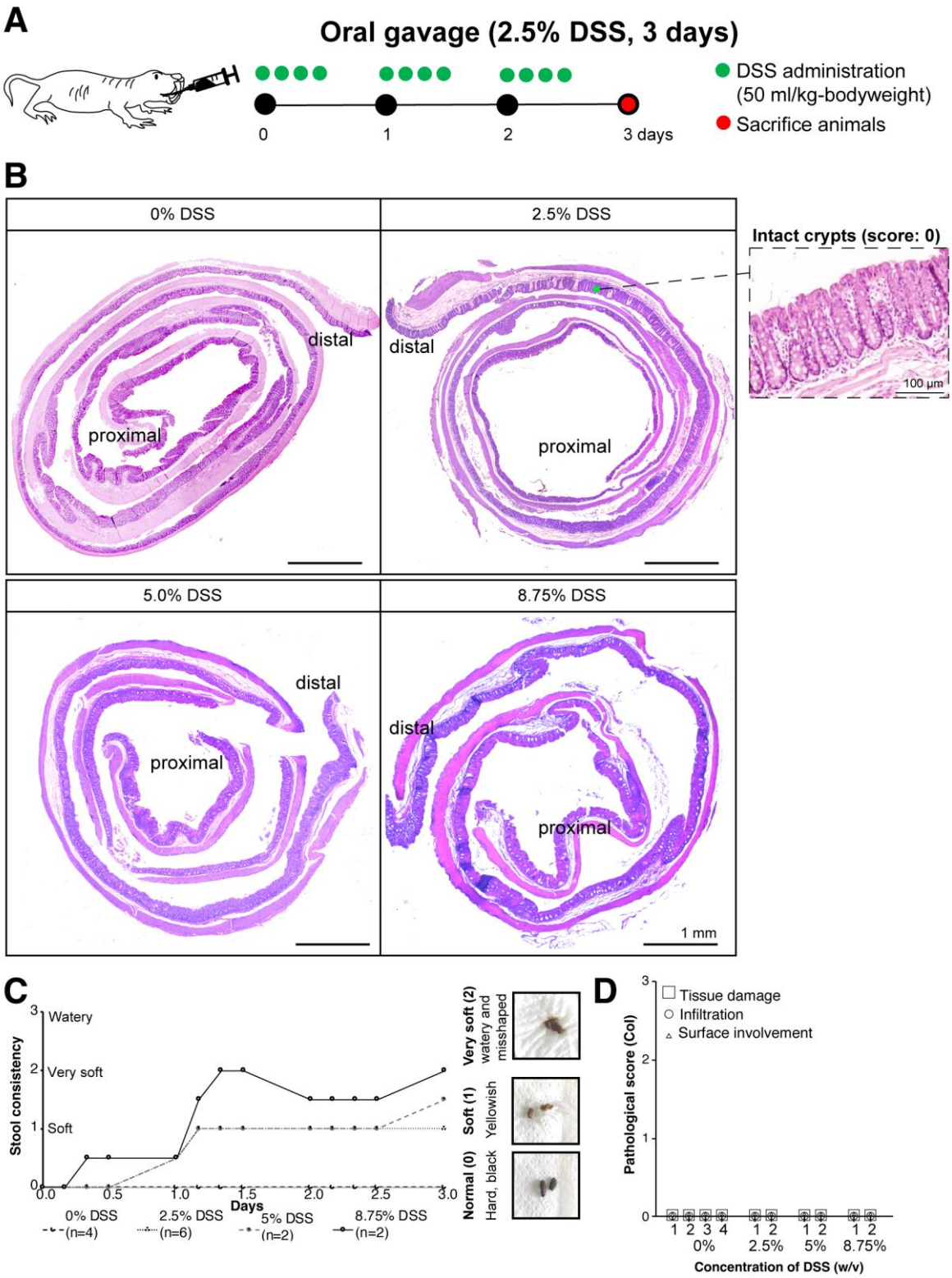

Figure 5. 3: Histopathological examination of epithelial injury in naked mole rat colon after DSS treatment via oral gavage.
(A) Schema illustrating the experimental design for administering DSS via oral gavage at specific time points (green dots) and day of tissue harvest (red dot) in NMRs. **(B)** Photomicrographs of Haematoxylin and Eosin staining showing no damage in the colon of NMRs treated with 0-8.75% DSS (oral gavage for 3 days). **(C)** Line graph showing a gradual change in the stool consistency of NMRs subjected to DSS treatment (2.5%, 5% and 8.75%) (2 to 6 animals per treatment group). Photographs beside the graph show three different stool consistencies observed (hard, black: Score

0; soft and yellowish: Score 1; very soft and slightly watery: Score 2). **(D)** Pathological scores (criteria outlined in Figure 5.1D) showing no damage in DSS-treated NMRs (2.5%, 5% and 8.75%; n=2 animals per treatment group) compared to the controls (0% DSS, n=4). Numbers on the x-axis show numeric identifiers tagged to each animal.

5.2.2 *Lgr5*-expression in DSS-treated mouse and naked mole rat intestines

Researchers have previously reported the loss of (*Lgr5*$^{+}$) adult stem cells in the distal colon of mice following 2.5-3.0% DSS treatment in drinking water for 5-6 days[148,228]. To elucidate the effect of DSS treatment via oral gavage for 3 days on the *Lgr5* expression, intestinal tissues of DSS-treated (oral gavage) mice and NMRs were stained with species-specific *Lgr5* probes, and the crypt sections were analysed under a confocal microscope (Figure 5.4A-B, left). After analysing *Lgr5* expression in both normal and atypical crypt bases in the colon of the DSS-treated mice, no significant change was found in the number of intestinal stem cells per crypt between the mice gavaged with 2.5% DSS (2.62 cells ± 0.15) and unsupplemented water for 3 days (2.73 cells ± 0.19) (Figure 5.4A, right). This observation is in agreement with the previous report demonstrating that the loss of *Lgr5* expression in the mouse colon is dependent on the DSS dose and duration administered[228]. Total *Lgr5* expression is lost only after administering 3% DSS in drinking water for 6 days where approximately 50-80% loss of *Lgr5* expression is observed for 0.5% to 1.5% DSS administration for 6 days when compared to the control[228]. The possibility of loss of *Lgr5*$^{+}$ cells in murine colon if oral gavage with 2.5% DSS had been continued for longer than 3 days cannot be excluded. The analysis was then extended to the most proximal part of the small intestine (SB1) and a similar number of *Lgr5*$^{+CBC}$ cells per crypt was observed between mice dosed with 0% (4.22 cells ± 0.16) and 2.5% (4.12 cells ± 0.27) DSS via oral gavage.

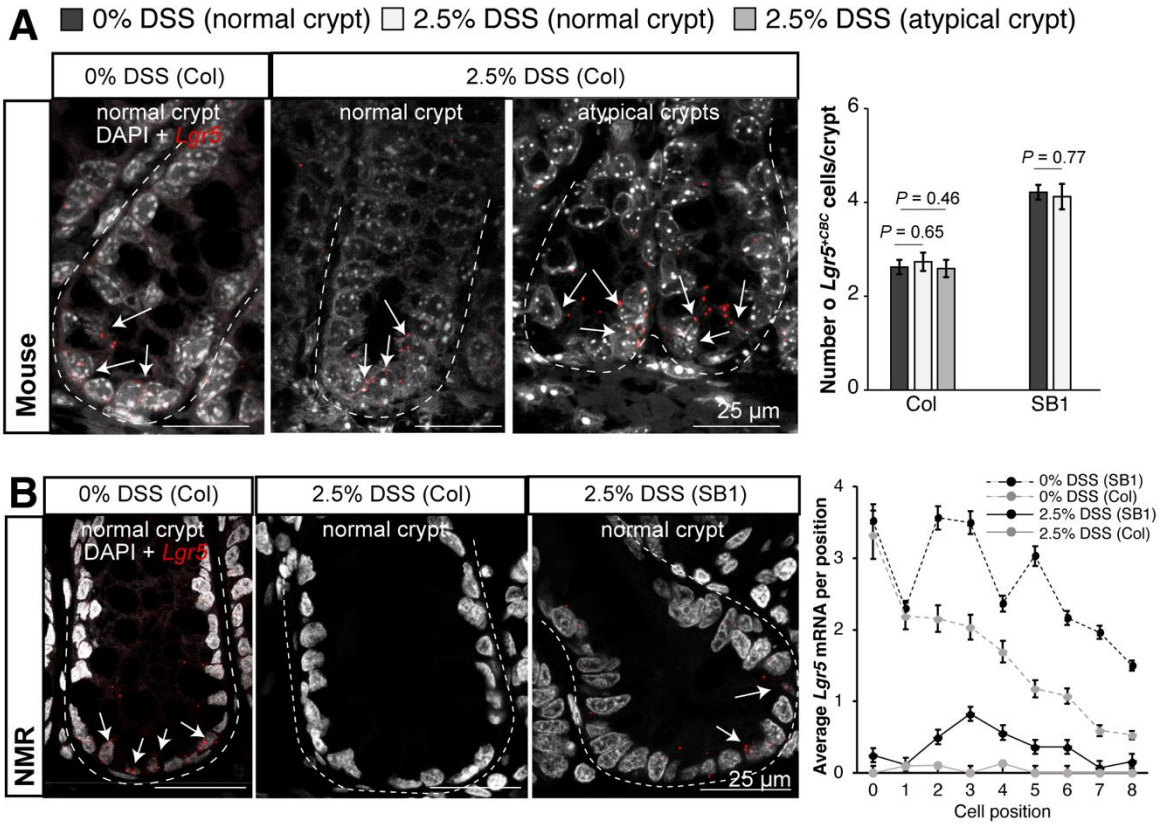

Figure 5. 4: *Lgr5*-expression in the intestines of mice and NMRs following DSS treatment via oral gavage.
(A) Confocal images (left) showing staining with mouse-specific RNAscope *Lgr5* probe (red) and DAPI (grey) in the distal colonic crypts in untreated and 2.5% DSS-treated mice (oral gavage for 3 days). White arrows indicate *Lgr5*$^{+}$ cells. Bar graph (right) showing no change in the number of *Lgr5*$^{+CBC}$ cells between untreated and 2.5% DSS treated mice (n=40 crypts from 3 animals per group, *P*>0.05, two-tailed unpaired t-test with unequal variances). Each bar represents the mean ± standard error of the mean. **(B)** Confocal images (left) showing staining with NMR-specific RNAscope *Lgr5* probe (red) and DAPI (grey) in the distal colonic and duodenal crypts in untreated and 2.5% DSS-treated NMRs. White arrows indicate *Lgr5*$^{+}$ cells. Line graph (right) showing *Lgr5* mRNA expression levels in cells at specific positions in the NMR intestinal crypts. Each dot represents mean ± sem (n=50 crypts from 3 animals per group). Scale bars are indicated on the images (25 µm).

In NMRs, despite showing no obvious sign of epithelial injury following DSS administration, a near-complete loss of *Lgr5*-expression was observed at the base and above the base of the crypt in the colon of DSS-treated NMRs compared to the controls (Figure 5.4B, right). Even in the small intestine which remains apparently unaffected by high doses of DSS treatment in mice, 2.5% DSS treatment via oral gavage for 3 days in NMRs resulted in roughly 80% loss of *Lgr5* mRNA puncta in

the undamaged small intestinal (SB1) crypts (Figure 5.4B, right). Number of *Lgr5*$^{+}$ cells in DSS-treated NMRs was reduced to 1.13 cells ± 0.18 per SB1 crypt compared to the control (8.05 cells ± 0.37). These data suggest that NMR small intestinal (SB1) and colonic *Lgr5*$^{+}$ cells are more sensitive to DSS treatment compared to mice.

5.2.3 Apoptosis in DSS-treated mouse and naked mole rat intestines

Apoptosis is a coordinated process of cell death that involves early degradation of mRNA followed by the disruption of lipid membranes and proteins, and fragmentation of DNA[237,238]. After observing the loss of *Lgr5* expression following DSS administration in the NMR intestines, apoptotic cells in the intestinal crypts of mice and NMRs treated with DSS via oral gavage for 3 days were quantified. Intestinal tissue sections were stained for degraded DNA, a feature of the late stage of apoptosis, using Terminal-deoxynucleotidyl-transferase dUTP Nick End Labelling (TUNEL) assay[238] and the number of apoptotic cells per 100 crypts (i.e. apoptotic index) was quantified at the crypt base (cell positions 0 to +4) and above the base within the proliferation zone (+5 to +13).

A borderline significant (P = 0.05 in Wilcoxon rank-sum test, n = 3 per group) increase in the apoptotic index at the crypt base (1.35 ± 0.15 in control and 5.78 ± 0.98 in DSS-treated mice) and above the crypt base (4.42 ± 0.92 in control and 13.76 ± 4.51 for DSS-treated mice) was observed in the small intestine (SB1) and colon of mice treated with 0% and 2.5% DSS via oral gavage (Figure 5.5A). This data agrees with the undiminished number of *Lgr5*$^{+}$ cells in the mouse intestines

following DSS treatment (Figure 5.4A) and the marginally significant increase in apoptosis is most likely occurring in *Lgr5*$^{-}$ cells. However, in NMRs where *Lgr5*

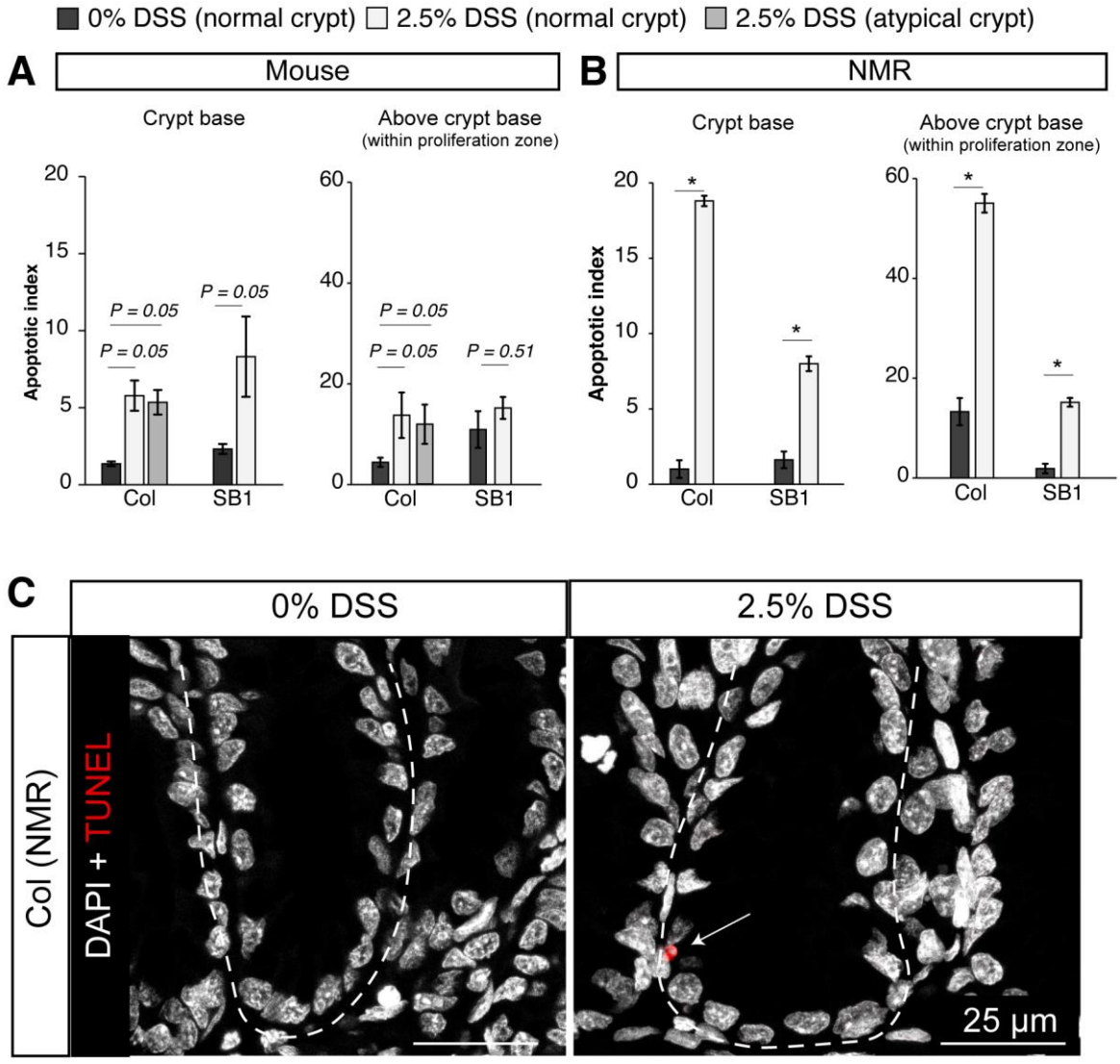

Figure 5. 5: Apoptosis in mouse and NMR intestines after DSS treatment via oral gavage. **(A-B)** Bar graphs showing the number of TUNEL^{+} cells per 100 crypts (apoptotic index) at the crypt base (left) and above crypt base within the proliferation zone (right) in the distal colon and small intestine of 0% and 2.5% DSS-treated **(A)** mice and **(B)** NMRs (n=3 animals per group, *P*-values from two-tailed Wilcoxon rank-sum test are indicated on the graphs. Significant *P*-value was denoted as *<0.05.) **(C)** Confocal images showing staining for DNA degradation using TUNEL-kit (red) and DAPI (grey) in the distal colonic crypts of 0% and 2.5% DSS-treated NMRs. White arrows indicate TUNEL^{+} cells. Scale bars are indicated on the images (25 µm).

expression is either lost (in the colon) or greatly reduced (in the SB1) by exposure to DSS (Figure 5.4B), a significantly higher apoptotic index (*P* = 0.03 in Wilcoxon rank-sum test, n = 3 per group) was detected both at the crypt base (1.01 ± 0.57 in

control and 19.07 ± 0.33 in DSS-treated NMRs) and above the crypt base (13.29 ± 2.73 in control and 53.70 ± 1.73 in DSS-treated NMRs) in the small intestine (SB1) and colon of NMRs dosed with DSS compared to the controls (Figure 5.5 B-C). In brief, DSS administration via oral gavage for 3 days results in an 18-times significantly higher apoptotic index detected by TUNEL assay in NMR colonic crypt-base while only a borderline significant increase in apoptotic index is observed in the mouse colon.

5.2.4 Proliferation status of DSS-treated mouse and naked mole rat intestines

To assess the impact of DSS administration on the overall proliferation status of the intestinal crypts, DSS-treated mouse and NMR intestinal tissues were stained with proliferation marker Ki67 and the proliferation index (percentage of all epithelial cells in a crypt that are $Ki67^{+}$) was quantified. The analysis was first focused on the colonic stem (*Lgr5*$^{+CBC}$) cells and no significant change (*P*-value = 0.85, t-test) was found in their proliferation index in both normal (41.55% ± 4.39) and atypical crypts (43.77% ± 5.59) of mice treated with 2.5% DSS (via oral gavage for 3 days) compared to the controls (42.62% ± 3.28) (Figure 5.6A). Similarly in the small intestinal (SB1) crypts, no significant difference (*P*-value = 0.12, t-test) was observed in the proliferation index of *Lgr5*$^{+CBC}$ cells between mice treated with 0% (80.30% ± 2.41) and 2.5% DSS (85.66% ± 2.41) (Figure 5.6A). In NMRs, the *Lgr5*$^{+CBC}$ cells that survived in the small intestine following 2.5% DSS treatment (via oral gavage for 3 days) also exhibited a similar (*P*-value = 0.32, t-test) proliferation index (47.56% ± 6.81) as the control animals (55.82% ± 4.50) (Figure 5.6B).

The analysis was further extended to the proliferation of all crypt cells regardless of their *Lgr5*-expression status to assess any difference in the progenitor cell population. DSS treatment via oral gavage in mice resulted in a 24% reduction of the proliferation index in the colonic crypts (from 31.97% ± 1.74 to 24.30% ± 1.23) and a 13% reduction in the small intestinal (SB1) crypts (from 67.85% ± 1.28 to 59.29% ± 1.03) compared to the controls (Figure 5.6C). However, in NMRs, similar treatment with DSS caused an 88% reduction in the proliferation index of colonic crypts (from 12.97% ± 1.79 to 1.58% ± 0.40) and 62% reduction in the small intestinal (SB1) crypts (from 35.83% ± 1.72 to 13.79% ± 3.32) compared to the controls (Figure 5.6D).

In summary, 2.5% DSS administration via oral gavage for 3 days instigates a modest (13 to 24%) loss of proliferation in mouse intestinal crypts while a drastic decrease (62 to 88%) in cell proliferation was observed in the NMR intestinal crypts. The loss of proliferation is observed in the progenitor (*Lgr5*$^{-}$) cells, not in the stem (*Lgr5*$^{+CBC}$) cells, in both species. However, there is a greater degree of decrease in proliferation index in NMR intestines following DSS treatment than in mouse intestines.

Table 5.1 summarises the changes observed in the intestinal crypts following DSS-treatment in mice and NMRs (section 5.2.2 to 5.2.4).

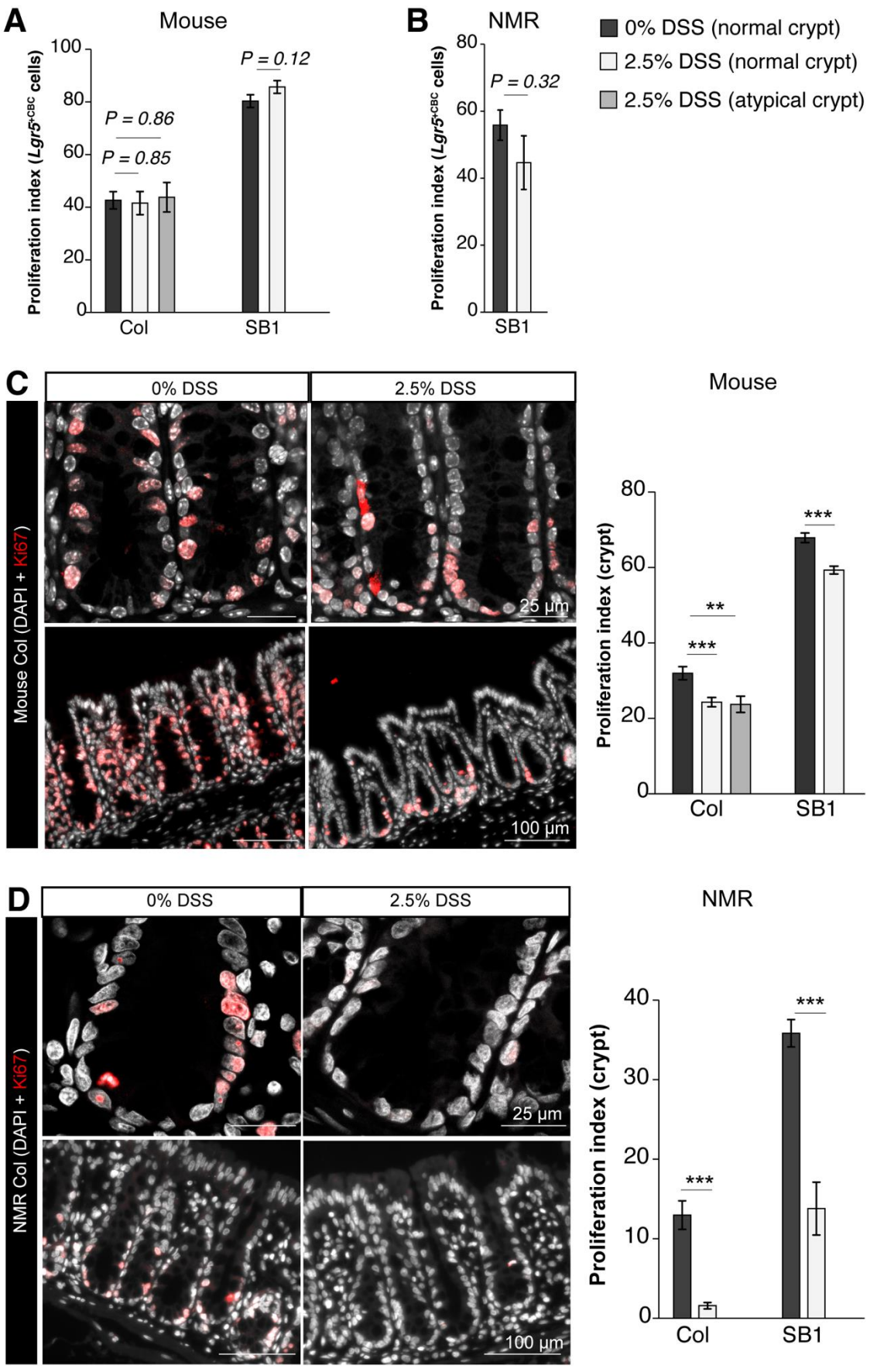
A
Mouse
Proliferation index (Lgr5+CBC cells)
P = 0.86
P = 0.85
P = 0.12
Col
SB1
B
NMR
P = 0.32
SB1
0% DSS (normal crypt)
2.5% DSS (normal crypt)
2.5% DSS (atypical crypt)
C
0% DSS
2.5% DSS
Mouse Col (DAPI + Ki67)
25 µm
100 µm
Mouse
Proliferation index (crypt)
**
***
***
Col
SB1
D
0% DSS
2.5% DSS
NMR Col (DAPI + Ki67)
25 µm
100 µm
NMR
Proliferation index (crypt)
***
***
Col
SB1

Figure 5. 6: Alteration of proliferation index in mouse and NMR intestines after DSS treatment via oral gavage.
(A-B) Bar graphs showing proliferation index (percentage of *Lgr5*$^{+CBC}$ cells that are Ki67^{+}) following 0% and 2.5% DSS treatment via oral gavage for 3 days in **(A)** mice and **(B)** NMRs (n=40 crypts from 3 animals per group). **(C)** Photomicrographs (left) showing staining for proliferation marker, Ki67 (red) and DAPI (grey) in the distal colonic crypts of 0% and 2.5% DSS-treated mice at high magnification (top panel) and low magnification (bottom panel). Bar graphs (right) showing changes in the crypt proliferation index (Ki67^{+} cells/total cells per crypt) between the control and 2.5% DSS-treated mouse crypts from colon and SB1 (n=40 crypts from 3 animals were analysed per group). (D) Confocal images (left) showing distal colonic crypts form NMRs treated with 0% and 2.5% DSS stained with anti-Ki67 antibody (red) and DAPI (grey) at high magnification (top panel) and low magnification (bottom panel). Bar graphs (right) displaying significant differences in the overall proliferation index in the small intestinal (SB1) and colonic crypts from control and 2.5% DSS-treated NMRs (n=40 crypts from 3 animals were analysed per group). Each bar represents the mean ± standard error of the mean. In all cases, statistical significances were determined by a two-tailed, unpaired t-test with unequal variances. Significant *P*-values were denoted as **≤ 0.01, ***<0.001. Scale bars are indicated on the images (25 µm, 100 µm).

Table 5. 1: Summary of changes observed in the small intestine (SB1) and colon (Col) following 2.5% DSS treatment in NMRs and mice.

Parameter of comparison	**NMR 2.5% DSS for 3 days via oral gavage) compared to controls**		**Mouse (2.5% DSS for 3 days via oral gavage) compared to controls**	
	Col	**SB1**	**Col**	**SB1**
Number of *Lgr5*$^{+CBC}$ cells/crypt	100% loss*	86% loss*	No significant change	No significant change
Apoptotic index (Number of TUNEL+ cells/ 100 crypt) at crypt base	18-times increase*	5-times increase*	Borderline significant increase	Borderline significant increase
Apoptotic index (Number of TUNEL+ cells/ 100 crypt) above crypt base	3-times increase*	8-times increase*	Borderline significant increase	No significant change
Proliferation index of *Lgr5*$^{+CBC}$ cells	----	No significant change	No significant change	No significant change
Proliferation index of crypt	88% decrease*	62% decrease*	24% decrease*	13% decrease*

*statistically significant change (*P*-values < 0.05)

5.2.5 Restoration of *Lgr5* expression upon DSS withdrawal in naked mole rat intestines

Researchers have reported the ability of mouse intestinal crypt to restore its lost *Lgr5*$^{+}$ cell population following damage from either a reserve pool of (Bmi1^{+}) stem cells[150] or the plasticity of several differentiated cell populations[239-241]. To assess similar properties of *Lgr5*$^{+}$ cells in NMR intestines, animals were dosed with 2.5% DSS for 3 days via oral gavage and intestinal tissues were collected at regular intervals after stopping the treatment (Figure 5.7A). Staining of the intestinal tissues with an *Lgr5* probe revealed the re-emergence of *Lgr5*$^{+}$ cells in the small intestine and distal colon (Figure 5.7B).

Quantification of *Lgr5*$^{+}$ cell number at crypt-base showed that small intestinal *Lgr5*$^{+CBC}$ cells restored their population to homeostatic level (8.67 cells ± 0.93 per crypt) within 3 days after DSS withdrawal (7.89 cells ± 0.52 per crypt) while the colonic *Lgr5*$^{+}$ cell population is restored (4.17 cells ± 0.58 per crypt) by day 5 of recovery (Figure 5.7C). These durations of recovery are consistent with the relatively slower cycling status of *Lgr5*$^{+}$ cells in the NMR colon compared to the small intestine.

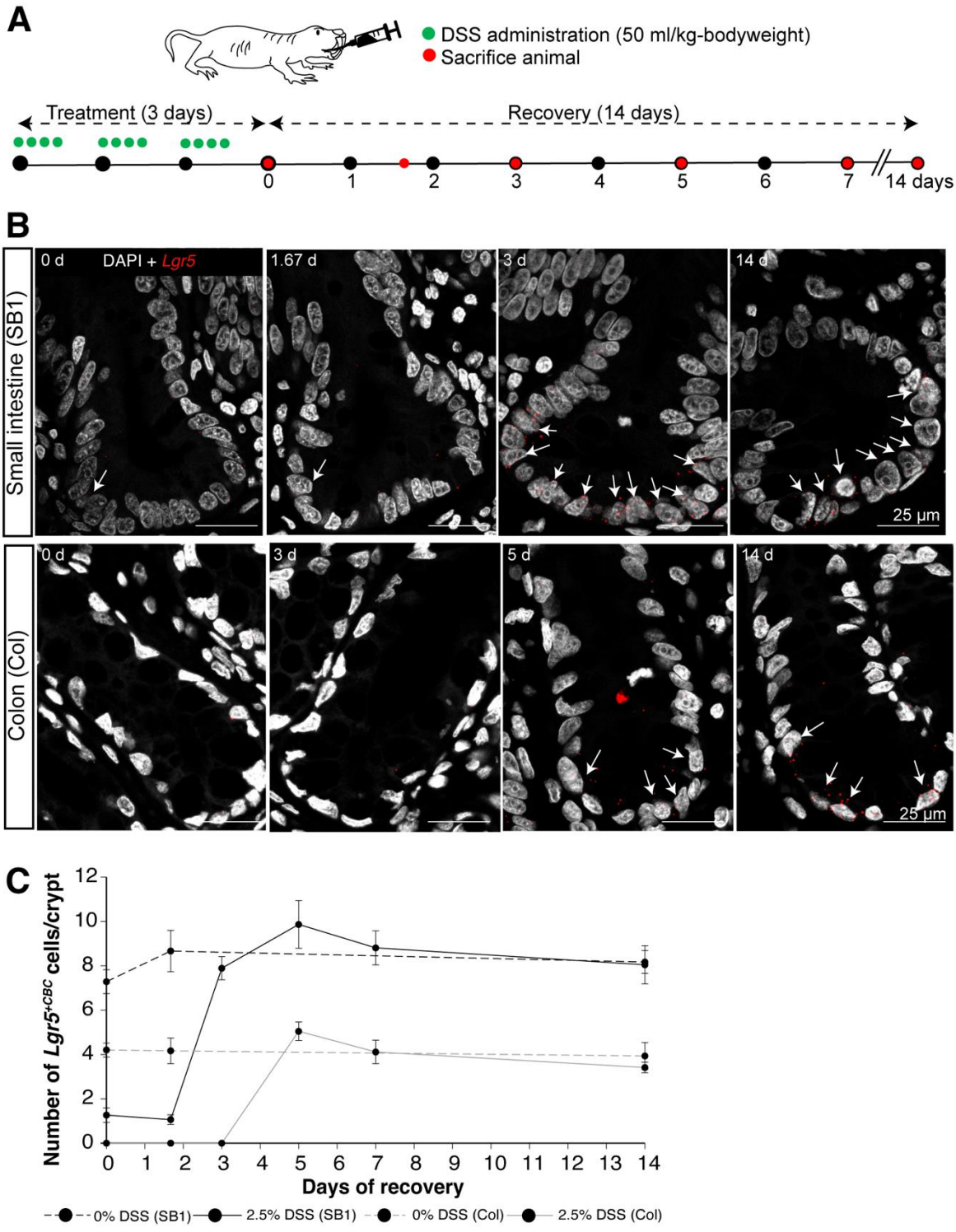

Figure 5. 7: Re-emergence of *Lgr5*$^{+CBC}$ cells in the NMR intestines following DSS withdrawal. **(A)** Schema showing the period of recovery in NMRs after 2.5% DSS treatment (green) and time points when animals were sacrificed (red). **(B)** Confocal images showing staining with NMR-specific RNAscope *Lgr5* probe (red) and DAPI (grey) exhibiting the re-expression of *Lgr5* in cells at the crypt base (marked with white arrows) after day 3 of recovery in the small intestine (SB1, top) and day 5 of recovery in the colon (bottom). Scale bars are indicated on the images (25 µm) **(C)** Line graph showing the re-emergence of *Lgr5*$^{+CBC}$ cells in both the small intestinal (SB1, black) and colonic (Col, grey) crypts of NMRs during the recovery phase (n=20 crypts from 1 animal at each time-point). Each dot represents the mean ± standard error of the mean.

5.3 Discussion

The first challenge in performing a wound-healing experiment using DSS in NMRs was establishing its effective mode of administration. At the beginning of this chapter, it was demonstrated that 2.5% DSS treatment via oral gavage in mice for 3 days resulted in mild epithelial injury in the colon that resembles a chronic colitis model described previously[236]. On the other hand, administration of 2.5% DSS in drinking water for 7 days in mice resulted in severe colonic damage as reported in the literature[19,22-24]. This result shows that administering 2.5% DSS via oral gavage for only 3 days is effective to create a mild injury model. As naked mole rats do not drink water[233], oral gavage (4 times a day for 3 days) was selected as an alternative method to administer DSS in NMRs.

Having higher resistance to damage is an effective way to maintain tissue homeostasis during a species' lifetime as this reduces the demand for stem cell division in a damage prone environment. A higher percentages of goblet cells in NMR intestines has been reported in section 3.2.2.1. This expanded proportion of goblet cells secrete a thicker mucus layer in the colon compared to mice (section 3.2.2.1) which can exert protection against chemical and microbial damage[112]. A previous study in mice has also demonstrated that enhancing the expression of goblet cells using dibenzazepine (DBZ) can ameliorate the manifestation of acute colitis following DSS treatment[242]. In line with these observations, administration of 2.5-8.75% DSS via oral gavage failed to induce any visible histological feature of damage in the colonic epithelia of NMRs. The thicker mucus layer secreted by an increased percentage of goblet cells may have protected NMRs from developing the mild epithelial damage observed in mice following DSS treatment. Such

response agrees with a previous report showing that NMRs are resistant to oxidative damage in DNA, RNA, and protein during acute and chronic hypoxia across multiple organs (heart, brain, kidney, liver, and muscle)[243]. Additionally, NMR cartilage is significantly stiffer than mice due to the accumulation of high-molecular-weight hyaluronan resulting in resistance to post-traumatic osteoarthritis[244]. Fibroblasts in NMRs have been shown to exhibit 2 to 20 folds higher resistance to cytotoxins, heat, heavy metals, genotoxic, and xenobiotic agents than mice[245]. Therefore, the data presented in this chapter, along with previous studies, indicate that naked mole rats exhibit a higher resistance to damage than short-lived mice.

Another key strategy for maintaining disease-free tissue is to halt proliferation and induce apoptosis in damage-prone environment. Despite exhibiting no obvious signs of epithelial injury, a drastic (80%) reduction in *Lgr5* expression was observed in the NMR small intestine (SB1) and colon following DSS administration. TUNEL staining showed an 18-times higher apoptotic index at the base of crypts in NMR colon following DSS treatment compared to the controls. A similar treatment in mice did not alter the number of intestinal *Lgr5*$^{+}$ cells. Therefore, NMR *Lgr5*$^{+}$ cells are more sensitive to DSS treatment than murine *Lgr5*$^{+}$ cells. Moreover, most of the progenitor cells in DSS-treated NMR crypts stopped proliferating, unlike those in mice. These findings showed that NMR intestinal crypts responded to the low concentration of DSS more drastically than mice. This observation agrees with a previous study demonstrating that NMR fibroblasts also halt proliferation in the presence of minute levels of toxins whereas mouse fibroblasts continue proliferation in a damage-prone environment[245]. Therefore, a robust anti-proliferative and pro-

apoptotic response to damage inducing agents in NMRs may also contribute to their healthy tissue maintenance.

Finally, upon withdrawal of DSS, the NMR intestine returns to homeostasis, with the re-emergence of *Lgr5*$^{+}$ cells at crypt base within 3-5 days. In mice, quiescent Bmi1^{+} cells residing at the +4 position of the intestinal crypts can regenerate the Lgr5^{+} cell population following damage[150]. Moreover, dedifferentiation of goblet, Paneth, enteroendocrine cells, and enterocytes can also repopulate the lost Lgr5^{+} cells in mouse intestines[239-241]. The rapid regeneration (3-5 days) of *Lgr5*$^{+}$ cells in NMR intestines upon DSS withdrawal suggests the existence of reserve stem cells and/or dedifferentiation pathways of differentiated cell populations in this species.

The major limitation of this chapter is the short duration of DSS administration via oral gavage that was followed to minimise stress in the animals. In future, a longer administration strategy (7 days) of DSS via oral gavage or mixed with semi-solid food (porridge) should be tried to further assess the resistance of NMR intestines to damage. Besides, further characterisation of reserve stem cell population (e.g. Bmi1^{+}) and dedifferentiation pathways should be conducted in NMR intestines to elucidate whether their response to damage and injuries contributes to their long-term tissue maintenance.

5.3.1 Conclusion

In this chapter, I have demonstrated that DSS administration via oral gavage can cause mild epithelial injury in the mouse colon. This strategy can deliver DSS effectively to the NMR colon. I also found that NMR intestines are more resistant to

DSS-induced damage than mice, probably due to their thicker mucus layer secreted by a higher proportion of goblet cells found in NMRs. Without developing DSS-mediated injuries in the colon, *Lgr5*$^{+}$ cells in NMR small intestine (SB1) and colon undergo rapid apoptosis and most progenitor cells halt proliferation. This pro-apoptotic and anti-proliferative response by the crypt cells in NMR intestines in the presence of DSS, in addition to the higher resistance of the colonic tissue to DSS mediated damage, most likely contribute to tissue maintenance in NMRs upon injury. Finally, DSS withdrawal in NMR intestines has revealed the possibility of reserve stem cell population and/or plasticity of differentiated cells that can restore the homeostatic level of the stem (Lgr5^{+}) cell population.

Chapter 6: Discussion

6.1 General discussion

Naked mole rats (NMRs) are the longest-living rodents on earth[2,24]. These eusocial mammals live in the under burrows of north-east Africa amid the scarcity of food, water, and oxygen[2]. Phylogenetic analyses based on genome sequence[5] and distribution of hippocampal cell population[7] have revealed a close kinship of NMRs to mice, humans, rats, monkeys, and other African mole rats. NMRs live in colonies dominated by a queen who performs all the reproductive activities with 1-3 large male individuals (breeders) while the rest of the colony members (subordinates) carry out digging and foraging for food, rearing pups, and fighting against predators[8,11]. The sexual maturation of subordinate NMRs is socially suppressed by the aggressive behaviour of the queen[14] that result in the production of RFRP-3, a negative regulator of gonadotropin-releasing hormone, responsible for delaying puberty[23]. The breeders maintain an undiminished fecundity throughout their lifespan[24]. This is thought to be possible due to the persistence of proliferation in primordial germ cells (PGCs) in female NMRs at least up to 90 days after birth resulting in a large ovarian reserve[28], unlike humans and mice where ovarian reserve is established before[246,247].

NMRs exhibit negligible senescence (i.e., no ageing-related changes in fertility[24], basal metabolic rate[30], bone mineral density[30], oxidative damage[248], and glucose tolerance[249]) and very low incidences of ageing-associated diseases (e.g. cancer, cardiovascular, and neurodegenerative diseases)[10,36,245,250,251], making them an ideal model to study mechanisms of healthy ageing. Previous studies have already identified important molecular features that could potentially be associated with NMR's longevity. For example, skin fibroblasts in NMRs express a High Molecular

Mass Hyaluronic Acid (HMM-HA) which is 3-11 MDa larger than that found in mice and humans[36]. This HMM-HA in NMRs is capable of activating $p16^{INK4a}$-mediated early contact inhibition and thus prevents tumour growth[36]. Transgenic mice expressing the NMR version of *Has2*, the gene responsible for the production of HMM-HA, exhibit a 12% extended maximum lifespan, no age-related loss of mucus-secreting goblet cells in the intestine, and preservation of the regenerative capacity of $Lgr5^{+}$ intestinal stem cells (ISCs) even at older ages[252]. Mutations in *Tp53* and *Rb1* tumour suppression genes result in the apoptosis of skin fibroblasts in NMRs[35] where similar genetic aberrations lead to a rapid cellular proliferation in mice and humans[38]. Following UV exposure, NMR skin fibroblasts exhibit a 1.5 to 3-fold higher efficiency in base excision and nucleotide excision repair compared to mice[41]. Unlike mouse and rat blood cells[46], telomere length in NMRs remains unchanged during ageing probably due to their stable expression of TERT enzyme[50] and two gain-of-function mutations in the *TRF1* sequence[52].

Protein homeostasis (i.e., proteostasis) is maintained by efficient translation, accurate folding, and controlled degradation of proteins inside a cell. The loss of proteostasis, a key hallmark of ageing[25], can result in ageing-associated conditions like Alzheimer's disease, Parkinson's disease, and cataracts[253]. Interestingly, the expression levels of genes involved in protein degradation increase linearly with the lifespan of a species[58]. The rate of protein degradation also slows down as species live longer[59]. Even the rate of RNA polymerase II enzyme is slower in long-lived species when compared to the short-lived ones[60]. Therefore, it appears that adaptation for a long lifespan helps a species maintain superior proteostasis throughout its life by slowing down protein synthesis and degradation. Additionally,

NMRs exhibit a much higher translational fidelity than mice[61]. There are also reports of elevated levels of autophagy, better heat-shock protein response, and 20S proteasome activity in NMR skin fibroblasts than mice[62]. Under protein denaturing conditions (exposure to Urea, L-AZC), NMRs can better prevent misfolding of proteins than mice[59,64]. These studies indicate that specific molecular adaptations for longevity resulted in robust proteostasis in NMRs.

Ageing is associated with the functional decline of adult stem cells resulting in a poor regeneration of tissue after injury[25,254,255]. However, the mechanisms by which long-lived species avoid stem cell exhaustion has remained largely unexplained. A recent study on the human colon has shown the existence of a stem cell population that is slower cycling than mice[94]. Hematopoietic stem and progenitor cells in NMRs cycle at a slower rate than mice and exhibit a lower metabolic rate[65]. Similarly, adult stem cells in the NMR brain have also been demonstrated to be slower cycling than in mice while exhibiting an undiminished regenerative potential[67]. Therefore, it appears that NMRs have slower cycling ASCs across tissues studied so far. The work presented in this thesis has focused on characterising the intestinal stem cells of NMRs in a cross-species comparison with mice and humans to identify features and strategies that may be linked to NMR's longevity.

The intestine provides a relatively easy tissue to study in animal models. Therefore, we focused on the small intestine (SB1) and colon of NMRs to assess the composition, cell turnover, and phenotypes of adult stem cells. In section 3.2.2, we have characterised the macro and microscopic features of the NMR intestine. Our analyses show that NMRs have 55% shorter small intestine and 31% shorter colon

than mice. This observation is similar to the adaptations described in other xerocoles (gerbils and sand rats)[166] and birds (hummingbirds, sparrows, robins)[167] which are thought to reduce body mass and energy demand. To compensate the limitations of having a shorter intestine, xerocoles have a higher electrolyte absorption ability[166] while birds have an enhanced paracellular signalling aiding in efficient glucose and amino acid absorption[167]. In NMRs, we show that the shorter intestinal tract is accompanied by 79% longer villi that increase the total surface area of the intestine. This accommodates a 40% higher number of differentiated epithelial cells which support efficient nutrient absorption from the lumen. More specifically, an undiminished presence of enterocytes in the NMR villi is seen throughout the small intestine, including in the distal region, while mouse small intestinal villi show a gradual decrease in the percentage of this cell type from the proximal to the distal end. The higher percentages of these absorptive cells in the NMR small intestinal tract are likely to increase nutrient uptake via microvilli present in the brush border[99-101].

We also observed a higher proportions of other differentiated cell types in the NMR intestines. NMRs have 3-times higher enteroendocrine (hormone-secreting) cells in the small and large intestines than mice (section 3.2.2.2). These cells secrete chromogranin A, synaptophysin, cholecystokinin, somatostatin, and serotonin[119-122] which help the intestine in assessing the presence of food, secretion of digestive enzymes, and absorption[123].

Similarly, we found 67% higher percentage of goblet cells in the NMR small intestine compared to mice (section 3.2.2.1). In NMR colons, we detected a 1.65-times

thicker mucus layer than mice. Goblet cells secrete gel-forming mucins (Muc2, Muc5AC, Muc6 and Muc5B[256]) to lubricate the passage of food. Another role of mucins is to exert protection against microbial damage in the intestines by forming a mucus layer[112,190]. Pharmacological intervention (using Dibenzazepine) resulting in a thicker mucus layer in mice can prevent colitis formation by chemicals like Dextran Sodium Sulphate (DSS)[242] which is widely used to induce epithelial injury in rodent models[83,226-228,231,232]. When we attempted to induce damage in NMR intestines by administering DSS (section 5.2.1.3), NMRs resisted epithelial injury even after the administration of 2.5-8.75% DSS while mice formed a mild degree of colitis only at 2.5% DSS administration by oral gavage for 3 days. It is possible that the thicker mucus layer created by a higher percentage of goblet cells appears to result in higher resistance to DSS-induced damage in NMR intestines compared to mice. Previous studies have also reported that NMR cells (chondrocytes, fibroblasts) and tissues (brain, heart) are more resistant to oxidative stress[243], osteoarthritis[244], cytotoxins[245], heat[245], heavy metals[245], and xenobiotics[245] than mice. Therefore, it appears that survival in a damage-prone hypoxic environment has resulted in adaptations in NMRs, such as having increased goblet cells, resulting in a higher resistance to damage-inducing agents in these animals.

After characterizing the differentiated cell populations in NMR intestines, we focused on the intestinal stem cells responsible for the continuous production of these cells. Lgr5 expression has been used as a marker to identify stem cells across species (mice, humans)[83,181] and organs (small intestine, colon, liver, kidney, hair follicle)[182-185]. By using NMR-specific *in situ* hybridisation probe to detect *Lgr5* mRNA in section 3.2.3, we reported that colonic crypts in NMRs contain nearly 50%

higher percentage of *Lgr5*$^{+}$ cells than mice and humans while small intestinal crypts in NMRs contain a 150% higher proportion of *Lgr5*$^{+}$ cells than mice. The majority (76-87% in the small intestine and 62-80% in the colon) of these cells are located at the crypt base (0 to +4) while the rest reside between +5 and +10 cell positions in all three species. Our data showing the percentage and localisation of *Lgr5*$^{+}$ cells in mouse and human intestines are similar to previous reports[83,94,186,257]. The higher number of *Lgr5*$^{+}$ cells accommodated by the wider crypt structure in NMRs is likely required to fuel the higher numbers of differentiated cells over a longer lifespan. This possibly has a secondary consequence of limiting mutations accumulating in the intestinal crypts as any mutated intestinal stem cell (ISC) would have to compete with a higher number of basal ISCs to become the dominant clone in the crypt that would result in crypt monoclonality[132]. However, this also raises the question whether NMR poses a higher chance of cancer initiation due to having a large number of stem cells. Interestingly, an expanded pool of ISCs is not the only protective mechanism observed in NMR intestines. The data presented in Chapter-4 has shown that NMR ISCs cycle 2-times slower than mice while spending 3-times longer duration in G1/G2 phases (G1/S and G2/M checkpoints) that can contribute to genomic integrity and thus lower the chance of mutation accumulation. Therefore, the large pool of stem cells combined with slowly cycling ISCs will most likely lower than chance of cancer initiation in NMRs compared to mice.

In mice, *Lgr5*$^{+CBC}$ cells have been shown to turnover approximately every 24 hours in the small intestine[93,145,146] while no such analysis has been done in the mouse colon. In humans, orthotopic xenotransplantation of *LGR5-EGFP* knock-in colon organoids has shown the *in vivo* cell division time of colonic LGR5^{+CBC} cells to be

7.3 days[94]. In our study, we aimed to determine the turnover rate of NMR ISCs and compare it to mice or humans. We first determined the proportion of $Lgr5^{+}$ cells that were proliferating using Ki67 as a marker (section 4.2.1). We found that NMR *Lgr5*$^{+CBC}$ cells were less proliferative than mice in the small intestine. Our proliferation index for mouse small intestine showed that the majority (82%) of *Lgr5*$^{+CBC}$ cells were positive for Ki67-expression, a value similar to that reported previously[202]. In the colon, NMR *Lgr5*$^{+CBC}$ cells have a similar proliferation index (47%) to mice which is 6-times higher than humans (7%). However, assessing Ki67 status only provides a snapshot of the proliferation status of a cell population. To accurately determine the cell division rate of ISCs *in vivo*, we injected NMRs with BrdU, a nucleoside analogue that incorporates into the DNA during replication, to calculate the length of cell cycle in NMR *Lgr5*$^{+CBC}$ cells.

The first challenge in estimating the cell division time of ISCs in NMRs was to establish an injection regimen that would ensure the BrdU bioavailability for a duration long enough to label majority of the target cells[163]. We first determined the BrdU dose (100 mg/kg body mass) that would achieve a labelling saturation in the intestine (section 4.2.3.1). Then we established that injecting BrdU in NMRs every 8 hours achieved a similar labelling index as injecting every hour. This indicates that the BrdU clearance time in NMRs is longer than 8 hours. We then assessed the BrdU concentration in NMR plasma and reported that BrdU is cleared from NMR blood between 8 hours and 16 hours after one injection. This is significantly slower than the BrdU clearance time in mice (1 hour)[156] probably due to a 75% slower basal metabolic rate in NMRs[207]. Finally, we used a second thymidine analogue, EdU, to demonstrate that 15 repeated BrdU injections in NMRs do not affect the EdU

labelling index. This indicates that the administration of nucleoside analogue (BrdU) itself does not alter the cell kinetics in NMRs. A similar result has been previously reported for multiple 5-chloro-2'-deoxyuridine (CldU) injections in mice[145]. Finally, we injected NMRs with BrdU every 8 hours for 5 days which allowed all/majority of the proliferating ISCs to enter S-phase and no ISCs could go through S-phase without acquiring the label.

Having established the BrdU labelling protocol in NMRs, we found that NMR *Lgr5*$^{+CBC}$ cell numbers double every 4.43 days in the small intestine which is roughly 2-times longer than the turnover time in mice (1.56 days). While colonic *Lgr5*$^{+CBC}$ cells cycle more slowly than small intestinal ones in both rodent species, it takes 7.20 days in the NMR colon, which is nearly 2-times slower than mice (2.21 days in the colon), but similar to humans (7.30 days in the colon[94]). This study is the first to report the total cell division time of *Lgr5*$^{+CBC}$ cells in the NMR small intestine (SB1) and colon, and mouse colon.

We further extended our analysis to the *Lgr5*$^{+}$ cells residing above the crypt base and found these to be faster cycling than the *Lgr5*$^{+CBC}$ cells in both NMRs and mice (section 4.2.6). This agrees with previous studies in mice[93] and humans[94]. Ishikawa *et al.* have reported *Lgr5*$^{+}$ cells outside the crypt base as transit-amplifying cells in the human colon[94]. Another study has also reported Ki67^{+} progenitor cells residing above the crypt base in mouse small intestines to be faster cycling than the *Lgr5*$^{+CBC}$ cells[93]. Therefore, based on cellular kinetics, it appears that *Lgr5*$^{+}$ cells above the crypt base represent a population of faster-cycling cells in all three species. Overall, NMR *Lgr5*$^{+}$ cells cycle more slowly than mice regardless of their position in the crypt.

This observation supports the previous reports of NMRs having slower cycling stem and progenitor cells in the bone marrow[65] and brain[67] compared to mice, which is thought to contribute to genomic maintenance in NMRs by allowing efficient repair of DNA lesions during the long lifespan of this species.

After estimating the turnover rate of NMR *Lgr5*$^{+CBC}$ cells, we then carried out a detailed analysis of the length of specific cell cycle phases in the ISCs of mice, humans, and NMRs. The durations of the S and M phases were similar in all three species. The difference in cell division time between the three species came from the length of the gap phases (G0, G1, G2) of the cell cycle. ISCs in NMRs spend approximately 3-times longer duration (3.90 ± 0.27 days in SB1, 6.66 ± 0.81 days in colon) in G1 and G2 phases than mice (1.09 ± 0.10 days in SB1, 1.74 ± 0.18 days in colon) (section 4.2.6). This gives them time to make proliferation decisions (G1/S checkpoint)[147] and potentially amend errors after DNA replication (S/G2 checkpoint)[258-260] and, in turn, contribute to maintaining genomic integrity in NMRs. We also showed that human ISCs spend 70% of their time in G0 while NMRs spend 93% time in G1 and/or G2 phases. Therefore, it appears that long-lived NMRs and humans have slower-cycling intestinal stem cells which may explain the lower mutation rates observed in NMR and human colonic crypts compared to fast-cycling mice[26].

Finally, another feature of NMR ISCs and progenitors that is distinct from mice is their response to damage-inducing stimuli. Despite no overt sign of epithelial damage, we showed that ISCs in NMRs exhibited hypersensitivity to DSS treatment that resulted in the loss of *Lgr5*-expressing cells in the intestinal crypts while no loss

of *Lgr5*$^{+}$ cells was observed in mice. In a previous study, NMR fibroblasts have also been shown to halt proliferation in the presence of minute levels of genotoxic heavy metal (chromium) while mice continue to proliferate even with DNA damage[245]. In our study, while mouse intestinal cells retain most of their proliferation status during DSS treatment, NMRs halt proliferation and induce apoptosis in *Lgr5*$^{+}$ cells presumably due to increased detection of stress in these cells. This also prevents any accumulation of damage in these critical cells in NMRs that give rise to all the progenies in the intestine.

The slower cycling and hypersensitive stem cells also raise the question of whether NMRs, following *Lgr5*$^{+}$ cell loss via apoptosis, can replenish the lost ISCs once the damage-inducing chemical has been removed. To test this, we allowed 14 days of recovery after DSS treatment and showed that NMRs can restore homeostatic balance after the withdrawal of DSS despite having slower cycling ISCs. NMR intestinal crypts replenish their *Lgr5*$^{+}$ cell population within 3-5 days of DSS withdrawal (section 5.2.5). This indicates the presence of a protected reserve stem cell population in NMRs, similar to Bmi1^{+} cells in mice that repopulate the ISCs at the crypt base after damage induced by diphtheria toxin[150]. Alternately, the de-differentiation of non-stem cells following damage can also be involved in the regeneration of ISCs, similar to the *fallback* phenomena observed in enterocytes, goblet cells, and Dll1^{+} secretory progenitor cells in mice exposed to irradiation or diphtheria toxin[239-241]. Therefore, the slower cycling kinetics of NMR cells does not affect the ability of other reserve cells to repopulate their intestinal crypts.

The key findings presented in this thesis has been summarised in Figure 6.1.

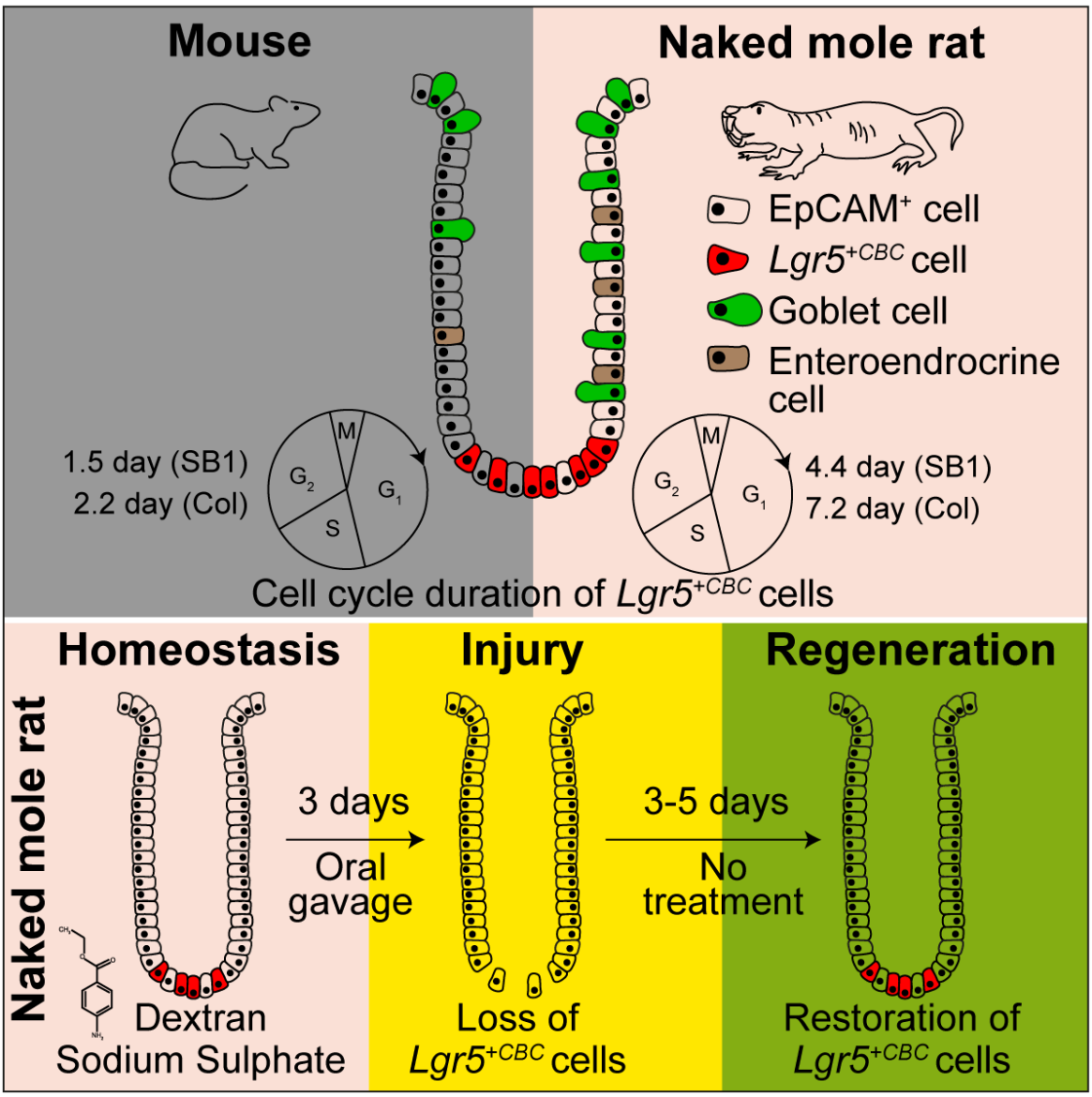

Figure 6. 1: Features of naked mole rat intestine for long-term tissue maintenance.
Top panel, a schema showing higher percentages of *Lgr5*$^{+CBC}$, goblet, and enteroendocrine cells in NMR intestines when compared to mice. *Lgr5*$^{+CBC}$ cells in NMR small intestine (SB1) and colon (Col) cycles at 2-times slower rate than mice. Bottom panel, *Lgr5*$^{+CBC}$ cells in NMR small intestine and colon undergo apoptosis following Dextran Sodium Sulphate (DSS) administration via oral gavage for 3 days. The lost *Lgr5*$^{+CBC}$ cell population is replenished within 3 to 5 days of withdrawal of DSS.

6.2 Conclusion

Our data has shed some interesting insights into the biology of NMRs that provide clues to their longevity and disease-free survival. Our study is the first to characterise the stem and differentiated cell populations of NMR intestinal epithelium and compared them to mice and humans. The increased proportion of differentiated cells (goblet, enterocytes, and enteroendocrine) per crypt-villus unit aid in the efficient absorption of nutrients in NMRs that possess shorter intestinal tract than mice. Moreover, the higher goblet cells and mucin layer thickness in NMR intestines provide protection against damage from DSS as no overt injury is seen in NMRs subjected to very high concentrations of DSS. We show that the NMR intestines also possess a higher percentage of putative (*Lgr5*$^{+}$) stem cells compared to mice and humans which most likely are required for fuelling the higher proportion of differentiated cell types seen in NMRs. Furthermore, having more ISCs suggests NMRs can maintain tissues for longer while also lowering the risk of mutations becoming dominant within the crypts. The slower ISC kinetics in NMRs involving longer gap phases of the cell cycle is another way to ensure genomic integrity. Finally, we have also demonstrated hypersensitivity of NMR ISCs to DSS treatment which ensures that these critical tissue-resident cells are not subject to irreversible damage that can persist in future progeny and can potentially give rise to cancers.

A number of questions remain to be addressed in future studies. While we show that *Lgr5*$^{+}$ cells reside in the intestinal crypts at locations similar to that previously defined in mice and humans, we have not demonstrated the stemness of these cells in NMRs. This can be achieved by generating a genetically modified NMR model where reporter *EGFP* is knocked into the *Lgr5* gene to show lineage tracing[83]. The

other method of showing the stemness of Lgr5^{+} cells is by growing intestinal crypts in a 3D culture (organoids) and then knocking *EGFP* into the *Lgr5* gene[261] to perform *in vitro* lineage tracing. Alternatively, orthotopic xenotransplantation of NMR organoids (knocked in with *EGFP* into the *Lgr5* gene) into immunocompromised mouse[181] can be used to perform *in vivo* lineage tracing. Our lab has already started optimising the culture conditions for growing organoids from the NMR small intestine which would help to assess the stemness of *Lgr5*$^{+}$ cells in this species. Additionally, the sensitivity of NMR *Lgr5*$^{+}$ cells to other damage-causing agents such as 5-FU and low-dose irradiation should be tested. To assess the response to epithelial injuries in the intestine, ethanol enema[228], TNBS[230], and high-dose ionizing radiation[83] can be used to test whether these also show a similar response as that seen with DSS in NMRs. Finally, further characterisation of the Bmi1^{+} cell population needs to be conducted to understand what types of cells act as reserve stem cells in NMR intestines and how these cells differ from those described in mice and humans.

References

1 Buffenstein, R. The naked mole-rat: a new long-living model for human aging research. *J Gerontol A Biol Sci Med Sci* **60**, 1369-1377 (2005). https://doi.org:10.1093/gerona/60.11.1369

2 Buffenstein, R. & Jarvis, J. U. The naked mole rat--a new record for the oldest living rodent. *Sci Aging Knowledge Environ* **2002**, pe7 (2002). https://doi.org:10.1126/sageke.2002.21.pe7

3 Patterson, B. D. & Upham, N. S. A newly recognized family from the Horn of Africa, the Heterocephalidae (Rodentia: Ctenohystrica). *Zoological Journal of the Linnean Society* **172**, 942-963 (2014).

4 Sherman, P. W. & Jarvis, J. U. Extraordinary life spans of naked mole-rats (Heterocephalus glaber). *J Zool* **258**, 307-311 (2002).

5 Kim, E. B. *et al.* Genome sequencing reveals insights into physiology and longevity of the naked mole rat. *Nature* **479**, 223-227 (2011). https://doi.org:10.1038/nature10533

6 Zoo, S. s. N. Vol. 1800 x 1203 (ed 6257901764_3c171e874c_o.jpg) (Flicker, Flicker.com, 2011).

7 van Dijk, R. M., Huang, S. H., Slomianka, L. & Amrein, I. Taxonomic Separation of Hippocampal Networks: Principal Cell Populations and Adult Neurogenesis. *Front Neuroanat* **10**, 22 (2016). https://doi.org:10.3389/fnana.2016.00022

8 Jarvis, J. U., O'Riain, M. J., Bennett, N. C. & Sherman, P. W. Mammalian eusociality: a family affair. *Trends Ecol Evol* **9**, 47-51 (1994). https://doi.org:10.1016/0169-5347(94)90267-4

9 Clarke, F. M. & Faulkes, C. G. Dominance and queen succession in captive colonies of the eusocial naked mole-rat, Heterocephalus glaber. *Proc Biol Sci* **264**, 993-1000 (1997). https://doi.org:10.1098/rspb.1997.0137

10 Ruby, J. G., Smith, M. & Buffenstein, R. Naked Mole-Rat mortality rates defy gompertzian laws by not increasing with age. *Elife* **7** (2018). https://doi.org:10.7554/eLife.31157

11 Jarvis, J. U. Eusociality in a mammal: cooperative breeding in naked mole-rat colonies. *Science* **212**, 571-573 (1981). https://doi.org:10.1126/science.7209555

12 Reeve, H. K., Westneat, D. F., Noon, W. A., Sherman, P. W. & Aquadro, C. F. DNA "fingerprinting" reveals high levels of inbreeding in colonies of the eusocial naked mole-rat. *Proc Natl Acad Sci U S A* **87**, 2496-2500 (1990). https://doi.org:10.1073/pnas.87.7.2496

13 O'Riain, M. J., Jarvis, J. U. & Faulkes, C. G. A dispersive morph in the naked mole-rat. *Nature* **380**, 619-621 (1996). https://doi.org:10.1038/380619a0

14 Bens, M. *et al.* Naked mole-rat transcriptome signatures of socially suppressed sexual maturation and links of reproduction to aging. *BMC Biol* **16**, 77 (2018). https://doi.org:10.1186/s12915-018-0546-z

15 Barker, A. J. *et al.* Cultural transmission of vocal dialect in the naked mole-rat. *Science* **371**, 503-507 (2021). https://doi.org:10.1126/science.abc6588

16 Watarai, A. *et al.* Responses to pup vocalizations in subordinate naked mole-rats are induced by estradiol ingested through coprophagy of queen's feces. *Proc Natl Acad Sci U S A* **115**, 9264-9269 (2018). https://doi.org:10.1073/pnas.1720530115

17 Reeve, H. K. Queen activation of lazy workers in colonies of the eusocial naked mole-rat. *Nature* **358**, 147-149 (1992). https://doi.org:10.1038/358147a0

18 Buffenstein, R., Park, T., Hanes, M. & Artwohl, J. E. Naked Mole Rat. *The Laboratory Rabbit, Guinea Pig, Hamster, and Other Rodents*, 1055-1074 (2012).

19 Bennett, N. C. & Jarvis, J. U. The social structure and reproductive biology of colonies of the mole-rat, Cryptomys damarensis (Rodentia, Bathyergidae). *Journal of Mammalogy* **69**, 293-302 (1988).

20 Roellig, K., Drews, B., Goeritz, F. & Hildebrandt, T. B. The long gestation of the small naked mole-rat (Heterocephalus glaber Ruppell, 1842) studied with ultrasound biomicroscopy and 3D-ultrasonography. *PLoS One* **6**, e17744 (2011). https://doi.org:10.1371/journal.pone.0017744

21 Margulis, S. W., Saltzman, W. & Abbott, D. H. Behavioral and hormonal changes in female naked mole-rats (Heterocephalus glaber) following removal of the breeding female from a colony. *Horm Behav* **29**, 227-247 (1995). https://doi.org:10.1006/hbeh.1995.1017

22 Jarvis, J., Sherman, P. & Alexander, R. The biology of the naked mole-rat. *The biology of the naked mole-rat. Princeton University Press, Princeton*, 467-483 (1991).

23 Faykoo-Martinez, M., Kalinowski, L. M. & Holmes, M. M. Neuroendocrine regulation of pubertal suppression in the naked mole-rat: What we know and what comes next. *Mol Cell Endocrinol* **534**, 111360 (2021). https://doi.org:10.1016/j.mce.2021.111360

24 Buffenstein, R. Negligible senescence in the longest living rodent, the naked mole-rat: insights from a successfully aging species. *J Comp Physiol B* **178**, 439-445 (2008). https://doi.org:10.1007/s00360-007-0237-5

25 Lopez-Otin, C., Blasco, M. A., Partridge, L., Serrano, M. & Kroemer, G. The hallmarks of aging. *Cell* **153**, 1194-1217 (2013). https://doi.org:10.1016/j.cell.2013.05.039

26 Cagan, A. *et al.* Somatic mutation rates scale with lifespan across mammals. *Nature* **604**, 517-524 (2022). https://doi.org:10.1038/s41586-022-04618-z

27 Taylor, K. R., Milone, N. A. & Rodriguez, C. E. Four Cases of Spontaneous Neoplasia in the Naked Mole-Rat (Heterocephalus glaber), A Putative Cancer-Resistant Species. *J Gerontol A Biol Sci Med Sci* **72**, 38-43 (2017). https://doi.org:10.1093/gerona/glw047

28 Brieno-Enriquez, M. A. *et al.* Postnatal oogenesis leads to an exceptionally large ovarian reserve in naked mole-rats. *Nat Commun* **14**, 670 (2023). https://doi.org:10.1038/s41467-023-36284-8

29 Grimes, K. M., Reddy, A. K., Lindsey, M. L. & Buffenstein, R. And the beat goes on: maintained cardiovascular function during aging in the longest-lived rodent, the naked mole-rat. *Am J Physiol Heart Circ Physiol* **307**, H284-291 (2014). https://doi.org:10.1152/ajpheart.00305.2014

30 O'Connor, T. P., Lee, A., Jarvis, J. U. & Buffenstein, R. Prolonged longevity in naked mole-rats: age-related changes in metabolism, body composition and gastrointestinal function. *Comp Biochem Physiol A Mol Integr Physiol* **133**, 835-842 (2002). https://doi.org:10.1016/s1095-6433(02)00198-8

31 Seluanov, A., Gladyshev, V. N., Vijg, J. & Gorbunova, V. Mechanisms of cancer resistance in long-lived mammals. *Nat Rev Cancer* **18**, 433-441 (2018). https://doi.org:10.1038/s41568-018-0004-9

32 Zhang, L. *et al.* Maintenance of genome sequence integrity in long- and short-lived rodent species. *Sci Adv* **7**, eabj3284 (2021). https://doi.org:10.1126/sciadv.abj3284

33 Yamaguchi, S. *et al.* Characterization of an active LINE-1 in the naked mole-rat genome. *Sci Rep* **11**, 5725 (2021). https://doi.org:10.1038/s41598-021-84962-8

34 Tian, X. *et al.* INK4 locus of the tumor-resistant rodent, the naked mole rat, expresses a functional p15/p16 hybrid isoform. *Proc Natl Acad Sci U S A* **112**, 1053-1058 (2015). https://doi.org:10.1073/pnas.1418203112

35 Seluanov, A. *et al.* Hypersensitivity to contact inhibition provides a clue to cancer resistance of naked mole-rat. *Proc Natl Acad Sci U S A* **106**, 19352-19357 (2009). https://doi.org:10.1073/pnas.0905252106

36 Tian, X. *et al.* High-molecular-mass hyaluronan mediates the cancer resistance of the naked mole rat. *Nature* **499**, 346-349 (2013). https://doi.org:10.1038/nature12234

37 Hanahan, D. & Weinberg, R. A. Hallmarks of cancer: the next generation. *Cell* **144**, 646-674 (2011). https://doi.org:10.1016/j.cell.2011.02.013

38 Rangarajan, A., Hong, S. J., Gifford, A. & Weinberg, R. A. Species- and cell type-specific requirements for cellular transformation. *Cancer Cell* **6**, 171-183 (2004). https://doi.org:10.1016/j.ccr.2004.07.009

39 Deuker, M. M. *et al.* Unprovoked Stabilization and Nuclear Accumulation of the Naked Mole-Rat p53 Protein. *Sci Rep* **10**, 6966 (2020). https://doi.org:10.1038/s41598-020-64009-0

40 MacRae, S. L. *et al.* Comparative analysis of genome maintenance genes in naked mole rat, mouse, and human. *Aging Cell* **14**, 288-291 (2015). https://doi.org:10.1111/acel.12314

41 Evdokimov, A. *et al.* Naked mole rat cells display more efficient excision repair than mouse cells. *Aging (Albany NY)* **10**, 1454-1473 (2018). https://doi.org:10.18632/aging.101482

42 Grube, K. & Burkle, A. Poly(ADP-ribose) polymerase activity in mononuclear leukocytes of 13 mammalian species correlates with species-specific life span. *Proc Natl Acad Sci U S A* **89**, 11759-11763 (1992). https://doi.org:10.1073/pnas.89.24.11759

43 Kosova, A. A. *et al.* Poly(ADP-ribosyl)ation and DNA repair synthesis in the extracts of naked mole rat, mouse, and human cells. *Aging (Albany NY)* **11**, 2852-2873 (2019). https://doi.org:10.18632/aging.101959

44 Hadi, F. *et al.* Transformation of naked mole-rat cells. *Nature* **583**, E1-e7 (2020). https://doi.org:10.1038/s41586-020-2410-x

45 Hayflick, L. & Moorhead, P. S. The serial cultivation of human diploid cell strains. *Exp Cell Res* **25**, 585-621 (1961). https://doi.org:10.1016/0014-4827(61)90192-6

46 Adwan Shekhidem, H. *et al.* Telomeres and Longevity: A Cause or an Effect? *Int J Mol Sci* **20** (2019). https://doi.org:10.3390/ijms20133233

47 Harley, C. B., Futcher, A. B. & Greider, C. W. Telomeres shorten during ageing of human fibroblasts. *Nature* **345**, 458-460 (1990). https://doi.org:10.1038/345458a0

48 Rossiello, F., Jurk, D., Passos, J. F. & d'Adda di Fagagna, F. Telomere dysfunction in ageing and age-related diseases. *Nat Cell Biol* **24**, 135-147 (2022). https://doi.org:10.1038/s41556-022-00842-x

49 Sandin, S. & Rhodes, D. Telomerase structure. *Curr Opin Struct Biol* **25**, 104-110 (2014). https://doi.org:10.1016/j.sbi.2014.02.003

50 Leonida, S. R. L., Bennett, N. C., Leitch, A. R. & Faulkes, C. G. Patterns of telomere length with age in African mole-rats: New insights from

quantitative fluorescence in situ hybridisation (qFISH). *PeerJ* **8**, e10498 (2020). https://doi.org:10.7717/peerj.10498

51 Evfratov, S. A. *et al.* Structural Features of the Telomerase RNA Gene in the Naked Mole Rat Heterocephalus glaber. *Acta Naturae* **6**, 41-47 (2014).

52 Augereau, A. *et al.* Naked mole rat TRF1 safeguards glycolytic capacity and telomere replication under low oxygen. *Sci Adv* **7** (2021). https://doi.org:10.1126/sciadv.abe0174

53 Tan, L. *et al.* Naked Mole Rat Cells Have a Stable Epigenome that Resists iPSCáReprogramming. *Stem Cell Reports* **9**, 1721-1734 (2017).

54 Kerepesi, C. *et al.* Epigenetic aging of the demographically non-aging naked mole-rat. *Nat Commun* **13**, 355 (2022). https://doi.org:10.1038/s41467-022-27959-9

55 Lowe, R. *et al.* DNA methylation clocks as a predictor for ageing and age estimation in naked mole-rats, Heterocephalus glaber. *Aging (Albany NY)* **12**, 4394 (2020).

56 Lowe, R. *et al.* Ageing-associated DNA methylation dynamics are a molecular readout of lifespan variation among mammalian species. *Genome Biol* **19**, 22 (2018). https://doi.org:10.1186/s13059-018-1397-1

57 Horvath, S. *et al.* DNA methylation clocks tick in naked mole rats but queens age more slowly than nonbreeders. *Nat Aging* **2**, 46-59 (2022). https://doi.org:10.1038/s43587-021-00152-1

58 Rodriguez, K. A. *et al.* Determinants of rodent longevity in the chaperone-protein degradation network. *Cell Stress Chaperones* **21**, 453-466 (2016). https://doi.org:10.1007/s12192-016-0672-x

59 Swovick, K. *et al.* Interspecies Differences in Proteome Turnover Kinetics Are Correlated With Life Spans and Energetic Demands. *Mol Cell Proteomics* **20**, 100041 (2021). https://doi.org:10.1074/mcp.RA120.002301

60 Debes, C. *et al.* Ageing-associated changes in transcriptional elongation influence longevity. *Nature* (2023). https://doi.org:10.1038/s41586-023-05922-y

61 Azpurua, J. *et al.* Naked mole-rat has increased translational fidelity compared with the mouse, as well as a unique 28S ribosomal RNA cleavage. *Proc Natl Acad Sci U S A* **110**, 17350-17355 (2013). https://doi.org:10.1073/pnas.1313473110

62 Pride, H. *et al.* Long-lived species have improved proteostasis compared to phylogenetically-related shorter-lived species. *Biochemical and biophysical research communications* **457**, 669-675 (2015).

63 Triplett, J. C. *et al.* Age-related changes in the proteostasis network in the brain of the naked mole-rat: Implications promoting healthy longevity.

Biochim Biophys Acta **1852**, 2213-2224 (2015). https://doi.org:10.1016/j.bbadis.2015.08.002

64 Perez, V. I. *et al.* Protein stability and resistance to oxidative stress are determinants of longevity in the longest-living rodent, the naked mole-rat. *Proc Natl Acad Sci U S A* **106**, 3059-3064 (2009). https://doi.org:10.1073/pnas.0809620106

65 Emmrich, S. *et al.* Characterization of naked mole-rat hematopoiesis reveals unique stem and progenitor cell patterns and neotenic traits. *EMBO J* **41**, e109694 (2022). https://doi.org:10.15252/embj.2021109694

66 Shaw, A. C., Joshi, S., Greenwood, H., Panda, A. & Lord, J. M. Aging of the innate immune system. *Curr Opin Immunol* **22**, 507-513 (2010). https://doi.org:10.1016/j.coi.2010.05.003

67 Yamamura, Y. *et al.* Isolation and characterization of neural stem/progenitor cells in the subventricular zone of the naked mole-rat brain. *Inflamm Regen* **41**, 31 (2021). https://doi.org:10.1186/s41232-021-00182-7

68 Savina, A. *et al.* Single-cell transcriptomics reveals age-resistant maintenance of cell identities, stem cell compartments and differentiation trajectories in long-lived naked mole-rats skin. *Aging (Albany NY)* **14**, 3728-3756 (2022). https://doi.org:10.18632/aging.204054

69 Hong, S. & Kim, M. M. IGFBP-3 plays an important role in senescence as an aging marker. *Environ Toxicol Pharmacol* **59**, 138-145 (2018). https://doi.org:10.1016/j.etap.2018.03.014

70 Johnson, S. C., Rabinovitch, P. S. & Kaeberlein, M. mTOR is a key modulator of ageing and age-related disease. *Nature* **493**, 338-345 (2013).

71 Fontana, L., Partridge, L. & Longo, V. D. Extending healthy life span--from yeast to humans. *Science* **328**, 321-326 (2010). https://doi.org:10.1126/science.1172539

72 Al-Attar, R., Childers, C. L., Nguyen, V. C., Pamenter, M. E. & Storey, K. B. Differential protein phosphorylation is responsible for hypoxia-induced regulation of the Akt/mTOR pathway in naked mole rats. *Comparative Biochemistry and Physiology Part A: Molecular & Integrative Physiology* **242**, 110653 (2020).

73 Sahm, A. *et al.* Long-lived rodents reveal signatures of positive selection in genes associated with lifespan. *PLoS Genet* **14**, e1007272 (2018). https://doi.org:10.1371/journal.pgen.1007272

74 Kotze, S. H., Van Der Merwe, E. L., Bennett, N. C. & O'Riain, M. J. The comparative anatomy of the abdominal gastrointestinal tract of six species of African mole-rats (Rodentia, Bathyergidae). *J Morphol* **271**, 50-60 (2010). https://doi.org:10.1002/jmor.10778

75 Yahav, S. & Buffenstein, R. Caecal function provides the energy of fermentation without liberating heat in the poikilothermic mammal, Heterocephalus glaber. *J Comp Physiol B* **162**, 216-218 (1992). https://doi.org:10.1007/BF00357526

76 Buffenstein, R. & Yahav, S. The effect of diet on microfaunal population and function in the caecum of a subterranean naked mole-rat, Heterocephalus glaber. *Br J Nutr* **65**, 249-258 (1991). https://doi.org:10.1079/bjn19910084

77 Cong, W. *et al.* The microbiota in the intestinal and respiratory tracts of naked mole-rats revealed by high-throughput sequencing. *BMC Microbiol* **18**, 89 (2018). https://doi.org:10.1186/s12866-018-1226-4

78 Debebe, T. *et al.* Unraveling the gut microbiome of the long-lived naked mole-rat. *Sci Rep* **7**, 9590 (2017). https://doi.org:10.1038/s41598-017-10287-0

79 Huizinga, J. D. *et al.* The origin of segmentation motor activity in the intestine. *Nat Commun* **5**, 3326 (2014). https://doi.org:10.1038/ncomms4326

80 Gehart, H. & Clevers, H. Tales from the crypt: new insights into intestinal stem cells. *Nat Rev Gastroenterol Hepatol* **16**, 19-34 (2019). https://doi.org:10.1038/s41575-018-0081-y

81 Clevers, H. The intestinal crypt, a prototype stem cell compartment. *Cell* **154**, 274-284 (2013). https://doi.org:10.1016/j.cell.2013.07.004

82 Tullie, L., Jones, B. C., De Coppi, P. & Li, V. S. W. Building gut from scratch - progress and update of intestinal tissue engineering. *Nat Rev Gastroenterol Hepatol* **19**, 417-431 (2022). https://doi.org:10.1038/s41575-022-00586-x

83 Barker, N. *et al.* Identification of stem cells in small intestine and colon by marker gene Lgr5. *Nature* **449**, 1003-1007 (2007). https://doi.org:10.1038/nature06196

84 Powell, D. W., Pinchuk, I. V., Saada, J. I., Chen, X. & Mifflin, R. C. Mesenchymal cells of the intestinal lamina propria. *Annu Rev Physiol* **73**, 213-237 (2011). https://doi.org:10.1146/annurev.physiol.70.113006.100646

85 Meran, L., Baulies, A. & Li, V. S. W. Intestinal Stem Cell Niche: The Extracellular Matrix and Cellular Components. *Stem Cells Int* **2017**, 7970385 (2017). https://doi.org:10.1155/2017/7970385

86 Cifarelli, V. & Eichmann, A. The Intestinal Lymphatic System: Functions and Metabolic Implications. *Cell Mol Gastroenterol Hepatol* **7**, 503-513 (2019). https://doi.org:10.1016/j.jcmgh.2018.12.002

87 Obata, Y. *et al.* Neuronal programming by microbiota regulates intestinal physiology. *Nature* **578**, 284-289 (2020). https://doi.org:10.1038/s41586-020-1975-8

88 Spencer, N. J. & Hu, H. Enteric nervous system: sensory transduction, neural circuits and gastrointestinal motility. *Nat Rev Gastroenterol Hepatol* **17**, 338-351 (2020). https://doi.org:10.1038/s41575-020-0271-2

89 Hussey, G. S., Keane, T. J. & Badylak, S. F. The extracellular matrix of the gastrointestinal tract: a regenerative medicine platform. *Nat Rev Gastroenterol Hepatol* **14**, 540-552 (2017). https://doi.org:10.1038/nrgastro.2017.76

90 Darwich, A. S., Aslam, U., Ashcroft, D. M. & Rostami-Hodjegan, A. Meta-analysis of the turnover of intestinal epithelia in preclinical animal species and humans. *Drug Metab Dispos* **42**, 2016-2022 (2014). https://doi.org:10.1124/dmd.114.058404

91 Cheng, H. & Leblond, C. P. Origin, differentiation and renewal of the four main epithelial cell types in the mouse small intestine. V. Unitarian Theory of the origin of the four epithelial cell types. *Am J Anat* **141**, 537-561 (1974). https://doi.org:10.1002/aja.1001410407

92 Schepers, A. & Clevers, H. Wnt signaling, stem cells, and cancer of the gastrointestinal tract. *Cold Spring Harb Perspect Biol* **4**, a007989 (2012). https://doi.org:10.1101/cshperspect.a007989

93 Itzkovitz, S., Blat, I. C., Jacks, T., Clevers, H. & van Oudenaarden, A. Optimality in the development of intestinal crypts. *Cell* **148**, 608-619 (2012). https://doi.org:10.1016/j.cell.2011.12.025

94 Ishikawa, K. *et al.* Identification of Quiescent LGR5(+) Stem Cells in the Human Colon. *Gastroenterology* (2022). https://doi.org:10.1053/j.gastro.2022.07.081

95 Rees, W. D., Tandun, R., Yau, E., Zachos, N. C. & Steiner, T. S. Regenerative Intestinal Stem Cells Induced by Acute and Chronic Injury: The Saving Grace of the Epithelium? *Front Cell Dev Biol* **8**, 583919 (2020). https://doi.org:10.3389/fcell.2020.583919

96 Barker, N., van de Wetering, M. & Clevers, H. The intestinal stem cell. *Genes Dev* **22**, 1856-1864 (2008). https://doi.org:10.1101/gad.1674008

97 Davis, H. *et al.* Aberrant epithelial GREM1 expression initiates colonic tumorigenesis from cells outside the stem cell niche. *Nat Med* **21**, 62-70 (2015). https://doi.org:10.1038/nm.3750

98 Vermeulen, L. & Snippert, H. J. Stem cell dynamics in homeostasis and cancer of the intestine. *Nat Rev Cancer* **14**, 468-480 (2014). https://doi.org:10.1038/nrc3744

99 Bjerknes, M. *et al.* Origin of the brush cell lineage in the mouse intestinal epithelium. *Dev Biol* **362**, 194-218 (2012). https://doi.org:10.1016/j.ydbio.2011.12.009

100 Fujita, M., Reinhart, F. & Neutra, M. Convergence of apical and basolateral endocytic pathways at apical late endosomes in absorptive cells of suckling rat ileum in vivo. *Journal of Cell Science* **97**, 385-394 (1990).

101 Mooseker, M. S. & Tilney, L. G. Organization of an actin filament-membrane complex. Filament polarity and membrane attachment in the microvilli of intestinal epithelial cells. *J Cell Biol* **67**, 725-743 (1975). https://doi.org:10.1083/jcb.67.3.725

102 Ubelmann, F. *et al.* Enterocyte loss of polarity and gut wound healing rely upon the F-actin-severing function of villin. *Proc Natl Acad Sci U S A* **110**, E1380-1389 (2013). https://doi.org:10.1073/pnas.1218446110

103 Chang, J. *et al.* Proteomic changes during intestinal cell maturation in vivo. *J Proteomics* **71**, 530-546 (2008). https://doi.org:10.1016/j.jprot.2008.08.003

104 Alpers, D. H., Mahmood, A., Engle, M., Yamagishi, F. & DeSchryver-Kecskemeti, K. The secretion of intestinal alkaline phosphatase (IAP) from the enterocyte. *J Gastroenterol* **29 Suppl 7**, 63-67 (1994).

105 Goldstein, D. J., Rogers, C. & Harris, H. Evolution of alkaline phosphatases in primates. *Proc Natl Acad Sci U S A* **79**, 879-883 (1982). https://doi.org:10.1073/pnas.79.3.879

106 Kiela, P. R. & Ghishan, F. K. Physiology of Intestinal Absorption and Secretion. *Best Pract Res Clin Gastroenterol* **30**, 145-159 (2016). https://doi.org:10.1016/j.bpg.2016.02.007

107 Tso, P. & Balint, J. A. Formation and transport of chylomicrons by enterocytes to the lymphatics. *Am J Physiol* **250**, G715-726 (1986). https://doi.org:10.1152/ajpgi.1986.250.6.G715

108 Mabbott, N. A., Donaldson, D. S., Ohno, H., Williams, I. R. & Mahajan, A. Microfold (M) cells: important immunosurveillance posts in the intestinal epithelium. *Mucosal Immunol* **6**, 666-677 (2013). https://doi.org:10.1038/mi.2013.30

109 Knoop, K. A. *et al.* RANKL is necessary and sufficient to initiate development of antigen-sampling M cells in the intestinal epithelium. *J Immunol* **183**, 5738-5747 (2009). https://doi.org:10.4049/jimmunol.0901563

110 Crosnier, C., Stamataki, D. & Lewis, J. Organizing cell renewal in the intestine: stem cells, signals and combinatorial control. *Nat Rev Genet* **7**, 349-359 (2006). https://doi.org:10.1038/nrg1840

111 Matsuo, K., Ota, H., Akamatsu, T., Sugiyama, A. & Katsuyama, T. Histochemistry of the surface mucous gel layer of the human colon. *Gut* **40**, 782-789 (1997). https://doi.org:10.1136/gut.40.6.782

112 Johansson, M. E., Larsson, J. M. & Hansson, G. C. The two mucus layers of colon are organized by the MUC2 mucin, whereas the outer layer is a legislator of host-microbial interactions. *Proc Natl Acad Sci U S A* **108 Suppl 1**, 4659-4665 (2011). https://doi.org:10.1073/pnas.1006451107

113 Specian, R. D. & Oliver, M. G. Functional biology of intestinal goblet cells. *Am J Physiol* **260**, C183-193 (1991). https://doi.org:10.1152/ajpcell.1991.260.2.C183

114 Gassler, N. Paneth cells in intestinal physiology and pathophysiology. *World J Gastrointest Pathophysiol* **8**, 150-160 (2017). https://doi.org:10.4291/wjgp.v8.i4.150

115 Batlle, E. *et al.* Beta-catenin and TCF mediate cell positioning in the intestinal epithelium by controlling the expression of EphB/ephrinB. *Cell* **111**, 251-263 (2002). https://doi.org:10.1016/s0092-8674(02)01015-2

116 Stahl, M. *et al.* The Muc2 mucin coats murine Paneth cell granules and facilitates their content release and dispersion. *Am J Physiol Gastrointest Liver Physiol* **315**, G195-G205 (2018). https://doi.org:10.1152/ajpgi.00264.2017

117 Sato, T. *et al.* Paneth cells constitute the niche for Lgr5 stem cells in intestinal crypts. *Nature* **469**, 415-418 (2011). https://doi.org:10.1038/nature09637

118 Gunawardene, A. R., Corfe, B. M. & Staton, C. A. Classification and functions of enteroendocrine cells of the lower gastrointestinal tract. *Int J Exp Pathol* **92**, 219-231 (2011). https://doi.org:10.1111/j.1365-2613.2011.00767.x

119 Worthington, J. J., Reimann, F. & Gribble, F. M. Enteroendocrine cells-sensory sentinels of the intestinal environment and orchestrators of mucosal immunity. *Mucosal Immunol* **11**, 3-20 (2018). https://doi.org:10.1038/mi.2017.73

120 Engelstoft, M. S. *et al.* Research Resource: A Chromogranin A Reporter for Serotonin and Histamine Secreting Enteroendocrine Cells. *Mol Endocrinol* **29**, 1658-1671 (2015). https://doi.org:10.1210/me.2015-1106

121 Muntjewerff, E. M., Dunkel, G., Nicolasen, M. J. T., Mahata, S. K. & van den Bogaart, G. Catestatin as a Target for Treatment of Inflammatory Diseases. *Front Immunol* **9** (2018). https://doi.org:ARTN 2199 10.3389/fimmu.2018.02199

122 Portela-Gomes, G. M., Stridsberg, M., Johansson, H. & Grimelius, L. Co-localization of synaptophysin with different neuroendocrine hormones in the

human gastrointestinal tract. *Histochem Cell Biol* **111**, 49-54 (1999). https://doi.org:10.1007/s004180050332

123 Latorre, R., Sternini, C., De Giorgio, R. & Greenwood-Van Meerveld, B. Enteroendocrine cells: a review of their role in brain-gut communication. *Neurogastroent Motil* **28**, 620-630 (2016). https://doi.org:10.1111/nmo.12754

124 Gerbe, F., Legraverend, C. & Jay, P. The intestinal epithelium tuft cells: specification and function. *Cell Mol Life Sci* **69**, 2907-2917 (2012). https://doi.org:10.1007/s00018-012-0984-7

125 Gerbe, F. *et al.* Intestinal epithelial tuft cells initiate type 2 mucosal immunity to helminth parasites. *Nature* **529**, 226-230 (2016). https://doi.org:10.1038/nature16527

126 von Moltke, J., Ji, M., Liang, H. E. & Locksley, R. M. Tuft-cell-derived IL-25 regulates an intestinal ILC2-epithelial response circuit. *Nature* **529**, 221-225 (2016). https://doi.org:10.1038/nature16161

127 Cheng, H. & Leblond, C. P. Origin, differentiation and renewal of the four main epithelial cell types in the mouse small intestine. I. Columnar cell. *Am J Anat* **141**, 461-479 (1974). https://doi.org:10.1002/aja.1001410403

128 van de Wetering, M. *et al.* The beta-catenin/TCF-4 complex imposes a crypt progenitor phenotype on colorectal cancer cells. *Cell* **111**, 241-250 (2002). https://doi.org:10.1016/s0092-8674(02)01014-0

129 Carmon, K. S., Gong, X., Lin, Q., Thomas, A. & Liu, Q. R-spondins function as ligands of the orphan receptors LGR4 and LGR5 to regulate Wnt/β-catenin signaling. *Proc. Natl. Acad. Sci. U.S.A.* **108**, 11452-11457 (2011).

130 Bahar Halpern, K. *et al.* Lgr5+ telocytes are a signaling source at the intestinal villus tip. *Nat Commun* **11**, 1936 (2020). https://doi.org:10.1038/s41467-020-15714-x

131 Sato, T. *et al.* Single Lgr5 stem cells build crypt-villus structures in vitro without a mesenchymal niche. *Nature* **459**, 262-265 (2009). https://doi.org:10.1038/nature07935

132 Ritsma, L. *et al.* Intestinal crypt homeostasis revealed at single-stem-cell level by in vivo live imaging. *Nature* **507**, 362-+ (2014). https://doi.org:10.1038/nature12972

133 Snippert, H. J. *et al.* Intestinal crypt homeostasis results from neutral competition between symmetrically dividing Lgr5 stem cells. *Cell* **143**, 134-144 (2010). https://doi.org:10.1016/j.cell.2010.09.016

134 Farin, H. F. *et al.* Visualization of a short-range Wnt gradient in the intestinal stem-cell niche. *Nature* **530**, 340-343 (2016). https://doi.org:10.1038/nature16937

135 Azkanaz, M. *et al.* Retrograde movements determine effective stem cell numbers in the intestine. *Nature* **607**, 548-554 (2022). https://doi.org:10.1038/s41586-022-04962-0

136 Porter, E. M., Bevins, C. L., Ghosh, D. & Ganz, T. The multifaceted Paneth cell. *Cell Mol Life Sci* **59**, 156-170 (2002). https://doi.org:10.1007/s00018-002-8412-z

137 Medema, J. P. & Vermeulen, L. Microenvironmental regulation of stem cells in intestinal homeostasis and cancer. *Nature* **474**, 318-326 (2011). https://doi.org:10.1038/nature10212

138 Itzkovitz, S. *et al.* Single-molecule transcript counting of stem-cell markers in the mouse intestine. *Nat Cell Biol* **14**, 106-114 (2011). https://doi.org:10.1038/ncb2384

139 Munoz, J. *et al.* The Lgr5 intestinal stem cell signature: robust expression of proposed quiescent '+4' cell markers. *EMBO J* **31**, 3079-3091 (2012). https://doi.org:10.1038/emboj.2012.166

140 Snippert, H. J. *et al.* Prominin-1/CD133 marks stem cells and early progenitors in mouse small intestine. *Gastroenterology* **136**, 2187-2194 e2181 (2009). https://doi.org:10.1053/j.gastro.2009.03.002

141 Sato, T. *et al.* Long-term expansion of epithelial organoids from human colon, adenoma, adenocarcinoma, and Barrett's epithelium. *Gastroenterology* **141**, 1762-1772 (2011). https://doi.org:10.1053/j.gastro.2011.07.050

142 Nalapareddy, K. *et al.* Canonical Wnt Signaling Ameliorates Aging of Intestinal Stem Cells. *Cell Rep* **18**, 2608-2621 (2017). https://doi.org:10.1016/j.celrep.2017.02.056

143 Pentinmikko, N. *et al.* Notum produced by Paneth cells attenuates regeneration of aged intestinal epithelium. *Nature* **571**, 398-402 (2019). https://doi.org:10.1038/s41586-019-1383-0

144 Li, L. & Clevers, H. Coexistence of quiescent and active adult stem cells in mammals. *Science* **327**, 542-545 (2010). https://doi.org:10.1126/science.1180794

145 Escobar, M. *et al.* Intestinal epithelial stem cells do not protect their genome by asymmetric chromosome segregation. *Nat Commun* **2**, 258 (2011). https://doi.org:10.1038/ncomms1260

146 Schepers, A. G., Vries, R., van den Born, M., van de Wetering, M. & Clevers, H. Lgr5 intestinal stem cells have high telomerase activity and randomly segregate their chromosomes. *EMBO J* **30**, 1104-1109 (2011). https://doi.org:10.1038/emboj.2011.26

147 Carroll, T. D., Newton, I. P., Chen, Y., Blow, J. J. & Nathke, I. Lgr5(+) intestinal stem cells reside in an unlicensed G(1) phase. *J Cell Biol* **217**, 1667-1685 (2018). https://doi.org:10.1083/jcb.201708023

148 Davidson, L. A. *et al.* Alteration of colonic stem cell gene signatures during the regenerative response to injury. *Biochim Biophys Acta* **1822**, 1600-1607 (2012). https://doi.org:10.1016/j.bbadis.2012.06.011

149 Sangiorgi, E. & Capecchi, M. R. Bmi1 is expressed in vivo in intestinal stem cells. *Nat Genet* **40**, 915-920 (2008). https://doi.org:10.1038/ng.165

150 Tian, H. *et al.* A reserve stem cell population in small intestine renders Lgr5-positive cells dispensable. *Nature* **478**, 255-259 (2011). https://doi.org:10.1038/nature10408

151 Yan, K. S. *et al.* The intestinal stem cell markers Bmi1 and Lgr5 identify two functionally distinct populations. *Proc Natl Acad Sci U S A* **109**, 466-471 (2012). https://doi.org:10.1073/pnas.1118857109

152 Takeda, N. *et al.* Interconversion between intestinal stem cell populations in distinct niches. *Science* **334**, 1420-1424 (2011).

153 Powell, A. E. *et al.* The pan-ErbB negative regulator Lrig1 is an intestinal stem cell marker that functions as a tumor suppressor. *Cell* **149**, 146-158 (2012).

154 Asfaha, S. *et al.* Krt19(+)/Lgr5(-) Cells Are Radioresistant Cancer-Initiating Stem Cells in the Colon and Intestine. *Cell Stem Cell* **16**, 627-638 (2015). https://doi.org:10.1016/j.stem.2015.04.013

155 Barriga, F. M. *et al.* Mex3a Marks a Slowly Dividing Subpopulation of Lgr5+ Intestinal Stem Cells. *Cell Stem Cell* **20**, 801-816 e807 (2017). https://doi.org:10.1016/j.stem.2017.02.007

156 Barker, J. M., Charlier, T. D., Ball, G. F. & Balthazart, J. A new method for in vitro detection of bromodeoxyuridine in serum: a proof of concept in a songbird species, the canary. *PLoS One* **8**, e63692 (2013). https://doi.org:10.1371/journal.pone.0063692

157 Rudling, R., Hassan, A. B., Kitau, J., Mandir, N. & Goodlad, R. A. A simple device to rapidly prepare whole mounts of murine intestine. *Cell Prolif* **39**, 415-420 (2006). https://doi.org:10.1111/j.1365-2184.2006.00391.x

158 Bialkowska, A. B., Ghaleb, A. M., Nandan, M. O. & Yang, V. W. Improved Swiss-rolling Technique for Intestinal Tissue Preparation for Immunohistochemical and Immunofluorescent Analyses. *J Vis Exp* (2016). https://doi.org:10.3791/54161

159 Tang, X., Falls, D. L., Li, X., Lane, T. & Luskin, M. B. Antigen-retrieval procedure for bromodeoxyuridine immunolabeling with concurrent labeling of nuclear DNA and antigens damaged by HCl pretreatment. *J Neurosci* **27**, 5837-5844 (2007). https://doi.org:10.1523/JNEUROSCI.5048-06.2007

160 Schindelin, J. *et al.* Fiji: an open-source platform for biological-image analysis. *Nat Methods* **9**, 676-682 (2012). https://doi.org:10.1038/nmeth.2019

161 Caldwell, C. *et al.* Validation of a DKK1 RNAscope chromogenic in situ hybridization assay for gastric and gastroesophageal junction adenocarcinoma tumors. *Sci Rep* **11**, 9920 (2021). https://doi.org:10.1038/s41598-021-89060-3

162 Simons, B. D. & Clevers, H. Stem cell self-renewal in intestinal crypt. *Exp Cell Res* **317**, 2719-2724 (2011). https://doi.org:10.1016/j.yexcr.2011.07.010

163 Nowakowski, R. S., Lewin, S. B. & Miller, M. W. Bromodeoxyuridine immunohistochemical determination of the lengths of the cell cycle and the DNA-synthetic phase for an anatomically defined population. *J Neurocytol* **18**, 311-318 (1989). https://doi.org:10.1007/BF01190834

164 Miller, I. *et al.* Ki67 is a Graded Rather than a Binary Marker of Proliferation versus Quiescence. *Cell Rep* **24**, 1105-1112 e1105 (2018). https://doi.org:10.1016/j.celrep.2018.06.110

165 Kwak, S. G. & Kim, J. H. Central limit theorem: the cornerstone of modern statistics. *Korean J Anesthesiol* **70**, 144-156 (2017). https://doi.org:10.4097/kjae.2017.70.2.144

166 Buret, A., Hardin, J., Olson, M. E. & Gall, D. G. Adaptation of the small intestine in desert-dwelling animals: morphology, ultrastructure and electrolyte transport in the jejunum of rabbits, rats, gerbils and sand rats. *Comp Biochem Physiol Comp Physiol* **105**, 157-163 (1993). https://doi.org:10.1016/0300-9629(93)90189-b

167 Caviedes-Vidal, E. *et al.* The digestive adaptation of flying vertebrates: high intestinal paracellular absorption compensates for smaller guts. *Proc Natl Acad Sci U S A* **104**, 19132-19137 (2007). https://doi.org:10.1073/pnas.0703159104

168 De Cuyper, A. *et al.* The uneven weight distribution between predators and prey: Comparing gut fill between terrestrial herbivores and carnivores. *Comp Biochem Phys A* **243** (2020). https://doi.org:ARTN 110683 10.1016/j.cbpa.2020.110683

169 Yilmaz, O. H. *et al.* mTORC1 in the Paneth cell niche couples intestinal stem-cell function to calorie intake. *Nature* **486**, 490-495 (2012). https://doi.org:10.1038/nature11163

170 Dekaney, C. M. *et al.* Expansion of intestinal stem cells associated with long-term adaptation following ileocecal resection in mice. *Am J Physiol Gastrointest Liver Physiol* **293**, G1013-1022 (2007). https://doi.org:10.1152/ajpgi.00218.2007

171 Muenchau, S. *et al.* Hypoxic Environment Promotes Barrier Formation in Human Intestinal Epithelial Cells through Regulation of MicroRNA 320a Expression. *Molecular and Cellular Biology* **39** (2019). https://doi.org:ARTN e00553-18
10.1128/MCB.00553-18

172 Barros, P. R., Costa, T. J., Akamine, E. H. & Tostes, R. C. Vascular Aging in Rodent Models: Contrasting Mechanisms Driving the Female and Male Vascular Senescence. *Front Aging* **2**, 727604 (2021). https://doi.org:10.3389/fragi.2021.727604

173 Wright, N. A., Carter, J. & Irwin, M. The measurement of villus cell population size in the mouse small intestine in normal and abnormal states: a comparison of absolute measurements with morphometric estimators in sectioned immersion-fixed material. *Cell Tissue Kinet* **22**, 425-450 (1989). https://doi.org:10.1111/j.1365-2184.1989.tb00227.x

174 Reicher, N., Melkman-Zehavi, T., Dayan, J. & Uni, Z. It's All About Timing: Early Feeding Promotes Intestinal Maturation by Shifting the Ratios of Specialized Epithelial Cells in Chicks. *Front Physiol* **11**, 596457 (2020). https://doi.org:10.3389/fphys.2020.596457

175 Tremblay, S. *et al.* Ileal antimicrobial peptide expression is dysregulated in old age. *Immun Ageing* **14**, 19 (2017). https://doi.org:10.1186/s12979-017-0101-8

176 Wang, R. & Hasnain, S. Z. Analyzing the Properties of Murine Intestinal Mucins by Electrophoresis and Histology. *Bio Protoc* **7**, e2394 (2017). https://doi.org:10.21769/BioProtoc.2394

177 Greco, V., Lauro, G., Fabbrini, A. & Torsoli, A. Histochemistry of the colonic epithelial mucins in normal subjects and in patients with ulcerative colitis. A qualitative and histophotometric investigation. *Gut* **8**, 491-496 (1967). https://doi.org:10.1136/gut.8.5.491

178 Xie, Q. M., Zhang, Y., Mahmood, S. & Alpers, D. H. Rat intestinal alkaline phosphatase II messenger RNA is present in duodenal crypt and villus cells. *Gastroenterology* **112**, 376-386 (1997). https://doi.org:10.1053/gast.1997.v112.pm9024291

179 Gomes, J. R. *et al.* Goblet cells and intestinal Alkaline phosphatase expression (IAP) during the development of the rat small intestine. *Acta Histochem* **119**, 71-77 (2017). https://doi.org:10.1016/j.acthis.2016.11.010

180 Narisawa, S. *et al.* Accelerated fat absorption in intestinal alkaline phosphatase knockout mice. *Mol Cell Biol* **23**, 7525-7530 (2003). https://doi.org:10.1128/MCB.23.21.7525-7530.2003

181 Sugimoto, S. *et al.* Reconstruction of the Human Colon Epithelium In Vivo. *Cell Stem Cell* **22**, 171-176 e175 (2018). https://doi.org:10.1016/j.stem.2017.11.012

182 Barker, N. *et al.* Lgr5(+ve) stem cells drive self-renewal in the stomach and build long-lived gastric units in vitro. *Cell Stem Cell* **6**, 25-36 (2010). https://doi.org:10.1016/j.stem.2009.11.013

183 Cao, W. *et al.* Dynamics of Proliferative and Quiescent Stem Cells in Liver Homeostasis and Injury. *Gastroenterology* **153**, 1133-1147 (2017). https://doi.org:10.1053/j.gastro.2017.07.006

184 Haegebarth, A. & Clevers, H. Wnt signaling, lgr5, and stem cells in the intestine and skin. *Am J Pathol* **174**, 715-721 (2009). https://doi.org:10.2353/ajpath.2009.080758

185 Barker, N. *et al.* Lgr5(+ve) stem/progenitor cells contribute to nephron formation during kidney development. *Cell Rep* **2**, 540-552 (2012). https://doi.org:10.1016/j.celrep.2012.08.018

186 Dehmer, J. J. *et al.* Expansion of intestinal epithelial stem cells during murine development. *PLoS One* **6**, e27070 (2011). https://doi.org:10.1371/journal.pone.0027070

187 Bennett, N. C. & Jarvis, J. U. M. Coefficients of Digestibility and Nutritional Values of Geophytes and Tubers Eaten by Southern African Mole-Rats (Rodentia, Bathyergidae). *J Zool* **236**, 189-198 (1995). https://doi.org:DOI 10.1111/j.1469-7998.1995.tb04487.x

188 Aiello, L. C. & Wheeler, P. The Expensive-Tissue Hypothesis - the Brain and the Digestive-System in Human and Primate Evolution. *Curr Anthropol* **36**, 199-221 (1995). https://doi.org:Doi 10.1086/204350

189 Duque-Correa, M. J. *et al.* Mammalian intestinal allometry, phylogeny, trophic level and climate. *Proc Biol Sci* **288**, 20202888 (2021). https://doi.org:10.1098/rspb.2020.2888

190 Johansson, M. E. V., Sjovall, H. & Hansson, G. C. The gastrointestinal mucus system in health and disease. *Nat Rev Gastro Hepat* **10**, 352-361 (2013). https://doi.org:10.1038/nrgastro.2013.35

191 Fre, S. *et al.* Notch signals control the fate of immature progenitor cells in the intestine. *Nature* **435**, 964-968 (2005). https://doi.org:10.1038/nature03589

192 Hooper, C. E. Cell turnover in epithelial populations. *J Histochem Cytochem* **4**, 531-540 (1956). https://doi.org:10.1177/4.6.531

193 Spalding, K. L., Bhardwaj, R. D., Buchholz, B. A., Druid, H. & Frisen, J. Retrospective birth dating of cells in humans. *Cell* **122**, 133-143 (2005). https://doi.org:10.1016/j.cell.2005.04.028

194 Milo, R., Jorgensen, P., Moran, U., Weber, G. & Springer, M. BioNumbers--the database of key numbers in molecular and cell biology. *Nucleic Acids Res* **38**, D750-753 (2010). https://doi.org:10.1093/nar/gkp889

195 Ohlstein, B. & Spradling, A. The adult Drosophila posterior midgut is maintained by pluripotent stem cells. *Nature* **439**, 470-474 (2006).

196 Rijke, R. P., Plaisier, H. M. & Langendoen, N. J. Epithelial cell kinetics in the descending colon of the rat. *Virchows Arch B Cell Pathol Incl Mol Pathol* **30**, 85-94 (1979). https://doi.org:10.1007/BF02889093

197 Cheshier, S. H., Morrison, S. J., Liao, X. & Weissman, I. L. In vivo proliferation and cell cycle kinetics of long-term self-renewing hematopoietic stem cells. *Proc Natl Acad Sci U S A* **96**, 3120-3125 (1999). https://doi.org:10.1073/pnas.96.6.3120

198 Gerdes, J. *et al.* Cell cycle analysis of a cell proliferation-associated human nuclear antigen defined by the monoclonal antibody Ki-67. *J Immunol* **133**, 1710-1715 (1984).

199 Ishida, S. *et al.* Role for E2F in control of both DNA replication and mitotic functions as revealed from DNA microarray analysis. *Mol Cell Biol* **21**, 4684-4699 (2001). https://doi.org:10.1128/MCB.21.14.4684-4699.2001

200 Sobecki, M. *et al.* Cell-Cycle Regulation Accounts for Variability in Ki-67 Expression Levels. *Cancer Res* **77**, 2722-2734 (2017). https://doi.org:10.1158/0008-5472.CAN-16-0707

201 Kill, I. R. Localisation of the Ki-67 antigen within the nucleolus. Evidence for a fibrillarin-deficient region of the dense fibrillar component. *J Cell Sci* **109 (Pt 6)**, 1253-1263 (1996). https://doi.org:10.1242/jcs.109.6.1253

202 Basak, O. *et al.* Mapping early fate determination in Lgr5+ crypt stem cells using a novel Ki67-RFP allele. *EMBO J* **33**, 2057-2068 (2014). https://doi.org:10.15252/embj.201488017

203 Susaki, E., Nakayama, K. & Nakayama, K. I. Cyclin D2 translocates p27 out of the nucleus and promotes its degradation at the G0-G1 transition. *Mol Cell Biol* **27**, 4626-4640 (2007). https://doi.org:10.1128/MCB.00862-06

204 Besson, A. *et al.* A pathway in quiescent cells that controls p27Kip1 stability, subcellular localization, and tumor suppression. *Genes Dev* **20**, 47-64 (2006). https://doi.org:10.1101/gad.1384406

205 Oki, T. *et al.* A novel cell-cycle-indicator, mVenus-p27K-, identifies quiescent cells and visualizes G0-G1 transition. *Sci Rep* **4**, 4012 (2014). https://doi.org:10.1038/srep04012

206 Grimes, K. M. *et al.* The naked mole-rat exhibits an unusual cardiac myofilament protein profile providing new insights into heart function of this naturally subterranean rodent. *Pflugers Arch* **469**, 1603-1613 (2017). https://doi.org:10.1007/s00424-017-2046-3

207 Schulze-Makuch, D. The Naked Mole-Rat: An Unusual Organism with an Unexpected Latent Potential for Increased Intelligence? *Life (Basel)* **9** (2019). https://doi.org:10.3390/life9030076

208 Mandyam, C. D., Harburg, G. C. & Eisch, A. J. Determination of key aspects of precursor cell proliferation, cell cycle length and kinetics in the adult mouse subgranular zone. *Neuroscience* **146**, 108-122 (2007). https://doi.org:10.1016/j.neuroscience.2006.12.064

209 Taupin, P. BrdU immunohistochemistry for studying adult neurogenesis: paradigms, pitfalls, limitations, and validation. *Brain Res Rev* **53**, 198-214 (2007). https://doi.org:10.1016/j.brainresrev.2006.08.002

210 Falconer, E., Chavez, E., Henderson, A. & Lansdorp, P. M. Chromosome orientation fluorescence in situ hybridization to study sister chromatid segregation in vivo. *Nat Protoc* **5**, 1362-1377 (2010). https://doi.org:10.1038/nprot.2010.102

211 Hirata, A. *et al.* Characterization of a monoclonal antibody, HTA28, recognizing a histone H3 phosphorylation site as a useful marker of M-phase cells. *J Histochem Cytochem* **52**, 1503-1509 (2004). https://doi.org:10.1369/jhc.4A6285.2004

212 Goto, H. *et al.* Identification of a novel phosphorylation site on histone H3 coupled with mitotic chromosome condensation. *J Biol Chem* **274**, 25543-25549 (1999). https://doi.org:10.1074/jbc.274.36.25543

213 Matthews, H. K., Bertoli, C. & de Bruin, R. A. M. Cell cycle control in cancer. *Nat Rev Mol Cell Biol* **23**, 74-88 (2022). https://doi.org:10.1038/s41580-021-00404-3

214 MacRae, S. L. *et al.* DNA repair in species with extreme lifespan differences. *Aging (Albany NY)* **7**, 1171-1184 (2015). https://doi.org:10.18632/aging.100866

215 Shyh-Chang, N. & Ng, H. H. The metabolic programming of stem cells. *Genes Dev* **31**, 336-346 (2017). https://doi.org:10.1101/gad.293167.116

216 Tothova, Z. *et al.* FoxOs are critical mediators of hematopoietic stem cell resistance to physiologic oxidative stress. *Cell* **128**, 325-339 (2007). https://doi.org:10.1016/j.cell.2007.01.003

217 Suda, T., Takubo, K. & Semenza, G. L. Metabolic regulation of hematopoietic stem cells in the hypoxic niche. *Cell Stem Cell* **9**, 298-310 (2011). https://doi.org:10.1016/j.stem.2011.09.010

218 Cameron, I. L. & Greulich, R. C. Evidence for an essentially constant duration of DNA synthesis in renewing epithelia of the adult mouse. *J Cell Biol* **18**, 31-40 (1963). https://doi.org:10.1083/jcb.18.1.31

219 Govindasamy, N., Murthy, S. & Ghanekar, Y. Slow-cycling stem cells in hydra contribute to head regeneration. *Biol Open* **3**, 1236-1244 (2014). https://doi.org:10.1242/bio.201410512

220 Fuchs, E. The tortoise and the hair: slow-cycling cells in the stem cell race. *Cell* **137**, 811-819 (2009). https://doi.org:10.1016/j.cell.2009.05.002

221 da Silva, P. F. L. & Schumacher, B. DNA damage responses in ageing. *Open Biol* **9**, 190168 (2019). https://doi.org:10.1098/rsob.190168

222 Omotoso, O., Gladyshev, V. N. & Zhou, X. Lifespan Extension in Long-Lived Vertebrates Rooted in Ecological Adaptation. *Front Cell Dev Biol* **9**, 704966 (2021). https://doi.org:10.3389/fcell.2021.704966

223 Koh, J. *et al.* ABCB1 protects bat cells from DNA damage induced by genotoxic compounds. *Nat Commun* **10**, 2820 (2019). https://doi.org:10.1038/s41467-019-10495-4

224 Siddiqui, R., Maciver, S., Elmoselhi, A., Soares, N. C. & Khan, N. A. Longevity, cellular senescence and the gut microbiome: lessons to be learned from crocodiles. *Heliyon* **7**, e08594 (2021). https://doi.org:10.1016/j.heliyon.2021.e08594

225 Hilton, H. G. *et al.* Single-cell transcriptomics of the naked mole-rat reveals unexpected features of mammalian immunity. *PLoS Biol* **17**, e3000528 (2019). https://doi.org:10.1371/journal.pbio.3000528

226 Okayasu, I. *et al.* A novel method in the induction of reliable experimental acute and chronic ulcerative colitis in mice. *Gastroenterology* **98**, 694-702 (1990). https://doi.org:10.1016/0016-5085(90)90290-h

227 Yan, Y. *et al.* Temporal and spatial analysis of clinical and molecular parameters in dextran sodium sulfate induced colitis. *PLoS One* **4**, e6073 (2009). https://doi.org:10.1371/journal.pone.0006073

228 Girish, N. *et al.* Persistence of Lgr5+ colonic epithelial stem cells in mouse models of inflammatory bowel disease. *Am J Physiol Gastrointest Liver Physiol* **321**, G308-G324 (2021). https://doi.org:10.1152/ajpgi.00248.2020

229 Adamkova, P. *et al.* Dextran Sulphate Sodium Acute Colitis Rat Model: A Suitable Tool for Advancing Our Understanding of Immune and Microbial Mechanisms in the Pathogenesis of Inflammatory Bowel Disease. *Vet Sci* **9** (2022). https://doi.org:10.3390/vetsci9050238

230 Brenna, O. *et al.* Relevance of TNBS-colitis in rats: a methodological study with endoscopic, histologic and Transcriptomic [corrected] characterization and correlation to IBD. *PLoS One* **8**, e54543 (2013). https://doi.org:10.1371/journal.pone.0054543

231 Leonardi, I. *et al.* Oral administration of dextran sodium sulphate induces a caecum-localized colitis in rabbits. *Int J Exp Pathol* **96**, 151-162 (2015). https://doi.org:10.1111/iep.12117

232 Iwanaga, T., Hoshi, O., Han, H. & Fujita, T. Morphological analysis of acute ulcerative colitis experimentally induced by dextran sulfate sodium in the guinea pig: some possible mechanisms of cecal ulceration. *J Gastroenterol* **29**, 430-438 (1994). https://doi.org:10.1007/BF02361239

233 Menon, G. K., Catania, K. C., Crumrine, D., Bradley, C. & Mauldin, E. A. Unique features of the skin barrier in naked mole rats reflect adaptations to their fossorial habitat. *J Morphol* **280**, 1871-1880 (2019). https://doi.org:10.1002/jmor.21072

234 Turner, P. V., Brabb, T., Pekow, C. & Vasbinder, M. A. Administration of substances to laboratory animals: routes of administration and factors to consider. *J Am Assoc Lab Anim Sci* **50**, 600-613 (2011).

235 Bonfiglio, R. *et al.* Extensive Histopathological Characterization of Inflamed Bowel in the Dextran Sulfate Sodium Mouse Model with Emphasis on Clinically Relevant Biomarkers and Targets for Drug Development. *Int J Mol Sci* **22** (2021). https://doi.org:10.3390/ijms22042028

236 Randall-Demllo, S. *et al.* Characterisation of colonic dysplasia-like epithelial atypia in murine colitis. *World J Gastroenterol* **22**, 8334-8348 (2016). https://doi.org:10.3748/wjg.v22.i37.8334

237 Thomas, M. P. *et al.* Apoptosis Triggers Specific, Rapid, and Global mRNA Decay with 3' Uridylated Intermediates Degraded by DIS3L2. *Cell Rep* **11**, 1079-1089 (2015). https://doi.org:10.1016/j.celrep.2015.04.026

238 Banfalvi, G. Methods to detect apoptotic cell death. *Apoptosis* **22**, 306-323 (2017). https://doi.org:10.1007/s10495-016-1333-3

239 Tetteh, P. W. *et al.* Replacement of Lost Lgr5-Positive Stem Cells through Plasticity of Their Enterocyte-Lineage Daughters. *Cell Stem Cell* **18**, 203-213 (2016). https://doi.org:10.1016/j.stem.2016.01.001

240 van Es, J. H. *et al.* Dll1+ secretory progenitor cells revert to stem cells upon crypt damage. *Nat Cell Biol* **14**, 1099-1104 (2012). https://doi.org:10.1038/ncb2581

241 Buczacki, S. J. *et al.* Intestinal label-retaining cells are secretory precursors expressing Lgr5. *Nature* **495**, 65-69 (2013). https://doi.org:10.1038/nature11965

242 Shinoda, M. *et al.* Early-stage blocking of Notch signaling inhibits the depletion of goblet cells in dextran sodium sulfate-induced colitis in mice. *J Gastroenterol* **45**, 608-617 (2010). https://doi.org:10.1007/s00535-010-0210-z

243 Hadj-Moussa, H., Eaton, L., Cheng, H., Pamenter, M. E. & Storey, K. B. Naked mole-rats resist the accumulation of hypoxia-induced oxidative damage. *Comp Biochem Physiol A Mol Integr Physiol* **273**, 111282 (2022). https://doi.org:10.1016/j.cbpa.2022.111282

244 Taguchi, T. *et al.* Naked mole-rats are extremely resistant to post-traumatic osteoarthritis. *Aging Cell* **19**, e13255 (2020). https://doi.org:10.1111/acel.13255

245 Lewis, K. N., Mele, J., Hornsby, P. J. & Buffenstein, R. Stress resistance in the naked mole-rat: the bare essentials - a mini-review. *Gerontology* **58**, 453-462 (2012). https://doi.org:10.1159/000335966

246 Findlay, J. K., Hutt, K. J., Hickey, M. & Anderson, R. A. What is the “ovarian reserve”? *Fertility and Sterility* **103**, 628-630 (2015).

247 Wallace, W. H. & Kelsey, T. W. Human ovarian reserve from conception to the menopause. *PLoS One* **5**, e8772 (2010). https://doi.org:10.1371/journal.pone.0008772

248 Andziak, B. & Buffenstein, R. Disparate patterns of age-related changes in lipid peroxidation in long-lived naked mole-rats and shorter-lived mice. *Aging Cell* **5**, 525-532 (2006). https://doi.org:10.1111/j.1474-9726.2006.00246.x

249 Buffenstein, R., Kang, J. & Biney, A. (Wiley Online Library, 2007).

250 Edrey, Y. H., Hanes, M., Pinto, M., Mele, J. & Buffenstein, R. Successful aging and sustained good health in the naked mole rat: a long-lived mammalian model for biogerontology and biomedical research. *ILAR J* **52**, 41-53 (2011). https://doi.org:10.1093/ilar.52.1.41

251 Oka, K., Yamakawa, M., Kawamura, Y., Kutsukake, N. & Miura, K. The Naked Mole-Rat as a Model for Healthy Aging. *Annual Review of Animal Biosciences* **11**, 207-226 (2023).

252 Zhang, Z. *et al.* Increased hyaluronan by naked mole-rat HAS2 extends lifespan in mice. *bioRxiv*, 2023.2005. 2004.539405 (2023).

253 Powers, E. T., Morimoto, R. I., Dillin, A., Kelly, J. W. & Balch, W. E. Biological and chemical approaches to diseases of proteostasis deficiency. *Annu Rev Biochem* **78**, 959-991 (2009). https://doi.org:10.1146/annurev.biochem.052308.114844

254 Conboy, I. M. *et al.* Rejuvenation of aged progenitor cells by exposure to a young systemic environment. *Nature* **433**, 760-764 (2005). https://doi.org:10.1038/nature03260

255 Morrison, S. J., Wandycz, A. M., Akashi, K., Globerson, A. & Weissman, I. L. The aging of hematopoietic stem cells. *Nat Med* **2**, 1011-1016 (1996). https://doi.org:10.1038/nm0996-1011

256 Pelaseyed, T. *et al.* The mucus and mucins of the goblet cells and enterocytes provide the first defense line of the gastrointestinal tract and interact with the immune system. *Immunol Rev* **260**, 8-20 (2014). https://doi.org:10.1111/imr.12182

257 Martin, M. L. *et al.* Logarithmic expansion of LGR5(+) cells in human colorectal cancer. *Cell Signal* **42**, 97-105 (2018). https://doi.org:10.1016/j.cellsig.2017.09.018

258 Hustedt, N. & Durocher, D. The control of DNA repair by the cell cycle. *Nat Cell Biol* **19**, 1-9 (2016). https://doi.org:10.1038/ncb3452

259 Nakamura, K. *et al.* H4K20me0 recognition by BRCA1-BARD1 directs homologous recombination to sister chromatids. *Nat Cell Biol* **21**, 311-318 (2019). https://doi.org:10.1038/s41556-019-0282-9

260 Beerman, I., Seita, J., Inlay, M. A., Weissman, I. L. & Rossi, D. J. Quiescent hematopoietic stem cells accumulate DNA damage during aging that is repaired upon entry into cell cycle. *Cell Stem Cell* **15**, 37-50 (2014). https://doi.org:10.1016/j.stem.2014.04.016

261 Dame, M. K. *et al.* Identification, isolation and characterization of human LGR5-positive colon adenoma cells. *Development* **145** (2018). https://doi.org:10.1242/dev.153049